High Speed Instrumentation for Inspection of Transparent Parts

by

Dean Ljubicic

Submitted to the Department of Mechanical Engineering
in partial fulfillment of the requirements for the degree of

Doctor of Philosophy in Mechanical Engineering

at the

MASSACHUSETTS INSTITUTE OF TECHNOLOGY

June 2013

Author .....
Department of Mechanical Engineering
May 18th, 2013

Certified by .....
Dr. Brian Anthony
Lecturer in Mechanical Engineering
Thesis Supervisor

Accepted by .....
David E. Hardt
Chairman, Department Committee on Graduate Theses

High Speed Instrumentation for Inspection of Transparent Parts

by

Dean Ljubicic

Submitted to the Department of Mechanical Engineering
on May 18th, 2013, in partial fulfillment of the
requirements for the degree of
Doctor of Philosophy in Mechanical Engineering

Abstract

In micro manufacturing (MEMS, polymer hot-embossing, polymer roll-to-roll imprint, etc.) precise micro and nano-sized features are distributed over large areas. In order to inspect for defects or employ statistical process control on micromanufactured parts, metrological instruments must collect data with submicron resolution at a rate fast enough to keep up with the pace of production. Commercial inspection instruments fall short on meeting these challenging demands. This doctoral thesis details the design, implementation, and results of an optical system built to provide real-time inspection for transparent polymer microfluidic devices.

Our instrument utilizes a high speed camera (500 fps) in conjunction with submicron precision positioning stages (20 nm resolution) to rapidly collect topological data on the microfluidic devices. The stream of images are processed using a depth from focus technique to provide surface inspection with 0.5 micron lateral resolution and 1 micron vertical resolution at an inspection speed of 640,000 voxels per second. The instrument also demonstrates the ability to measure vertical sidewalls as a result of the tilted orientation of the camera system providing access to these typically hidden or eclipsed areas. The 3D contour plots generated by the instrument are used to characterize a manufacturing process demonstrating automatic defect detection, repeatability analysis, and run charts that can be used in process control.

This thesis also explores the design and experimentation of a novel sensor that can simultaneously measure the thickness and lateral position of a transparent object. This capability is especially useful to control the lateral position of a transparent web with a feedback system during a manufacturing roll to roll process. The sensor measurement has demonstrated submicron repeatability over millimeters of range in both thickness and position.

Thesis Supervisor: Dr. Brian Anthony
Title: Lecturer in Mechanical Engineering

Acknowledgments

I would like to first and foremost thank my advisor Dr. Brian Anthony. His expertise in both image processing and optical engineering was an integral component to my success as a student. Furthermore, I found Brian to be a top notch advisor who was able to give me direction when I was stuck and allow me to pursue my own direction when I was not. It is clear from his heavy involvement in a myriad of other MIT programs that Dr. Anthony's talent and capability to lead does not go unnoticed.

Secondly I would like to thank Professor David Hardt who played a heavy role throughout my research as the leader of the MuFac project and Professor David Seering served as the final member of my committee. In my experience, Professor Hardt has an incredible ability to disseminate and understand complicated subject material with ease. He has a fitting role as the graduate officer for it is clear that Professor Hardt has a deep and genuine care for the wellbeing of the students. This level of expertise and amiable demeanor is mirrored by Professor Seering who has always given me great advice since my undergraduate years.

Lastly I want to again express my gratitude to my family whose encouragement and support has never faltered. While they stand 100 miles away it feels as though they have always been by my side.

Contents

List of Figures

List of Tables

Chapter 1

Introduction

This thesis presents two novel metrology instruments designed to be faster or more accurate than their commercial alternatives. The instruments developed over the course of the degree are built to measure transparent parts in a manufacturing process. First, a high speed profilometer is designed to rapidly measure the topographies of microfluidic parts made via hot embossing or injection molding. Secondly, a novel sensor is created to measure both the thickness and lateral position of a transparent web in a roll to roll process. This thesis explores the purpose, design, and results of both instruments.

1.1 High Speed Profilometer Summary

The growth rate of the micromanufacturing industry has shown a steady increase over the past decade and is forecast to continue growing well into the future. Recent developments show that production of polymer based parts can provide low cost alternative to glass or silicon substrates and are well suited for mass production [9]. The pliant nature of these parts makes them susceptible to poor feature replication and warping from residual stresses resulting in inadequate process yield. Currently metrological instrumentation capable of measuring with submicron resolution is too slow to provide in-line inspection of micromanufactured parts. This inability has been described as "one of the barriers to growth of micro-manufacturing both as

an enabling technology and a new market." [10] The lack of adequate inspection instrumentation hampers the ability to employ statistical process control.

The high speed profilometer has been created to address this micromanufacturing inspection need providing an instrument that attains both high speed and high resolution. The functional requirements of the instrument are:

0.5 micron lateral resolution

0.5 micron vertical resolution

20,000,000 data points per second inspection speed

100's of microns vertical range

100's of millimeters lateral range

Current metrological instruments with the ability to measure with submicron resolution have an estimated 30,000 data point per second inspection speed. At this rate it would take over 24 hours to measure a one inch square area at 0.5 micron resolution, far too slow to give any meaningful real time data. The instrument developed by this research was designed to overcome barriers to inspection speed in the mechanical, optical, and software domains.

A photograph of the high speed profilometer is presented in Figure 1-1 with overlain visual cues. The schematic shown in Figure 1-2 details the flow of information, signals, and power between the profilometer's components. A high speed camera focuses light through a microscope objective lens to acquire imagery of a manufactured part. The camera is tilted at an angle 45° from the vertical with each row focusing on an independent elevation. Each row of the camera collects an image in similar fashion to a line scan camera allowing the collection of 1024 line scan images simultaneously. A frame grabber imports the camera imagery which is processed by offline into a topographical map and then saved in the central computer. The part moves with constant velocity with respect to the camera allowing simplified dynamics in the mechanical system. A "depth from focus" optical technique utilizes low cost, high powered lighting that meets the light flux required for high speed imaging. Lastly,

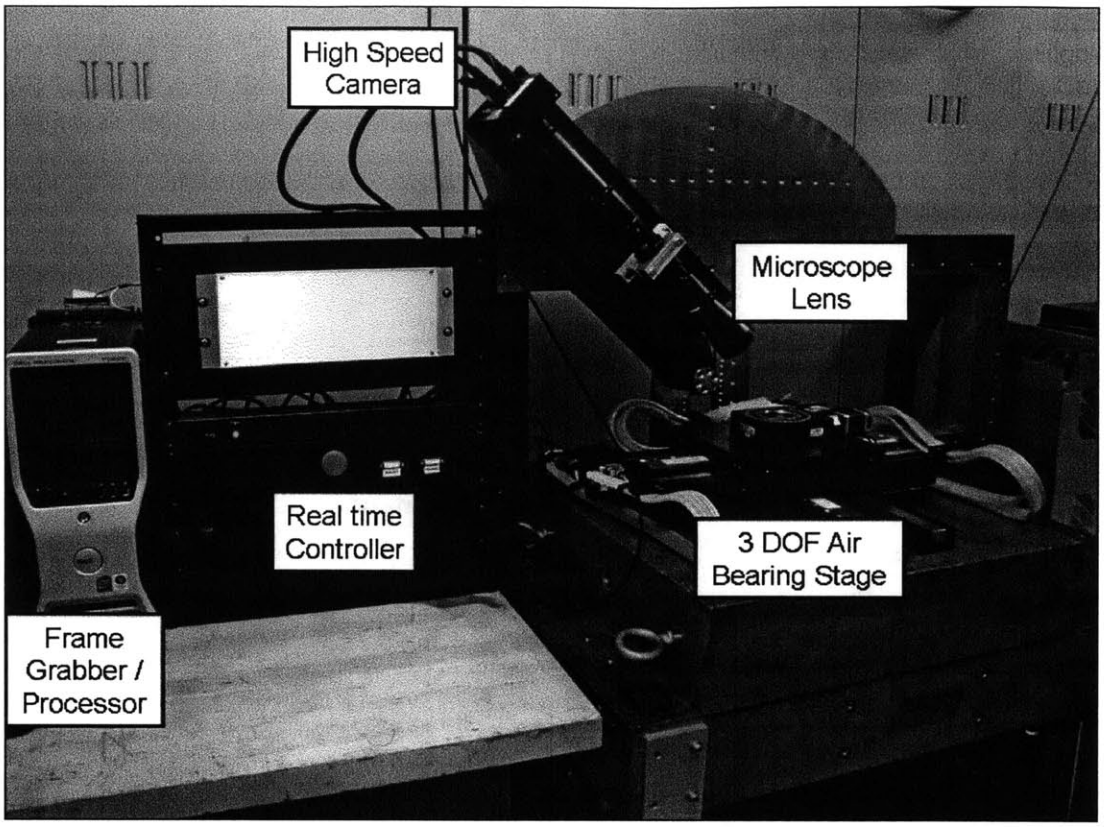

Figure 1-1: Photograph of High Speed Profilometer. This photograph labels the major components of the mechanical, optical, and software systems of the high speed profilometer to give an overview of their locations and setup.

the software algorithms are built with simple operators that can be parallelized in an FPGA. Each system has been designed to maximize the inspection speed of this profilometer.

The high speed profilometer has demonstrated the ability to scan at 0.6 μm lateral and 1 μm vertical resolution at an inspection speed of 640,000 points per second with a 135 micron vertical range. Its inspection speed is currently over ten times faster than the best comparable commercial alternative. An apples to apples comparison of our instrument against a white light interferometer and color laser scanner upon the measurement of a transparent plastic part is shown in Figure 1-3. This comparison can also be viewed parametrically by plotting the inspection speed and lateral resolution

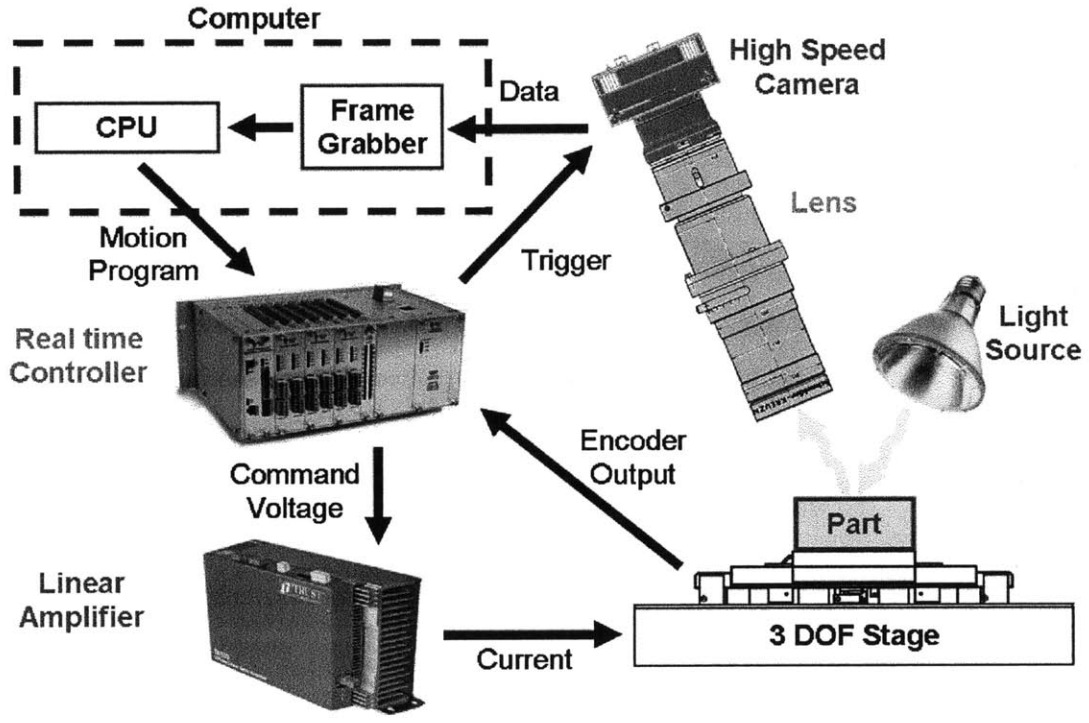

Figure 1-2: Schematic Overview of the Instrument. This schematic details the transfer of information among each component in the instrument. A central CPU programs a Delta Tau Motion controller to move the 3 DOF air bearing stage. Linear encoders in the air bearing stage measure its position which is used to trigger the camera to synchronize the motion. The images taken by the camera are collected by the frame grabber and later processed offline by the CPU.

of our instrument against commercial white light interferometers and structured light profilometers in Figure 1-4. The results displayed in this graph represent how fast our camera can collect data while processing it off line. Future work predicts the inspection speed of our instrument can be improved by an additional factor of 50 with the use of faster cameras available on the market today. Fully utilizing the camera's data stream would make the instrument reach the speed and resolution targets set forth in the functional requirements.

1.2 Edge and Thickness Detector Sensor Summary

The second arm of the research focuses on the design of a novel sensor that can simultaneously measure the thickness and lateral position of a transparent object. The transparent object being measured by the sensor needs to be flat in nature with a straight and well defined edge. In its primary application, this sensor can be used to monitor and control a transparent sheet or "web" in a roll to roll manufacturing process. The manufacturing equipment must properly unwind, process, and rewind the webs in a continuous fashion. The position of the web perpendicular to its direction of travel must be controlled to ensure proper registration between the web and its tooling.

The new sensor detailed in this research takes measurements of a transparent object by using the object as an element in the optical path. A digital camera equipped with a high numerical aperture microscope objective is used to image a known object. The appearance of the known object is altered when the unknown transparent object is inserted into the field of view of the camera. By observing and calculating this alteration the sensor can simultaneously measure the thickness and lateral position of the unknown transparent object or web with submicron resolution. These principles are depicted in Figure 1-5.

Current state-of-the-art technology uses acoustic sensors to measure the lateral position with a resolution of approximately 6 microns. The optical based sensor de-

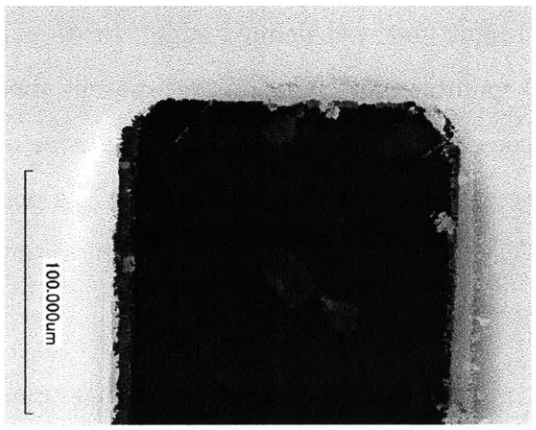

Figure 1-3: Topographical Comparison Against Industrial Profilometers. An apples to apples comparison between the high speed profilometer and the commercial alternatives was conducted by measuring the same part with all three instruments. The three images shown were collected by a white light interferometer, color laser scanner, and our instrument.

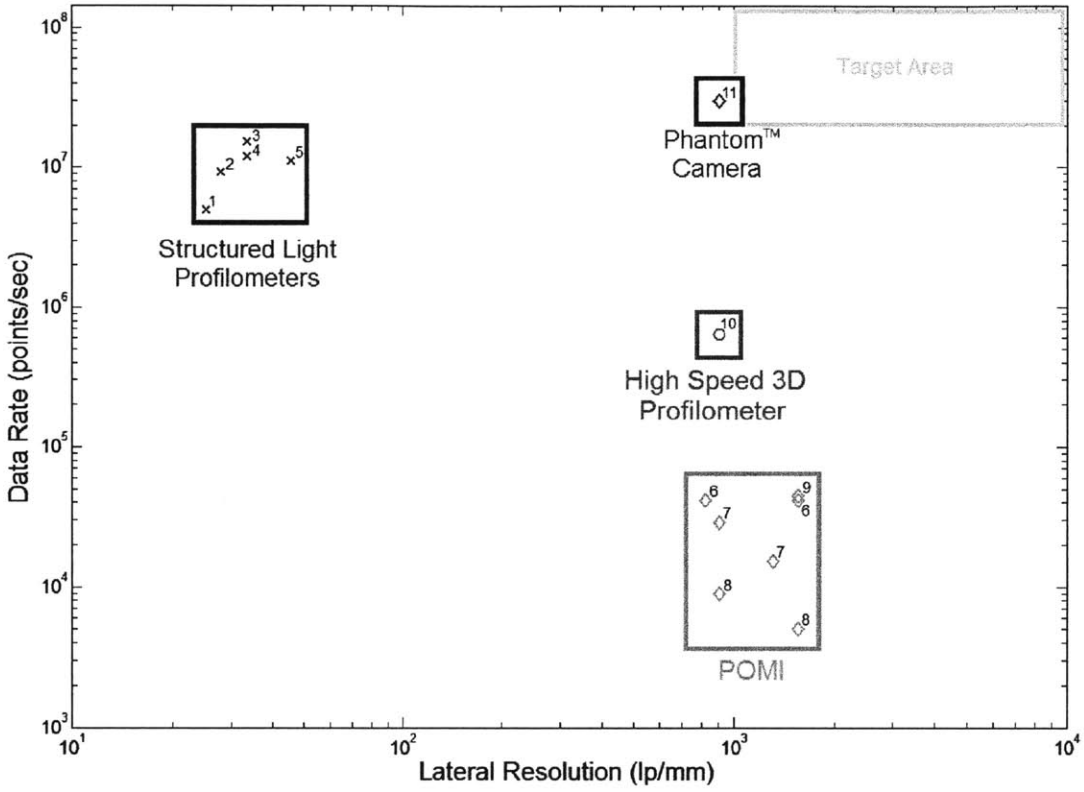

Figure 1-4: Performance Comparison Against Commercial Profilometers. Lateral resolution and inspection speed have been identified as the two most important performance parameters when evaluating commercial profilometers. Structured light profilometers have excellent speed but poor resolution while white light interferometers have excellent resolution but poor speed. Our instrument has demonstrated the ability to collect 640,000 data points per second at 0.5 micron lateral resolution and process the data off line. With faster cameras it may be possible to increase this speed by an additional factor of 50 as shown by the brown data point.

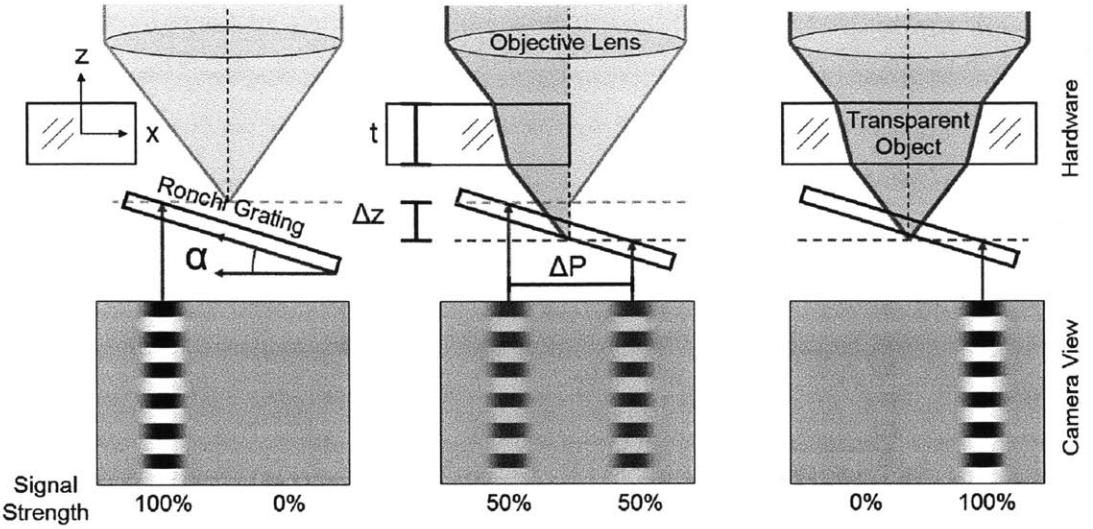

Figure 1-5: Comprehensive Cross Sectional Diagram of the Sensor. The three parts of the figure depict how the light bends about a transparent object that is absent, partially inserted, and fully inserted into the light path. The thickness of the object is measured by calculating the shift in pixels from the left and right signature while the lateral position is measured by observing their relative signal strength.

veloped in this research has demonstrated measurement of the lateral position with 0.2 micron resolution representing a 30 fold improvement. A simultaneous measurement taken by both instruments on the same transparent medium is shown in Figure 1-6.

The novel optical sensor also has the ability to measure the thickness of the glass substrate with 0.5 micron repeatability. This level of precision is comparable to a host of thickness measuring methods. In a first order comparison, the thickness of six glass slides were measured by both our instrument and a micrometer. The results are shown in Figure 1-7 bound by the theoretically derived values.

The ability of the novel sensor to accurately measure thickness and lateral position of a transparent medium makes it attractive for use on web handling processes. Future work to make a paired down version of this sensor with commercial optics can introduce a competitive product to this market.

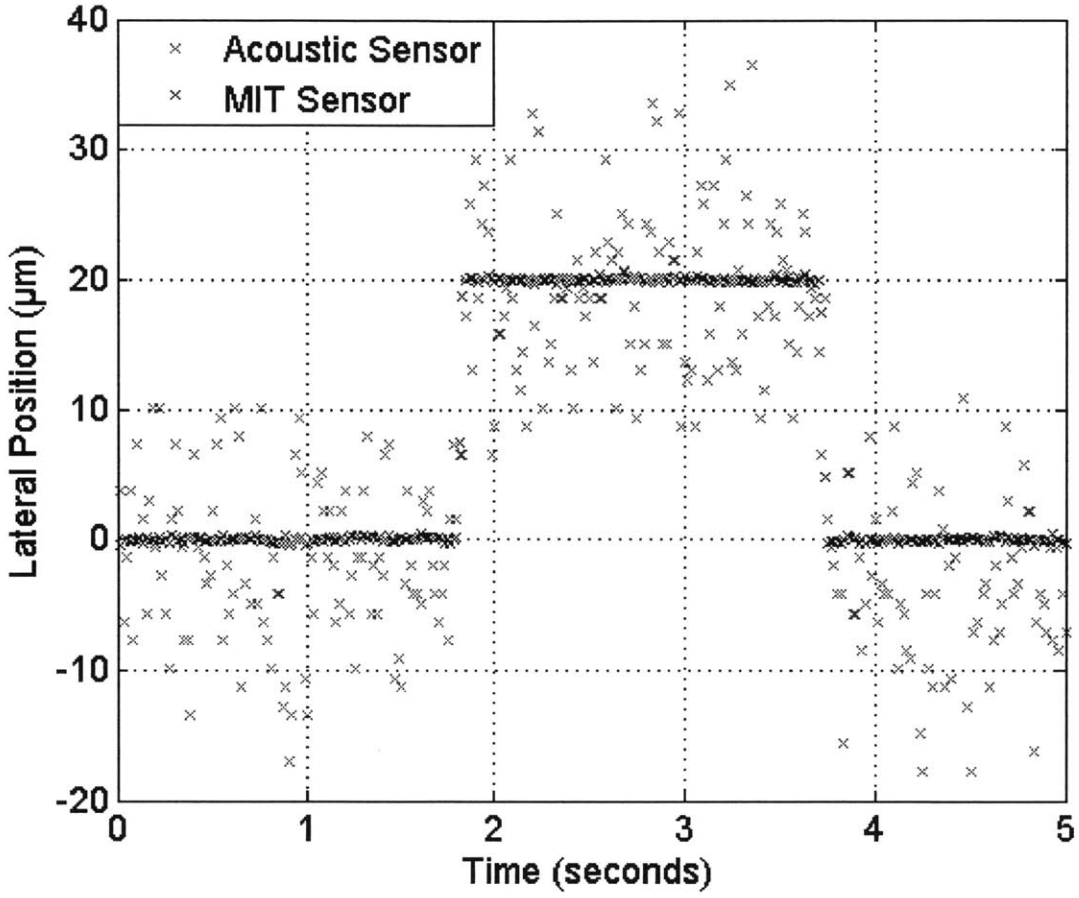

Figure 1-6: Comparison Against State of the Art Web Handling Equipment. This graph shows data collected from both the state-of-the-art acoustic sensor in blue and the novel optical sensor in red while simultaneously measuring a 20 micron displacement in position of a glass slide.

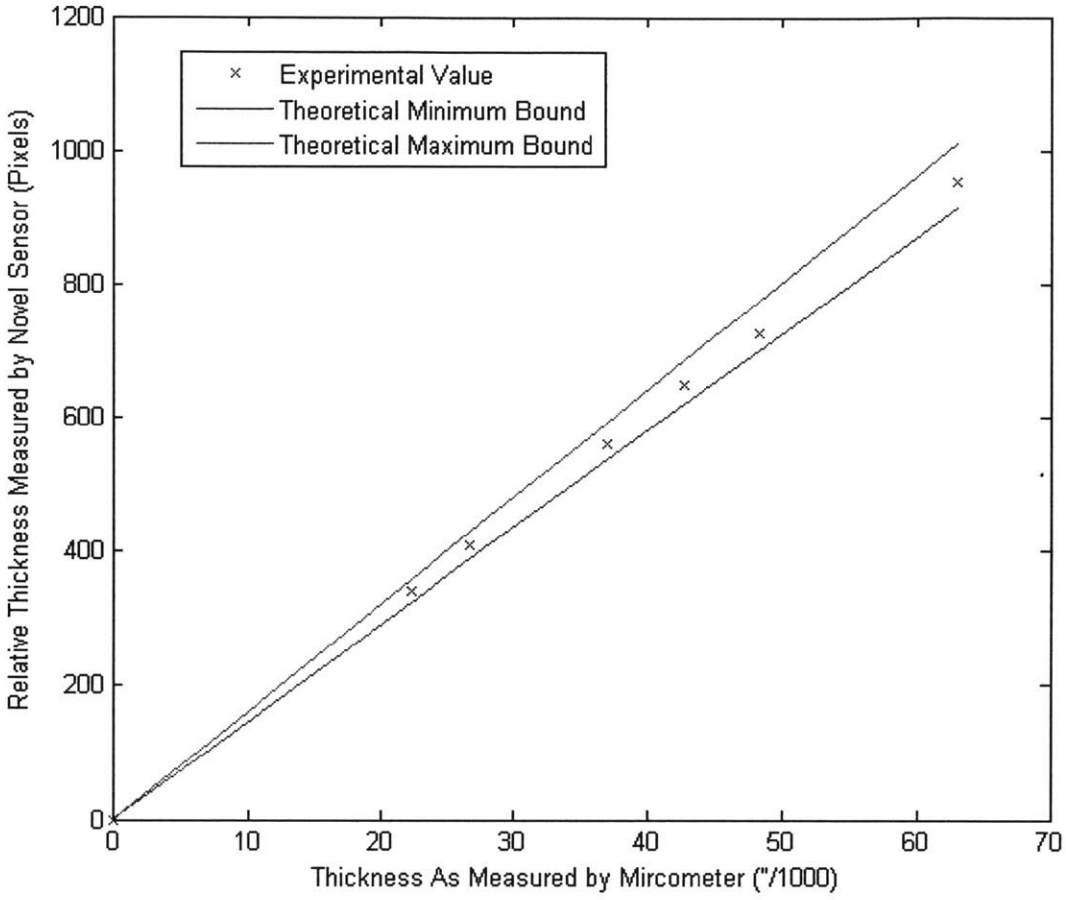

Figure 1-7: Demonstration of Thickness Measurement. Six glass slides of varying thicknesses were measured by both a micrometer and the novel thickness sensor. This graph plots both measurements against each other as well as minimum and maximum values predicted by the theoretical work.

1.3 Thesis Overview

This overview of the thesis summarizes each chapter individually. Chapter 2 brushes up on basic optical principles that serve as a foundation of knowledge to discuss and describe the design of the optical instruments. Chapters 3 and 4 compare the similarities and differences of the high speed profilometer against background research and commercial products. The depth from focus technique used by our profilometer is then described in Chapter 5. Chapters 6, 7, and 8 detail the mechanical, optical, and software design of the high speed profilometer respectively while Chapter 9 shows the collective results. Chapter 10 describes the design and implementation of the edge and thickness detector. Lastly, Chapter 11 speaks to the future work to be done on both systems.

Chapter 2

Basics of Optical Engineering

This section reviews the principles of optical engineering used in this research. An explanation of these basic principles provides a foundation of knowledge to discuss and describe the design of our optical profilometer. These concepts are used over the course of the research to ultimately quantify the limits on inspection speed, range, and lateral resolution of various profilometers. The experienced reader can omit the contents of this chapter.

2.1 Numerical Aperture

The numerical aperture (NA) is a dimensionless number that is used to quantify the performance and geometry of a lens. As depicted in Figure 2-1, a lens has an angular limit to which it can accept and bend light. This angle θ can be approximated by dividing the focal length by half the diameter of the entrance pupil. The numerical aperture is also a function of the index of refraction of the medium in which the light travels through and is defined mathematically in Equation 2.1.

$$NA = n \cdot sin\theta = n \cdot sin\left(arctan\left(\frac{D}{2 * f}\right)\right) \approx n \cdot \frac{D}{2 * f} \tag{2.1}$$

Most inspectional metrology profilometers are used in open air conditions where the index of refraction n is approximately equal to 1.0. As the maximum value of

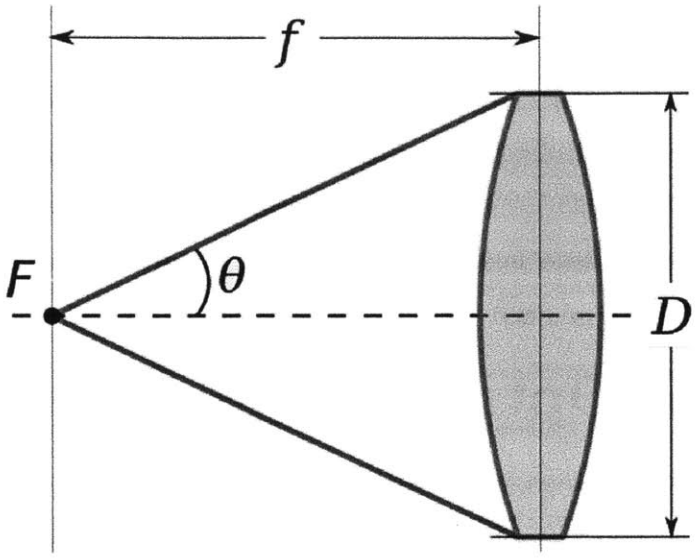

Figure 2-1: Cross Section of an Objective Lens. This simple cross sectional diagram demonstrates the geometric quantities that define the numerical aperture namely the acceptance angle θ, focal distance f, and entrance pupil D.

sin θ also equals 1, it is found that the largest numerical aperture of an optical lens used in open air conditions is 1.0. A second nomenclature for numerical aperture called f-number is commonly used in photography. These two quantities are related by Equation 2.2.

$$F/\# = \frac{1}{2 \cdot NA} \tag{2.2}$$

This inverse relationship can cause some confusion in the field of optics. A higher powered lens will have a large numerical aperture but a small F-number. It is approximately true that the lateral resolution of a lens in microns is equal to its F-number.

2.2 Lateral Resolution and the Rayleigh Criterion

Optical systems reach physical limitations to their performance based upon the physics of light. The diffraction of light phenomena is common boundary in microscopy limits the lateral resolution of a microscope. Lateral resolution has a subjective definition but can be summarized as the minimum distance between two point sources of light

in which both points can be distinguished as separate. A commonly accepted mathematical relationship for lateral resolution referred to as the Rayleigh Criterion states:

$$L = \frac{0.61 \cdot \lambda}{NA} \tag{2.3}$$

where L = Diffraction limited lateral resolution (m)

λ = Wavelength of incident light (m)

NA = Numerical aperture of the optical system

In many applications it is desirable to have a fine lateral resolution for the maximum amount of detail. As such, the wavelength of incident light is minimized given their proportional relationship. Most commercially available sensors only absorb wavelengths in the visible spectrum (400 to 750 nm) which is complimented by most light sources that only radiate light within the visible spectrum. Using light in this range ensures safety to the observer and facilitates troubleshooting. Using wavelengths of light below the visible spectrum starting at approximately 200 nm can lead to a phenomenon called "compaction." Compaction occurs when high energy light particles strike glass lenses made out of pure glass or SiO_2. Over time, the impact of the photons can change the geometry of the lens which has large consequences on the quality of the image. To avoid this problem, semiconductor manufacturers can construct their lenses out of Calcium Fluorite (CaF_2), an isometric mineral with a unique transparency to ultraviolet light. In practice, CaF_2 lenses are most commonly used in conjunction with 157 nm excimer lasers light source for lithography. CaF_2 remains an uncommon and brittle material and is relatively expensive to produce and machine. Decreasing the wavelength of incident light to the ultraviolet range introduces a host of complications that significantly increases the cost and decreases the availability of light sources, lenses, and sensors that function below the wavelength of visible light. In light of the complications associated with compaction, lithography companies now rely solely on optics that reflect light as opposed to those that transmit light.

Our instrument falls under a series of constraints that allow us to practically

evaluate its finest lateral resolution. Given the intent to use the instrument in an open air environment without liquid contaminants the index of refraction is rated at a maximum of 1.0. Based upon the practical constraints of the light source it is estimated that the lowest possible wavelength of light able to be used is 400 nm. Upon review of many microscope objectives the greatest numerical aperture commercially available is 0.95. Using these numbers the minimum theoretical lateral resolution of our optical system is calculated to be 257 nanometers.

2.3 Modulation Transfer Function (MTF)

The modulation transfer function (MTF) is used in practice to measure the lateral resolution of a system and equivalently the numerical aperture of a lens. The MTF is called a transfer function for it measures optical performance as a function of spatial frequency. Lateral resolution can be defined as the minimum distance between two point sources of light in which an optical system can distinguish both points as separate. This concept is emulated by illuminating a repeating pattern of opaque and transmissive lines printed onto a piece of glass called a Ronchi Grating. The illuminated pattern is imaged by an imaging system. The sharp edges and high contrast of the Ronchi grating gets compromised as the spatial frequency becomes more finely pitched due to the diffraction of light. The MTF is calculated by measuring the magnitude of contrast between light and dark stripes at a given spatial frequency. Figure 2-2 shows an original pattern along with a simulation of how the pattern would be imaged by a lens. The limit to lateral resolution is sometimes defined as the spatial frequency in which the MTF is equal to 40% contrast.

2.4 The Nyquist Criterion

When selecting the magnification for an optical system both the diffraction limited lateral resolution and Nyquist criterion must be taken into account. In accordance with these principles, the magnified pixel size is chosen to be at least two times

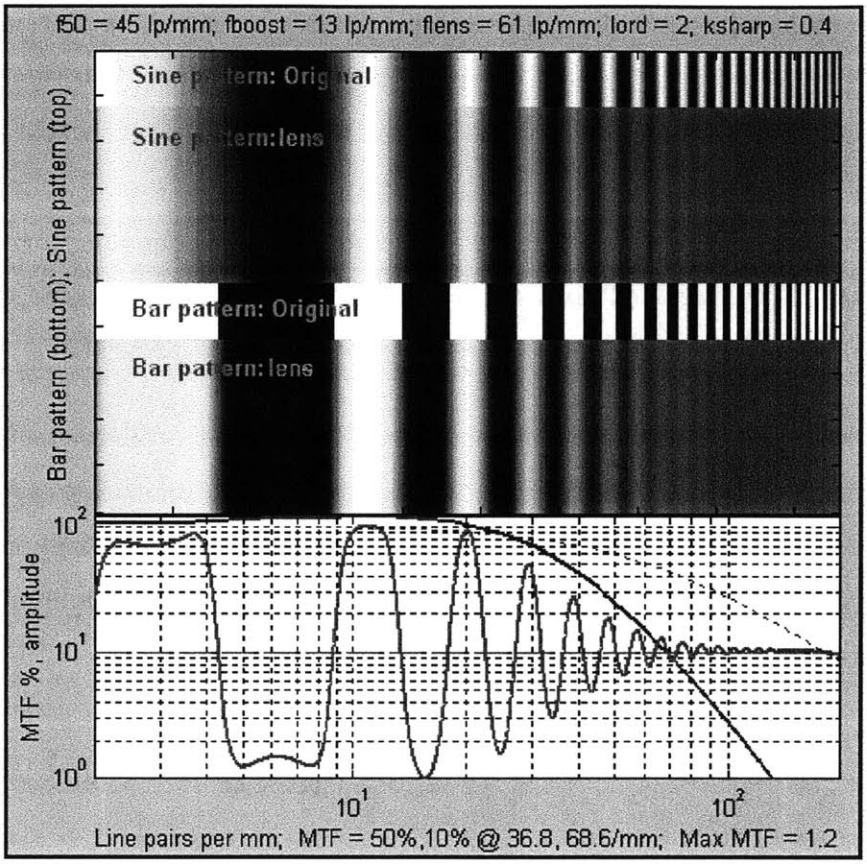

Figure 2-2: Modulation Transfer Function Graph. This diagram is crafted to demonstrate the concept of the modular transfer function, or MTF. A sine and bar pattern of repeating black and white regions is presented. These patterns become blurred by the diffraction of light when viewed through a microscope. The bottom graph displays the MTF which is calculated by finding the relative intensity difference between the light and dark regions. The red line represents the intensity of the pixels while the blue line represents the magnitude of the envelope bounding these values. A lens is said to have reached its maximum lateral resolution when the MTF reads 40%.

finer than the theoretical lateral resolution. The purpose and effect of this additional magnification is explained visually in Figure 2-3. Suppose a microscope objective was imaging a Ronchi grating with a pitch equal to its lateral resolution. If the pixels were to line up exactly with the grating the camera would record a 100% contrast between the light and dark lines. Suppose the camera pixels were to remain stationary and the grating were to be moved laterally one half of a pixel. Now each camera pixel would output a gray value for its field of view would be split half white and half black resulting in a 0% contrast. In this scenario an optical system fully capable of resolving these lines does not have a great enough spatial sampling frequency to image them. If the magnified pixel size is at least two times finer than the minimum lateral resolution the system is guaranteed to capture its maximum MTF.

From these principles we can mathematically solve for the minimum pixel size based upon the optical hardware. The Nyquist criterion recommends to sample the object at 2 times the diffraction limited lateral resolution. Any magnification beyond this pixel size does not add information or value to the image. The minimum pixel size is represented in Equation 2.4.

$$\text{Minimum Pixel Size} = \frac{\lambda}{3.28 \cdot NA} \tag{2.4}$$

2.5 Depth of Field

The depth of field of an optical system is another important performance metric dictated by physical parameters. The depth of field is described as the physical range in which imaged objects are acceptably sharp. Like lateral resolution, the depth of field is a subjective measure but also can be approximated via a generally accepted mathematical relationship shown in Equation 2.5. Depending upon the application an optical system designer may want the depth of field to be large or small. Additionally it is noted that "Depth of Focus" refers to the range of image sharpness about the object plane while "Depth of Field" refers to the sharp range about the image plane

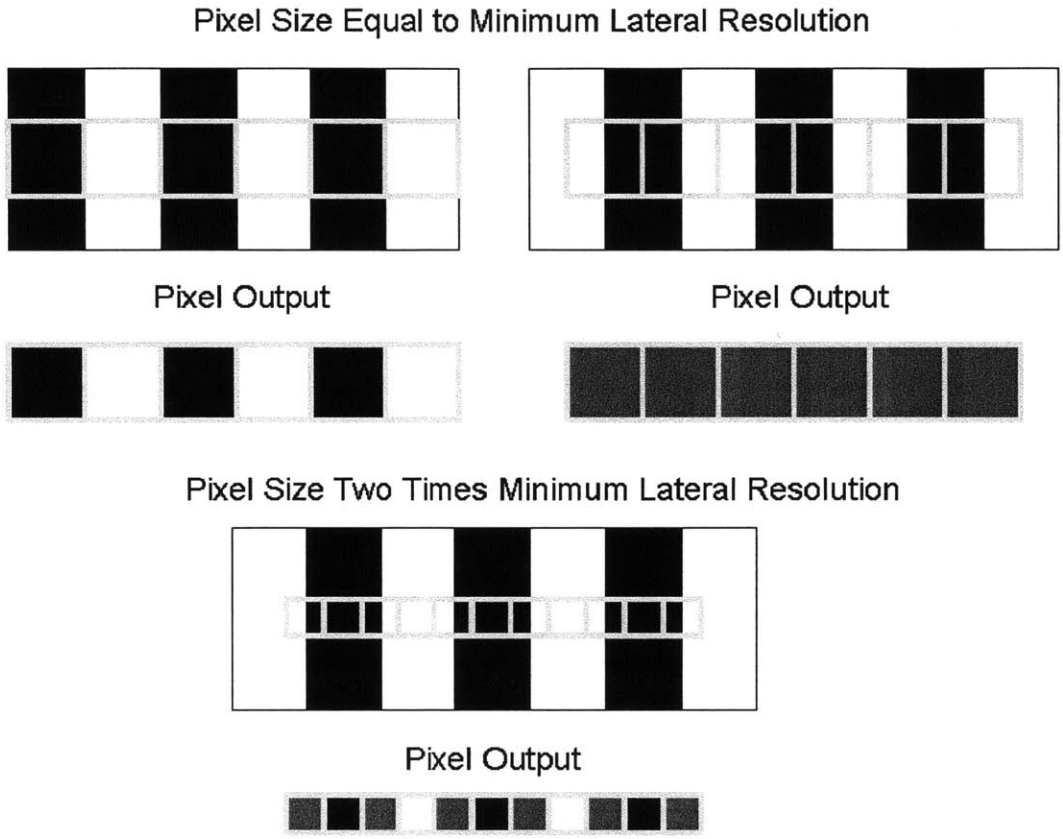

Figure 2-3: Using Nyquist Criterion to Determine Minimum Required Resolution. This simple diagram illustrates the effect of sampling a pattern without observing the Nyquist criterion. The sampling frequency must be at least two times finer than the minimum lateral resolution ensure an accurate measurement. If the sampling size is larger than the Nyquist criterion the output of the sensor can change from 100% contrast to 0% contrast when observing the same target.

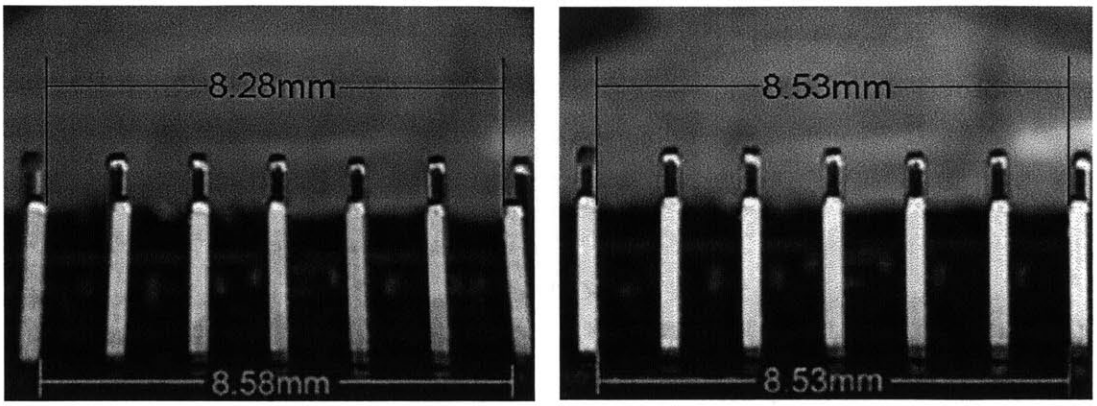

Figure 2-4: Effect of a Telecentric and Non-Telecentric Lens in a Metrology Application. These two photographs demonstrate the difference between a telecentric lens (right) and non-telecentric lens (left). The telecentric lens minimizes the magnification distortion which causes the objects viewed on the outside of the image to look skewed [12].

or camera sensor.

$$DoF = \frac{\lambda}{4 \cdot n \left(1 - \sqrt{1 - \left(\frac{NA}{n}\right)^2}\right)} [11] \tag{2.5}$$

2.6 Telecentric Optics

Telecentric optics are specifically designed to minimize optical distortions caused by changes in magnification. They provide an image with a vanishing point at infinity whereby objects viewed at the periphery of an image retain their geometric shape. Thus, within a certain range an object placed farther away from the lens does not look any smaller than an object placed closer to the lens. Figure 2-4 shows the difference in using telecentric versus non telecentric optics.

While telecentric lenses provide great advantages in metrology applications, the lenses must abide by the same physics that govern the performance of all other lenses. Because of their complex nature, telecentric lenses have a numerical aperture far smaller than a typical microscope objective. As a consequence their lateral resolution

is relatively poor and their depth of field relatively wide. The telecentric lens with the greatest numerical aperture on the market today is found to be the Invarigon ELWD M, sold by Melles Griot. This lens provides 5X magnification with a numerical aperture of 0.089 whose value is over ten times smaller than the maximum value found in microscope objectives. While these lenses have great applicability in demagnifying applications such as structured light profilometery, they do not provide adequate performance for high magnification microscopy.

2.7 Measuring Optical Performance

The performance of the optical components can be empirically measured to see how they stack up against their specifications. An experiment was conducted whereby a Navitar 2X telecentric lens with a 0.028 numerical aperture was used to image an optical target with lines printed at various spatial pitches. The image itself is shown in Figure 2-5. The difference in light intensity between the light and dark lines is calculated for each line pair combination. Table 2-5 displays these intensity differences as well as the spacing for each line pair. It is shown that the intensity difference between light and dark or Modulation Transfer Function reaches 40% of its original value at a line spacing of 38 lines per millimeter. This performance is characteristic of a lens with 13.2 μm lateral resolution or a numerical aperture of 0.025 as per Equation 2.3. Figure 2-5 also shows a graph of the line pairs per millimeter plotted against the Modulation Transfer Function.

Group	Sub-group	Max Intensity	Min Intensity	Δ Intensity	Line Pairs/mm	% MTF
4	1	124	46	78	16	100.0
4	2	128	57	71	17.95	91.0
4	3	118	58	60	20.16	76.9
4	4	114	64	50	22.62	64.1
4	5	110	68	42	25.39	53.8
4	6	108	69	39	28.5	50.0
5	1	115	75	40	32	51.3
5	2	112	78	34	36	43.6
5	3	113	86	27	40.3	34.6
5	4	113	89	24	45.3	30.8
5	5	115	96	19	50.8	24.4
5	6	116	100	16	57	20.5

Table 2.1: An experiment to measure the MTF and numerical aperture of our lens was conducted. This table holds the intensity difference between each line spacing as well as their pitch.

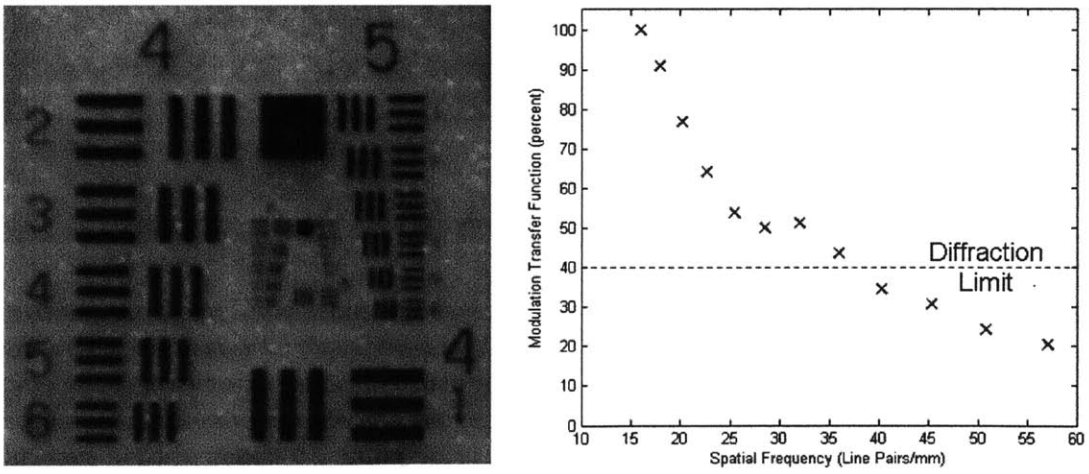

Figure 2-5: Empirically Finding the Numerical Aperture. This test was conducted to measure the numerical aperture of our lens. A target with a series discretely spaced line pairs is presented on the left. The percent contrast in intensity values as a function of spatial frequency on the right as taken from the data in Table 2-5. The lateral resolution of the lens is said to reach its limit when the MTF drops below 40%.

Chapter 3

High Speed Profiler Research Background

The overall goal of our research is to create a mass manufacturing process capable of producing inexpensive, disposable medical devices with microscale features. This task calls for the invention of new tooling, equipment, and inspection capabilities. The contribution from this research to this novel manufacturing capability is the creation of a high resolution, high speed inspection system able to measure transparent parts with submicron resolution. This new equipment enables the ability to conduct defect detection and in-line process control on the mass manufactured medical devices. Such inspection capability is required to monitor the process to increase its yield. This chapter first explains the need for such a device before exploring the research that has been done recently to address it. Each of the research papers included will be evaluated on how well they meet the functional requirements laid out in the first chapter of this thesis.

3.1 Motivation for the Project

The medical devices targeted to be produced by the new manufacturing processes are commonly called "Lab on a Chip" or LOC devices. These disposable, diployable

diagnostic tools are designed to test medical samples in the field as opposed to in the lab. Lab on a Chip devices have demonstrated progress in testing for many communicable diseases such as AIDS [13], malaria [14], syphilis [15], and tuberculosis [16]. Such diagnostics can alert infected individuals and curb the spread of disease. Furthermore, LOC devices have shown to diagnose non-communicable diseases such as cardiovascular disease [17], glaucoma [18], and cancer [19]. The early and proper identification of these diseases can mitigate their harmful effects. All in all, lab on a chip devices have a "tremendous but unproven potential to improve the health of people in developing countries."[20]

The potential benefit from mass manufacturing LOC devices has far reaching implications around the globe. In 1st world countries these devices can take the place of otherwise expensive laboratory tests and work to lower the cost of healthcare. Their potential low cost also puts them in reach of a price point that is required for use in the third world. Their instantaneous results help to directly deliver important information to people who otherwise may have been lost or forgotten over the transfer of samples. Also, their compact and self contained nature erodes the need for brick and mortar laboratories that are expensive to build and maintain in countries with unstable governments. Furthermore, LOC devices can be designed to provide far greater sensitivity to the agents that are being tested (proteins, antibodies, etc.) allowing the users to provide more accessible bodily fluids such as urine or saliva instead of intrusive fluids such as blood or serum.[17] This flexibility in sample collection encourages the adoption of testing and reduces the risk of infection because of dirty needles.

Given all the potential benefits of lab on a chip devices, one may wonder why they have not yet been commercialized. In short, the manufacturing processes required to produce such high precision polymer parts with low cost simply does not exist. Matteo Calaon in the Journal of Advanced Manufacturing Technology states "the conventional methods used nowadays to manufacture these micro- and nano-functional surface topographies are very expensive, and they do not fit the requirements for industrial production."[21] Additionally, Asger Vig adds "an inexpensive

and high-volume fabrication method [for lab on a chip systems] is one of the remaining bottlenecks to be addressed before the systems can be commercialized in price sensitive markets."[22] The press to commercialize the lab on a chip devices led Curtis Chin in the Lab on a Chip Journal to note "no matter which manufacturing approach, we found it is crucial to implement the final mass-manufacturing technique, and not a simplified manufacturing procedure, as early as possible in the product development process."[23] This again points to the fact that while researchers have been able to make batches of devices suitable for testing, no one has been able to accurately mass produce polymer parts on such a scale.

This need for new manufacturing technology has given the Laboratory for Manufacturing and Productivity (LMP) at MIT the opportunity to tackle this challenge. A "MicroFactory" or "μFac" project has been assembled to study the high volume production of microfluidic devices. The emphasis of the research has been to develop new tooling, equipment, processes control and inspection techniques. The goal is to understand and overcome the manufacturing challenges such that a research scientist with a specific lab-on-a-chip tool could use the mass manufacturing process to bring their product to market. A photograph and diagram of the "μFac" chip that was selected by researchers at the LMP is shown in Figure 3-1.[24] The layout for the automated manufacturing line is shown in Figure 3-2. Raw sheets of polymer are first cut into squares and labeled with a laser cutter. A robotic arm stacks up the materials in a hopper. The blanks are then pressed with the specific design using a hot embossing process. At this point in the process each device is to be inspected by a novel instrument, the focus of this PhD thesis. Lastly, a cover slide is put on top of the parts, thus completing the channels.

The inspection process has two very important functions integral to the manufacturing of any product. First, the inspection of each part allows for quality control or the ability to make sure each part (or a select portion of the parts) meets its specifications. Part of quality control in the microfluidic manufacturing process is to scan each part for defects that would compromise their functionality. Defect detection currently

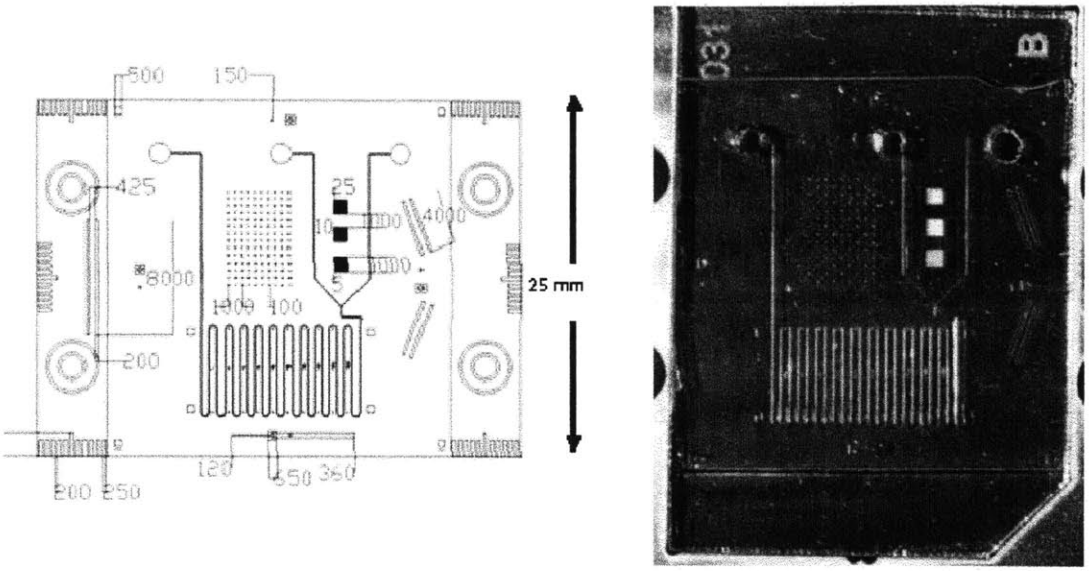

Figure 3-1: Photograph and Schematic of MuFac Chip. This side by side figure shows the important dimensions and layout of the μFac chip on the left and a photograph of a manufactured part on the right. This part was made though the method of hot embossing and is photographed before trimming away the top and bottom portions.

done by eye is "slow and inaccurate" while still requiring the people involved to "require extreme concentration.[25]" The same paper suggests instead computer vision to be used for defect detection. In such an application, a master image is produced that represents what the part is supposed to look like. Then, each part is individually imaged by the imaging system. Lastly, defects are detected by subtracting the part image from the master image, a process demonstrated by three pictures in Figure 3-3.

Secondly, the ability to inspect manufactured parts in a timely manner allows the implementation of process control. In process control, important indicators of quality are measured to test if the product is meeting its specifications. Any discrepancy between the measured part and its specifications are then fed back into the process such that the next manufactured part can be adjusted in the correct direction. The time required to measure each part is often the main factor in defining how quick the manufacturing process can mitigate errors.

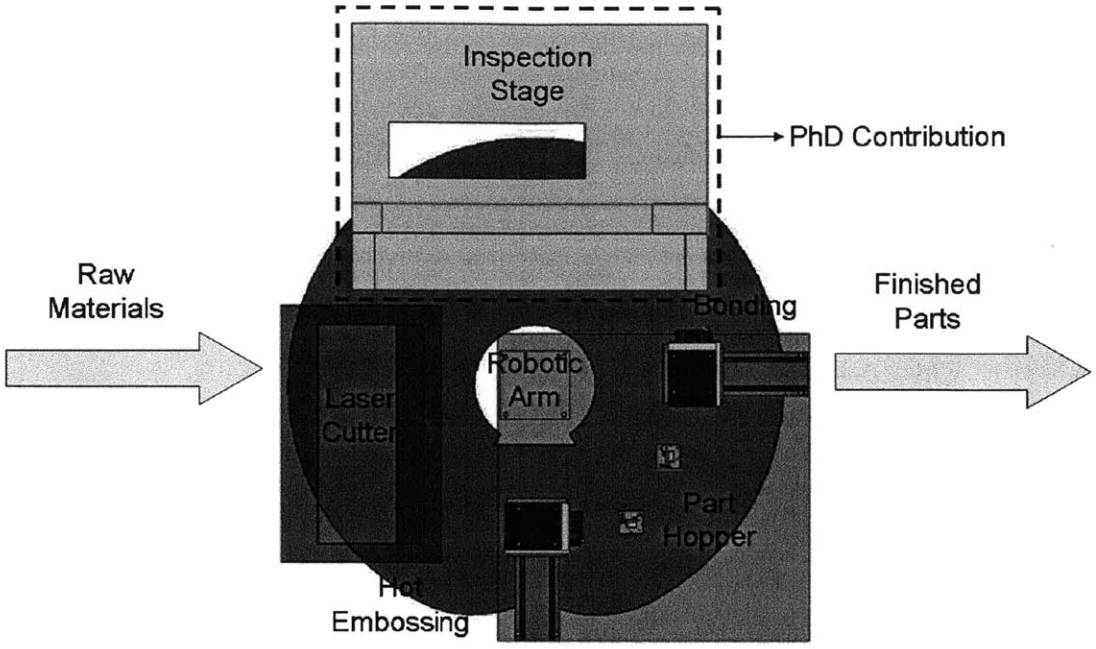

Figure 3-2: Schematic of the MicroFactory Layout. The microfactory project headed by David Hardt in the LMP is designed to input raw materials and output microfluidic devices with limited human interaction. The major contribution to the microfactory from this research is the inspection stage outlined in black.

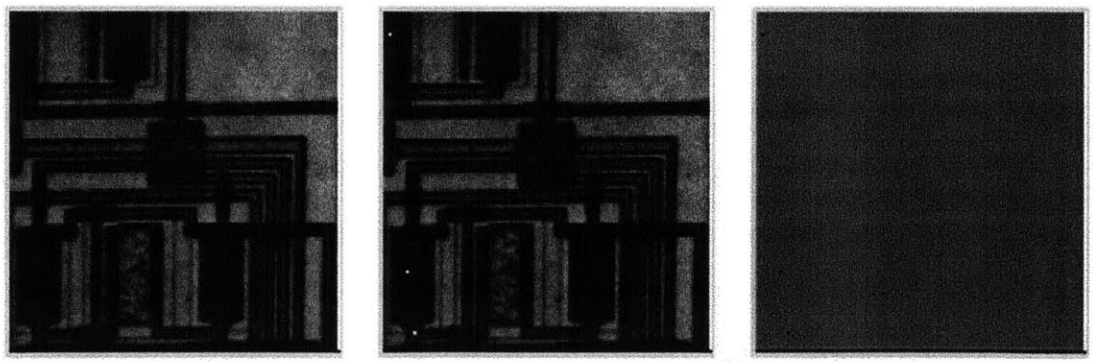

Figure 3-3: Defect Detection via Image Processing. This figure shows how the image of a singular part can be detected for defects. A "Part Image" is subtracted from the "master image" to reveal and identify defects via computer vision.

While there exist profilometers that provide metrological services in the submicron range, no commercial instrument has demonstrated the capability to inspect micromanufactured parts. This deficiency is noted by Thomas Kurfess in the International Assessment of Research and Development of Micromanufacturing when he noted "few metrology systems for process and product control are available ... Most of the measurement systems are fairly slow, which makes them suitable for research and development as their measurement speeds limits their utility on actual production lines.[10]" This position is alow mirrored by H. Hansen when he states "In general a variety of 2D and 2.5D metrology systems are currently available. They are relatively expensive and slow. From the standpoints of both robustness and inspection speed, metrology systems lack the ability to be used in a production setting.[26]" To illustrate this point, it is estimated that a white light profilometer is capable of measuring 30,000 points per second through a vertical range of 135 μm. At this inspection speed it would take over 24 hours to completely measure a 1" x 1" square at 0.5 micron resolution, an amount of time far too long to be useful in a production setting.

This chapter presents an in depth study into research efforts that have been made to tackle the inspection needs required by the micromanufactring industry. When applicable each research paper reviewed is evaluated on how well it can achieve the functional requirements laid out in Section 1.1. As most of these efforts are still in a preliminary phase these qualities are often not addressed or difficult to measure. Thus these methods can not be compared against the high speed profilometer as thoroughly as can commercial metrology instruments. Beside their speed, resolution, and range abilities each studied case will also be evaluated on how well their method replicates the surface, whether or not it damages the measured part, and to what extent it gains information on all the free surfaces.

3.2 Film Thickness Measurement as Observed by Florescence Reabsorption [1]

Carlos Hidrovo and Douglas Hart

In this paper Hidrovo, Brau, and Hart discuss a metrology technique that measures the thickness of a thin film by measuring the intensity of fluorescence emanating form the liquid. The intensity of light received from a column of fluorescent liquid is related to the thickness of the column. Using this relationship the sensor can solve for the thickness of the film from the measurement of intensity. Yet, the temporal measurement of intensity will vary significantly given changes in laser intensity, reabsorption, surface reflectivity, and other variables. Thus using one dye to measure thickness will yield a very noisy and inaccurate result. Hidrovo uses two fluorescent liquids that emit light at different frequencies to minimize the effect of these non linear uncertainties. By looking at the ratio of intensity between the two liquids, the nonlinear elements that change with time can be canceled out since they affect both liquids similarly.

This technique can be used to measure the topology of a sample. In this paper Hidrovo immerses a US quarter in the two fluorescent liquids. The liquid fills into the crevasses of the coin thus making a negative imprint of the object. By taking the inverse of the thin film thickness resting on top of the quarter Hidrovo can successfully measure the topology. The intensity of light emanating from each liquid is shown in Figure 3-4 while the ratio of intensities is shown in Figure 3-5.

It is inferred that this system will have the same drawback as structured light profilometers whereby the vertical range will be limited by the depth of field of the optics. Again this puts constraints on the lateral resolution of the image. Using the numerical aperture and depth of field equations it is calculated that an instrument with a vertical range of 200μm can only attain a minimum lateral resolution of 8.6μm.

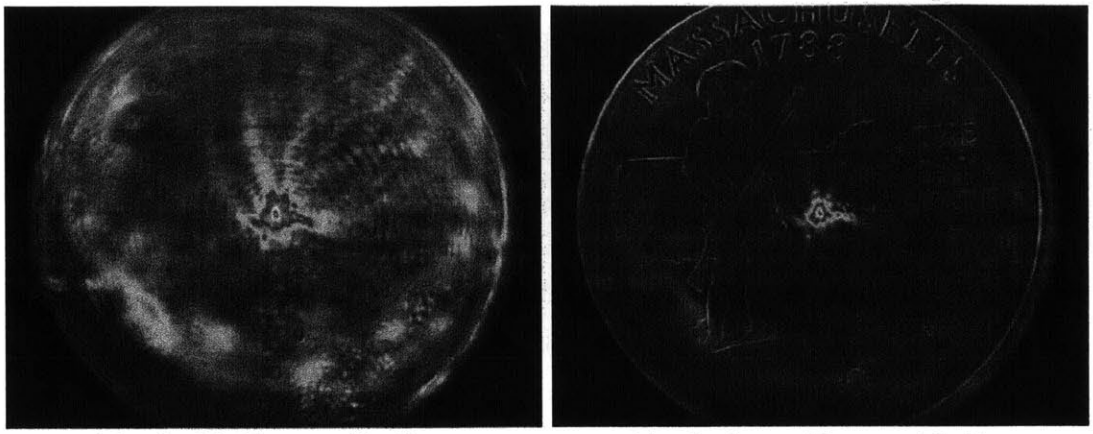

Figure 3-4: Using Common Mode Rejection to Clean Up Fluorescence Images. The florescent light captured from this technique is as function of the liquid thickness can have many nonlinearities. These two pictures show the resulting intensity when excited with two separate wavelengths of light.

Figure 3-5: Improved Two Wavelength Imagery. This output shows the ratio of light between the two fluorescent liquids revealing a low noise image where intensity is proportional to thickness.

It is suggested that this technique emits an abundance of light thus allowing high frame rates and rapid measurement of the topology. The ultimate quantity of light emitted by the system and collected by the camera is a difficult quantity to calculate. To start, the amount of light emitted by a volume of fluorescent fluid dV is estimated in Equation 3.1:

$$F = I_e \epsilon(\lambda_{laser}) C \Phi dV \tag{3.1}$$

whereby

F = Amount of Flourescent light emitted

I_e = Input excitation energy typically lower than 370 MW/cm2

ϵ = Molar absorptivity: Amount of light per molecule producing state level transitions

C = Concentration of dye: Amount of molecules present

Φ = Quantum efficiency: Energy Emitted / Energy Absorbed per interaction

The first problem exists with calculating the amount of reabsorption. From the variable Φ it is understood that the molecule losses some energy in the absorption and emission process. If the light is to be reabsorbed multiple times it will lose energy with each iteration. Hidrovo calculates that this effect is small and therefore negligible for thin films. Secondly notion of "monitoring efficiency" must be examined. As described by Hidrovo:

"In reality, since the fluorescent light is directed in all directions, only a fraction of the total fluorescence emitted by a differential volume element is collected by the CCD detector. This is referred to as the 'monitoring efficiency' of the system..."

Hidrovo goes on to explain that this quantity is dependent upon many variables in the optics such as size of aperture and distance to the sample. For the purposes of Hidrovo in this paper this detail is to some degree overlooked by the following logic:

"This constant (monitoring efficiency) is eliminated in the ratio of dye emission

intensities and is, thus, inconsequential."

While this quantity may be inconsequential for the purposes of Hidrovo's paper, it is of the utmost importance when trying to determine the feasibility of using this technique in high speed metrology. Given the complexity of calculating this efficiency as well as the dependence upon the particular experimental setup, the estimation of this monitoring efficiency becomes simply too difficult to estimate.

Although this technique is not natively set up to measure vertical sidewalls, it has the potential to measure an even more elusive quantity: the geometry of buried channels. The feasibility of the ability remains speculative for it has not yet been demonstrated. The measurement of vertical sidewalls by this technique could be realized if principles from the high speed 3D profilometer were used.

This technique is expected to have moderately good replication of the surface features. There may exist features narrow enough that hypertension of the liquid does not allow it to flow into the crevasses. Also, if the samples features were viewed from the bottom there is a possibility that air bubbles would get trapped on the surface's features resulting in unreliable topographies.

This system is an example of destructive testing. Once these fluids are introduced onto the sample, it is unlikely that they can be used again for the testing of biological materials. Furthermore, the presence of such fluids in an open air manufacturing line makes it difficult and costly to maintain in a clean manner. This fluid based, destructive testing makes the instrument unable to be used in a high speed microfluidic inspection line.

3.3 Using Laser Fluorescent Confocal Microscopy to Measure Sidewalls [2]

Shiguang Li, Zhiguang Xu, Ivan Reading, Soon Fatt Yoon, et al.

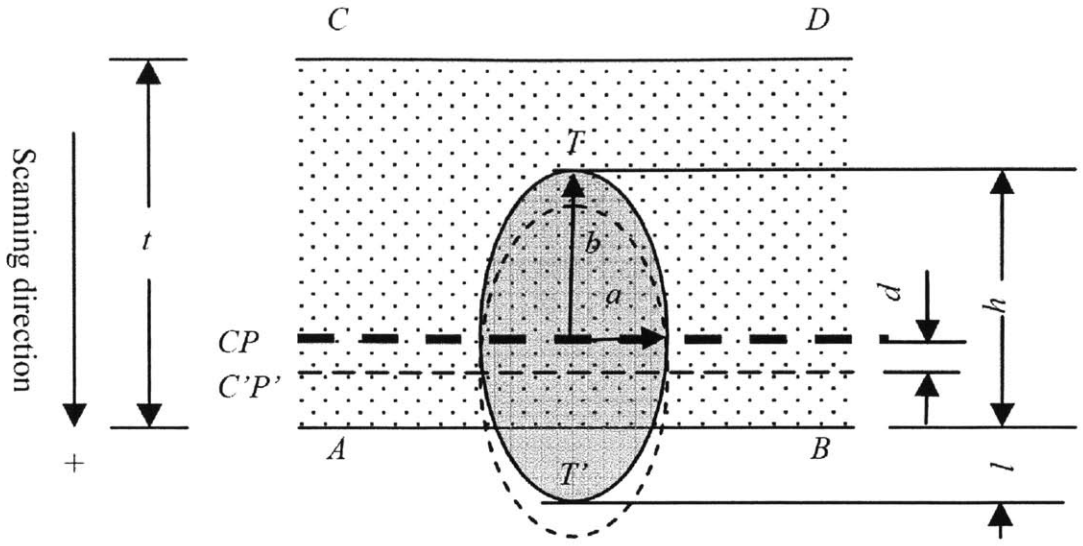

Figure 3-6: Laser Spot Schematic. This figure demonstrates the concept of using an ellipsoidal laser spot to probe for the presence or absence of florescent liquid. A minimum vertical resolution "d" (approximately 100 nm) can distinguish the borderline between the thickness of florescent liquid "h" and sold matter "l."

In this paper Li et. all demonstrate measurement of vertical sidewalls on microchannels in PDMS parts with submicron resolution. The group first fills the channels with fluorescent liquid. Using a confocal microscope they focus a laser onto an ellipsoidal spot size of approximately 320 nm wide and 800 nm tall in a volume V_{laser}. A photoelectric device is used to collect the light that is emitted by the liquid. The intensity of light is proportional to the percentage of the volume V_{laser} that is filled with fluorescent liquid. When sweeping across a fluid-polymer interface the intensity of light drops from I_{max} to zero. Li uses an algorithm to determine the physical location of the interface from this data. This concept is illustrated in Figure 3-6. Here the fluorescent fluid is indicated by the dotted area with AB and CD representing the fluid-polymer interface.

As also noted by Hidrovo's paper, Li explains that the use of but one fluorescent fluid in this type of metrology is subject to noise created by "nonuniform fluorophore distribution, non-constant florescence response, nonuniform or unstable laser intensity, or non-constant electrical signal response." In light of these noise

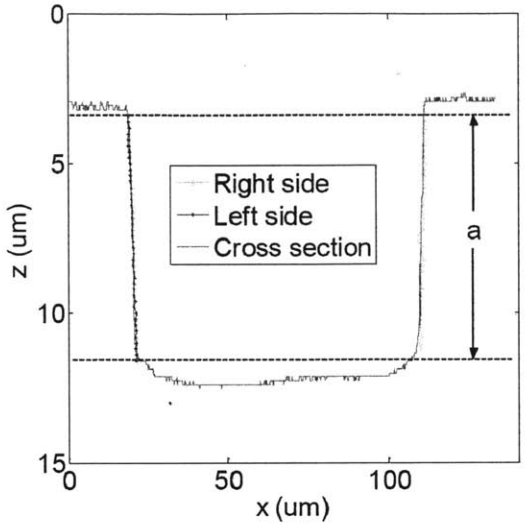

Figure 3-7: Cross Sectional Comparison of MicroFluidic Channel. Data showcasing the sidewall measurements made by the laser fluorescent system in green and blue. The red data was collected by cutting the sample open and measuring it using an SEM.

sources, Li has taken his laser fluorescent vertical sidewall measurements and compared them against a cross sectional profile of the sample obtained after the sample was carefully cut. Li shows that the RMS difference between the two measurements was 0.15 microns. This congruency is shown in Figure 3-7.

This system demonstrates a spatial resolution that meets the functional requirements. The lateral resolution is estimated to be approximately the half diameter of the laser spot size around 160 nanometers. The vertical scanning resolution or "scanning step interval" is denoted by the variable "d" in Figure 3-6. Although this quantity is theoretically calculated and referenced multiple times throughout Li's paper, it is never numerically defined. It is estimated this quantity to be a minimum of 400 nanometers. It is noted that these spot sizes were attained by using an oil immersed lens with a numerical aperture of 1.4.

The rate at which the instrument collects data was largely unaddressed in this paper. Li mentions that the "data acquisition time is shorter" than that of a CD-SEM or CD-AFM which says the instrument probably can obtain at least 4,000

points per second.

Similar to Hidrovo's laser fluorescent metrology method, Li's technique can change the shape of the measured object if the liquid does not fully fill in the profile of the object. He refers to a possible "minor geometry variation ... due to the wetting property of the samples." Here again the surface tension of the liquid may prevent it from filling in micro or nano scale features. Yet, the use of flourescent material again gives instrument has a great capability to measure the complete profile of a microfluidic channel.

Li refers to his system as nondestructive because it does not change the shape of the measured part. For micromanufacturing purposes this technique is found destructive for it contaminates the biological device. Furthermore, this method would be destructive in a semiconductor solder array industry where there was risk of unintentional shorting of electrical components because of liquid interaction. As previously mentioned, this system requires the use of two different fluids in order to make its high resolution measurements. The introduction of a second liquid further complicates the technique and compromises its practicality in a manufacturing environment.

3.4 Three-dimensional shape sensor based on lateral focused-plane sectioning [3]

Akira Ishii, Jun Mitsudo, and Yuuka Fujinaka

Ishii presents a profilometer with a tilted plane of focus (POV) that uses depth from focus to scan a volume. The instrument is able to continuously sweep through a volume by taking images at set intervals. This type of scanning contrasts conventional profilometers that splice together volumes that were scanned vertically each at an independent X,Y location. Contrary to the high speed profilometer, Ishii

is able to tilt the plane of focus by tilting the camera with respect to the lens, keeping the lens and the measured object in parallel planes. This optical effect is achieved through the "Scheimpflug Principle" the effects of which are further documented and explored in a paper by Ikeoka. [27] Unfortunately tilting the plane of focus in this manner has makes the thickness of the space in-focus (or depth of focus) vary with position and does not allow for the ability to measure vertical sidewalls.

The tilt of the camera with respect to the lens is seen in Figure 3-8. The CCD image sensor has been tilted by an angle ϕ. The image sensor uses a telecentric lens to bring into focus the plane labeled "A-B." The plane "A-B" is tilted with respect to the horizontal axis by an angle θ. Lastly, successive images are taken after a step in the translation axis and then compared against each other to determine depth.

In this experiment, Ishii used a telecentric lens with a 1X magnification with an approximate NA of 0.06. He tilted the camera sensor to $\phi = 45$ degrees which by equation 3.2 found in Ishii's paper makes $\theta = 45$ degrees. Ishii uses a simple high pass filter to determine focus. The measurement data from Ishii's work is presented in Figure 3-9.

$$\text{Magnification} = f_b/f_a = \tan\theta/\tan\phi \tag{3.2}$$

Ishii lists his lateral resolution or "pixel pitch" as 7.3 microns. Also, he reports a vertical resolution of 16 microns as derived from the noise in his measurement capability. These numbers match those of a structured light profilometer and do not meet the functional requirements. Although Ishii does not directly address the issue of rate, from the first line in his paper he identifies the process as a "practical shape-from-focus method for measuring three-dimensional shapes on production lines." Here the implication is that the process is meant for high speed imagery of indefinitely long samples. Ishii's mentions in his conclusions that "cutting-edge digital cameras with a resolution of more than 1280 x 1024 pixels and a speed of

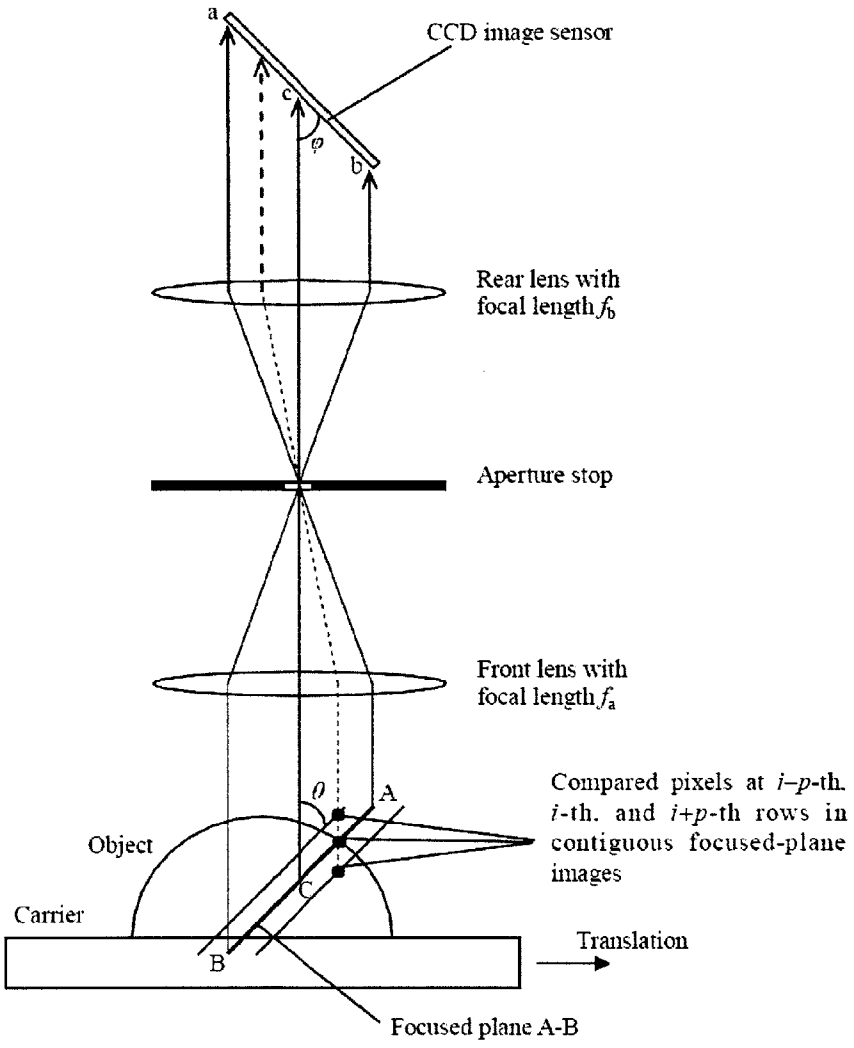

Figure 3-8: Cross Section of the Instrument Used in Ishii's Work. A CCD image sensor tilted an an angle ϕ results in a tilted field of view at an angle θ. The object is then translated horizontally to ready its position for the next image. Lastly, the pixels which share the same vertical axis are compared in focus to determine the topography of the part.

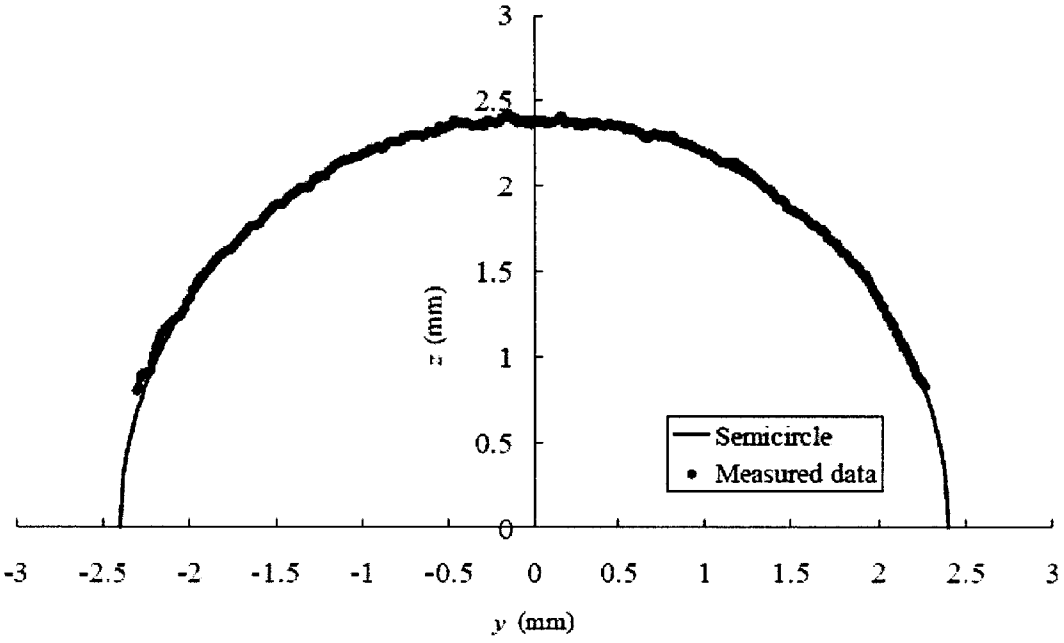

Figure 3-9: Slice of Data Taken From Ishii's Profilometer. In this experiment the surface of a semicircle was measured to determine the noise limited vertical resolution of the instrument.

more than 74 frames/s hold promise, especially in the real-time inspection of shapes ... such as the arrays of solder bumps for LSI packaging." Assuming that high speed cameras can be integrated into the system, the design behind Ishii's work shows excellent promise for high data rate collection. Furthermore, there are no foreign contaminants or fluids used in Ishii's non contact profilometer making it easily implementable into a manufacturing process.

3.5 Lateral Scanning White-Light Interferometer [4], [5]

Artur Olszak

The research presented in this paper tilts a white light interferometer on its side to achieve high accuracy lateral scanning. The tilted configuration allows the instrument acquire imagery of elongated objects with only a lateral scanning direction of motion. As Olszak describes, this lateral scanning strategy is advantageous over its vertical scanning counterpart for "all the inconvenience associated with slower speed and stitching errors is eliminated." Olszak lays the operation of his instrument visually in Figure 3-10. In this condensed figure, each consecutive row of pixels in the camera is spaced that it has exactly 90 degrees of phase difference. Thus the pattern recorded by the camera when the parts surface is one working distance away from the optics will exude evenly spaced wavelike properties.

Similar to the work done by Ishii, this tilted configuration profilometer is well suited for manufacturing applications. The instrument can measure parts that are indefinitely long. By using high numerical aperture optics Olszak demonstrates that his instrument can achieve 0.5 μm lateral pixel spacing. Furthermore, the use of high speed cameras with frame rates up to 955 frames per second demonstrate a lateral scanning speed of 0.48mm / second. The non contact measurement

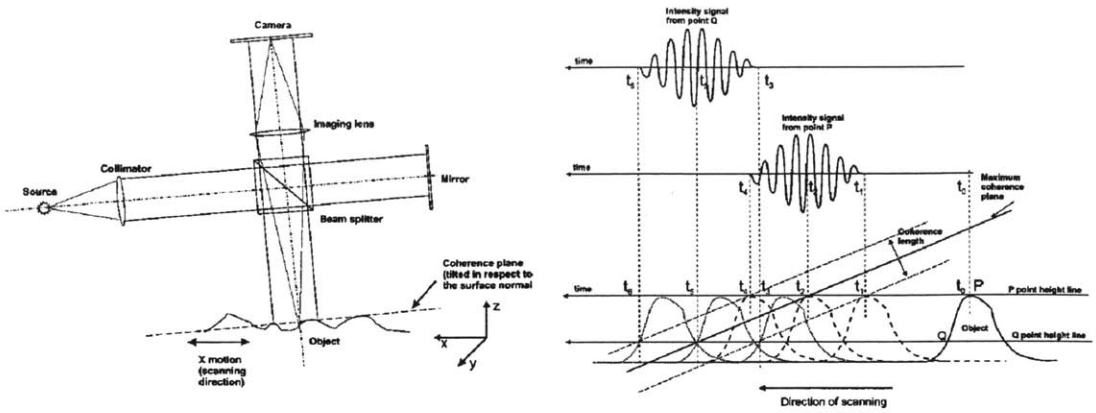

Figure 3-10: Side View Schematic of Olszak's Instrument. Schematic of a lateral scanning interferometer based on a Twymann-Green interferometer. The optical setup is tilted along the θ_y axis to angle the focal plane.

eliminates contamination or destructive testing.

Unfortunately, the vertical range of this system is compromised given the shallow tilt angle of the instrument of approximately five degrees. Assuming a 0.5 μm magnified pixel spaced upon a 640 x 480 pixel array, the instrument would only have a maximum vertical range of approximately 28 μm: an insufficient range for our functional requirements. Additional tilt of the camera is prohibited by the geometry of the lens and would disrupt the specific relationship chosen to space each subsequent row of pixels at 90 degrees apart in phase difference. Secondly, it is unclear and doubtful that the instrument could collect sufficient light into the camera that had reflected off a transparent surface for high speed acquisition. The samples measured by this instrument and shown in Figure 3-11 are made from reflective materials. Overcoming this issue by using powerful laser light sources is not only prohibitively expensive, but adds an abundance of thermal energy into the part which can result in significant errors.

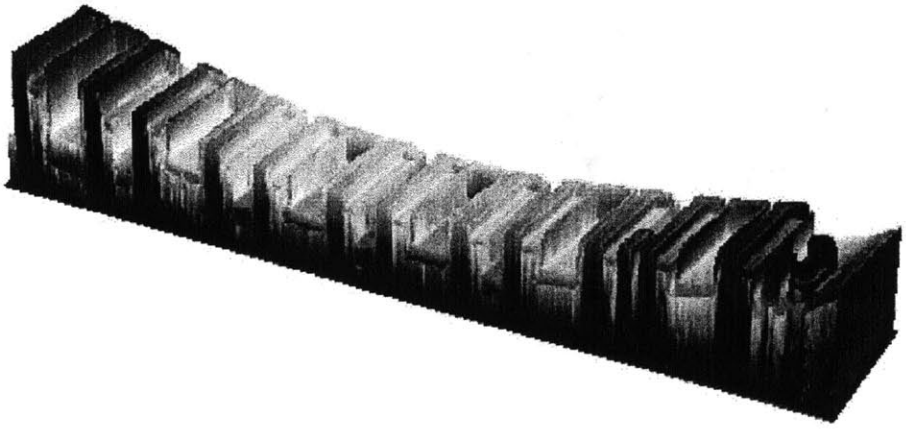

Figure 3-11: Measurement Results from Olsazk's Research. Profile map of a magnetic head slider bar obtained with the LSI setup. The depth of the slider pattern is on the order of 6 μm.

3.6 Two-Wavelength Interferometry for 3-D surface profiling [6]

U. Paul Kumar, Basanta Bhaduri, M.P. Kothiyal, N. Krishna Mohan

In this paper the authors demonstrate how to extend the shallow depth of inherit to single wavelength interferometer systems brought upon by the 2 pi ambiguity. A single wavelength interferometer will show repeating light and dark patters that reflect back from the surface that repeat every time the height of the surface changes one wavelength of light. Any surface of the part whose height is an integer multiple of the wavelength of light will have recorded the same, ambiguous intensity value into the camera. To circumvent this issue, Kumar has independently exposed the measured object to a repeating source at two different wavelengths of 532 and 633 nanometers. Cross referencing one intensity value against the other allows the instrument to discern the difference between the 2 pi phase ambiguity. This technique can extend the range of a single wavelength interferometer by an order of magnitude effectively capturing 10's of microns of range without the need for vertical scanning. The effect of these two wavelengths is demonstrated in Figure

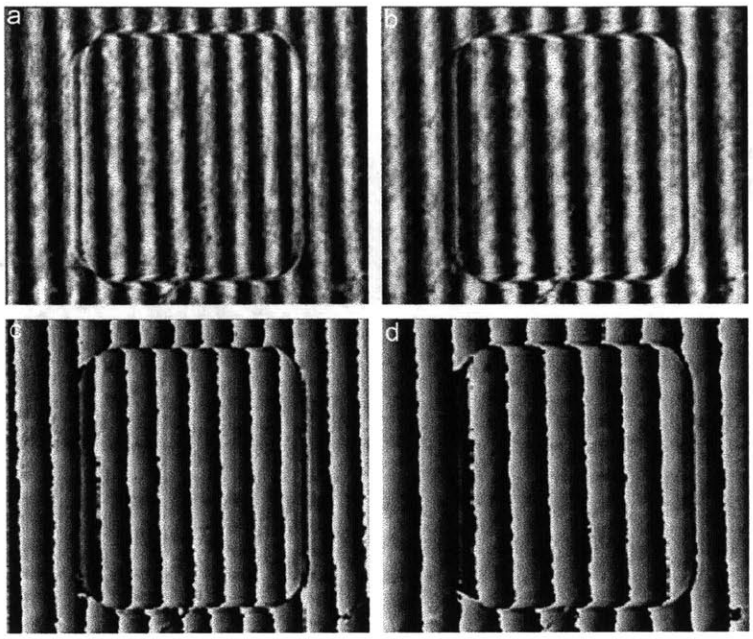

Figure 3-12: Raw Data From Kumar's Instrument. This figure presents the data collected by the interferometer at 532 nm (a) and 633 nm wavelength (b). Using these two sets of data independently, a wrapped phase map for the first wavelength (c) and second wavelength (d) are presented. The wrapped data repeats itself multiple times within the same plane making it impossible to know the distance between the top and bottom of the step height measurement as a consequence of the 2 pi ambiguity.

3-12 while their output topography is shown in Figure 3-13.

The great expansion of vertical range without having to vertically scan makes this instrument far more attractive than the white light interferometer when compared with inspection speed. Yet, as noted in the paper, the effective wavelength of these two frequencies is still 3.34 microns serving as vertical range limitation before repeating the 2 pi phase ambiguity. It is possible that a third wavelength could extend the range an additional order of magnitude, but until that capability is presented this instrument fails to reach the vertical range functional requirement. Although the paper does not specifically cite the lateral resolution of the instrument it is clear that such an optical setup can achieve performance in the submicron range.

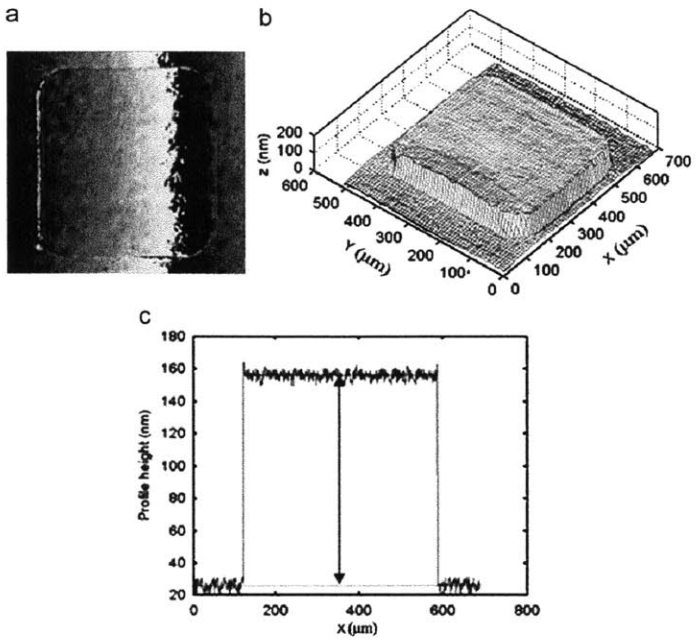

Figure 3-13: Combining Information from Both Images. The information collected at both wavelengths are now combined to provide an unambiguous wrapped phase map (a). This information is also presented as a 3-D profile (b) and cross sectional measurement (c).

3.7 High Speed Inspection via Real-Time FPGA Image Processing [7]

P. Montgomery, F. Anstotz, and J. Montagna

This conference paper by Montgomery concentrates on all the elements one needs to acquire and process mounds of data in order to output real-time 3D imagery. The abstract is loaded with specific numbers and details normally handwavingly brushed over by other papers. For example, this research instrument can output 20 images per second at an image size of 256 x 320 pixels over a 5 μm depth by processing 160Mb/s through an FPGA. While this paper addresses and tames most data acquisition and processing challenges, the method in which the data is collected poses restrictions in the mechanical domain that will ultimately bound the inspection speed. As shown in Figure 3-14, a piezo actuator must elevate the sample

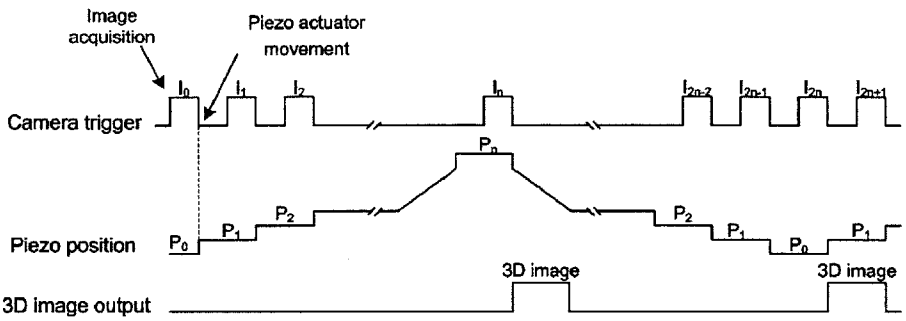

Figure 3-14: Synchronization of Signals in the Time Domain. The instrument in this paper focuses on high speed collection of 3D data. This time diagram details how the different elements of the instrument are synchronized in order to output real time topography.

vertically through a series of exposures before moving onto a different X,Y position. This stop and go motion requires a generous amount of settling time between exposures which limits the frequency of 3D image collection.

Figure 3-15 shows the 3D data output by Montgomery's instrument. In this particular scan the lateral resolution is calculated to be 2.3 μm but it is clear from other images that their instrument can magnify to 0.30 μm with higher magnification objectives. The instrument can also output an impressive 1.3 million 3D data points per second, but it is calculated that up to 99.5% of each image taken shows repeated data when laterally scanning. Thus, this instrument does a great job of 4D microscopy of stationary things, but has its inspection speed cut down to about 10,000 data points per second over a vertical range of 5 microns. While the image processing of its full inspection speed is certainly impressive for an instrument with submicron resolution, the instrument still does not meet the functional requirements.

3.8 Using CD-SEM Imaging to Measure Sidewall Information [8]

Thomas Marschner and Christian Stief

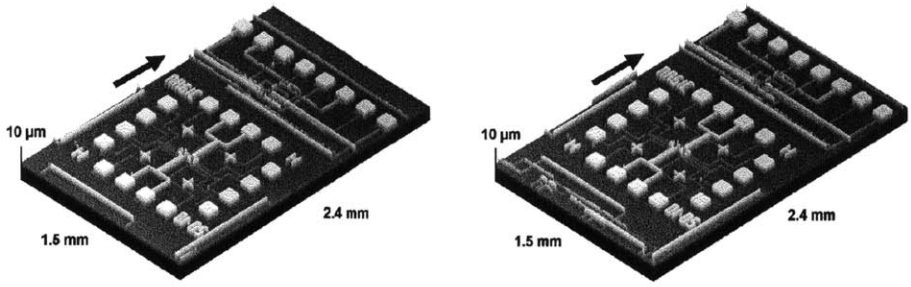

Figure 3-15: Real Time Imaging Results. Two 3D real time images of a CMOS magnetic probe being translated sideways at 20 μm/s, measured at a 3D image rate of 1.9 images/s with the 4X Michelson objective.

In a preliminary conference paper [28] and subsequent journal article [8], Marschner et. all tilt a scanning electron microscope off axis in order to measure the slope and height of vertical sidewalls. The instrument must take images from two different angles and use stereovision principles in order to make the measurement. Marschner measures the thickness of the sidewall as seen by the tilted SEM and calls it "edge width" or EW. By taking two measurements from tilt angles θ_1 and θ_2 the side wall height and angle can be approximated using basic trigonometry via equations 3.3 and 3.4. This principle is illustrated in Figure 3-16. The raw data collected by Marschner is also shown in Figure 3-17.

$$h = \frac{EW_1 - EW_2}{\beta_1 - \beta_2} \tag{3.3}$$

$$\alpha = \frac{EW_1}{h} - \beta_1 \tag{3.4}$$

The assumptions made by Marschner when taking these measurements are reviewed. Firstly, the technique does not measure a "profile" or a "depth map" but instead two parameters recorded at a singular location: height and angle. He assumes that the sidewall is completely linear and its profile runs a straight line when plotted as cross section as seen in Figure 3-17. Also, the channel itself needs to be straight or have a clear normal direction where the edge width can be measured across. Although this measurement technique provides relatively limited

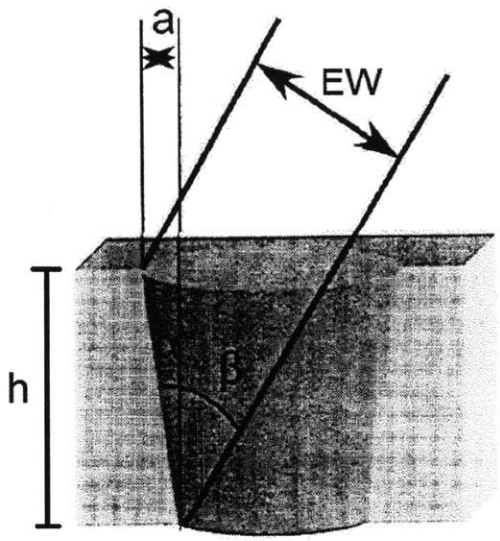

Figure 3-16: Cross Sectional Diagram of a Canonical Well. The technique used in the paper measures the depth of the well "h" and the steepness of its angle α by observing it from an an angle β.

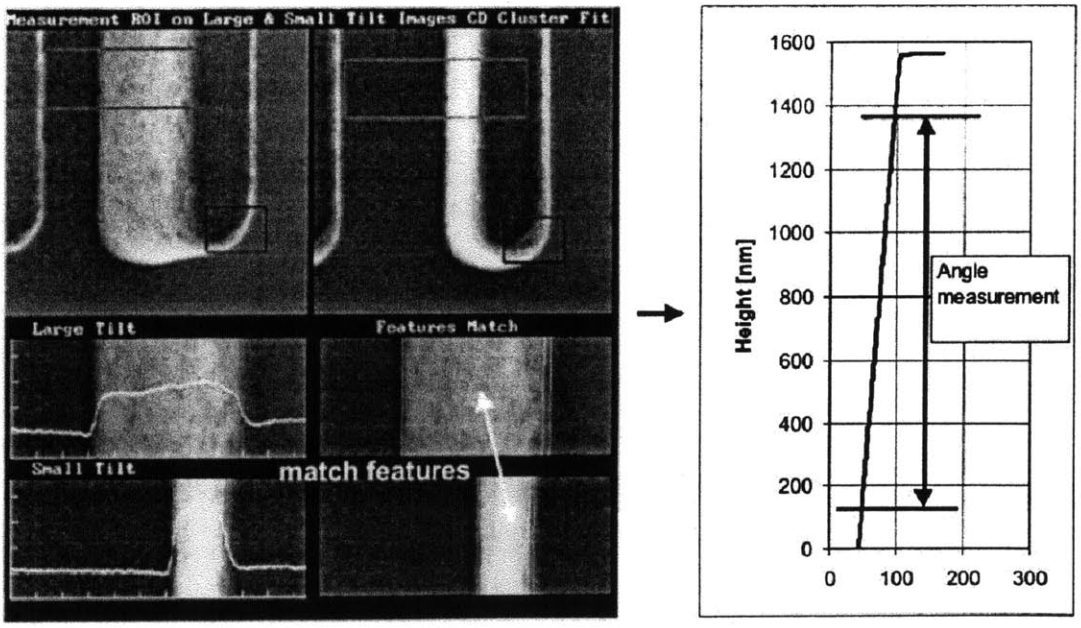

Figure 3-17: Data Captured From Marschner's 3D Sidewall Measurements. From the image on the left, Marschner is able to determine the height and angle of this sidewall. The measurement results are presented on the right.

information built upon varied assumptions, it provides a niche utility undelivered by other instruments: an incredible lateral resolution on the order of one nanometer. By feeding back electrons instead of photons, the instrument is not limited by the diffraction of light parameterized by the Rayleigh criterion.

The instrument must raster scan over the area meaning only one point of data is taken at a time. The expected rate at which this instrument collects data is about five thousand points per second. This instrument has the capability to measure vertical sidewalls, but lacks the ability to measure flat planes. Thus it can not measure all free surfaces interestingly enough for the opposite reason that most profilometers have incomplete free surface data.

The SEM uses a stream of high energy electrons to image the surface meaning that each sample must be electrically conductive. In order to image our polymer sample it would have to be sputter coated with a layer of gold. The thickness of these coats can be on the order of nanometers. This can significantly change the shape if the resolution of the instrument is on the same order.

A scanning electron microscope is not well suited for a manufacturing environment. Any object being measured must be placed into a vacuum chamber. The positioning of the object and time required to draw vacuum makes it difficult to prepare the measurement in a timely manner. Also, the object being measured typically must be electrically conductive to enable the measurement requiring most biological or organic samples to be sputter-coated with gold. This conditioning would also apply to plastic PMMA parts making it impractical to measure them with CD-SEM technology.

3.9 Review of Research Papers

The seven research papers reviewed in this literature search represent the most innovative research being conducted to solve our inspection problem. Each method

Criterion	Low Value: 1	High Value: 5
Lateral Resolution	10 microns	10 nanometers
Vertical Resolution	15 microns	10 nanometers
Inspection Speed	4,000 voxels/sec	1,000,000 voxels/sec
Vertical Range	100 nanometers	200 microns
Use in Manufacturing	Liquid / Vacuum	Non-Contact Optical

Table 3.1: Performance Criterion for Research Papers. Each one of the papers reviewed in this thesis are now evaluated on five performance criterion to determine how well they stand up to the original functional requirements.

Research Paper	Lateral Res (μm)	Vertical Res (μm)	Inspection Speed ($\frac{\text{voxels}}{\text{sec}}$)	Vertical Range (μm)	Use in Manufacturing
Hidrovo, Hart	3	3	3	4	1
Li, Xu	4	4	2	4	1
Ishii, Mitudo	1	1	5	5	5
Olszak	4	5	2	2	5
Kumar	4	5	3	2	5
Montgomery	4	4	2	2	5
Marschner	5	5	1	2	1

Table 3.2: Review of Research Papers. Each paper presented in this thesis is now evaluated on how well it met the performance criterion as described in the previous table.

will be evaluated on how well it serves the original functional requirements. While none of the research methods meet all of the criterion, they each demonstrate good performance other a wide range or a superlative in one. A ranking from one to five will be given to each paper on the following criterion and values in Table 3.1.

Using these metrics, the research papers are individually evaluated in Table 3.2.

Chapter 4

Evaluation of Commercial Profilometers

The field of micromanufacturing is currently inhibited by the lack of adequate instrumentation to conduct in-line inspection of its manufactured goods. Currently two types of instruments stand out as the most qualified to address this need but fail to meet the performance criterion. It is found that structured light profilometers have insufficient lateral resolution while scanning white light interferometers (SWLI) have slow inspection speeds. These two parameters lateral resolution and inspection speed are identified as the most critical parameters that effect performance. For example, the vertical resolution of both instruments is at least an order of magnitude finer than their respective lateral resolutions. Thus, an improvement in vertical resolution would not significantly effect performance. In this chapter, the physical limitations in the mechanical and optical domains of both instruments are explored to explain their speed and resolution performance boundaries.

4.1 Optical Limitations

Both structured light profilometers and SWLI's use microscope objectives to focus the light emitted from the measured object onto the camera sensor. Yet, both instruments take a radically different metrological approach. This section examines

the optical limitations and implications on range and resolution waged by the different strategies.

4.1.1 Scanning White Light Interferometry

SWLI' s provide relatively high resolution metrology at relatively slow inspection speeds with respect to micromanufacturing needs. The interferometer emits a broadband spectrum of light normally centered about 550nm. The camera will only observe intensity variations when the sample is located at one working distance from the microscope objective. The intensity variations decay when the reflecting sample is perturbed a matter of microns from the working distance. The interferometer captures a light intensity signature by sampling the intensity as a function of height. The height of the object at every X,Y point is deduced from this signature. The repeatable and highly dense intensity information provided by the light source allows the interferometer to measure the height of each voxel with 1 nanometer repeatability. Interferometers using a high NA microscope objective with micron depths of field can still image the intensity signature in focus for it is only observed over a submicron range.

Interferometers must acquire large quantities of data in order to measure the profile of a surface as a result of their metrology strategy. The variations in intensity repeat in a sinusoidal nature with a spatial period equal to the center wavelength of light. In order to fully characterize the waveform, the intensity of the light must be measured at least twice per wavelength by the Nyquist sampling theorem. Stated by interferometry expert Peter de Groot, "Typically, a SWLI instrument acquires three to five intensity values per interference fringe per pixel and must process millions of data values to generate a single three-dimensional image."[29] In this same paper, de Groot shows how a minimalized data set sampling only once per wavelength can still produce accurate metrological results at the expense of a poorer 10 nanometer vertical repeatability. This tradeoff between accuracy and number of acquired data points becomes instrumental in calculating the maximum theoretical inspection

speed of SWLI's.

4.1.2 Structured Light Profilometery

Structured light profilometers provide high inspection speed with relatively poor lateral resolution. The 3D geometry of an object is assessed by exposing the object to patterned or structured light and observing its reflection. A pattern of lines is projected onto the part from four different angles. The height of any particular point can be determined from the four intensity values measured under the four illumination conditions. It is noted that because the structured light profilometer relies on the reflection of light from a sample they have difficultly measuring transparent parts.

Structured light profilometers achieve their great inspection speed by minimizing the amount of data required to measure the topography of the part. The optics are selected such that everything in the vertical range seen by the camera is in focus. Given these conditions, each voxel requires a minimum of four intensity values in order to calculate its height while a SWLI measuring the specified vertical range of 135 microns may easily require over 1,000. In order to view the entire vertical range in focus, the structured light profilometer must use a microscope objective with a relatively low numerical aperture which subsequently limits the profilometer's lateral resolution.

4.2 Inspection Speed of White Light Inteferometers

The inspection speed of SWLI's are recognized to be relatively slow, but how slow is slow? Unlike structured light profilometers, SWLI's do not advertise their inspection speed. The consumers of these goods do not seem to mind for they typically use the instruments in a metrology setting where time is not of the essence. During the capture of geometric information, a profilometer must go

Magnification	NA	Resolving Power (μm)	Magnified Pixel (μm)
100	0.85	0.353	0.176
50	0.55	0.545	0.273
20	0.4	0.75	0.375

Table 4.1: Limits on Lateral Resolution. This table calculates the diffraction limited pixel size for the different commercially available Mirau objectives based upon their numerical aperture.

though various phases each of which require a determinate amount of time. The purpose of this analysis is to first compartmentalize and then analyze the time required for each phase. This time budget analysis allows us to quantify the limitations on inspection speed for a SWLI.

4.2.1 Calculating the Maximum Pixels per Frame

This analysis calculates the theoretical inspection speed of a white light interferometer. The inspection speed is calculated by dividing the number of data points taken per field of view by the time required to collect them. In this section the maximum number of data points per field of view are calculated by examining the he tradeoffs between numerical aperture, magnification, and C-Mount optics geometry.

Each pixel in the array will give independent information if the optics are correctly sized. The optimal camera pixel size is calculated based upon the Mirau objective's magnification and numerical aperture. Table 4.1 shows the resolving power of three Mirau objectives based upon the Rayleigh criterion and Nyquist Sampling Theorem.

The magnified pixel sizes suggested in Table 4.1 represent an optimization of the optical hardware. A pixel size any smaller would provide "empty magnification" whereby the magnification is increased but no new information is collected. Empty

magnification cuts down on the inspection speed for the amount of data points collected per field of view decreases. Conversely, a pixel size any larger than the Rayleigh diffraction limit would not fully utilize the power of the microscope objective. High powered microscope objectives become more expensive as the numerical aperture increases. Using a magnified pixel size larger than the optimal pixel size would be a misappropriation of the hardware resources.

The optics used in SWLI have a finite diameter "D" over which they can collect and focus light. The rectangular camera sensor must be inscribed into this circle in order for all its pixel to receive illumination. Given sensor aspect ratio of W:H, Equations4.1 and 4.2 calculate the maximum width and height of a rectangular sensor that can be inscribed into a diameter D.

$$\text{Max Sensor Width} = D \cdot \frac{\left(\frac{W}{H}\right)}{\sqrt{\left(\frac{W}{H}\right)^2 + 1}} \tag{4.1}$$

$$\text{Max Sensor Height} = D \cdot \frac{1}{\sqrt{\left(\frac{W}{H}\right)^2 + 1}} \tag{4.2}$$

where W = Aspect Ratio Width

H = Aspect Ratio Height

D = Diameter of focussed light (m)

The maximum number of rows and columns on the sensor that can all collect independent information is found by dividing the maximum sensor width and height by the diffraction limited minimum pixel size.

$$\text{Maximum Rows} = \frac{3.28 \cdot D \cdot NA \cdot \left(\frac{W}{H}\right)}{\lambda \cdot M \cdot \sqrt{\left(\frac{W}{H}\right)^2 + 1}} \tag{4.3}$$

$$\text{Maximum Columns} = \frac{3.28 \cdot D \cdot NA}{\lambda \cdot M \cdot \sqrt{\left(\frac{W}{H}\right)^2 + 1}} \tag{4.4}$$

where M = Magnification of the Microscope Objective

Magnification	NA	Resolving Power (μm)	Magnified Pixel (μm)	Camera Pixel (μm)	Max Rows	Max Columns
100	0.85	0.395	0.197	19.7	855	684
50	0.55	0.61	0.305	15.25	1,106	885
20	0.4	0.839	0.419	8.38	2,012	1,609

Table 4.2: Limits on Pixels per Field of View. This table solves for the maximum rows and columns of optimally sized pixels that can fit into a C-Mount housing using parameters found in commercial products.

λ = Wavelength of Incident Light (m)

NA = Numerical Aperture of Microscope Objective

The incident wavelength of light λ can be a tricky number to quantify given the broadband spectrum of light present in white light interferometers. For the purposes of this study it will be estimated to be 550 nanometers. To calculate the maximum number of pixels per field of view the maximum number of rows are multiplied by the maximum number of columns in Equation 4.5.

$$\frac{\text{Pixels}}{\text{FOV}} = \frac{10.75 \cdot D^2 \cdot NA^2 \cdot \left(\frac{W}{H}\right)}{\lambda^2 \cdot M^2 \cdot \left(\left(\frac{W}{H}\right)^2 + 1\right)} \tag{4.5}$$

These equations can be used to calculate the maximum number of optimally sized pixels that can fit into C-Mount optics based upon the magnification and numerical aperture of three different commercially Mirau objectives. These numbers were calculated assuming a 21.6mm light diameter (or 4/3" optical size), a 5:4 aspect ratio, and a 550 nanometer wavelength of incident light.

4.2.2 Time Required per Field of View

The SLWI will conduct a series of events in order to capture the topography of the sample within the field of view. The diagram in Figure 4-1 was constructed to visualize the sequence of these stages. This section explains the nature of each

phase.

In the first phase the camera captures an image and then moves the focal plane vertically to the next location. The entire phase is carried out under constant vertical velocity. If the camera sensor remained completely exposed between frames the pixels would all output a uniformly gray intensity as the dark and light reflections from the intensity signature were averaged out. Thus, the exposure time is limited to only a fraction of the duty cycle. Under low speed conditions, it is assumed that the camera can collect a sufficient amount of light during this fractional duty cycle exposure time. Here, the time required t_{fps} to take each image and reposition the objective is limited by the frame rate of the camera. If high speed cameras (greater than 100 fps) were used with SWLI's, the instruments would only see a marginal benefit in speed for time required to capture an image would then be limited by the intensity of incident light.

Phase 2 accounts for the time to accelerate and decelerate the mass horizontally. This time limit can be affected by large signal, power bandwidth limitations where saturation of the driving force becomes an inhibitor. This limitation is more pronounced in for structured light profilometers for these instruments do not require movement in the vertical direction and spend the majority of the operating time moving horizontally to a new destination. The time allotted for phase 2 to move and settle the object to a new location with respect to the camera is denoted as $t_{horizontal}$.

With both phases identified the amount of time required to scan through a field of view can be estimated. For each field of view or X,Y location the instrument will capture a stack of images. The number of images in that stack will be a function of the range, incident wavelength of light, and the number of exposures per wavelength. Phase 1 is repeated once per image while Phase 2 is repeated once per field of view. Equation 4.6 sums up this behavior as it calculates the amount of time required per stack.

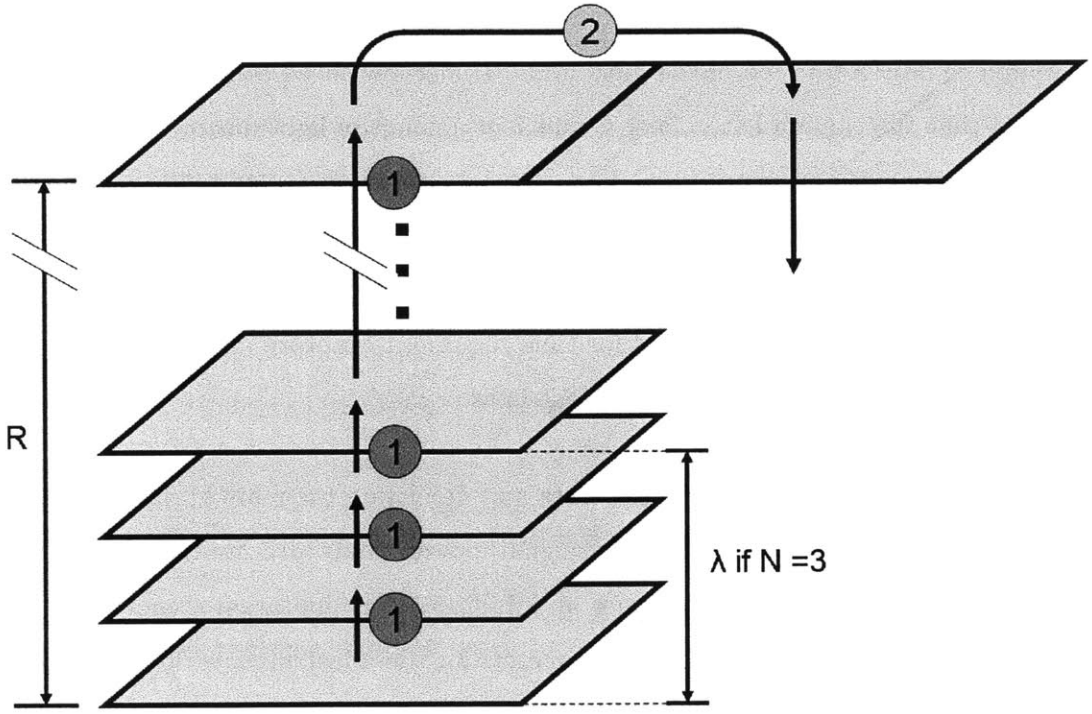

Figure 4-1: Sequence of Events in a Vertical Stack Configuration. This figure portrays the sequence of events that a SLWI will take in order to capture a volume of information with height R. Each blue parallelogram represents an image taken by the camera focused at that plane. The camera must first take a series of images in a vertical stack, each of which is denoted by a red circle, before relocating to the next X,Y location.

$$Time = \frac{R \cdot N}{\lambda} \cdot t_{fps} + t_{settle} \tag{4.6}$$

where λ = wavelength of incident light (m)

N = Number of exposures per wavelength

R = Vertical Range (m)

t_{fps} = Time required per frame (s)

t_{settle} = Time required to move horizontally (s)

As touched upon before, N represents the number of exposures taken to characterize the sample within a single wavelength of incident light. The value N has a high impact on the total amount of time required. While a typical value for N can be between 3 and 5, it has been shown that SLWI's still function but with reduced accuracy with N greater than 1.

The settling time is dependent upon the dynamics of the stage which moves the sample horizontally. Without proper details such as the mass, stiffness, and power of the stage it is very difficult to accurately predict this measure. Instead, the settling time is estimated by canvasing the commercial products built to provide microscopy positioning services. Thor Labs has engineered an impressive product dubbed MLS203 to provide such capabilities. From Thor Labs website, the MLS203:

"Thorlabs' MLS203 Series stages have been designed as drop-in replacements for the manual stages found on select Nikon, Olympus and Zeiss microscopes to provide motorized XY positioning of microscopy samples. Characterized by high-speed scanning capabilities and high positional accuracy, this stage is ideal for manually or automatically positioning a wide range of specimens and samples in many types of microscopy or imaging techniques and applications."

The Thor Labs MLS203 has the following interesting specifications:
Velocity (max): 250 mm/s
Acceleration (max): 2000 mm/s^2

Bidirectional Repeatability: 0.25 μm

Settling Time within 1.0 um: 0.10 seconds

Settling Time within 0.1 um: 0.60 seconds

Given an approximate pixel size of 0.5 μm, it is appropriate for the stage to settle to within 0.1 μm before taking the image. The 0.6 second horizontal settling time does not represent a lower bound, but simply a practical value to use in the calculation. This amount of time represents a small portion of the time budget whereby an uncertainty in its value will not have a large effect on the theoretically calculated inspection speed.

4.2.3 Theoretical Inspection Speed

The results of the last two sections can now be combined to solve for the theoretical inspection speed of a white light interferometer. In Equation 4.7, the number of data points per field of view is divided by the time required to scan each field of view.

$$\text{Inspection Speed} = \frac{10.75 \cdot D^2 \cdot NA^2 \cdot \left(\frac{W}{H}\right)}{M^2 \cdot \left(\left(\frac{W}{H}\right)^2 + 1\right)(R \cdot N \cdot \lambda \cdot t_{fps} + \lambda^2 \cdot t_{settle})} \tag{4.7}$$

From Equation 4.7 it is clear that the maximum inspection speed will change depending upon the microscope objective selected. The inspection speed is calculated for the three listed objectives using the values for the parameters derived in this section. Table 4.3 reviews the parameters used in calculation the inspection speeds in Table 4.4. Although the frame rate can be increased to push the instrument's performance boundaries, we use a frame rate of 30 Hz for this preliminary calculation because it most accurately represents the SLWI's on the market today.

The values for inspection speed presented in Table 4.4 represent the maximum values from the theoretical calculation. There are a variety of practical limitations that serve to deteriorate this number. Firstly, it is unlikely that a commercial

Parameter	Symbol	Value
Wavelength of Light	λ	550nm
Vertical Range	R	190 μm
Exposures per Wavelength	N	3
Exposure Time	t_{fps}	33ms
Settling Time	t_{settle}	600 ms

Table 4.3: Table to summarize the parameters used when calculating the Inspection Speed in Table 4.4.

Magnification	NA	Resolving Power (μm)	Inspection Speed (points/sec)
100	0.85	0.39	16,600
50	0.55	0.61	27,800
20	0.40	0.84	92,000

Table 4.4: Maximum Theoretical Inspection Speed. This table holds the theoretical inspection speed values for white light interferometers using the most common three Mirau Objectives.

camera will have exactly the optimal size and number of pixels calculated by Equations 4.3 and 4.4. Secondly, a single interferometer will use multiple objectives but a single camera to take images whereby the camera sensor can only be optimized for a single objective. Lastly, the estimatations do not account for duplications of pixels caused by stitching. A certain portion of each frame must be overlapped with the next to stitch together a large range from smaller fields of view.

The results from Table 4.4 show that lower magnification objectives yield faster inspection speeds. This effect can be understood by analyzing the information in Table 4.2 which shows the maximum number of optimally sized pixels that can fit in a C-Mount camera based upon the selected microscope objective. A 20X lens can pack 3.23 Megapixels into one exposure while a 100X lens can only fit 0.58 Megapixels. Thus, a SWLI equipped with a 100X lens must capture 5.5 stacks of information in order to output the same amount of data points the 20X lens can capture with one. This inspection speed relationship holds true insofar as the camera can maintain the same frame rate while outputting either 3.23 or 0.58 Megapixels per frame. This assumption breaks down as the frame rate increases for cameras have limited bandwidth.

4.3 Inspection Speed of Structured Light Profilometers

This section explores the inspection speed of structured light profilometers. The inspection speed of these instruments is far better documented than white light interferometers for it serves as the main metric when comparing performance across competitors.

Unlike the scanning white light interferometer, the structured light profilometer uses low powered numerical aperture lenses that image a relatively large depth of field in focus. In turn, these low numerical aperture objectives have relatively poor lateral

resolution. A low powered telecentric lens is typically used in this application to provide, in many cases, a demagnified image with minimal distortion. Equation 4.8 calculates the minimum lateral resolution attainable by a structured light profilometer using a microscope objective that must image an entire vertical range "R" in focus.

$$L = \frac{0.61 \cdot \lambda}{\sqrt{1 - \left(1 - \frac{\lambda}{4 \cdot R}\right)^2}} \tag{4.8}$$

where L = Diffraction limited lateral resolution (m)

λ = Wavelength of incident light (m)

R = Vertical range of the instrument (m)

Using a 550 nanometer wavelength light source and a 190 μm vertical range it is found that a structured light profilometer can achieve a diffraction limited 8.8 μm lateral resolution via a 0.038 numerical aperture lens.

The method in which structured light profilometers collect topographical data also be broken down into two similar phases. First in Phase 1 a camera will acquire imagery while both itself and the measured sample are stationary. The camera will take "n" redundant pictures at four different lighting conditions. The time required to complete phase 1 is simply the number of images acquired (four times n) divided by the frame rate of the camera t_{fps}. The speed in which the lighting conditions can be changed can become a rate limiting factor as frame rates increase. A creative solution to this problem is proposed by Caspar. [30]

In Phase 2 the instrument must move the measured part laterally a distance equal to the field of view to the new location before collecting the next set of images. The field of view dimensions are calculated by multiplying the image pixel size by the minimum number of either rows or columns in the array. The time required to travel this distance is dependent upon the maximum acceleration "A." In theory, the stage can apply constant acceleration through the first half of travel and constant deceleration through the second half to bring the stage to rest at a new

location. In practice applying such an instantaneous force would jerk the system sending vibrations through the frame ultimately requiring additional time to settle. For the purposes of this analysis the settling time is assumed to be zero. A more accurate estimation of this time would require specific information of the stage dynamics namely its crossover bandwidth and damping ratio.

The inspection speed is again calculated by dividing the number of points per field of view by the time required to capture each field of view. The theoretical maximum inspection speed for a structured light profilometer is governed by Equation 4.9.

$$\text{Inspection Speed} = \frac{M \cdot N}{4 \cdot n \cdot t_{fps} + 2\sqrt{\frac{I \cdot M}{A}}} \tag{4.9}$$

where N = Number of columns in the pixel array

M = Number of rows in the pixel array (where M $\leq$ N)

n = Number of images at each lighting condition

t_{fps} = Time required per frame (s)

I = Size of image pixels (m)

A = Maximum acceleration of the stage (m/s^2)

Using Equation 4.9 we can input reasonable values for the variables to get a practical limit on speed. Manufacturer Koh Young uses the Ademic Quartz series high speed camera which output 180 frames per second at 2,000 x 2,000 pixels per frame. Assuming that four pictures are taken at each illumination condition, 10 micron image pixels, and a maximum acceleration of 1g such a system could capture 22.3 million data points per second. This value again does not account for the time required to settle or the overlap of redundant pixels in the stitching phase. This theoretical inspection speed compared against the documented inspection speeds of various structured light profilometers in Table 4.5. [31], [32], [33], [34], [35]

Manufacturer	Model	Lateral Resolution (μm)	Inspection Speed (points/sec)
VI Technologies	3D SPI	20	5,000,000
Easy Braid Co.	SPI HS60	18	9,260,000
Koh Young	Prime	11	11,200,000
Omron	VP6000	15	12,000,000
Cyber Optics	SE500cp	15	15,400,000

Table 4.5: This table shows the documented inspection speeds and lateral resolutions of the structured light profilometers on the market today.

4.4 Comparison across Instruments: Inspection Speed vs Lateral Resolution

The performance of both structured light profilometers and white light interferometers can be evaluated by comparing their lateral resolution and inspection speeds. To graphically visualize how these instruments stack up against each other their performance parameters have been plotted in Figure 4-2. The inspection speed is plotted on the vertical axis while lateral resolution is plotted on the horizontal axis. The lateral resolution is expressed in terms of line pairs per millimeter, a common industry standard. The axis were selected such that larger magnitudes corresponded with higher performance. Equation 4.10 shows how to calculate line pairs per millimeter in terms of the numerical aperture. The inspection speed was chosen to be expressed in data points per second as to normalize the size of the pixel across instruments. Furthermore, it is assumed that all measured data points reside with a 190 μm vertical range. Lastly, it is noted that the plot is on log-log axis whereby the performance parameters can differ by multiple orders of magnitude.

$$\text{Line Pairs / mm} = \frac{1000}{2 \cdot L} = \frac{328 \cdot NA}{\lambda} \tag{4.10}$$

where L = Diffraction limited lateral resolution (m)

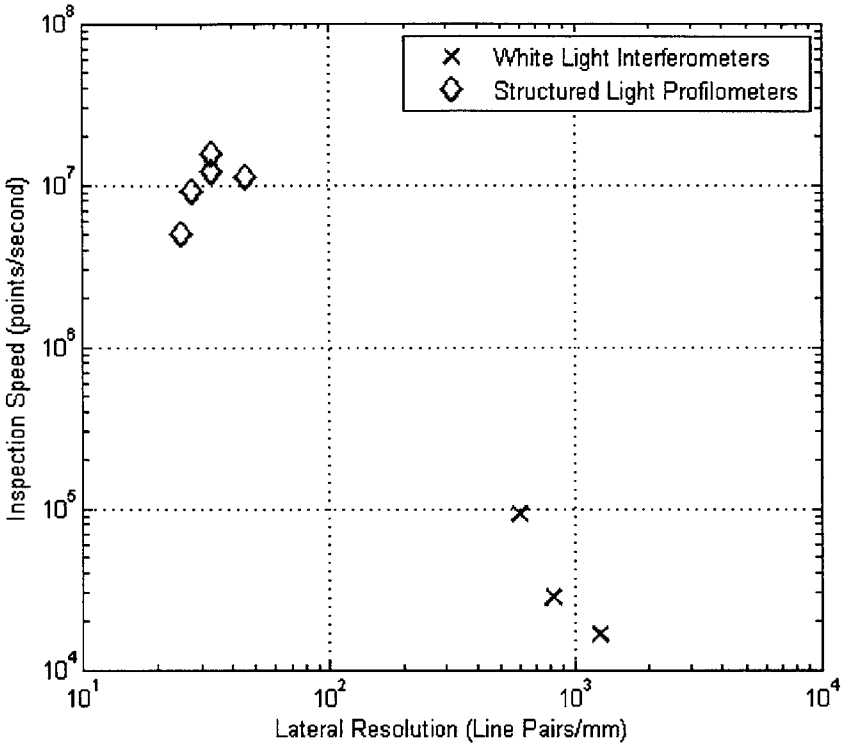

Figure 4-2: Inspection Speed versus Lateral Resolution Comparison. This graph plots the inspection speed of both structured light profilometers and white light interferometers against their lateral resolution. The blue data was theoretically calculated while the red data was collected empirically.

NA = Numerical Aperture of the objective lens

λ = Wavelength of incident light (m)

Chapter 5

Depth From Focus Design

The unique design of the high speed 3D profilometer utilizes a "depth from focus" metrology approach in order to maximize the measurement speed of the submicron resolution instrument. This section explains how the instrument was specifically designed to fully utilize the data acquisition potential of high speed cameras. The evolution of the instrument is laid out showing how the preliminary results were ultimately shaped into the final design. The purpose of this chapter is to conceptually introduce the depth from focus technique and show some of its results to give the reader enough background knowledge to understand the design decisions in the mechanical, optical, and software domains.

5.1 Depth From Focus Concept

The greatest bottleneck identified in collecting high resolution, high speed topographical information from a sample was the rate the raw data can be collected. As described in Chapter 2 a profilometer that uses high numerical aperture microscope objectives suffers from a small depth of field. This small depth of field requires that the part be sampled frequently in the vertical axis. In order measure each voxel a scanning white light interferometer or depth from focus profilometer often will collect hundreds if not thousands of data points. Conversely, a structured

light profilometer with low lateral resolution and wide depth of field must take only four data points per voxel. The need to capture large quantities of data in short amounts of time to serve the high resolution systems can be met by high speed cameras that have come to the market within the past decade.

The focus of the design was to maximize the use of the high speed camera. These cameras are designed to take a burst of high speed imagery to collect data on a rapidly moving object. Our application instead requires a continuous collection of high speed imaging on an object whose movement is slow and controlled. In order to maximize the utility of the camera in our application, each frame snapped by the camera must take unique information that has no overlap or redundancy from any prior or future frames. This constraint requires that the part be repositioned with respect to the camera between each frame. The high speed cameras considered for this instrument can output 50,000 frames per second at their full resolution leaving 20 microseconds to capture each image. This extremely brief amount of time makes it dynamically impossible for the object to be repositioned and then come to rest between each frame. Thus it was a necessity to have the part move at a constant velocity during acquisition.

A tilted camera configuration was used in order to accomplish both constant velocity movement of the part and unique capture of information of each frame. As the part moves across the tiled camera plane a volume is captured whose height and width are limited by the dimensions of the camera, but whose length is unbound. This configuration allows the camera to capture information on long swaths of volume without interruption. Each instance the part must stop or reverse its direction comes with down time during which the camera is being under utilized. Scanning white light interferometers have a significant amount of reversals given the way they capture information that our depth from focus profilometer does not fall victim to. Thus, this tilted camera configuration minimizes downtime by allowing the camera to continuously capture new information on each frame irrespective of its frame rate.

The mechanics of the tilted field of view design are summarized in the 3D Figure 5-1. The details behind this figure will be broken down in more detail after giving a brief overview of the tilted concept. Each horizontal line of pixels can be thought about as an independent line scan camera. By using an area scan camera, multiple hundreds of line scan images can be taken in parallel. A 1D line scan camera forms a 2D image by compiling a sequence photographs captured at equally spaced intervals. Each row of pixels in our camera can compile a 2D image with each image focused at a different focal plane. This concept is illustrated in Figure 5-1 whereby the color coded steps of the 3D object only show up in focus to their corresponding color coded row of pixels on the camera sensor array. The red pixels will see the surfaces in focus only if they within its depth of field. In this manner by identifying at which row of pixels a surface becomes in focus the instrument can then identify its height.

The mechanics of the tilted depth from focus concept are simplified into two dimensions and broken down by steps in Figure 5-2. Frame (a) depicts a side view of a camera sensor with M rows simplified to show six color coded pixels. The camera sensor is rotated with respect to the horizontal by an angle θ. Each row of pixels extends into the page and is represented by a singular rectangle. One working distance away from the optics lie the magnified pixels as represented by color coded circles. This row of magnified pixels is connected by a black line to indicate that the pixels are taken within the same frame. The purpose of the instrument is to take topographical information of the sample represented by an amorphous blue blob. In frame (b) the camera has stayed stationary while the sample has been moved a distance ΔX to the right. The new frame captured by the camera is shown to the left of the first. This step and capture process is repeated until the camera collects a series of N frames thus fully capturing the lattice of points shown in frame (c). Each horizontal line of pixels is grouped together to form M number of "Height Slices" in frame (d). Note that each height slice comes into focus at a different Z elevation. The data for each pixel is then grouped into vertical columns in frame (e) whereby

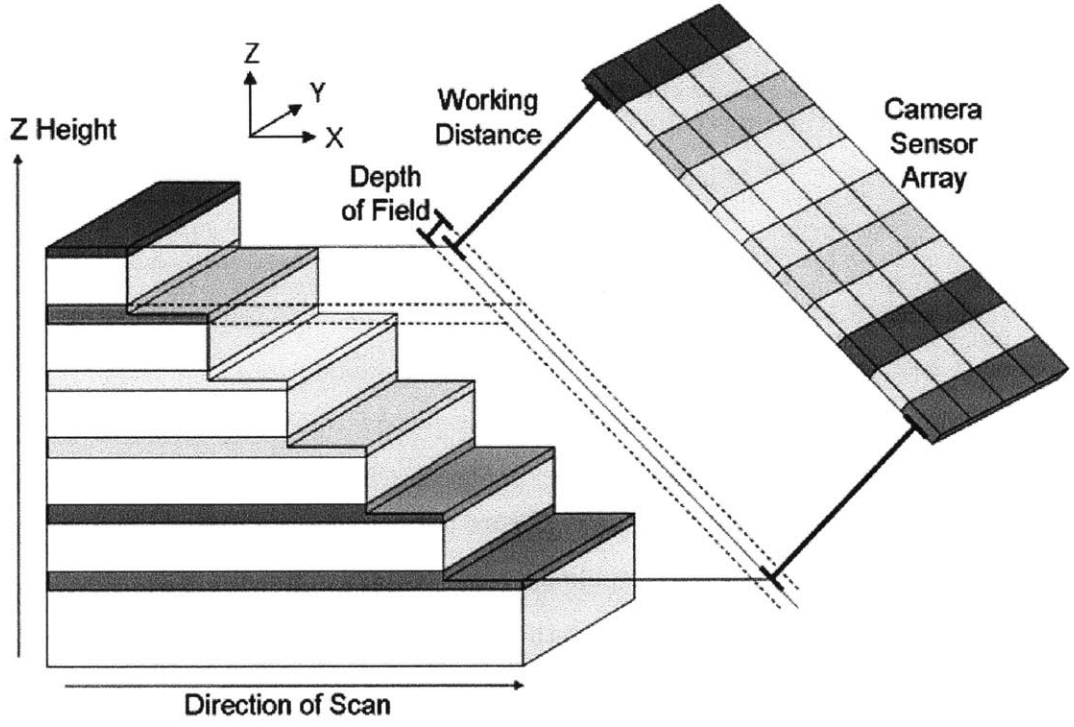

Figure 5-1: Conceptual Overview of Scanning Principles. This figure gives a basic overview on how the high speed profilometer collects multiple hundred line scans in parallel. Each row on camera sensor shown in the schematic on the right focuses on a different Z height and produces and independent image via relative movement of the part and camera exposure synchronization.

the height of the surface of point X(i) is determined by which pixel connected by the solid black line is most in focus. Lastly, all these processes are grouped together in frame (f) to give a compact 2D representation of the tilted depth from focus mechanics.

5.2 Preliminary Work with Telecentric Optics

The first iteration of our depth from focus profilometer used a telecentric lens to capture information. This lens was chosen to minimize distortion errors but came with a the drawback of a relatively low numerical aperture. This numerical aperture limited the optics to approximately a 6 micron lateral resolution and 100 micron depth of field. Although the depth of field was relatively large, the tilted configuration of the camera showed the pixels in the array could still measure depth by discriminating which portions of the image were either in or out of focus. A plastic μFac part was intentionally tilted such that its surface spanned across the focal planes of the camera pixels as illustrated simplistically in Figure 5-3. The information collected from these six lines of pixels are presented in their raw form in Figure 5-4. Each one of the six line scans was segmented into 50 x 50 pixel blocks. The standard deviation of the values in each 50 x 50 pixel block was calculated. A high standard deviation represented sharp, in-focus images and served as a measure to determine how "in-focus" each block was. The data from the block determined to be most in focus was imported into the line scan at the bottom of Figure 5-4. By using this technique an extended depth of field image was amalgamated from the six line scans. Figure 5-5 uses a color code to distinguish the line scans from one another. The amalgamation scan at the bottom of Figure 5-5 now shows a rudimentary height map of the scanned part. This data represented the first time our instrument was able to measure depth as a function of focus.

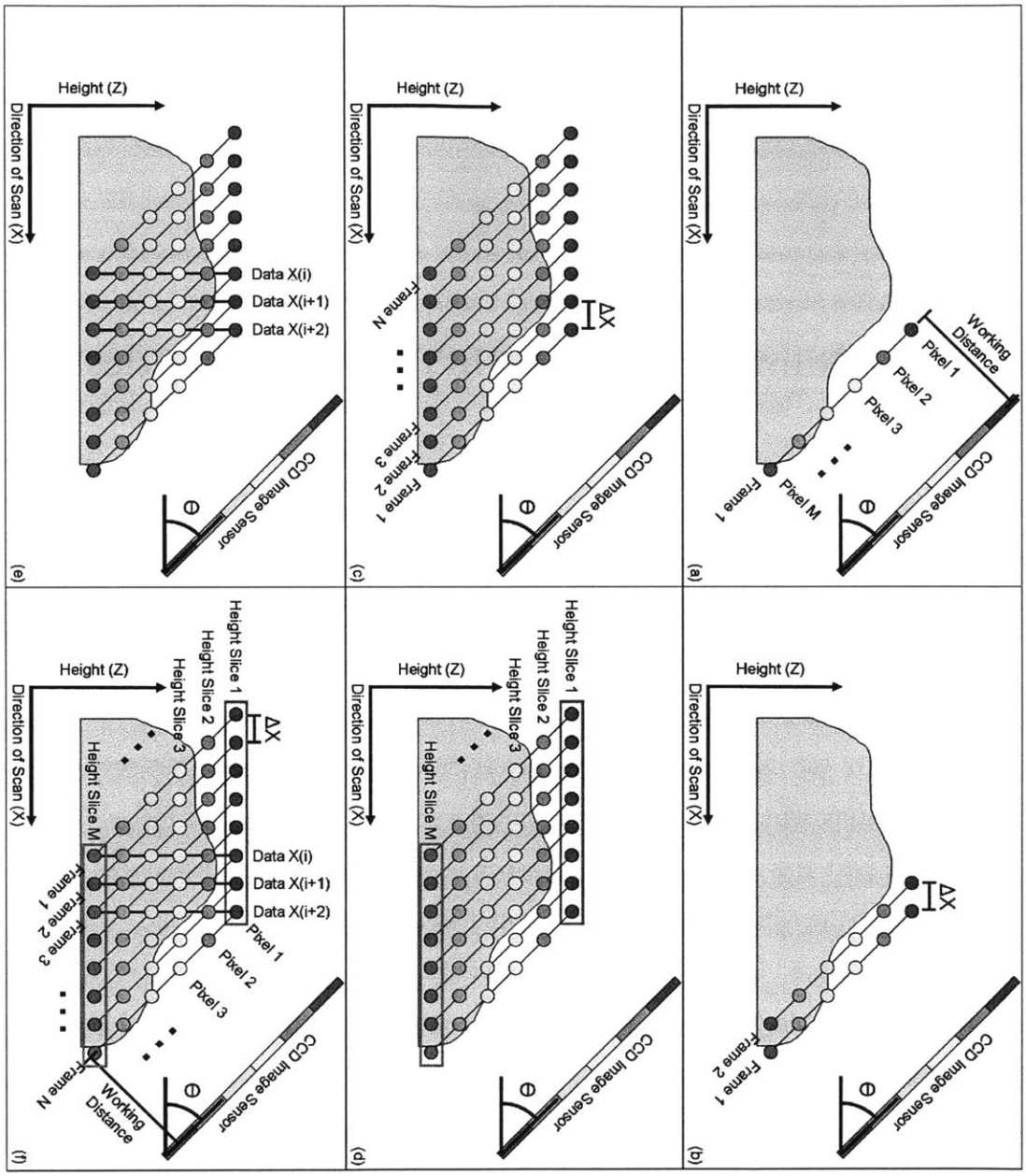

Figure 5-2: Step by Step Schematic Detailing Image Collection and Processing. This compilation of figures shows progressively how the tilted depth from focus configuration is able to collect height slices in parallel. (a) The camera takes a single image. (b) The part is moved a distance ΔX, another image is captured. (c) Image capture is repeated N times. (d) The data is segmented into "Height slices" to calculate local standard deviations. (e) The highest standard deviation is selected within each vertical stack of data to determine the topography.

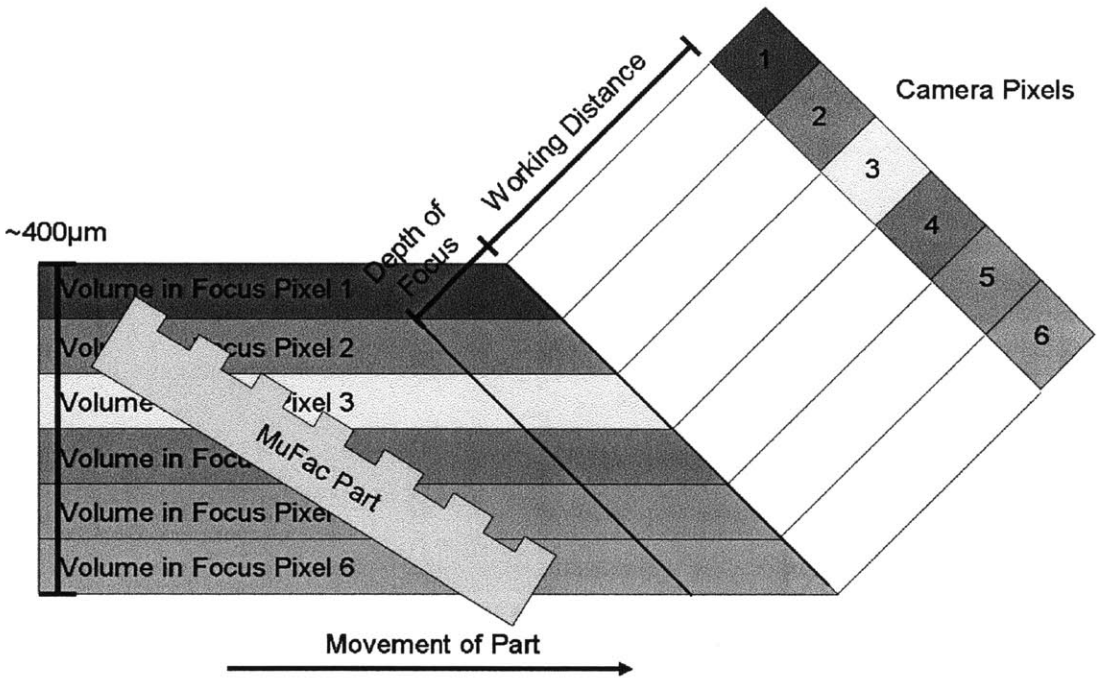

Figure 5-3: Historical Cross Sectional Schematic. This is the first figure created to explain the mechanics of the depth from focus profilometer. Although it is seemingly redundant, it was included for historical perspective as well as to give the reader better insight on how the μFac part was situated with respect to the camera pixels during the image capture of Figure 5-5.

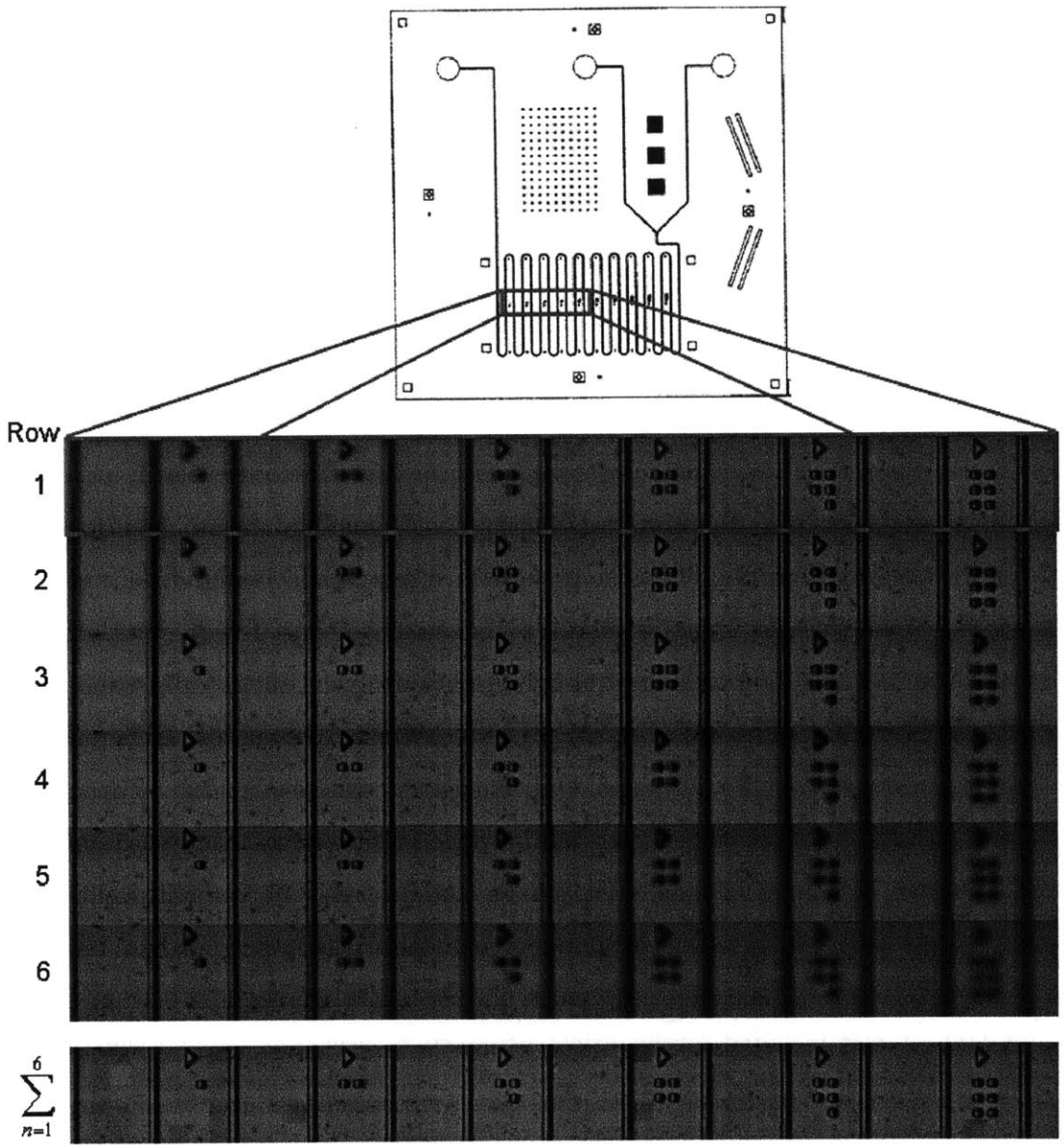

Figure 5-4: First Depth from Focus Information. This figure shows the same piece of the μFac part part being imaged by six different rows on the camera while using the telecentric lens. The amalgamation scan at the bottom of the figure selects and displays the scan with the highest standard deviation. This image shows the first extended depth of field image created by the high speed 3D profilometer.

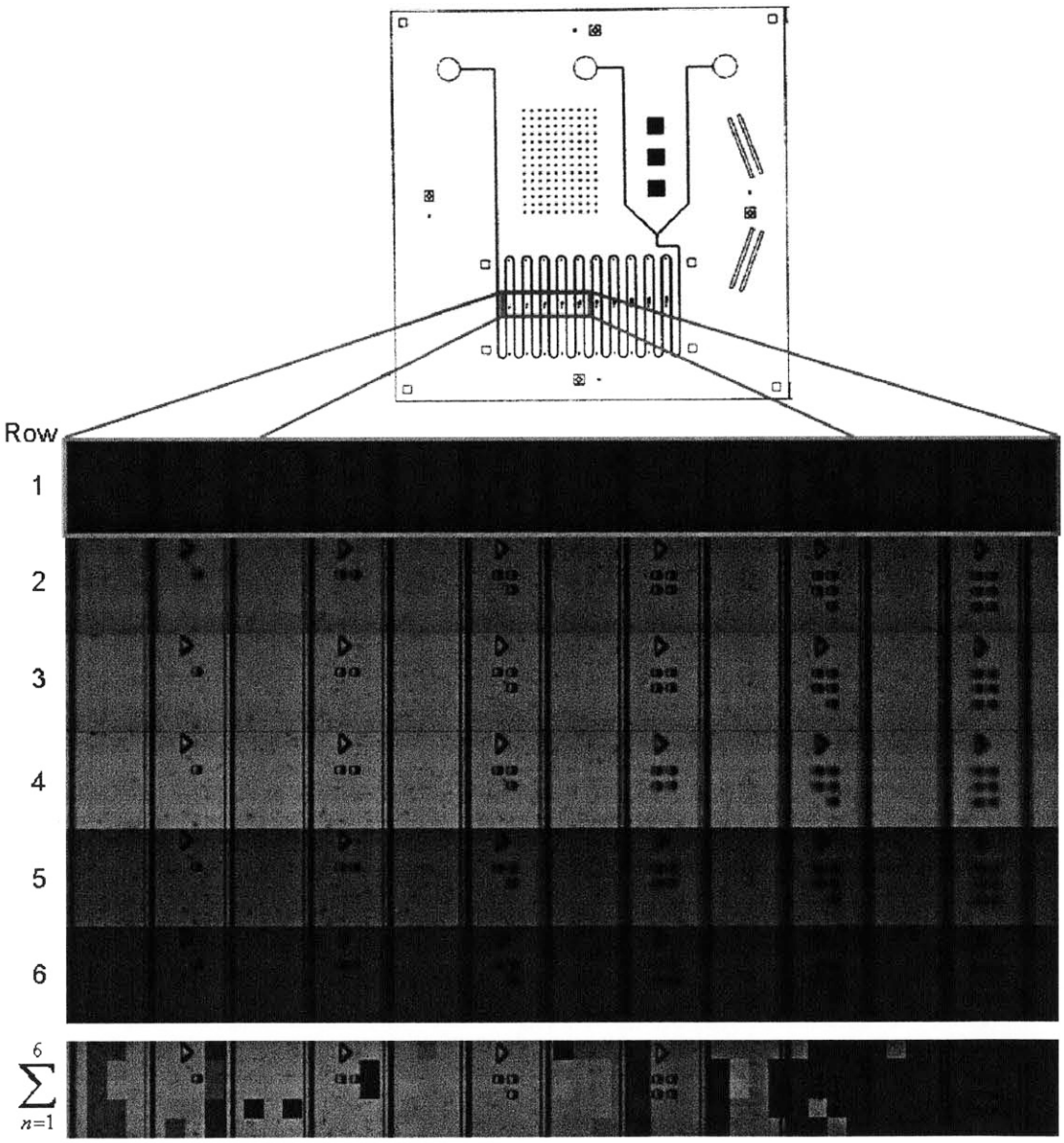

Figure 5-5: Color Coded Scan. The line scan information shown in Figure 5-5 has been color coded in this graphic to visually describe how the first rudimentary height ever conducted by our instrument was constructed. This height scan is shown as the amalgamation scan at the bottom of the figure.

5.3 Optimized Depth from Focus Results

Invigorated by the results collected with through telecentric optics, we looked to enhance the optical design by using a microscope objective with a large numerical aperture. The instrument was outfitted with a 50X Mitutoyo lens and used to measure the topography of an aluminum micromachined part with a 50 μm tall extrusion. The micromachining process produces a surface that is rich in texture thereby scattering light in various directions and producing contrast. This section will show the imagery taken of this micromachined surface and describe in broad strokes how the image processing algorithm works.

As described in this chapter, each row of the area scan camera can be thought about as a line scan camera. These "line scan cameras" capture imagery in parallel with each row capturing one height slice at a unique elevation. In Figure 5-6, six of height slices are shown side by side to give the reader a visual understanding of the camera's output. The figure was constructed such that the first height slice chosen had a focal plane at the top of the feature while the last height slice had a focal plane at its base. The borders of each height slice are color coded to symbolize their position relative to each other on the area scan camera as used in the explanatory cross sectional diagrams in Figures 5-2 and 5-3.

The image processing algorithm designed to evaluate focus works by first calculating the local standard deviation of the intensity values surrounding each pixel. This processes is demonstrated visually in Figure 5-7. In this figure, a green and a blue square define the perimeter for a subsection of the image. The histogram of intensity values present in each square is shown to the right of the image. The intensity values in the green area, considered to be out of focus, are very similar to one another while the intensity values in the blue area, considered to be in-focus, are more distributed. The standard deviation of in-focus values is relatively high compared to the standard deviation of the out-of-focus values. The standard deviation in turn is used as our measure of focus. This calculation is repeated for

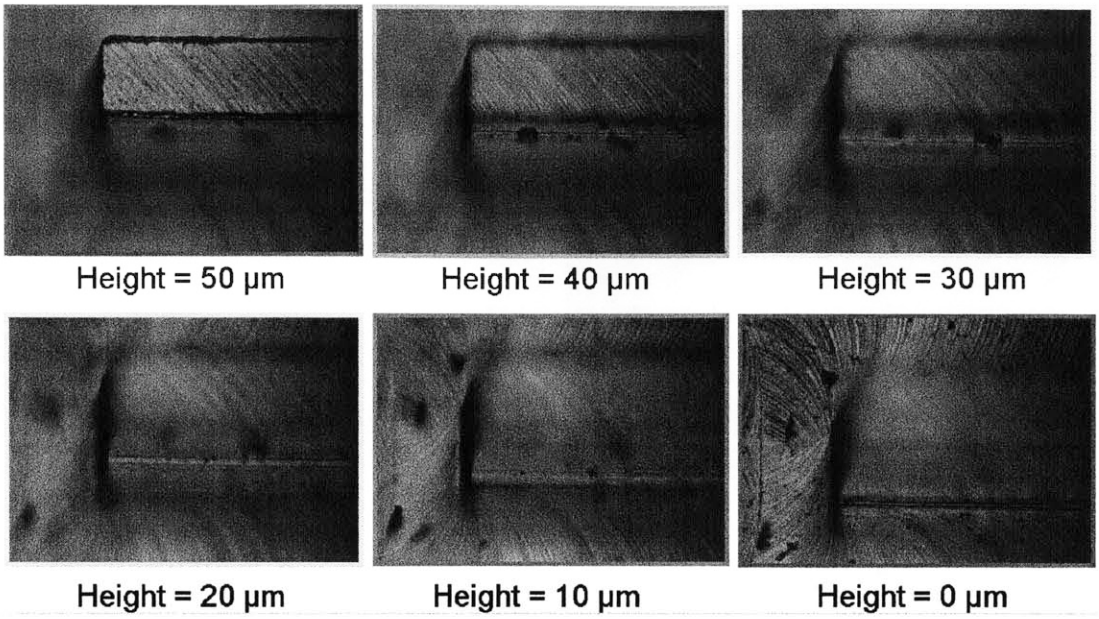

Figure 5-6: Individual Height Slices. This image shows six height slices that were captured in parallel by the area scan camera. Each slice has a different focal plane ultimately used by the camera to distinguish the sample's topography.

every pixel in the height slice. Figure 5-8 shows the result of processing the six height slices in Figure 5-6 by this technique.

Once the standard deviation values have been calculated for each height slice, the algorithm solves for the topography of the sample. A column of data is subselected for each X,Y point in the original image that takes one standard deviation value from each height slice. The Z height at any particular X,Y location is determined to be located at the height slice with the greatest standard deviation. This process is illustrated in Figure 5-9. The left graphic gives a visual demonstration of how this column of data is formed. On the right side of the figure, each standard deviation of intensity value at one X,Y location is graphed against its depth layer. The graph shows that this particular X,Y pixel most likely has a Z height that coincides with the 77th depth layer. This height finding algorithm is repeated for every pixel to produce a topographic image of the part as shown in Figure 5-10. The image uses the color bar indicated on the left to represent the height of the sample. It is

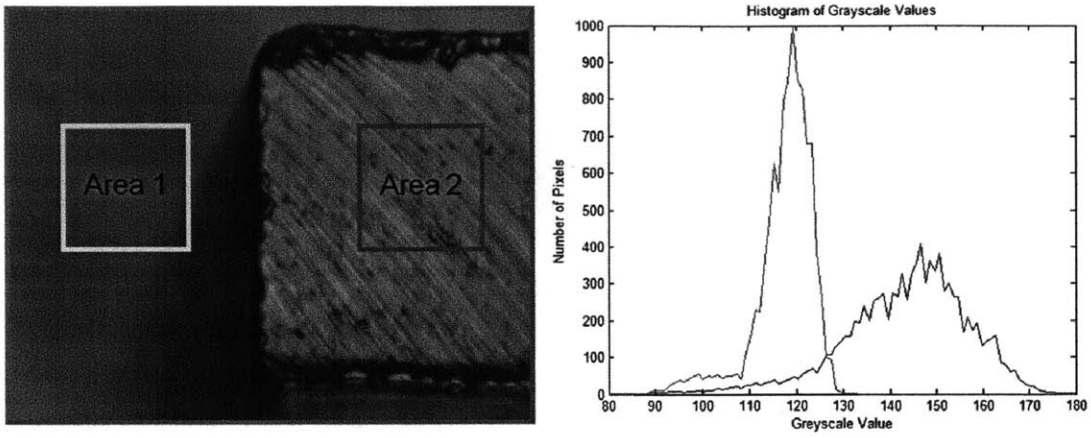

Figure 5-7: Standard Deviation Metric Defined. The histogram on the right shows the distribution of intensity values for the pixels circumscribed by the green and blue squares in the right image. The green out of focus pixels have a low standard deviation of intensity values while the blue in-focus pixels have a high standard deviation of intensity values.

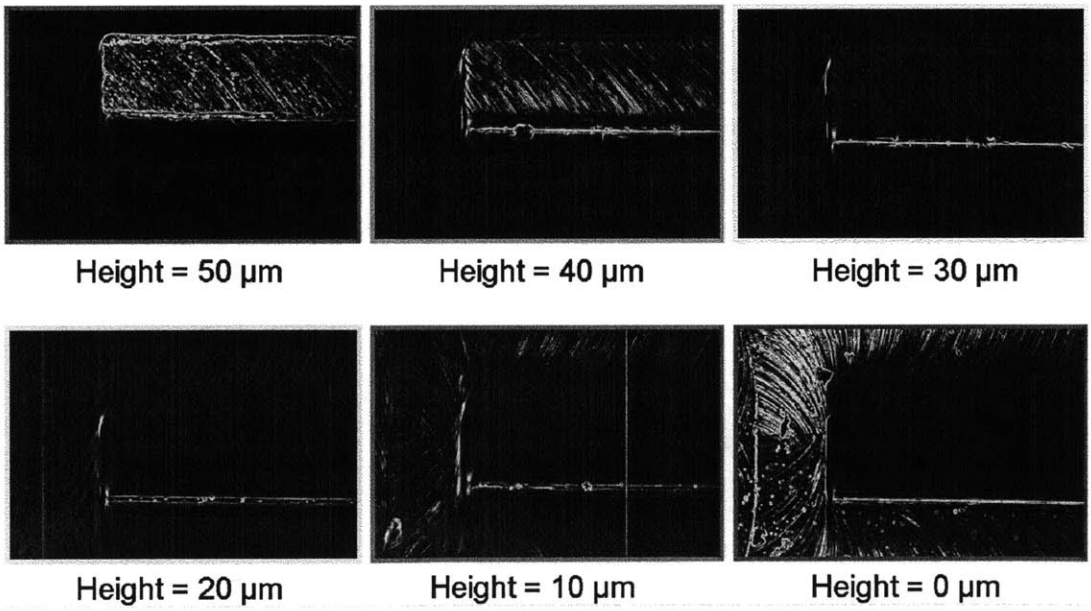

Figure 5-8: Localized Standard Deviation of Each Height Slice. The six height slice images shown in Figure 5-6 are processed to calculate the localized standard deviation. The red and blue colors represent high and low localized standard deviation values respectively.

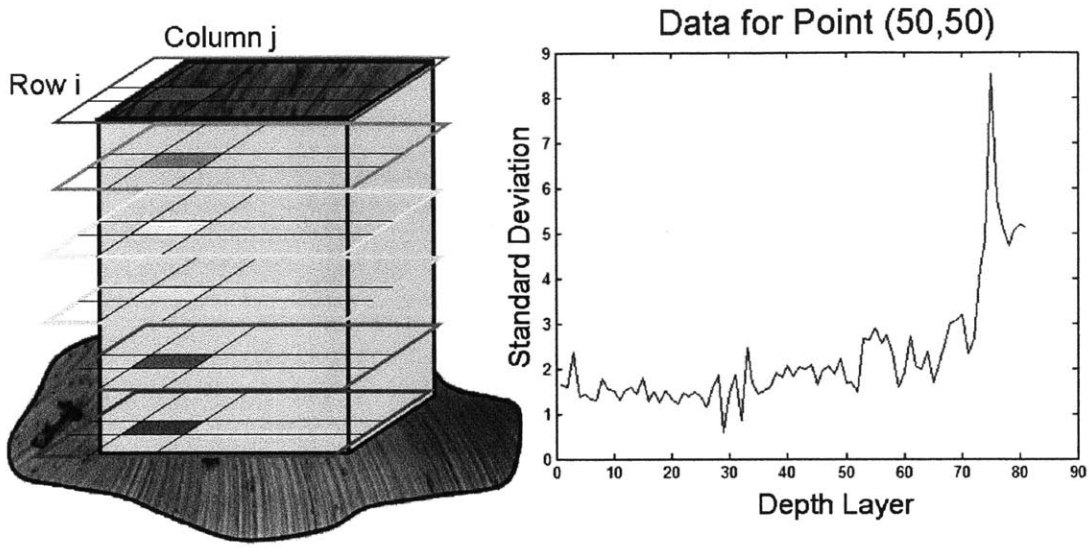

Figure 5-9: Determination of Highest Focus for Each Voxel. This graphic explains visually how the algorithm finds the height for each X,Y pixel. A column of standard deviation values is collected across all height slices and is graphed against its depth layer on the right. The depth layer corresponding to the maximum value is selected as the Z height.

important to note that the image does not show the topography top down, but instead at a tilted configuration. The area of the image showing a smooth transition from blue to red is a vertical surface. Once the image processing algorithm has identified the height slice corresponding to each X,Y location, the topographic information is used to compile an extended depth of field image. The intensity of the pixel located at the height slice selected by the maximum standard deviation is saved for each pixel and displayed in Figure 8-10. Through these means the instrument uses a tilted camera geometry coupled with a depth from focus algorithm to rapidly measure surface topography.

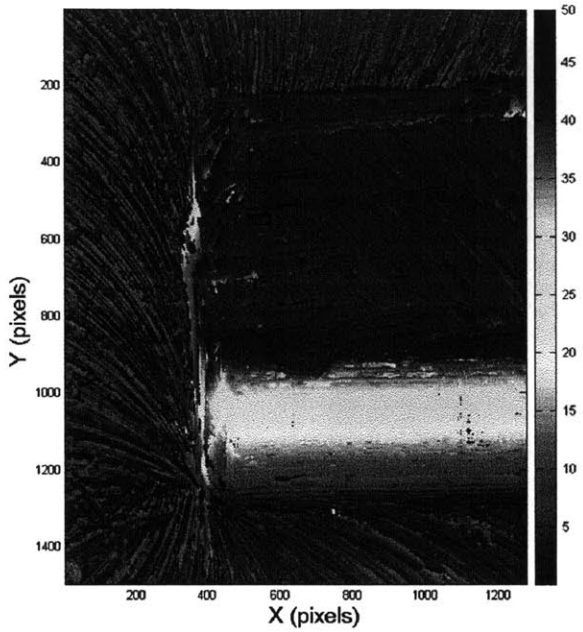

Figure 5-10: Height Map of Micromachined Part. This topographical measurement of a 50 μm tall aluminum extrusion is the first one of its kind measured by out instrument. The image demonstrates the instrument's capability to measure vertical sidewalls as a result its tilted camera configuration.

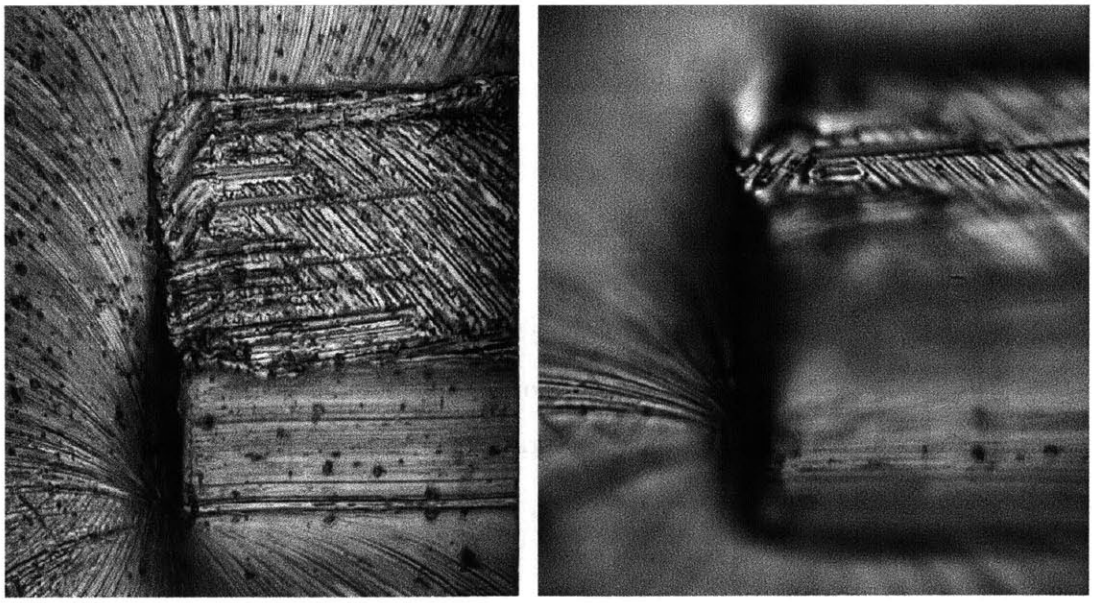

Figure 5-11: Extended Depth of Focus Image versus Original Content. This side by side image shows the extended depth of field image compiled by the above code against the original image captured by the camera.

Chapter 6

Mechanical Design of the 3D Profilometer

The high speed 3D profilometer uses a precision five axis stage to position the measured part with respect to the high speed camera. This section reviews the requirements for each axis and details the reasons behind the hardware selection. It was decided to keep the camera and lens apparatus stationary during scans given its large mass relative to the sample. The axis of motion are defined in Figure 6-1. Additionally, a comprehensive image of the mechanical stage and its components is shown next in Figure 6-2. Most components were chosen well before the design of the profilometer was finalized such that their capabilities were selected to provide flexibility in the design.

6.1 X,Y Air Bearing Stage

The high speed profilometer was built to rapidly measure relatively small features spaced apart by relatively large distances. This required the X,Y positioning system to have submicron repeatability over hundreds of millimeters of range. The constraints on the optical system are examined along with how the geometry of the μFac research drove these requirements.

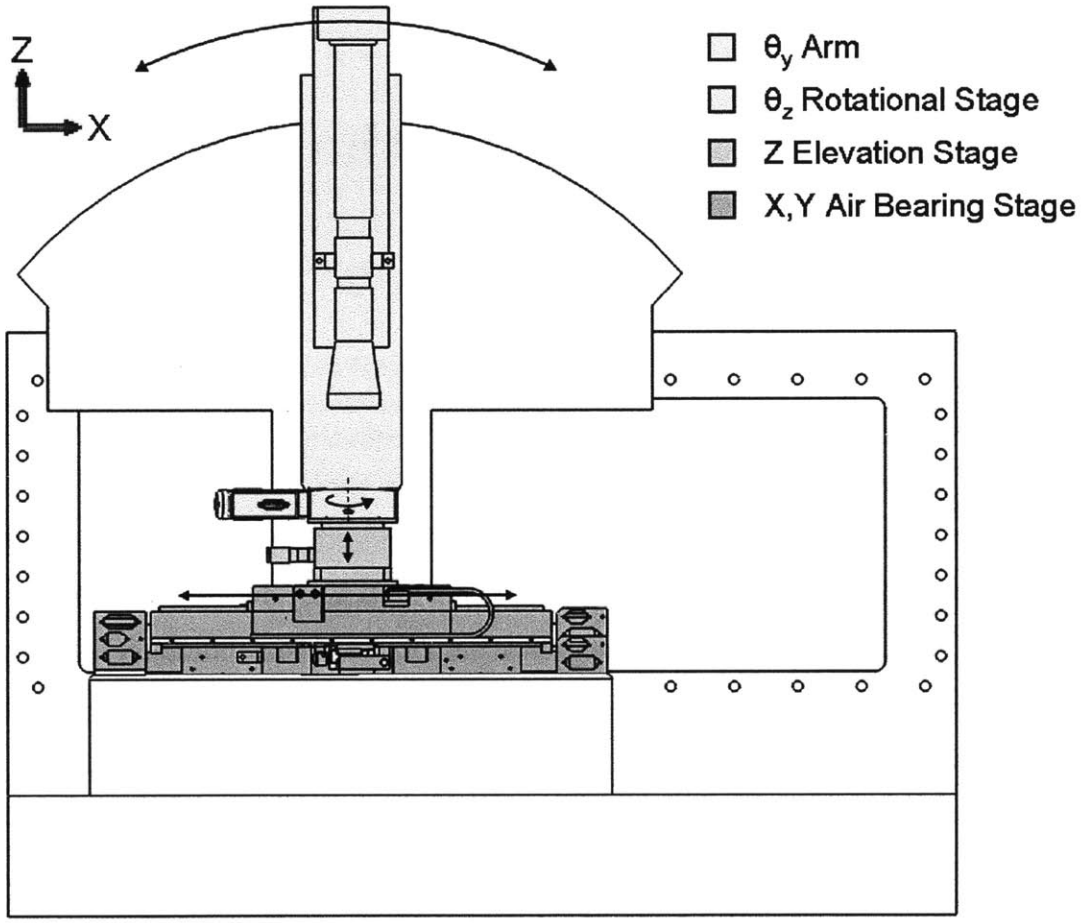

Figure 6-1: Overview of Motion Axis Schematic. This schematic identifies the actuators and bearings that move the stage in five degrees of freedom. The X, Y, Z, and θ_z axis are actively controlled while the θ_y arm is locked in once positioned.

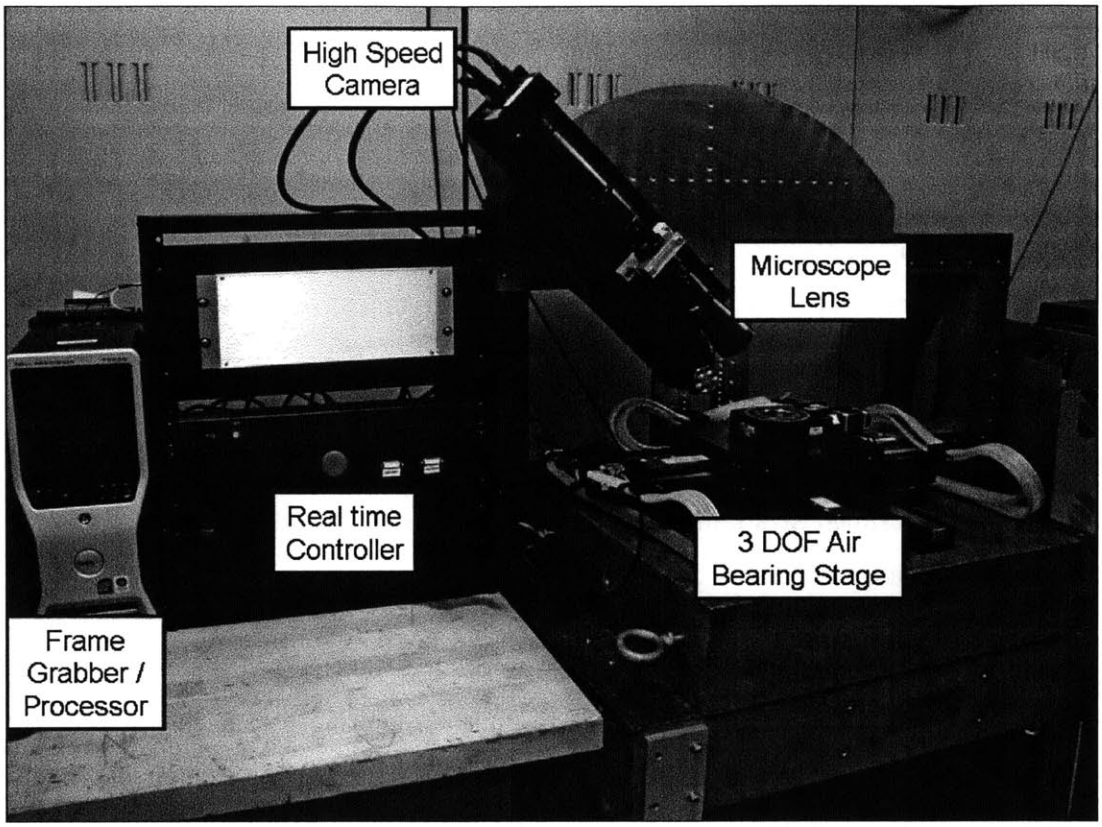

Figure 6-2: Photograph of the Stage Components. This figure labels all the components of the mechanical, optical, and software systems of the high speed profilometer to give an overview of their locations and setup.

The level of precision required of the stage was driven by the constraints in the optical system. As described in Section 2.2, the resolution of our optical system reaches a limit defined by the Rayleigh criterion dependent upon the numerical aperture of the lens and wavelength of incident light. Such an optical system can theoretically achieve a lateral resolution of 0.25 microns under optimum conditions. The repeatability of the X,Y stage needed to be about three times more precise than the Rayleigh criterion limit to ensure that the positioning errors of the stage did not induce errors into the optical measurement. Thus the target repeatability for the X,Y stage was set at 0.1 microns.

The range of the X,Y stage was set by the size of the parts intended to be measured by the instrument. The size of our original μFac Mircomixer measured 25mm x 25mm which served as the minimum range requirement. Knowing that such an instrument would be useful to the semiconductor industry, an X,Y stage with an 8" x 8" travel was desirable in order to measure 8" silicon wafers. The range of the X,Y stage was capped at a minimum of 25mm but was preferred to accommodate 200mm to provide the most flexibility for potential future measurements.

It was found that an air bearing stage with an optical encoder was the most economical means to reach the range and resolution requirements. A cheaper alternative would be to use preloaded ball bearings for the guide mechanism. Unfortunately these bearings suffer from contact phenomenon such as friction and stiction which ultimately limit their repeatability to 1.0 microns at best. Conversely, the air bearings allow all moving parts to move without contacting one another thus making the repeatability of the stage limited by the measurement device. A Heidenhain LIF481 optical encoder was chosen to measure the position of the carriage in X and Y. The read head of the encoder measures a tape with a four micron pitch and uses A quad B output signal. The A quad B signal natively outputs a resolution four times finer than the repeating period on the encoder giving it a resolution of 1 micron before interpolation. Using a 50X interpolator, the optical system outputs a resolution of 20 nanometers with a stated repeatability of 0.1

microns. The 40MHz bandwidth of the optical encoder insures that the metrology dynamics will have no noticeable effect on the mechanical dynamics or time synchronization. A laser interferometer system could have been used to enhance the repeatability of the X,Y stage but was found unnecessary given that the optical read head met the 0.1 micron repeatability requirement. A brief overview of these components including their specifications and configurations is shown in Figure 6-3.

A laser interferometer was used to to evaluate the repeatability of the optical encoder used to control the air bearing stage. To preform this test, the Y carriage was programmed to travel from one end of its travel to the other and back again. During this move the position of the carriage was measured simultaneously by both the optical encoder and a laser interferometer. The difference between the two measurements as a function of carriage position is plotted in Figure 6-4. If the laser interferometer is accurate to its stated repeatability of 1 nanometer, it can be assumed that any discrepancy between the two measurements greater than 1 nanometer can be attributed to errors in the optical encoder. By measuring the position on a forward and backward pass, the unrepeatable errors of the optical encoder can be quantified. From this data it is measured that the optical encoder has 0.12 μm repeatability.

6.2 θ_z Stage

The θ_z stage was incorporated into the design such that an object placed on the X,Y air bearing platform could be positioned automatically in all planar degrees of freedom. The stage has a large hole through the center to give the option for a light source to be placed behind the sample. A Newport URS100BPP rotational stage was selected to provide continuous 360° rotation at 0.0002° resolution. The open loop stepper motor drive guaranteed that the rotational position would remain constant while the rotational drive was not in use. Figure 6-5 shows the mechanical dimensions of the θ_z stage used in our high speed profilometer.

NOTES:
1. XY LINEAR AIR BEARING SYSTEM
2. TRAVEL: X:8" Y:18
3. VERTICAL LOAD CAPACITY: 100 LBS @ 80 PSI
4. MAGNETICALLY PRELOADED IN VERTICAL DIRECTION
5. MATERIALS: 6061 AL, BLACK HARDCOAT
6. OPERATING PRESSURE: 80 PSI

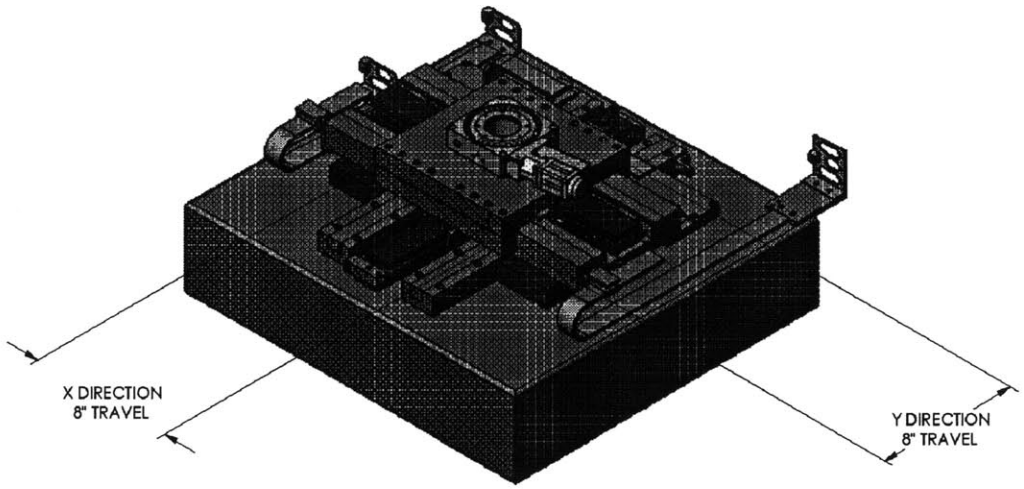

REVISIONS			
REV.	DESCRIPTION	DATE	APPROVED

ITEM NO.	PART OR IDENTIFYING NO.	NOMENCLATURE OR DESCRIPTION	MATERIAL SPECIFICATION	QTY REQD
		PARTS LIST		

UNLESS OTHERWISE SPECIFIED DIMENSIONS ARE IN INCHES
TOLERANCES ARE:
FRACTIONS DECIMALS ANGLES
± .XX± .01 ± _1
.XXX±.005

MATERIAL: 6061-6511
FINISH: BLACK HARDCOAT
DO NOT SCALE DRAWING

CAD GENERATED DRAWING. DO NOT MANUALLY UPDATE

	APP'D	DATE
DRAWN		
CHECKED		
ENG APP'D		
MFG APP'D		
QUALITY		

NELSON AIR CORP. 559 ROUTE 13 SOUTH, PO BOX 2 MILFORD, NH 03055 (603) 673-3505 FAX (603) 672-3005

PLANAR XY AIR BEARING STAGE 8X8" TRAVEL

SIZE B | DWG. NO. | REV.

SHEET 1 OF 1

NEXT ASSY	USED ON
APPLICATION	

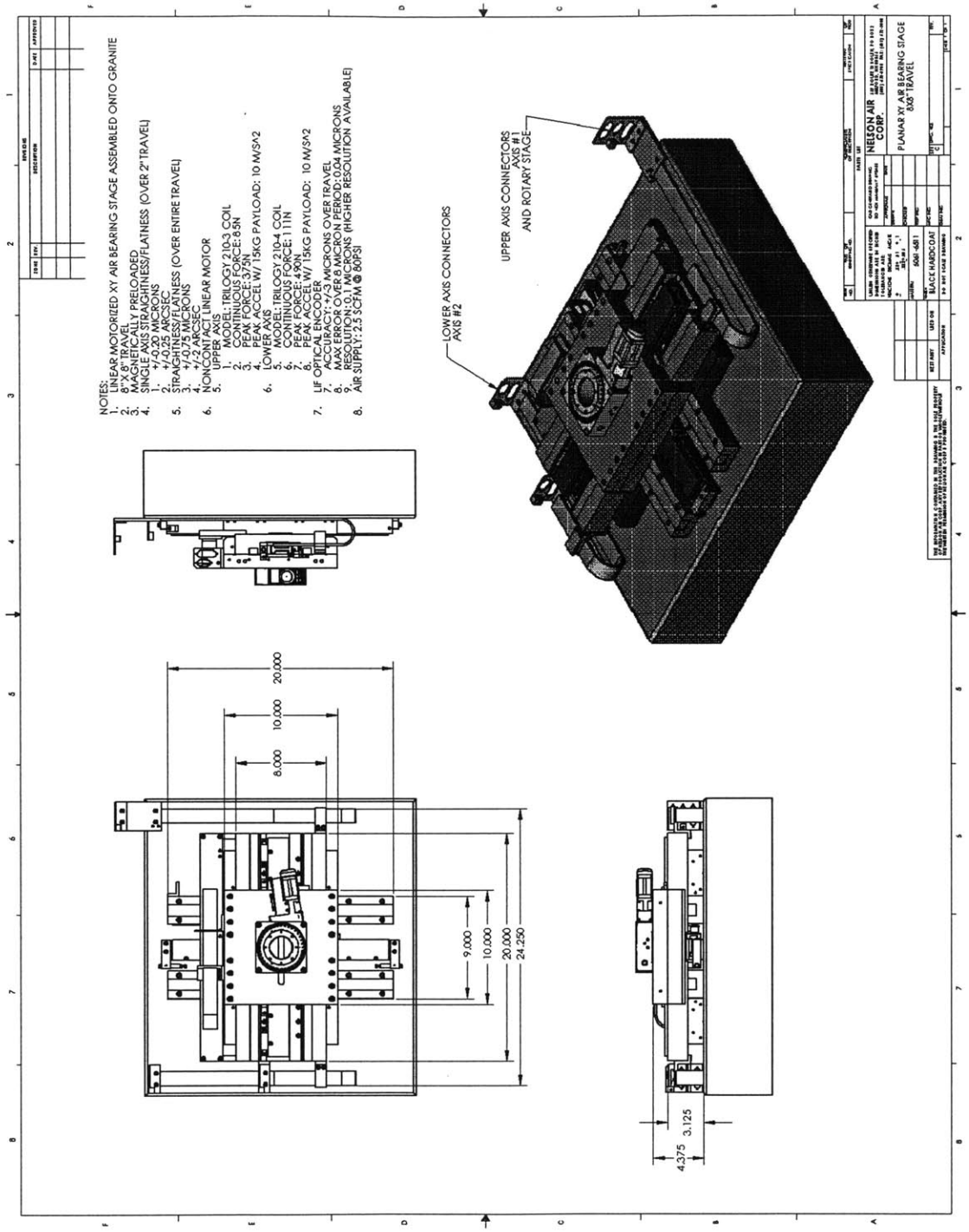

Figure 6-3: Technical Documents on the Air Bearing Stage. This two page document includes the important specifications of the stage such as details on the Trilogy linear motors, Heidenhain optical encoder, and Nelson Air Corp. air bearing stage.

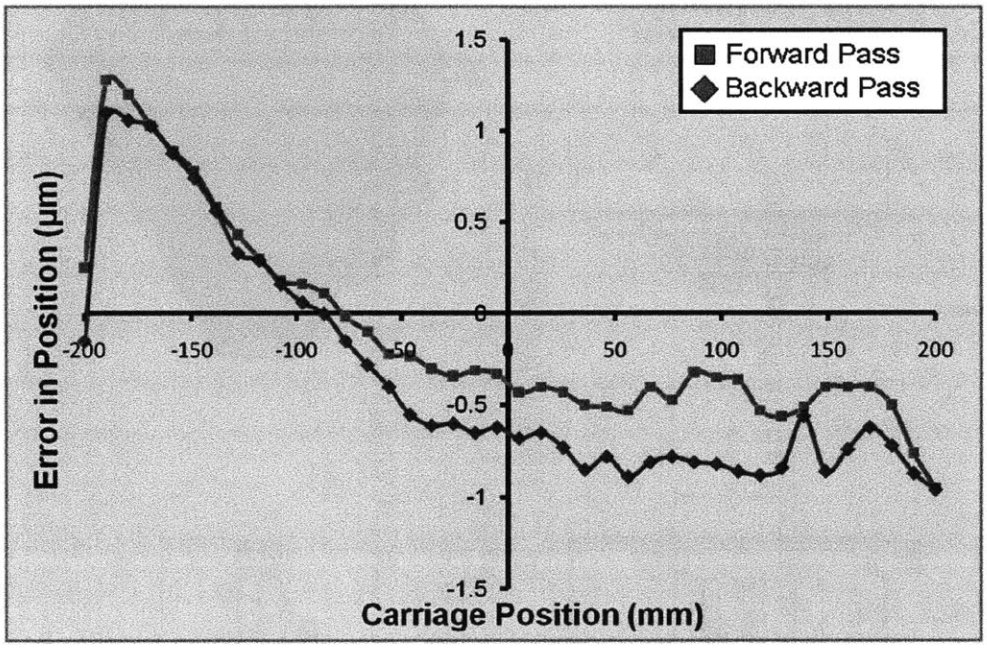

Figure 6-4: Repeatability in Positioning Along the X Axis. This graph shows the discrepancy between the laser interferometer and optical encoder measurements as a function of carriage position. Whereas the laser interferometer is orders of magnitude more precise than the optical encoder, it can be assumed that the discrepancy in the measurements is caused by positioning errors in the optical encoder.

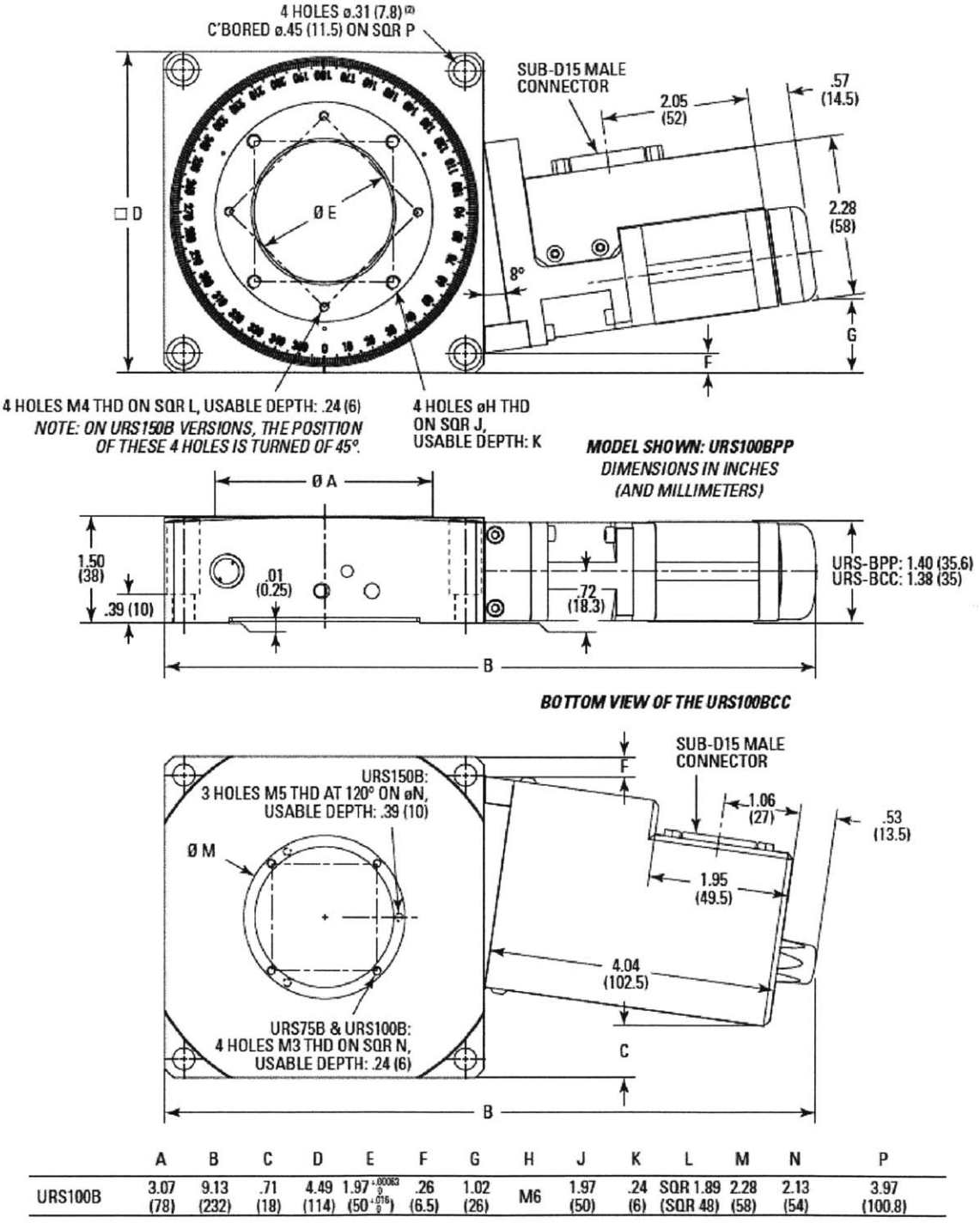

	A	B	C	D	E	F	G	H	J	K	L	M	N	P
URS100B	3.07 (78)	9.13 (232)	.71 (18)	4.49 (114)	$1.97^{+.0003}_{0}$ ($50^{+.016}_{0}$)	.26 (6.5)	1.02 (26)	M6	1.97 (50)	.24 (6)	SQR 1.89 (SQR 48)	2.28 (58)	2.13 (54)	3.97 (100.8)

Figure 6-5: Schematic of the Rotary θ_z drive. This diagram shows the mechanical dimensions of the rotary drive. The spacing and threads of the inner circle are particularly useful given that most fixtures are fastened to the θ_z stage as it is the top most element of the mechanical positioning stage.

6.3 Z Stage

The Z stage allowed automated positioning of the sample into the microscope objective's focal plane. When 1024 rows of camera pixels sized at 12 μm each are magnified 50X through the microscope objective, the resulting focal plane measures 245 μm long. The focal plane is tilted 45 degrees from the horizontal making it stand 124 μm tall. Thus, a resolution of 1.2 microns in the Z actuator was required to position the surface of the sample within 1% of the desired location with respect to the focal plane. The Z actuator was also used to accommodate measurement of different thickness samples without having to reposition the camera. Whereas the difference in thickness between our samples ranged on the order of millimeters, a Z actuator with a range of five millimeters was sought after. A Newport MVN80 stage with 12mm of travel was used to guide motion in the Z direction while a Micros MP-21 Micro Pusher was used to actuate it. The MP-21 has a resolution of 0.1 μm and a travel of 12.25 mm which translates into 6.125 mm of vertical motion given the wedge geometry of the MVN80 stage. This $\frac{1}{2}$ reduction of travel can be better understood by looking at the cut out view of the MVN80 stage in Figure 6-6.

6.4 θ_y Guide and Actuation

The rotational positioning of the camera about the θ_y axis proved to be the most challenging axis of motion to design and implement. Two different sized optical systems needed to be positioned with a rotational range of $\pm$ 45 degrees from the vertical. Each optical system and camera pair weighed approximately 10 kilograms. The movement was to be automated such that an actuator could rotate the hardware to a new location and then clamp down. During the stationary periods between rotary movements, the camera and optics were to be held stationary with vibrations less than 0.1 μm without expending energy. The nearly half meter long camera and optics combination needed to overhang the X,Y air bearing stage by 300mm such that the camera was focused in on the center of the air bearing stage's

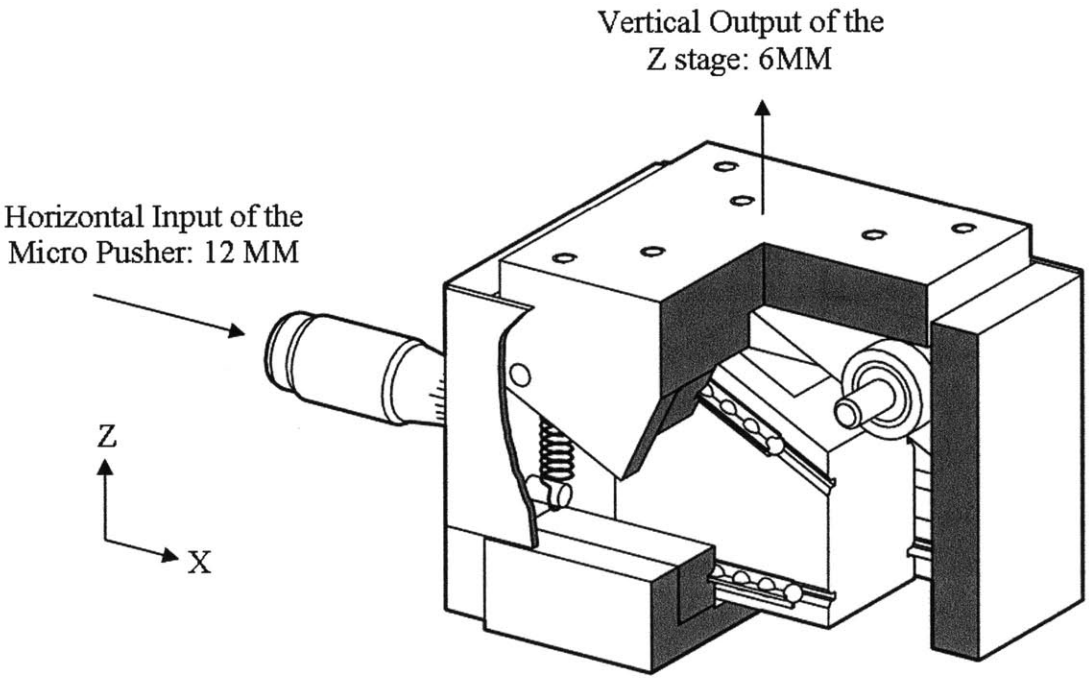

Figure 6-6: Cutaway Diagram of the Z Axis. A cutaway of the MVN80 stage in this figure shows the wedge design of the MVN80 stage. The combination of Newport MVN80 stage and Micros MP-21 Mirco Pusher yields Z actuation with 6.25mm travel and 0.05 μm resolution.

travel. Lastly, the Z height of the camera and optics unit needed the flexibility to be changed by $\pm$ 40mm in order to accommodate for different heights of the samples. Figure 6-7 shows the final design of the θ_y stage superimposed with the design requirements.

Two large metal structures were erected in order to implement the θ_y axis. The first structure, dubbed the "steel backplane," served as a backbone to mount the second structure dubbed the "aluminum standoff." The high speed 3D profilometer sits upon a granite table that was donated to the lab. The steel backplane acts as the interface between the vertical slab of granite and the aluminum standoff utilizing the tapped hole inserts present in the granite table from a previous design. The aluminum standoff is a welded structure which holds the camera and optics 8" out from the steel backplane. At the bottom of the aluminum standoff are two journal bearings that guide the entire object to rotate in the θ_y direction. These journal bearings are mounted into a block housing that can be bolted to the steel backplane to achieve the desired Z height of the camera and optics. Nested into the aluminum standoff is a magnetic chuck whose magnetic attractive force can be turned on or off via the turn of a screw mechanism. Once the camera and optics were rotated into the correct position, the magnetic chuck can be activated thus clamping the aluminum standoff to the steel backplane without expending continuous energy to hold the parts stationary. The rotary position of the camera in the θ_y direction is measured by a tilt meter bolted to the top of the aluminum backplane. A cutaway view of the aluminum backplane in Figure 6-8 reveals the position of the magnetic chuck and tilt meter. Secondly, a close-up view of the journal bearings shows in Figure 6-9 how the housing block can be bolted to the steel backplane at different positions to adjust the Z height of the camera and optics. Lastly, a cross sectional view of the entire instrument in Figure 6-10 depicts how the magnetic chuck can be used to secure the aluminum standoff to the steel backplane once it has been correctly positioned.

The full automation of the θ_y was designed for but never realized. In a fully

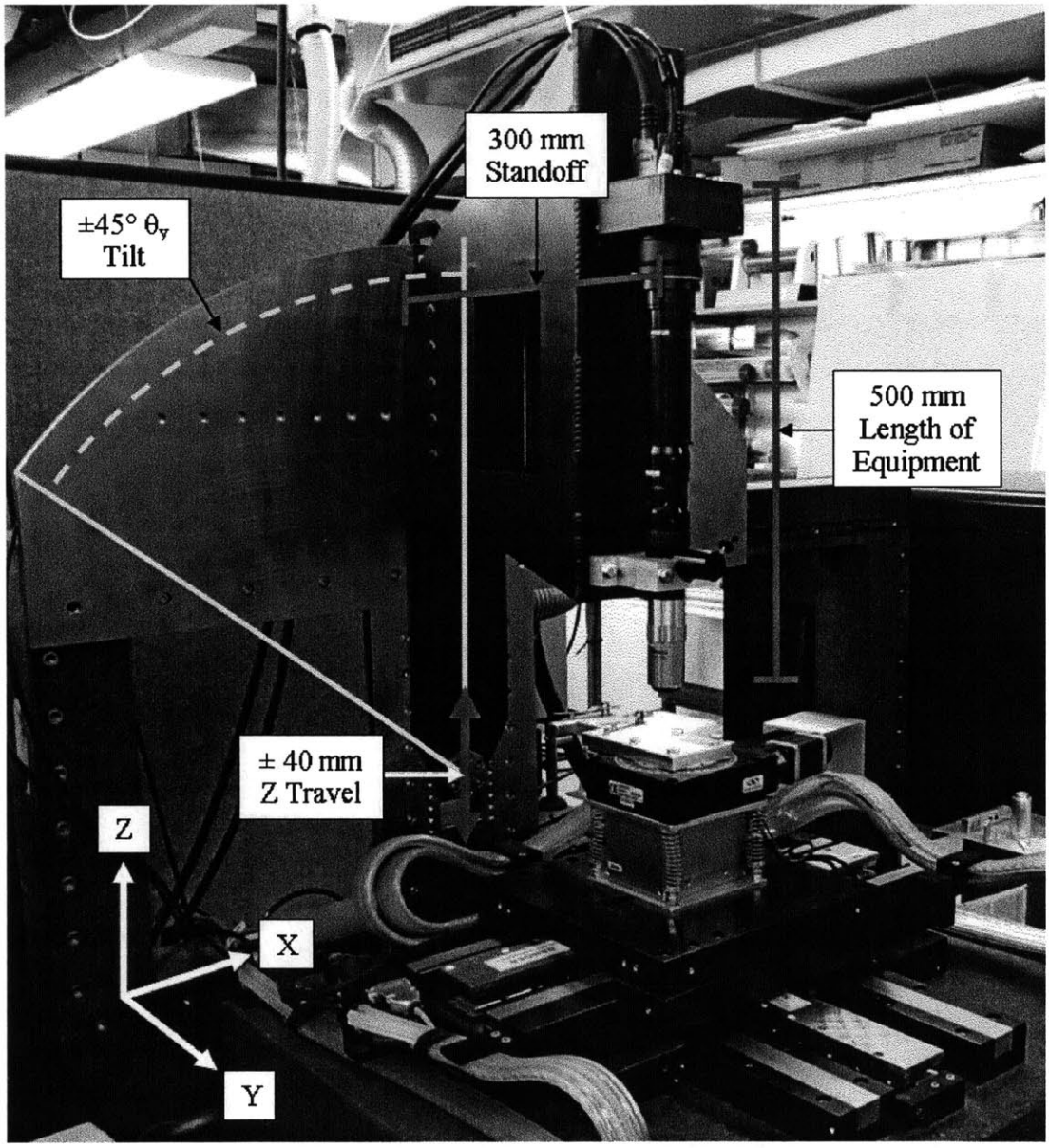

Figure 6-7: Photograph Containing Pertinent Geometric Information. This image shows the final design of the θ_y stage as incorporated in the high speed 3D profilometer. Superimposed onto the image are the requirements of the θ_y stage as they apply to positioning the camera and optics above the X,Y stage.

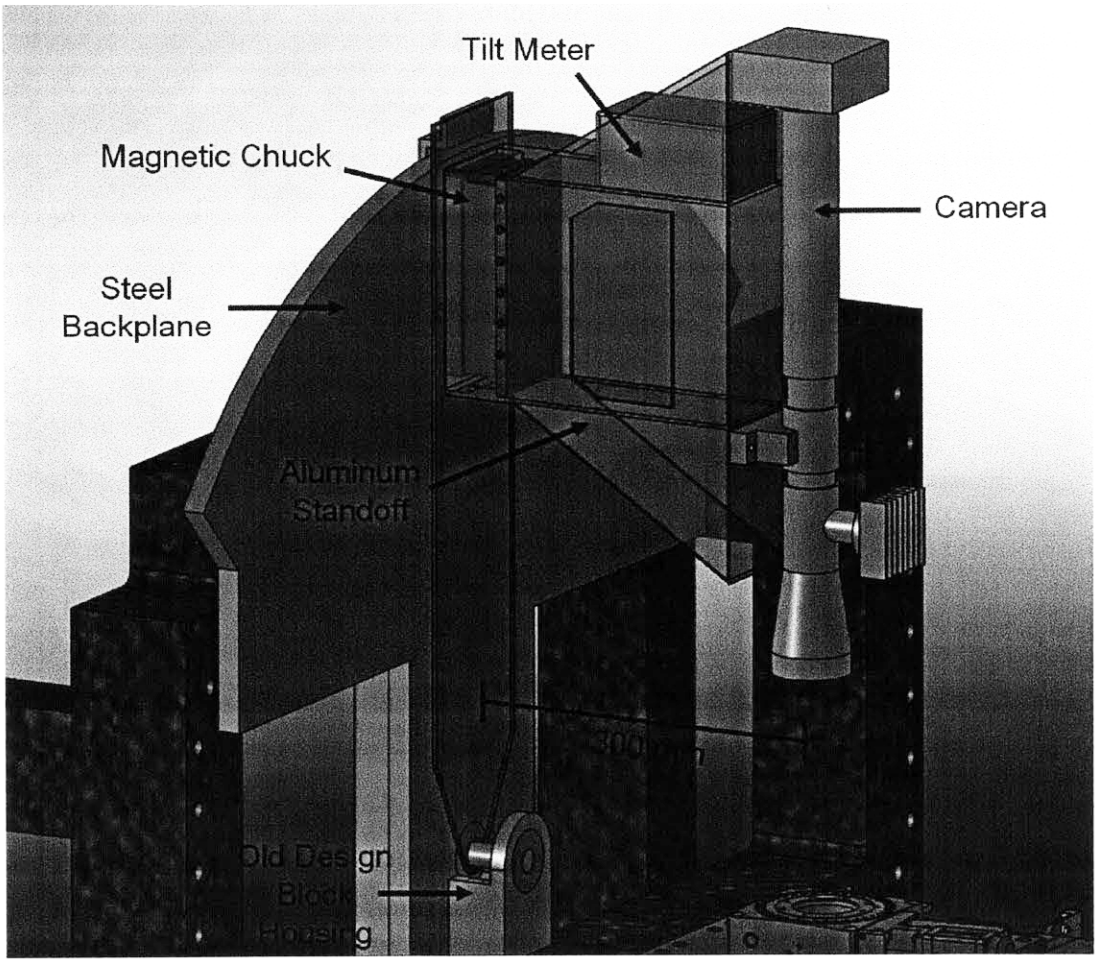

Figure 6-8: Locations of Tilt Meter and Magnetic Chuck for θ_y Movement. This cutaway image reveals how the magnetic chuck was designed to clamp the aluminum standoff to the steel backplane once it was positioned. The measurement of the rotary position is made by the tilt meter shown in red.

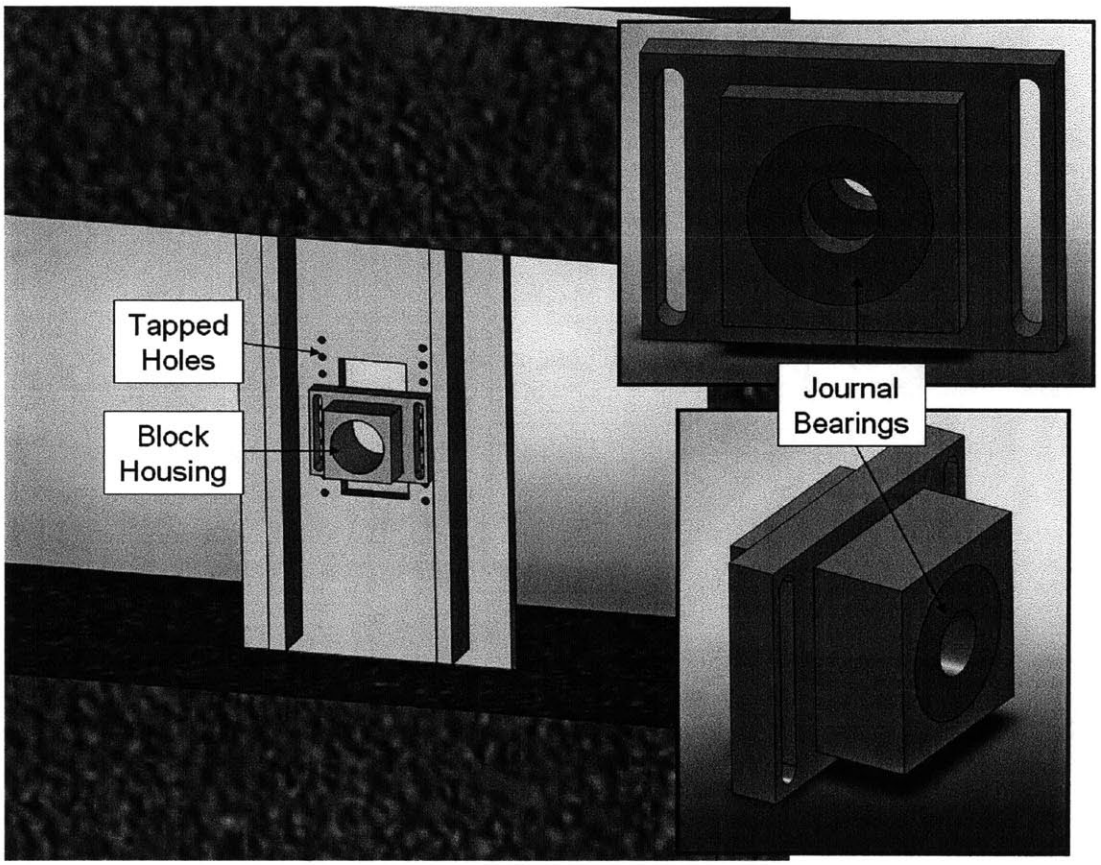

Figure 6-9: Solid Model of θ_y Bearing Housing. This screen shot shows the rear side of the steel backplane and highlights how the gray block housing can be bolted in at a variety of locations to define the Z height of the aluminum standoff. Shown in green are the journal bearings that were press fit into the block housing.

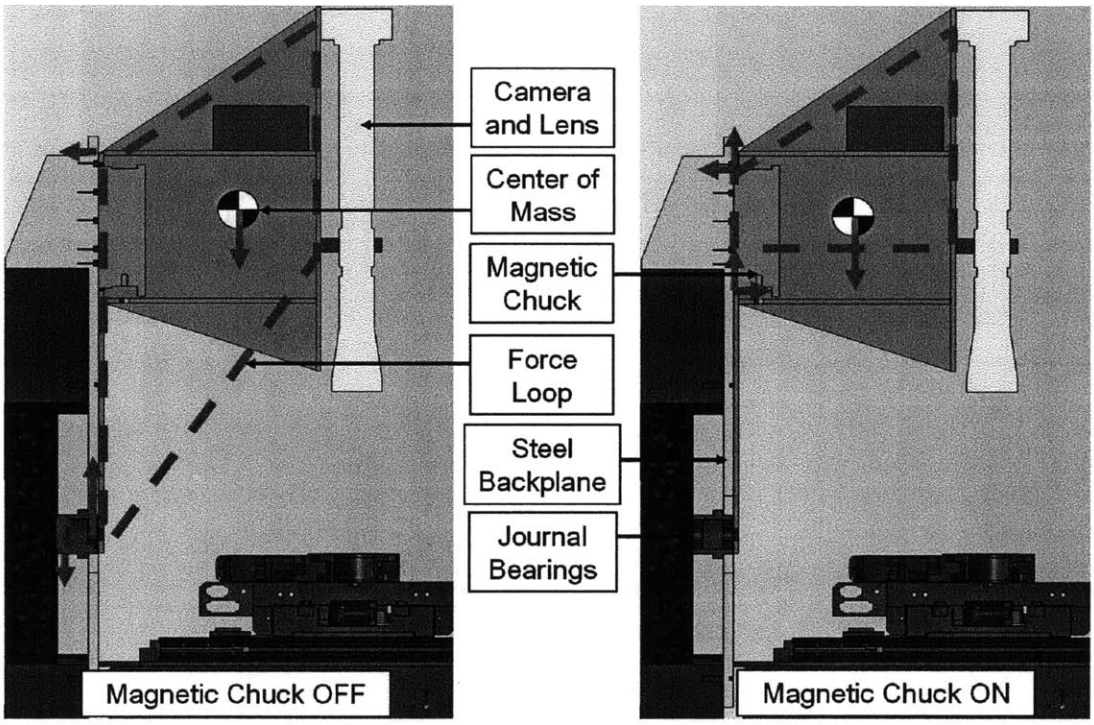

Figure 6-10: Demonstration of Force Loop With and Without Magnetic Chuck. This cross section shows the force loop when the magnetic chuck is turned on and off. When it is turned on the magnetic chuck takes the force off the journal bearings at the base of the aluminum standoff.

automated design, a high torque motor would have been coupled to the shaft held by the journal bearings in the block housing. This high torque motor would have rotated the aluminum standoff to the desired θ_y angle using feedback from the tilt meter. Once in place, a second motor would have engaged the magnetic chuck thereby holding the camera and optics in place without the continuous use of energy. As the design evolved, the need to reposition the camera and optics in the θ_y direction became very infrequent thus eliminating the need for automation.

Chapter 7

Optical Design of the 3D Profilometer

The optical design of the high speed 3D profilometer is the most innovative and unique portion of the overall instrument. The design employs a cross disciplinary optimization between the optical, mechanical, and data acquisition domains. The purpose of this chapter is to explain the tradeoffs and optimizations made among these three disciplines as they pertain to the selected optics.

7.1 Microscope Objective Tradeoffs

The selection of the microscope objective has important ramifications on the performance tradeoffs in the design. The Mitutoyo 50X microscope objective that was ultimately used in conjunction with the high speed Basler A504 camera may not be the best choice for a second iteration of the instrument when a different camera or set of priorities are needed. This section details how the mechanical characteristics of the microscope objective effect the performance of the high speed profilometer.

The chief optimization dictating the selection of the microscope objective is a trade off between lateral resolution, vertical resolution, and vertical range. As described in

Chapter 2, a larger numerical aperture of the objective lens will yield higher lateral resolution and sharper depth of field: both of which improve the performance of the instrument. Yet, microscope objectives with large numerical apertures are wide in diameter and short in working distance thus mechanically limiting the angle in which the optics can be tilted before the objective crashes into the workpiece. Because vertical range is proportional to the sine of the tilt angle, it is found that microscopes with large numerical apertures provide short vertical range and vice versa. By understanding these relationships the optimal tradeoff between lateral resolution, vertical resolution, and vertical range can be calculated.

In order to conduct such an optimization analysis the parameters of our study first must be defined. Each microscope objective can be characterized mechanically by its numerical aperture and the maximum angle of tilt from the vertical it can accommodate before hitting the workpiece. Both the diffraction limited lateral resolution and depth of field can be calculated from the numerical aperture using Equations 2.3 and 2.5. Because our instrument uses depth from focus to measure the topography of a sample, the depth of focus is defined as the minimum spacing between vertical pixels allowable before collecting redundant information. This concept is analogous to using the diffraction limited lateral resolution as the minimum spacing between lateral pixels before collecting redundant information: both limits represent how much the optics can magnify before reaching "empty magnification." An optimal camera and microscope objective combination would place the magnified lateral and vertical pixel spacing exactly at the diffraction limited lateral resolution and depth of field respectively.

This section describes the relationship between vertical range of the instrument and the maximum tilt angle of the microscope objective θ_y. Figure 7-1 shows a cross section of two microscope objectives each with the same diameter but different working distances. The tilt angle θ_y is defined as the angle from the vertical to the microscope axis while it's complementary angle is defined as α. In a vertical configuration where $\theta_y = 0$, the maximum value of $\alpha = 90°$ which leaves the

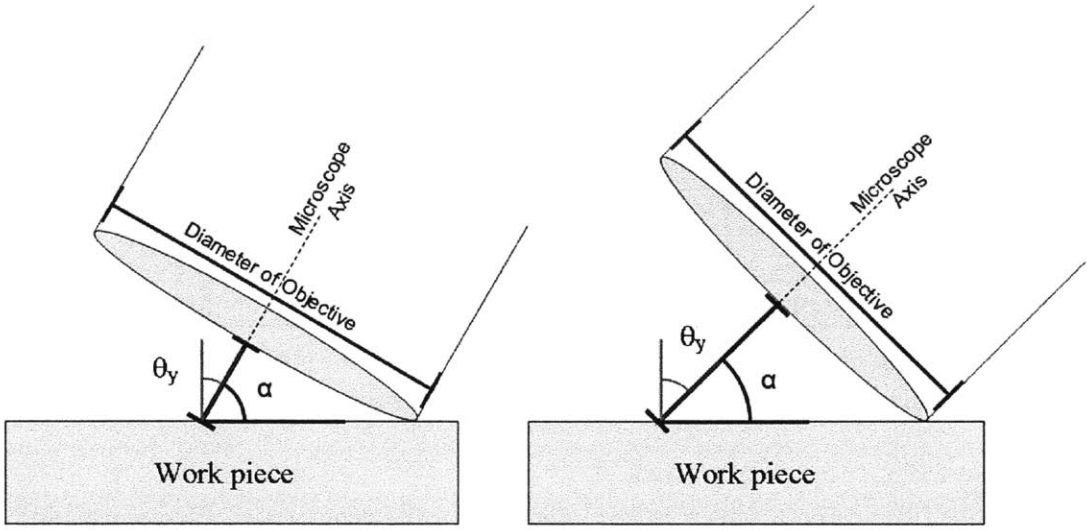

Figure 7-1: Maximum Amount of Tilt Versus Working Distance. This figure shows two configurations of a microscope objective with the same diameter. The figure shows how a longer working distance with the same diameter microscope objective returns a greater tilt angle θ_y.

diameter of the lens unbound. In theory the numerical aperture is calculated by taking $\sin(\alpha)$, but in practice this relationship rests heavily on the geometry of the lens. This direct relationship does not hold in practice for a non optical element of the objective lens will crash into the workpiece before the lens does. The two cross sections in Figure 7-1 demonstrate the tradeoff between a large numerical aperture objective with a small tilt and visa versa in the left and right images respectively. The magnified pixels are tilted by the same angle θ_y as the camera itself. The vertical range is equivalent to the height difference between the top and bottom rows of magnified pixels and is calculated in Equation 7.1 based upon the system parameters.

$$\text{Vertical Range} = \frac{H \cdot sin\,(\theta_y)}{M} \tag{7.1}$$

where H = Height of the camera sensor (m)

M = Magnification of the optics

Name	Diagonal (mm)	Width (mm)	Height (mm)
1/2"	8.00	6.40	4.80
2/3"	11.00	8.80	6.60
1"	16.00	12.80	9.60
4/3"	21.6	17.30	13
35mm	43.3	36	24.3

Table 7.1: This table displays the name and dimensions of common image sensor formats.

The height of the camera sensor is dependent upon the geometry of the camera and optical system. Although the remainder section will focus of insights can be gained from using the parameterized H, the values for H are given for the most common optical systems. Camera sensors often are sized in accordance with standard "image sensor formats." While the formats often come in sizes labeled in inches, the name of the image format does not describe its dimensions. Table 7.1 lists some of the most common image sensor formats along with their actual dimensions. It is noted that the ratio of height to width varies from format to format but is commonly chosen to be either 5:4 or 4:3. The camera can be rotated such that either the height or width value represents H, the height of the sensor.

The height of the camera sensor H can also be limited by the diameter of the light beam focused by the optics. If the optical system can only illuminate the middle portion of the sensor then the entire sensor can not be utilized to capture height information. C-Mount optics are used in our instrument to focus the light coming from the infinity corrected microscope objective onto the camera sensor. C-Mount optics can be purchased in either 1" or 4/3" image sensor formats. If the instrument uses a camera with a 4/3" sensor but only 1" C-Mount optics, only the pixels with a circle of 16mm diameter in the center of the camera sensor will be illuminated. Thus, the height of the sensor will be limited by the height of a rectangular block of active pixels inscribed into a 16mm circle. The remainder of the pixels can be illuminated by switching to 4/3" C-Mount or 35mm F-Mount optics or instead

introducing a second lens that spreads the illuminated area over the non illuminated pixels. A designer must be careful when using the second option that the conglomerate magnification of both lenses does not create empty magnification beyond the diffraction limit of the objective lens. While the F-Mount optics provide much larger diameter illumination, they are not always compatible with microscope objectives.

A survey of microscope objectives was conducted to summarize the numerical aperture and maximum angle of tilt for a host of different microscope objectives. The information for the majority of the objectives was taken from Olympus Microscope Components Guide [36]. The remaining information was collected from the Edmund Optics catalogue [37] on "Infinity Corrected Extra Long Working Distance" microscope objectives built by Mitutoyo. The maximum angle in which the objective could be tilted before hitting the workpiece was calculated for each entry in Table 7.3. This concept is shown graphically in Figure 7-2. The compilation of this information is presented in Table 7.3. The table also holds the maximum theoretical value for θ_y based upon the numerical aperture is also displayed as calculated as the inverse cosine of the numerical aperture.

In order to visually interpret the data in Table 7.3, the values of θ_y in theory and practice for each microscope objective are plotted against the numerical aperture as shown in Figure 7-3. It is found empirically that a good model for the practical limit of θ_y is estimated by subtracting 12 degrees from the theoretically calculated value. This approximation can be used to assess the design space of our instrument.

It is assumed in practice that the final microscope objective used in the instrument would be tilted to its maximum θ_y value to maximize the vertical range. Using a parameterized height of the sensor H, the microscope objectives can now be compared against one another visually to evaluate their performance. In Figure 7-4 the diffraction limited lateral resolution of each lens is plotted against the vertical range it can achieve based upon the maximum value of θ_y. It is assumed that each

Model	Magnification	Numerical Aperture	θ_y Theory	θ_y Practice
Standard	5	0.1	84.26	60.83
Standard	5	0.13	82.53	60.2
ELWD	5	0.14	81.95	65.54
Standard	5	0.15	81.37	59.93
ELWD	7.5	0.21	77.88	65.54
Standard	10	0.25	75.52	61.81
Standard	10	0.25	75.52	56.72
ELWD	10	0.28	73.74	65.6
Standard	20	0.25	75.52	63.53
Standard	10	0.3	72.54	51.75
Standard	50	0.35	69.51	57.99
Standard	20	0.4	66.42	50.18
Standard	20	0.4	66.42	21.8
ELWD	20	0.42	65.17	56.36
Standard	20	0.45	63.26	26.38
Standard	50	0.5	60	48.12
ELWD	50	0.55	56.63	47.22
Standard	100	0.6	53.13	32.91
ELWD	100	0.7	45.57	32.61
Standard	50	0.75	41.41	5.33
Standard	50	0.8	36.87	9.55
Standard	100	0.8	36.87	21.14
Standard	100	0.9	25.84	12.99
Standard	100	0.9	25.84	2.86
Standard	50	0.95	18.19	2.86
Standard	100	0.95	18.19	5.39

Table 7.2: This table holds the numerical aperture and maximum angle of tilt in theory and in practice for each of the microscope objectives in the conducted study.

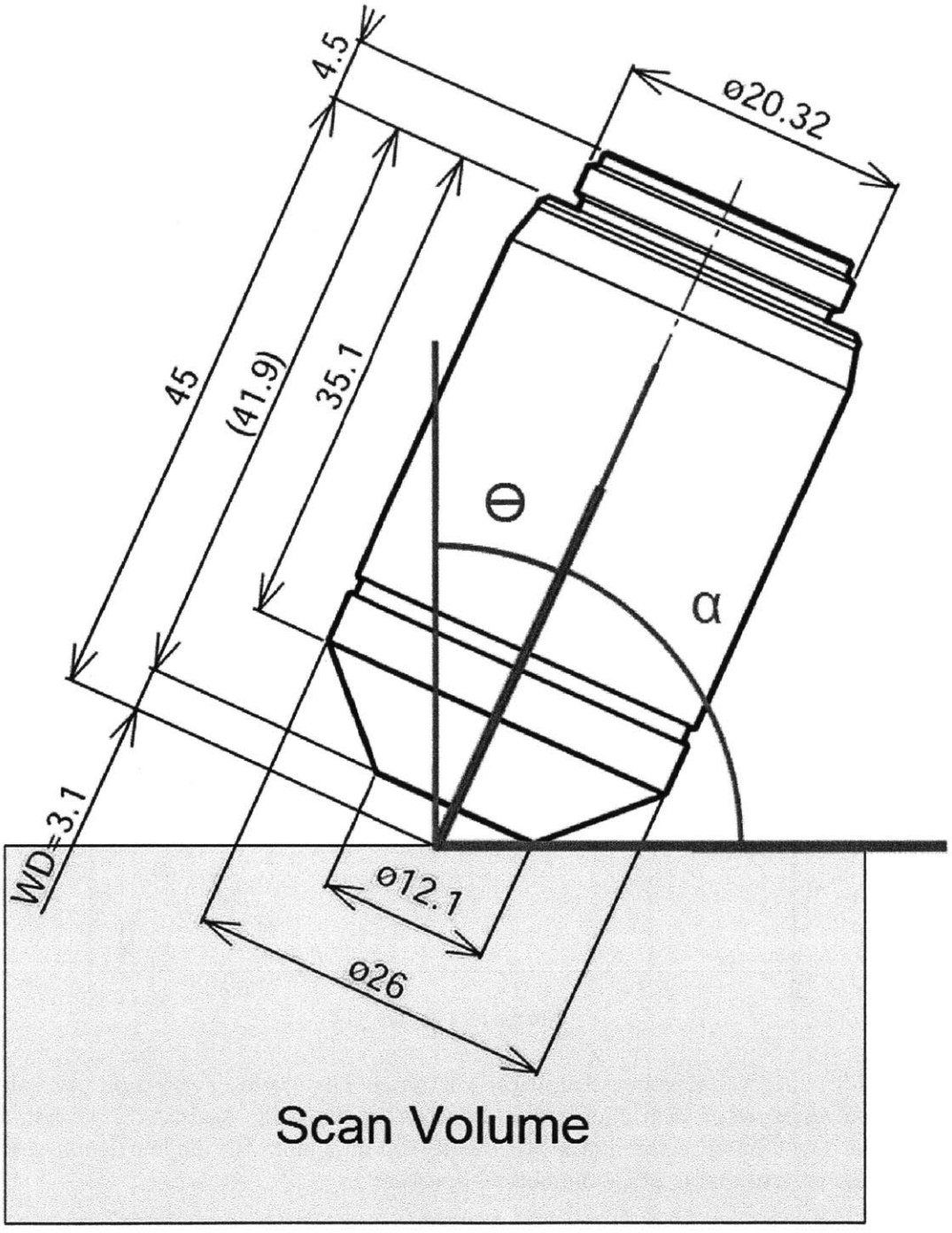

Figure 7-2: Calculating the Maximum Tilt Angle. This cross section of the microscope demonstrates how the maximum angle of tilt was calculated for each of the microscope objectives in the study. The maximum angle is defined as the largest tilt angle that can be applied before the first physical part of the objective hits the scan volume.

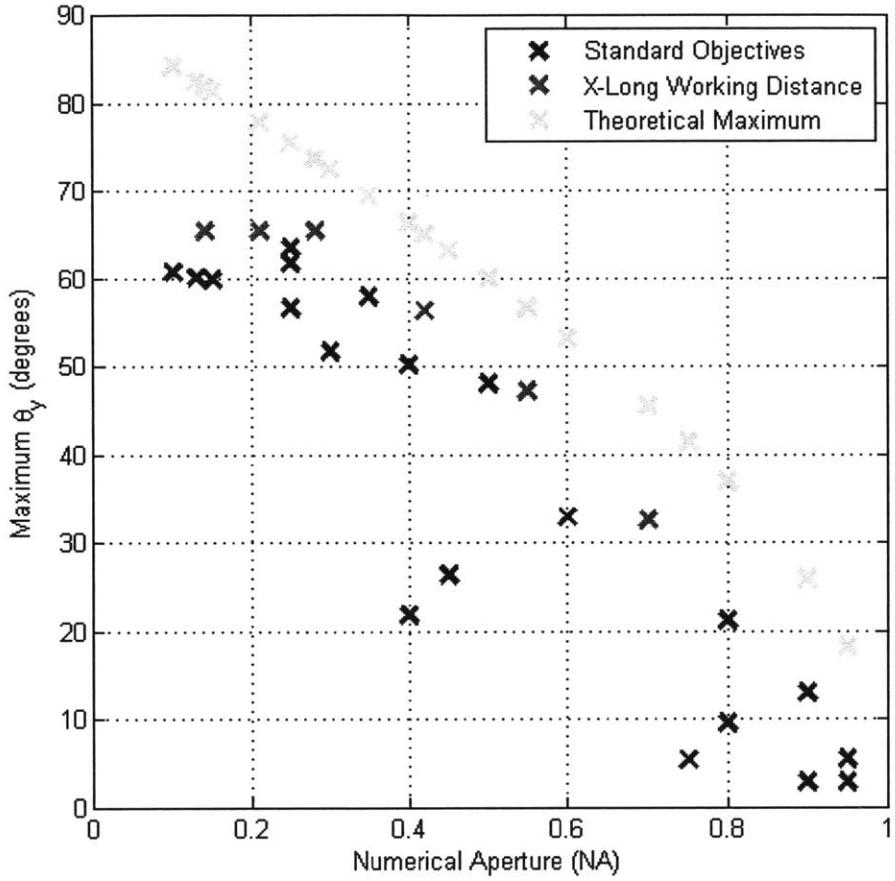

Figure 7-3: Theoretical Versus Empirical Maximum Tilt Angle. This graph plots the numerical aperture of each microscope objective in the study against its maximum tilt angle. Overlaid onto the plot is the theoretical maximum tilt angle calculated by taking the inverse cosine of the numerical aperture.

lens could be paired up with a correctly sized camera to fully utilize the numerical aperture of the lens. In order to optimize these parameters the instrument would benefit from a small numerical aperture and large vertical range. From this graph it is clear that the extra long working distance lenses exhibit advantageous performance. Ultimately the 20X Motic (SG01S032C3) and 50X Mitutoyo (NT46-146) extra long working distance microscope objectives were selected. The performance of these two microscope objectives are indicated in Figure 7-4 by the green circled data points. For this figure, the Rayleigh criterion was used to calculate the lateral resolution based upon the numerical aperture of each lens. For the purposes of the plot 9.6mm was used as the height of the sensor H for that is the size of the sensor on the Basler A504 camera purchased for this research. From this analysis it was found that the two selected microscope objectives gave the greatest tradeoff between lateral resolution, vertical resolution, and vertical range.

7.2 Optimizing the Spatial Resolution

The high speed 3D profilometer outputs data spaced on a three dimensional Cartesian coordinate frame. As a result of the tilt of the camera, the projection of pixels onto the Cartesian coordinate frame results in a elongated rectangular geometry differing from square pixels themselves. Also, the optical spacing of pixels in the vertical and lateral axis may be different depending upon the optical physics presented in Section 7.1. The spatial resolution of the pixels must be engineered to optimize the performance of the instrument. This section reviews the different techniques and strategies that can be used to balance the spatial resolutions in all three axis.

It is first important to define the the coordinate frame and nomenclature used to refer to the X, Y, and Z resolution. The camera pixels, microscope axis tilt, coordinate axis, and spatial resolution are all presented together in Figure 7-5. The θ_y tilt causes the projection of the camera pixel onto the sample to elongate the X

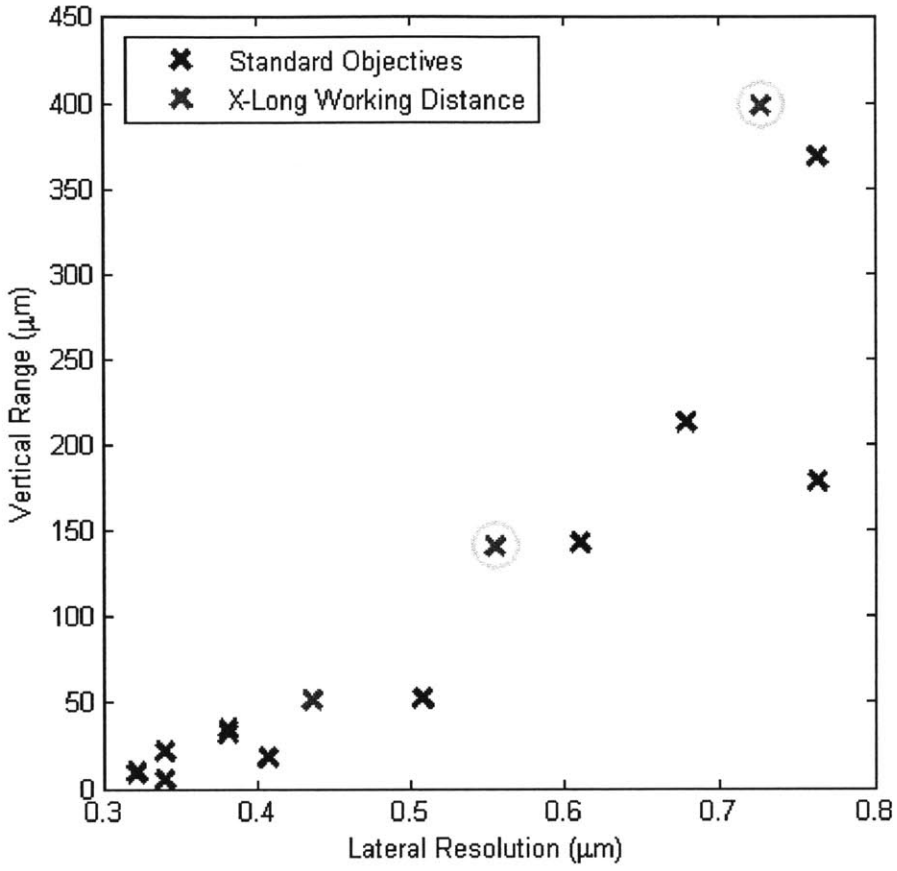

Figure 7-4: Vertical Range versus Lateral Resolution Tradeoff. This graph plots each microscope objective's diffraction limited lateral resolution based upon numerical aperture versus its maximum lateral range based upon θ_y. The green circles indicate the two microscope objectives purchased for the high speed 3D profilometer as they showed relatively high vertical range for relatively sharp lateral resolution.

resolution while the Y resolution remains the same. This effect can be seen when imaging a penny as shown in Figure 7-6. The elongation of pixels in the X direction causes the penny to look shorter than it does wide. The spacing of pixels in the vertical or Z axis is also a function of the camera tilt angle. Equations 7.2, 7.3, and 7.4 define the X, Y, and Z resolution respectively in terms of the native pixel width, magnification, and tilt angle θ_y.

$$\text{X Resolution} = \frac{N}{M \cdot cos\,(\theta_y)} \tag{7.2}$$

$$\text{Y Resolution} = \frac{N}{M} \tag{7.3}$$

$$\text{Z Resolution} = \frac{N \cdot sin\,(\theta_y)}{M} \tag{7.4}$$

where N = Native Pixel Size (m)

M = Magnification of the optics

θ_y = Microscope axis tilt angle (rad)

Given an instrument constrained to a selected native pixel size, magnification, and microscope tilt angle it is clear that the X, Y, and Z resolutions will not only differ from each other, but most likely from their optimal size as well. The following guidelines explain how to balance this problem. First the optimal Y resolution can be targeted by choosing the correct microscope objective and camera combination. In this research project the microscope objective was selected first requiring the camera to be selected such that its magnified pixel size or Y resolution lies between 0.5X to 1X the diffraction limited lateral resolution based upon the numerical aperture of the objective. It is suggested to use the instrument at a maximum tilt to maximize vertical range resulting in a fixed, elongated X resolution as per Equation 7.2. The flexibility of the line scan system is utilized in order to balance out this distortion. A line scan image is formed by stitching together a string of single line exposures. The spatial resolution of pixels in the X dimension is defined

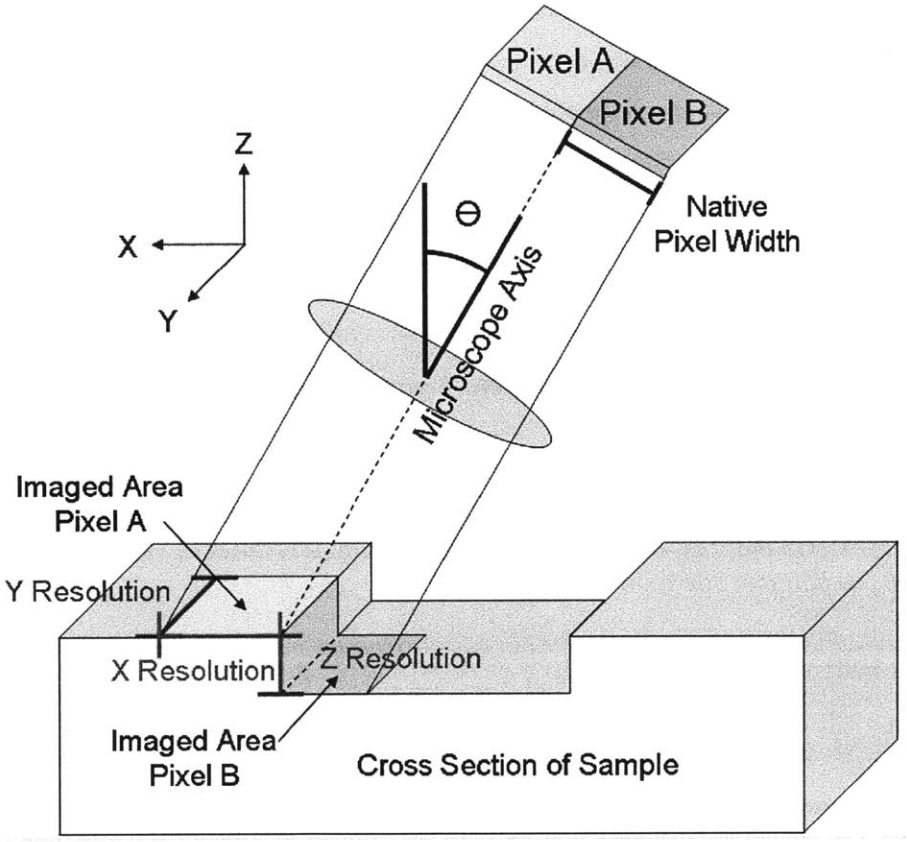

Figure 7-5: Schematic Detailing the Relationships Between X,Y, and Z Resolution. This cross sectional diagram of the camera illustrates how the X, Y, and Z resolutions of the instrument are effected by a change in the camera tilt angle θ_y. The Y Resolution will remain constant while Z and X will grow and shrink respectively with an increase in θ_y.

Figure 7-6: Example of Shortened X Resolution at Tilted Angle. This image was taken by our camera while tilted at a 45 degree angle with respect to the vertical axis. The naturally round penny now looks elliptical given the change in X resolution as the projection of the camera pixels onto the Cartesian coordinate frame is effected by the tilt angle.

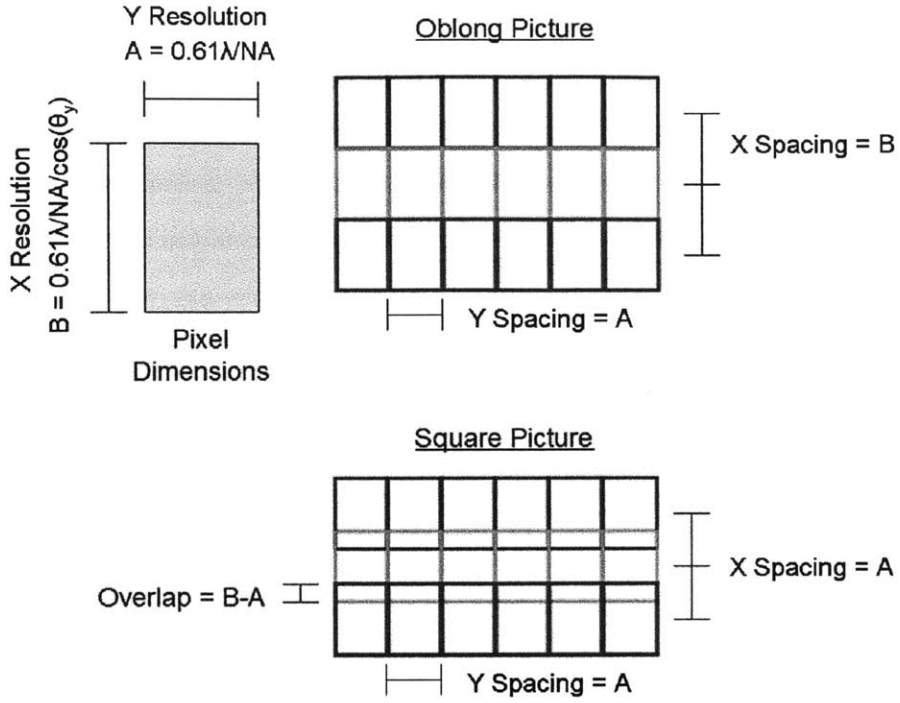

Figure 7-7: Specifying the X Resolution. This diagram illustrates how the line scan camera can change the spacing of pixels in the X direction in order to display an image with equal X and Y resolution. Although the pixels in the X direction overlap, their spacing can be specified by synchronizing the movement of the stage with the camera trigger.

by how far the part moves with respect to the camera between exposures. This line scan configuration allows the X resolution to be determined by the software. Therefore while the size of the projected pixels is predetermined, the spacing between pixels or X resolution can be specified. This concept is illustrated in Figure 7-7. By overlapping the rectangular pixels, an equal pixel spacing or resolution in the X and Y axis can be achieved. The details regarding programming the software to synchronize the camera triggering and X position are covered in Chapter 8.

The spacing of Z pixels along the vertical axis is prescribed by the relationship in Equation 7.4. The system is optimized when the Z spacing is equal to the depth of field of the microscope. In practice it is found that once the lateral resolution has been optimized, the resulting vertical resolution is usually two or three times finer

than the depth of field. This imbalance of Z resolution results in the oversampling and collection of redundant information. In theory the camera sensor can be custom built to only output every other line while boosting the frame rate by a factor of two. Therefore by augmenting the output of the camera, the Z resolution can be independently selected without affecting the X or Y resolutions. Such a change to the camera may not require the sensor itself to be rebuilt, but more simply a reconfiguration of the traces upon the PCB board that relays the information from the camera to the processors. This process remains outside the boundaries of our research and although it is theoretically possible it will be considered impractical for the purposes of this degree.

7.3 Camera Selection and Tradeoffs

The high speed 3D profilometer requires the use of high speed cameras that capture large quantities of data over short periods of time. These high speed cameras have only come out to the market within the past 10 years and serve as the enabling technology which allows the high speed 3D profilometer to capture surface topography multiple orders of magnitude faster than white light profilometers or laser confocal microscopes. This section explains how to select such a camera to optimize the performance of our 3D profilometer based upon camera pixel size, bandwidth, pixel output flexibility, and light sensitivity.

7.3.1 Pixel Size

The most important and straightforward consideration is to select a camera with the correct pixel size. Section 7.1 details how 20X Motic and 50X Mitutoyo microscope objectives were selected to yield an optimal balance between lateral resolution and vertical range. The Mitutoyo objective's 0.55 numerical aperture suggested that the magnified pixel size lie between 0.27 and 0.55 μm to abide by the Rayleigh and Nyquist criterion. Given a 50X magnification of the Mitutoyo

objective, the camera's native pixel size was called to lie between 14 and 28 μm. Similarly the Motic objective's 0.42 numerical aperture and 20X magnification called for a native pixel size between 7.2 and 14.5 μm. In order to balance the needs of both objectives the optimal pixel size for a selected camera was 14 μm.

7.3.2 Bandwidth

All cameras face a limitation as to how much information they can collect over a given period of time. This limitation is typically expressed as a frame rate at a given resolution. For example, the Basler A504 camera can output 500 frames per second at 1,280 by 1,024 pixels per frame at 8 bit resolution. A more holistic approach to understanding the speed at which cameras output data is to instead look at the amount of pixels captured per second: a metric that will be dubbed "bandwidth." By multiplying 1,280 by 1,024 pixels in each frame by 500 frames per second, it is calculated that the Basler A504 camera has a bandwidth of 655 million pixels per second. This bandwidth is relatively fast compared to other cameras in the same price range. As a visual comparison, Figure 7-8 plots the bandwidth of every camera in the Basler catalogue against its pixel size.[38] Given an optimal pixel size of 14 microns, it was clear from this plot that the Basler A504k was the best choice in this price range based upon bandwidth and pixel size.

7.3.3 Pixel Output Flexibility

Third, the cameras were evaluated on their pixel output flexibility. Pixel output flexibility refers to the ability to activate only a subset of pixels from the camera sensor without sacrificing bandwidth. The Basler A504k camera has a 1D pixel output flexibility which can decrease the number of captured rows in order to increase the frame rate proportionally. For example, our camera can output 1,000 frames per second by decreasing the rows to a resolution of 640 x 1024 pixels per frame. It is noted that a decrease in the number of columns does not increase the

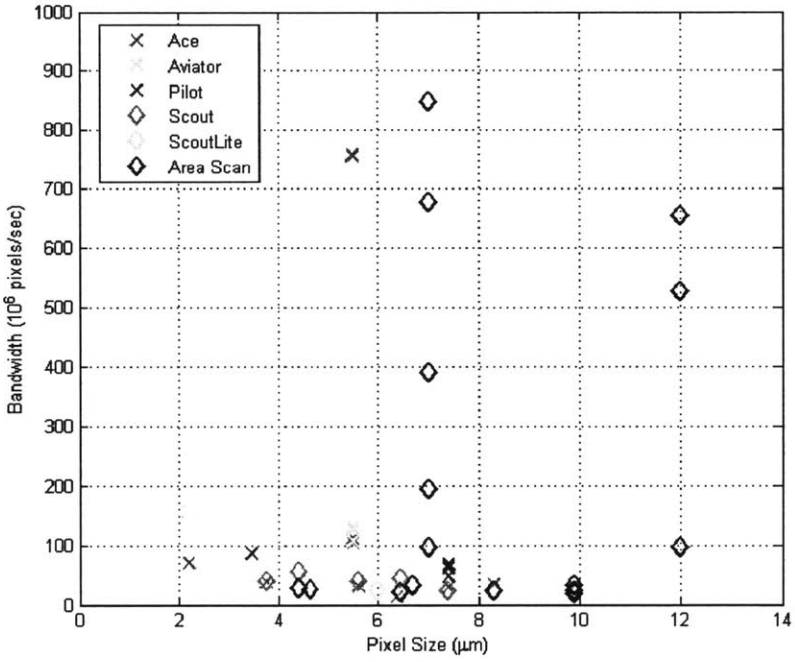

Figure 7-8: Graphical Comparison of Bandwidth Versus Pixel Size. This graph plots bandwidth versus pixel size for each camera in Basler's product line. Each mark shown in the legend represents a different model Basler camera. The camera best suited for the instrument's needs required a 14 micron pixel size and high bandwidth.

		Phantom v1610		Basler A504k	
Active Rows	Active Columns	Frames / Second	% Max Bandwidth	Frames / Second	% Max Bandwidth
1,280	800	16,600	100	640	100
1,280	720	18,500	100	711	100
1,024	800	19,800	95	640	80
896	800	21,800	92	640	70
768	768	25,400	88	667	60
640	480	45,700	82	1,067	50
512	512	49,300	76	1,000	40
512	384	65,300	75	1,333	40
384	384	76,800	66	1,333	30
256	256	137,100	53	2,000	20
128	128	322,400	31	4,000	10
128	64	566,500	27	8,000	10
128	32	911,500	22	16,000	10
128	16	1,000,000	12	32,000	10

Table 7.3: This table compares the effect of 1D vs 2D pixel output flexibility for the Basler and Phantom cameras and additionally highlights the 25X difference in their bandwidth.

frame rate of this camera resulting in a direct sacrifice of bandwidth. Conversely, the Phantom v1610 camera has 2D dimensional pixel output flexibility whereby it can proportionally increase frame rate by decreasing the number of either columns or rows. 2D dimensional pixel output flexibility is important for the optimization of the instrument for it allows the active pixels to retain the same aspect ratio to fully utilize the circular cross section of light focused by the microscope objective. Figure 7-9 plots the bandwidth of both Phantom and Basler cameras against the number of active pixels. While the bandwidth of the Phantom camera stays relatively constant over a large range, the bandwidth of the Basler camera reduces linearly as the number of active columns are cut. Note that the figure uses two different Y axis scales where the Phantom v1610 has 25X greater bandwidth than the Basler A504k at full resolution. The information is also presented in Table 7-9.

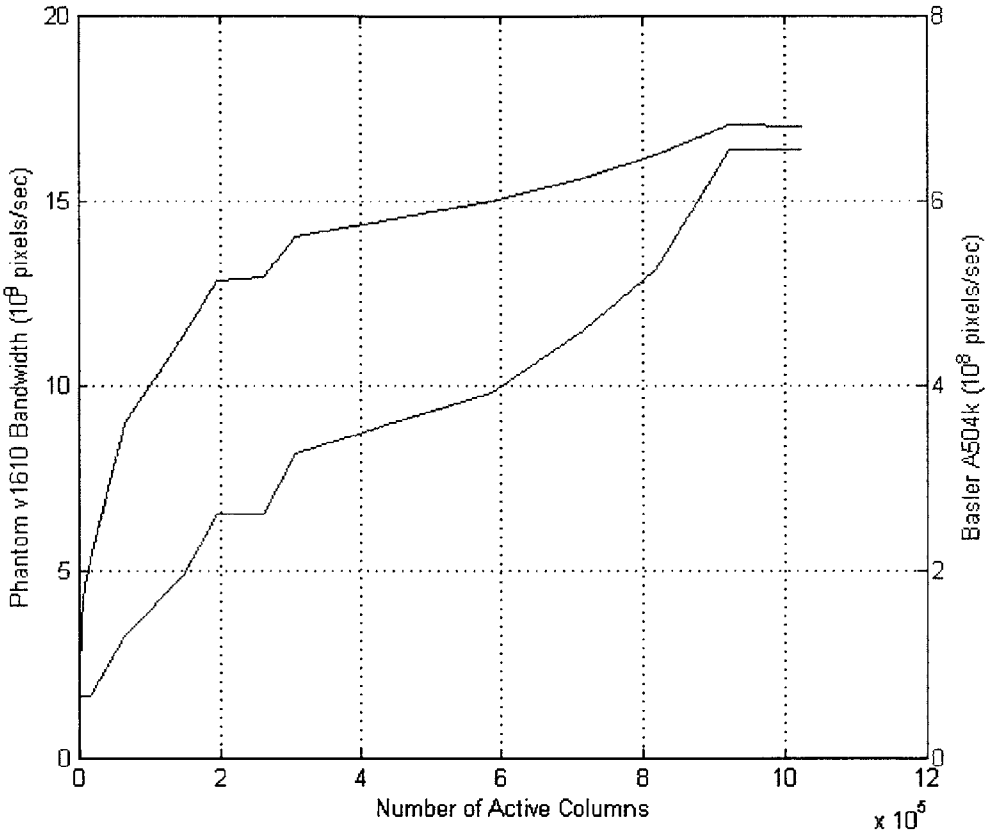

Figure 7-9: Demonstration of 2D Pixel Output Flexibility. This two Y axis plot graphs for both Phantom v1610 and Basler A504k cameras their bandwidth in pixels per second against the number of active columns. The plot highlights the effect of 1D vs 2D pixel output flexibility.

7.3.4 Light Sensitivity

Lastly the cameras were evaluated on their light sensitivity. The intensity of light required to capture an image increases proportionally with the camera's frame rate. While ambient light may provide enough intensity for point and shoot cameras or the human eye, high speed cameras require powerful light sources to collect enough information during their short exposure times. Employing powerful light sources is expensive and can cause unwanted effects such as thermal growth of the measured part. Alternatively, cameras can be built with high sensitivities or low noise such that they require less light per frame therefore alleviating the light intensity requirements. This section describes how to compare and contrast a camera's light sensitivity.

In 1974 the International Organization for Standardization (ISO) concocted a scale to grade the sensitivity of camera film based upon the amalgamation of the ASA and DIN film speed standards. The most common film was graded at an ISO 100 standard. An ISO 200 film had double the sensitivity and thus would produce an image with the same dynamic range at half the shutter speed or exposure time. Films became available with ISO ratings or "film speeds" of up to ISO 6400. Increase in film speed allows the photographer to take high quality low light images, but at increased cost of film, larger grains, and risk of overexposure. With the advent of digital cameras photographers stopped using film but the ISO system and sensitivity scale continued to be used to grade digital cameras. Unlike the ISO system ratings and units which were somewhat arbitrarily conceived, a new sensitivity metric has been defined based upon the physical parameters of digital cameras.

The sensitivity analysis allows the user to calculate the frame rate limitation based upon the intensity of the light source used by the instrument.The sensitivity scale is able to analytically compare cameras across all brands and models. We begin by theoretically calculating the minimum amount of light a single pixel must acquire in

order to output an image with full dynamic range. Each pixel stores current in a capacitor charged during the exposure time. The camera counts the number of electrons collected by each pixel over this exposure time which serves as the measure of intensity. We define the error associated with this measurement as "Electron noise" E measured in electrons (e-). The electron noise serves as the smallest resolvable unit whereby dividing the total measured electrons by the electron noise yields the dynamic range of the measurement as shown in Equation 7.5:

$$\mathrm{DR} = \int_0^t \frac{I(t)dt}{E} \tag{7.5}$$

where DR = Dynamic Range of the Measurement

I(t) = Current collected by the pixel as a function of time (e^-/s)

E = Electron Noise (e^-)

t = Exposure Time (seconds)

Each pixel can keep collecting electrons until it reaches its well depth. At this point the pixel has saturated and will not collect more information. If a constant current I is collected by the pixel over a time t, the number of electrons collected is simply the product I · t. By specifying the exposure time the user can use these equations to avoid saturation as well as determine the bit depth of the pixel. The dynamic range is redefined in the more common measure of bit depth.

$$\mathrm{BD} = log_2(DR) = log_2\left(\frac{I \cdot t}{E}\right) \tag{7.6}$$

where BD = Bit Depth

Digital cameras are able to sense light via the photoelectric effect whereby photons excite and mobilize electrons from a metal surface. The quantum efficiency of a camera sensor is defined as the ratio of photons striking the sensor to those that get converted to electrons. The quantum efficiency as a function of wavelength for four different cameras is plotted in Figure 7-10.

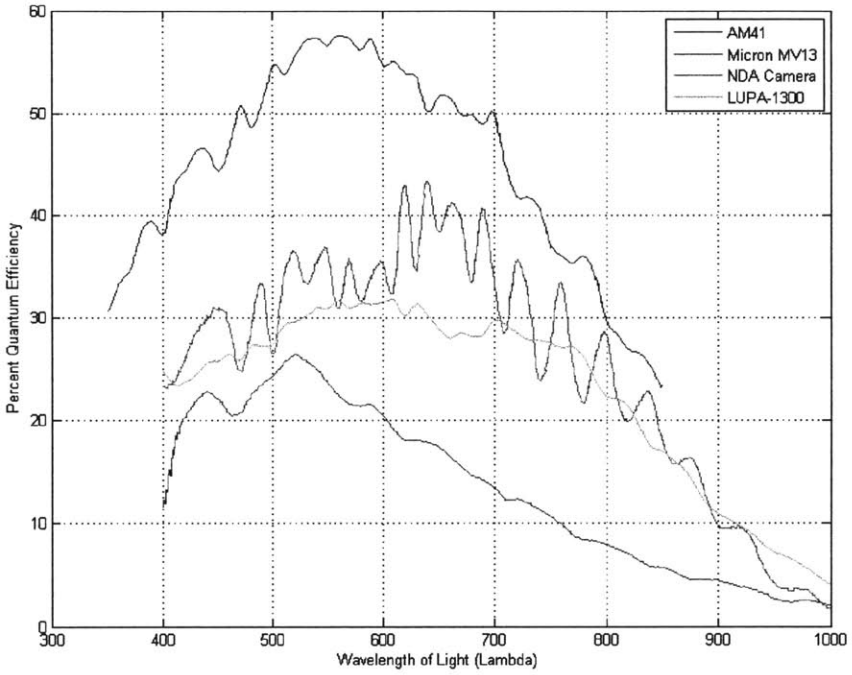

Figure 7-10: Comparison of Quantum Efficiency. The quantum efficiency of four separate cameras is graphed against the wavelength of incident light. Quantum efficiency is defined as the percentage of photons that get converted into electrons in a photo-electric sensor.

The number of photons per second Φ that must hit the pixel in order to produce a measurement at the desired bit depth can be solved for by dividing the current produced by the sensor by the quantum efficiency QE. There is only a subsection of the sensor array that is able to collect light. The ratio of active space that collects light to total area is called the fill factor. Photons that strike non active areas produce no electrons thus proportionally decreasing the output current. These relationships are reflected in Equation 7.7.

$$\Phi = \frac{I}{FF \cdot QE(\lambda)} = \frac{E \cdot 2^{BD}}{FF \cdot QE\lambda \cdot t} \tag{7.7}$$

where Φ = Photon Flux (photons/sec)

$QE(\lambda)$ = Quantum efficiency as a function of wavelength

E = Electron Noise (e-)

t = Exposure time (s)

BD = Bit Depth

FF = Fill Factor

Plank's relationship converts the energy of a photon into Joules. This relationship is used in Equation 7.8 to solve for the minimum laser power required to produce an image with specified bit depth from a singular pixel:

$$P_{pixel} = \Phi \cdot \frac{h \cdot c}{\lambda} = \frac{E \cdot 2^{BD} \cdot h \cdot c}{FF \cdot QE(\lambda) \cdot t \cdot \lambda} \tag{7.8}$$

where h = Plank's constant (J s)

c = Speed of light (m/s)

λ= Wavelength of incident light (m)

Given that each camera array has M rows by N columns, power required for each pixel is multiplied by the product M $\cdot$ N to solve for the laser power required from the array. Assuming no downtime between frames, the frame rate is defined to be the inverse of exposure time. Combining these equations the minimum power required to operate the camera at a specified frame rate and bit depth is solved for

in Equation 7.9.

$$P_{array} = \frac{E \cdot 2^{BD} \cdot h \cdot c \cdot M \cdot N \cdot F}{FF \cdot QE(\lambda) \cdot \lambda} \tag{7.9}$$

where M = Rows of pixels in the sensor Array

N = Columns of pixels in the sensor array

F = Frame rate of the camera (Frames / second)

At an incident wavelength of 550 nanometers, our Basler A504k camera has a quantum efficiency of 23%. The camera is able to take pictures at a rate of 500 frames per second at 1280 x 1024 pixels with an eight bit pixel depth. The fill factor for this camera is 40%. Using Equation 7.9 the light power required to run the camera is calculated to be 46 μJ. This power seems like a very manageable number for lasers can easily attain power on the order of one Watt. Yet, there a variety of factors that will cut down the laser light that the camera collects from the light source which makes these performance limits much more difficult to attain.

In a variety of conditions the light source may be limited by not only its power but also its power density (W/m^2). For example, the sun beams onto earth a light power of approximately 1,000 W/m^2. While taking imagery outdoors, it is difficult to change the power density of sunlight because of the optics required to focus the sun's energy on the sample object. When a user is faced with a limit in power density and still requires higher frame rates one must exploit the other variables in the equation.

It is found that the size of the camera pixels now play a large roll in calculating the maximum frame rate when using a power source of limited power density. Previously it was assumed that any powered laser could be concentrated to exactly the size of the sensor array regardless of pixel size thus removing the effect of pixel size from the equation. Equation 7.8 is augmented to solve for the minimum amount of power density required to take a full dynamic range exposure with one pixel:

Camera	Pixel Size (μm)	Fill Factor (%)	QE @ 550 nm	E(e^-)	Sensitivity
Micron MV13	12	40	23.6	70	19.4
Lupa-1300	14	50	30.9	45	67.3
NDA Camera	20	52	36.3	38	199
AM41	7	55	56.6	22	69.3

Table 7.4: The relative sensitivities for each camera are calculated in this table. It is found that the NDA Camera is 10X more sensitive than the Microm MV13 and thus could output the same amount of frames per second with 10X less light intensity.

$$PD_{pixel} = \frac{E \cdot 2^{BD} \cdot h \cdot c \cdot F}{FF \cdot QE(\lambda) \cdot \lambda \cdot S^2} \tag{7.10}$$

where PD = Power Density (W/m^2)

S = Pixel Spacing (m)

Power density may be limited by a variety of factors such as the laser power strength or a limit on the thermal heat allowed to be absorbed by the part. Camera sensitivity most commonly becomes an issue when the power density has been maximized but fails to deliver an adequate frame rate. With this analysis the user can estimate the change in maximum frame rate attainable by switching cameras. The the variables specific to the camera are isolated to redefine in physical terms the concept of camera sensitivity. The constants such as the speed of light and Planks constant are omitted from the equation in order to express the sensitivity of the camera in the variables that rely solely on its construction.

$$CS = \frac{QE(\lambda) \cdot S^2 \cdot FF}{E} \tag{7.11}$$

where CS = Relative Camera Sensitivity (m^2/photon)

An incident light source with 550 nanometers wavelength is assumed for the purposes of this study. The relative camera sensitivities of four different high speed cameras are compiled in Table 7.4.

Lastly, the effect of pixel size on data rate is noted. Based upon the physical limitations of the optics, the microscope lenses can only accommodate a camera sensor of a given size. The most common optics dubbed "C-Mount" have an inner diameter of approximately 22 mm. Any pixels that lie outside the 22 mm diameter circle will not collect information for the optics are not large enough to focus light onto their surface. The rate of information captured by the camera is defined as the frame rate multiplied by the amount of active pixls per frame. A larger pixel size will increase the sensitivity and therefore maximum frame rate of a camera but will correspondingly decrease the amount of active pixels per frame. Therefore it is found that the size of the pixels will not affect the rate of information collected by the camera.

Examining Equation 7.11 yields an interesting inverse relationship between the wavelength of incident light and the light power required. If there exists two light sources of equal power but different wavelength, the light source with the narrower wavelength would be limited to a slower frame rate. This is because the light with the narrower wavelength has more energy per photon and in a constant power comparison would thus emit less photons per second. In order to capture this effect, a metric called "responsivity" can be used to determine at which frequency of light the camera is most responsive or sensitive. Responsivity of a camera is calculated by multiplying the quantum efficiency at a given wavelength λ multiplied by the same wavelength λ as shown in Figure 7-11.

From Figure 7-12 it is found that although the AM41 sensor reaches its highest quantum efficiency at 500 nanometers, it would be more responsive to a light source of equal power at 700 nanometers. Looking at the camera's properties in this manner allows the designer to identify the optimal wavelength of light in which to illuminate the sample for maximum sensitivity.

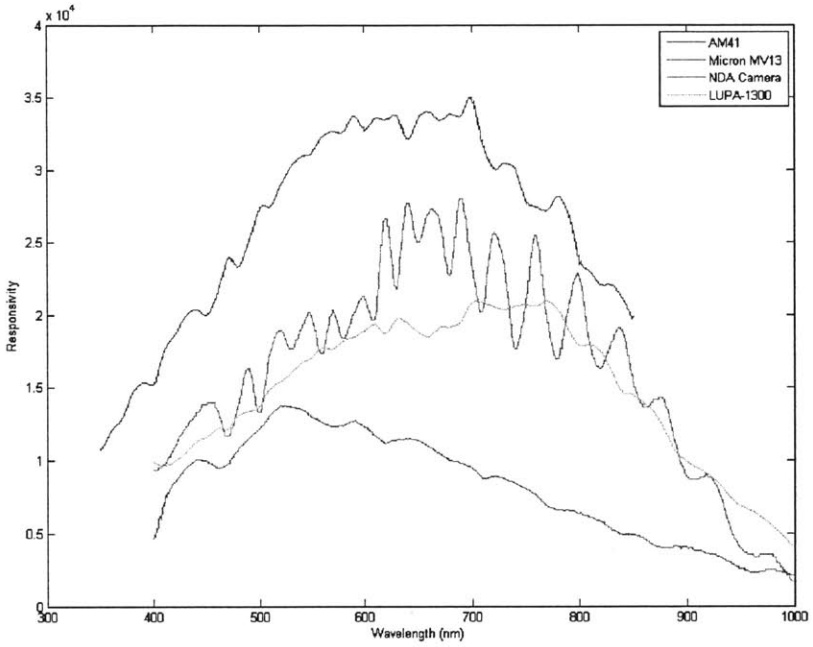

Figure 7-11: Comparison of Responsivity. The responsivity of the four cameras selected in this study are shown as a function of wavelength in this figure. Responsivity is defined as the quantum efficiency at a given wavelength divided by the wavelength. This metric takes into account the decrease in number of photons per unit of energy reflected in the decrease in wavelength.

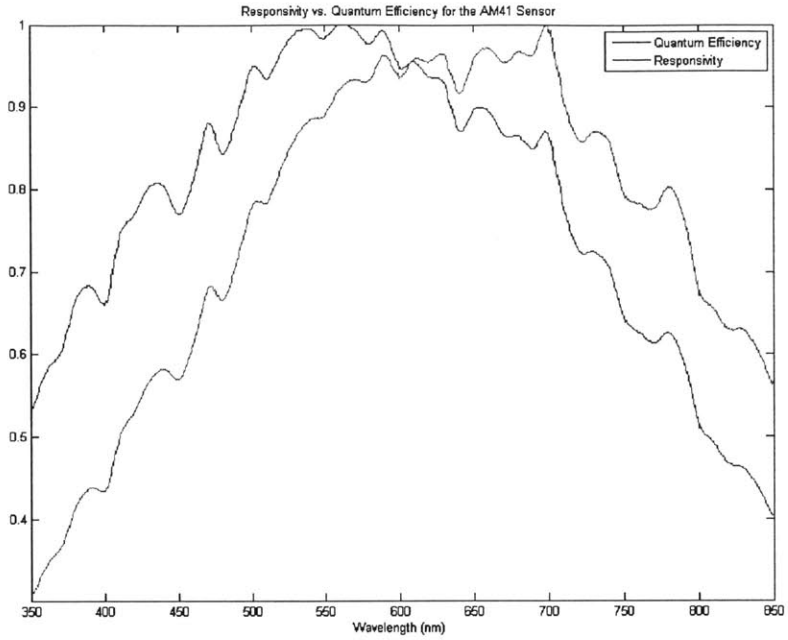

Figure 7-12: Responsivity Versus Quantum Efficiency. A direct comparison between a camera's maximum quantum efficiency and responsivity shows that the optimal wavelength to operate the camera shifts by 200 nanometers when working in light limited conditions.

7.4 Lighting Options and Configurations

The intensity of light available to image the sample can limit the frame rate of the camera. When the instrument is light limited the designer can either use a more sensitive camera sensor or a more powerful light source. This section reviews the different light sources used in the project as well as various configurations proposed to optimize the light collection. Having described the design choices regarding the microscope objective, camera, and optics we first present the entire system in Figure 7-13 to present the reader with a graphical view of the hardware.

7.4.1 Light Configurations

Three main light configurations were employed to optimize the performance of the profilometer based upon the transparency of the material and mode of access. The first configuration used a beam splitter positioned between the microscope objective

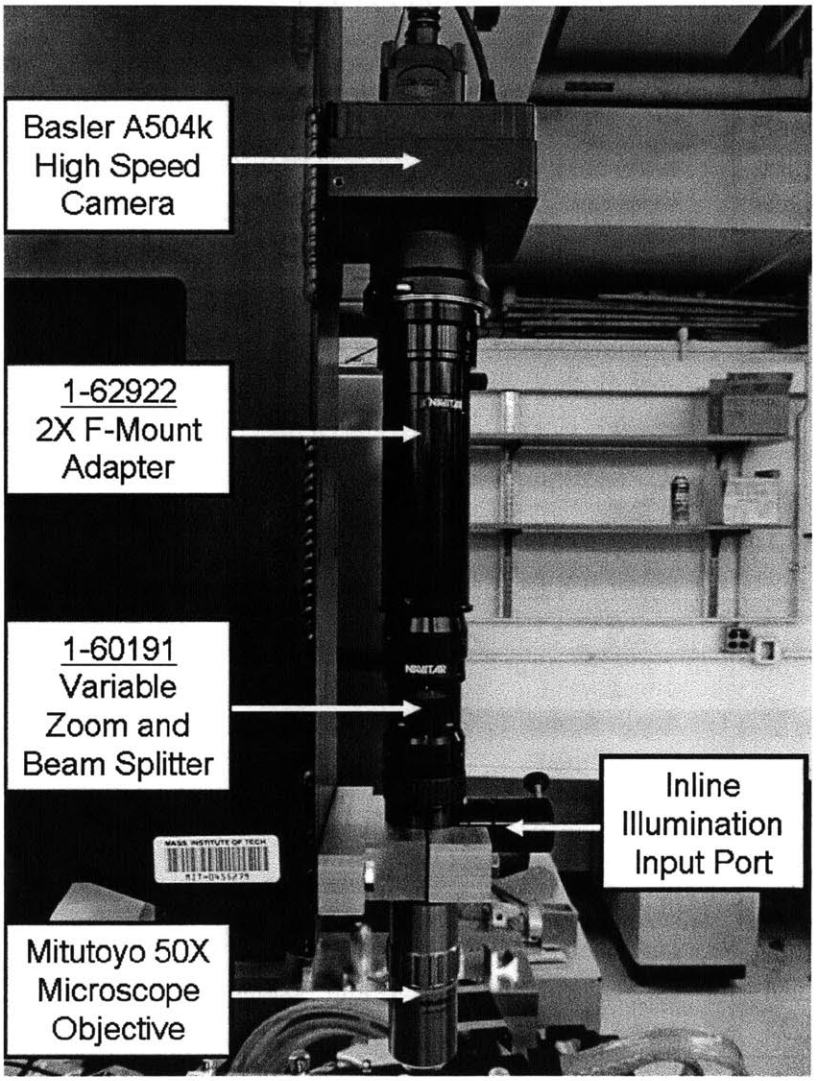

Figure 7-13: Assembly of Optical System. This photograph shows a side view of the entire optical system as it is assembled on the high speed 3D profilometer complete with part numbers.

and eyepiece lens to provide inline illumination. This type of illumination is most useful when using low working distance microscope objectives that inhibit access to the sample. A Navitar 1-62840 body tube placed a housed beam splitter in front of the inline illumination input port shown in Figure 7-13. A cross section of the light path is shown in Figure 7-14. Each time the light strikes the beam splitter, half of the photons are transmitted and the other half are reflected by 90 degrees. Thus, the green light traveling down the body of the tube is reduced to one half the intensity of the original blue light input into the system. Similarly, if all the green light is reflected back into the tube, is reduced by an additional factor of two when it travels through the beam splitter a second time shown as the yellow light that strikes the camera sensor. The colors of light in this diagram do not represent the wavelength of light, but are instead used to signify the relative intensities. This configuration allows for a compact way to illuminate a reflective sample inline with the optics but suffers from a three quarter reduction of intensity caused by the beam splitter.

The second and third configurations of light are used with the camera optics tilted at an angle. This tilt angle prohibits the use of high numerical aperture, low working distance lenses. For reflective samples, the light source can be placed at a complementary angle to the optics as seen in the photograph in Figure 7-15 to maximize light intensity. To add supplemental light from multiple angles, a second light source can simultaneously be input into the inline illumination port. The parallel combination of lights in these two configurations was used when collecting on the 100 μm tall metal part shown in Figure 5-10. For transparent samples the light source can be placed behind the sample to shine directly into the camera as seen in the diagram in Figure 7-16. Using this configuration and a halogen light source the high speed camera was able to collect images with full dynamic range at 1,000 frames per second. This light intensity limited frame rate could have been doubled if the beam splitter was removed from the optical path. While the beam splitter acts as a provider of light in the first configuration, the beam splitter acts to prohibit light from reaching the camera in the third.

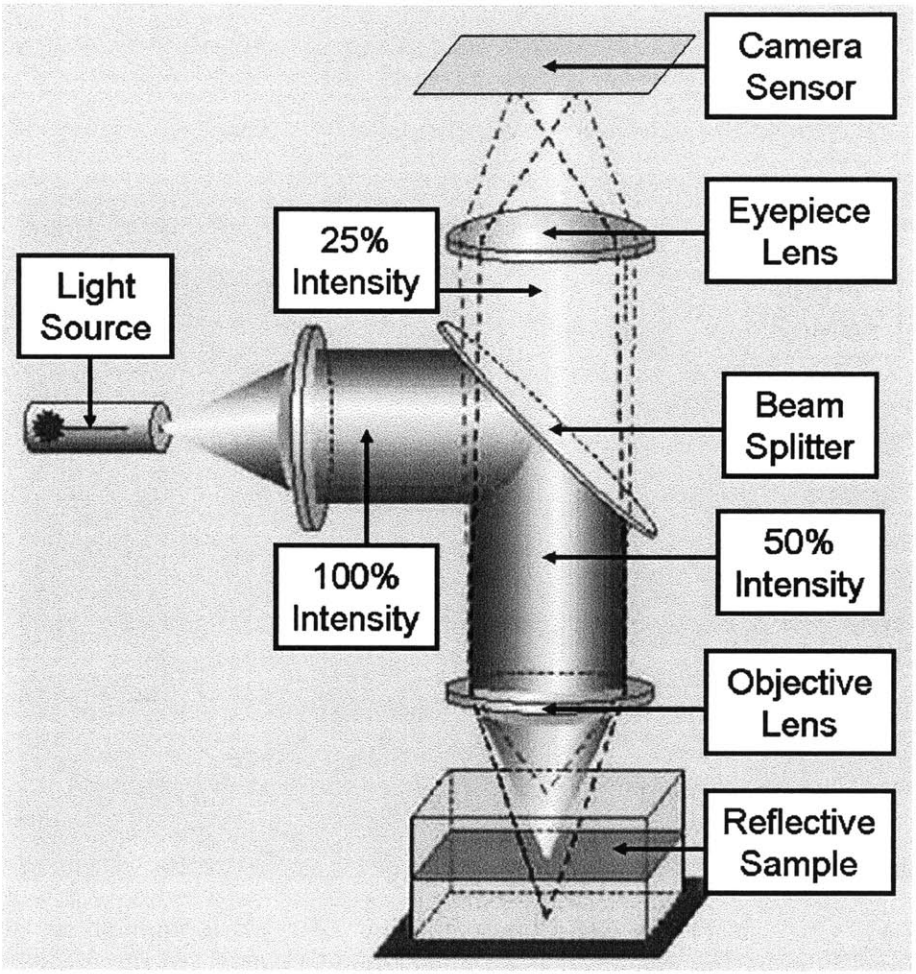

Figure 7-14: Reduction of Light In An Inline Beam Splitting Application. This diagram shows how the intensity of the inline light source is diminished four fold by the beam splitter before hitting the camera sensor. While inline illumination is practical for various reasons, its use can limit the frame rate of a high speed system in light limited conditions.

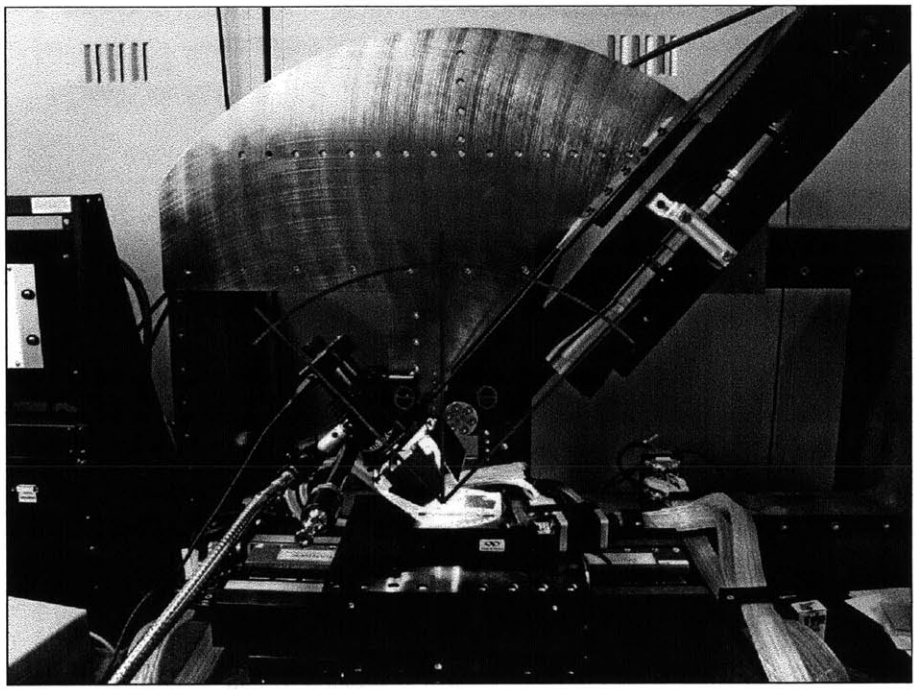

Figure 7-15: Cross Section of Reflectance Imaging. This photograph shows an LED light source illuminating a sample at an angle complementary to the optics. Additional light can be input into the inline port.

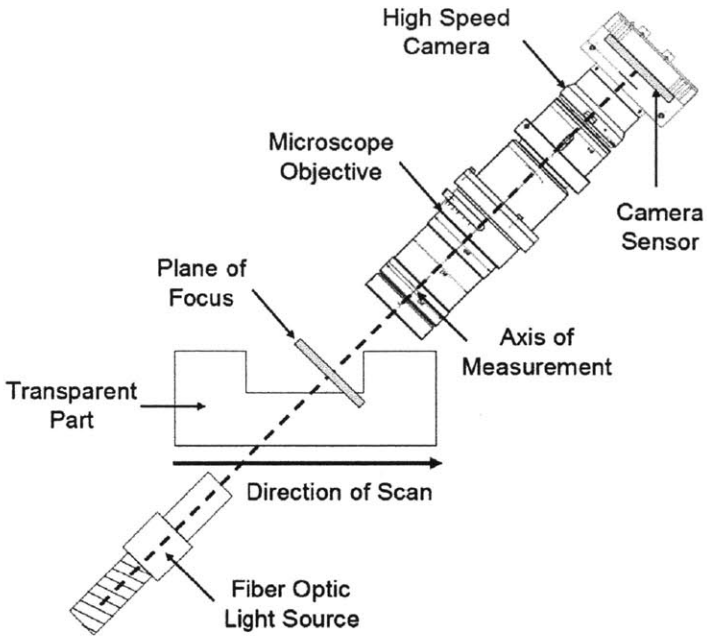

Figure 7-16: Cross Section of Transmission Imaging. This cross sectional diagram shows the configuration in which the maximum light intensity illuminates a transparent sample and reaches the high speed camera to capture images at 1,000 frames per second.

7.4.2 Light Sources

The first light purchased to illuminate the sample was an LED light source called "Zylight" which is typically used in photography and video production purposes. The LED lights were largely unfocused and engineered to create ambient light conditions. Most of the controls and options afforded by the camera were thus geared toward this industry. For example, the light source has a "color temperature" option used to emulate light coming from different temperature light sources from 2,500K to 9,000K. Although the light source itself was reasonably powerful, the light it produced was unable to be sufficiently focused onto our sample resulting in low light intensity and dim images at slow frame rates. Figure 7-15 shows the Zylight being used on a reflective surface at a complimentary angle to the telecentric lens.

The second light used in the high speed profilometer was a blue LED light called the BrightLight II purchased though Navitar Optics. The BrightLight II outputs a

low wavelength 455 nanometer light emission selected to both narrow the depth of field and minimize the lateral resolution when compared against ambient light with a mean wavelength of about 550 nanometers. Unfortunately this light source was also too weak to provide sufficient light intensity for high frame rate image capture. The light was used instead to provide supplementary light through the inline port as described the previous section. The model number of the Bright Light II and its control box are 1-51456 and 1-62802 respectively.

The primary light source used during the majority of image capture was a MO-150 Halogen lamp that concentrated light into a gooseneck fiber optic adapter. This halogen lamp provided the strongest and most concentrated light used in the high speed 3D profilometer. The drawbacks of this light were that its mean wavelength was higher than that of the LED lights and its intensity waxed and waned as it was subject to flicker. The exposure time of the camera had to be set to at least 1,000 milliseconds to average out these effects. Also, the bulb itself needs to be replaced after a given amount of hours (replacement part EKE 21V150W from Ushio, Inc.). Conversely, the use of a broadband light source washed out repeating patterns that sometimes show up with singular wavelength LED light sources.

The last light source to be purchased was Thor Labs M405L2 405 nanometer LED light source. This light was able to provide greater light intensity than the BrightLight II for its output was focused by a ACL2520-A Lens as shown in Figure 7-17. The LED driver can channel up to 1.2 amps of current through the light to provide stunningly bright results. The M405L2 light source was not primarily used to service the high speed 3D profilometer but proved to be useful in lighting endeavors detailed later in the thesis.

7.4.3 Structured Lighting

Metrology instruments will commonly project a specific pattern of light and dark areas onto their measured part. The surface topography of the part can then be

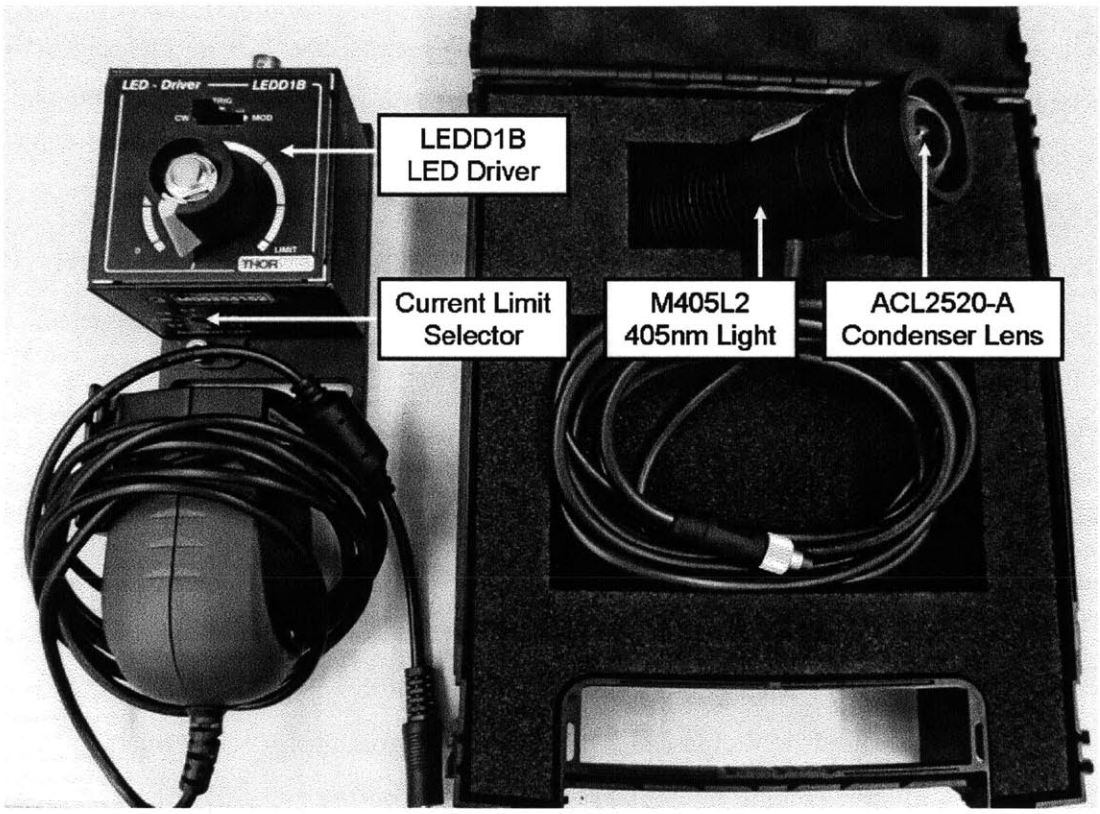

Figure 7-17: LED Light Source Package. This photograph shows the components of the Thor Labs M405L2 405 nanometer LED Light Source. This light source is useful for precision metrology applications, but is not strong enough to be used for inspection purposes.

assessed by observing how this pattern is reflected back into the camera. White light interferometers use a narrow band interference pattern while structured light profilometers use a series of lines. Both of these examples can be considered an application of "structured lighting." This section shows how structured lighting can and has been used to improve the output of the high speed profilometer.

The high speed profilometer is able to measure the surface of a part by identifying which planes are in focus. Unfortunately if the part is too smooth or lacks sufficient surface features the instrument is unable to accurately measure the part's topography. Simply stated,the algorithms can not find the plane that is most in focus if the surface has no contrast. The use of structured lighting is suggested to remedy this problem by projecting a pattern onto the part thus adding contrast or surface texture to the smooth areas.

Structured lighting was able to be implemented on our depth from focus profilometer with limited success. The techniques that used structured lighting by and large require the the structured light be reflected off from the surface. Because only 4% of light is reflected back from a transparent surface, it was very challenging or near impossible to gather enough light into the camera for high speed application while using structured light. Instead, the high speed profilometer relied on the transmission of light picking up contrast from texture on the part. This important difference is noted to clarify that the results posted in this section of the thesis can not be implemented for high speed profilometery in the same manner in which they were taken. A novel way of creating contrast via transmission would have to be worked out in order to move forward with this concept.

The contrasting structured light was created by placing the object plane of the optics at the end of the fiber optic bundle and the image plane at the part surface. The fiber optic bundle is comprised of hundreds of individual wires that individually carry light. By placing the bundle carefully into the inline port, the light from the bundle is focused by the objective lens to concentrate its light onto the sample. The

optics focusing this light have a relatively high numerical aperture such that the depth of focus about the image plane is only about one micron. Thus, the structured light pattern only exists in a narrow band. The pattern from the fiber optic bundle is selectively reflected back into the camera as the part is passed through this band. Figure 7-18 has been constructed to demonstrate this concept. The object being measured in this figure is a 50 μm tall channel extending from left to right. The images on the top and bottom half of the figure were taken by the camera when the focal plane coincided with the crest and base of the channel respectively. The images on the left and right halves were taken with and without the use of structured lighting respectively. This image clearly shows how the use of structured lighting can add contrast to areas of the part in which there are no features.

The images shown in Figure 7-18 are only a small subset of the stack of images taken by the camera in order to measure the profile of the object. A topography of the part can be assembled by using the entire stack. The topography of the part with and without structured lighting is shown in Figure 7-19. It is clear that structured lighting has the potential to improve the quality of the topographical maps.

This same set of pictures were taken of a transparent part. The part imaged in Figure 7-20 and reconstructed in Figure 7-21 is a product of the hot embossed μFac line. Its free surfaces cooled with a smooth texture making it difficult to measure with the high speed profilometer. Again it is clear that the use of structured light can help clean up the reconstructed topography.

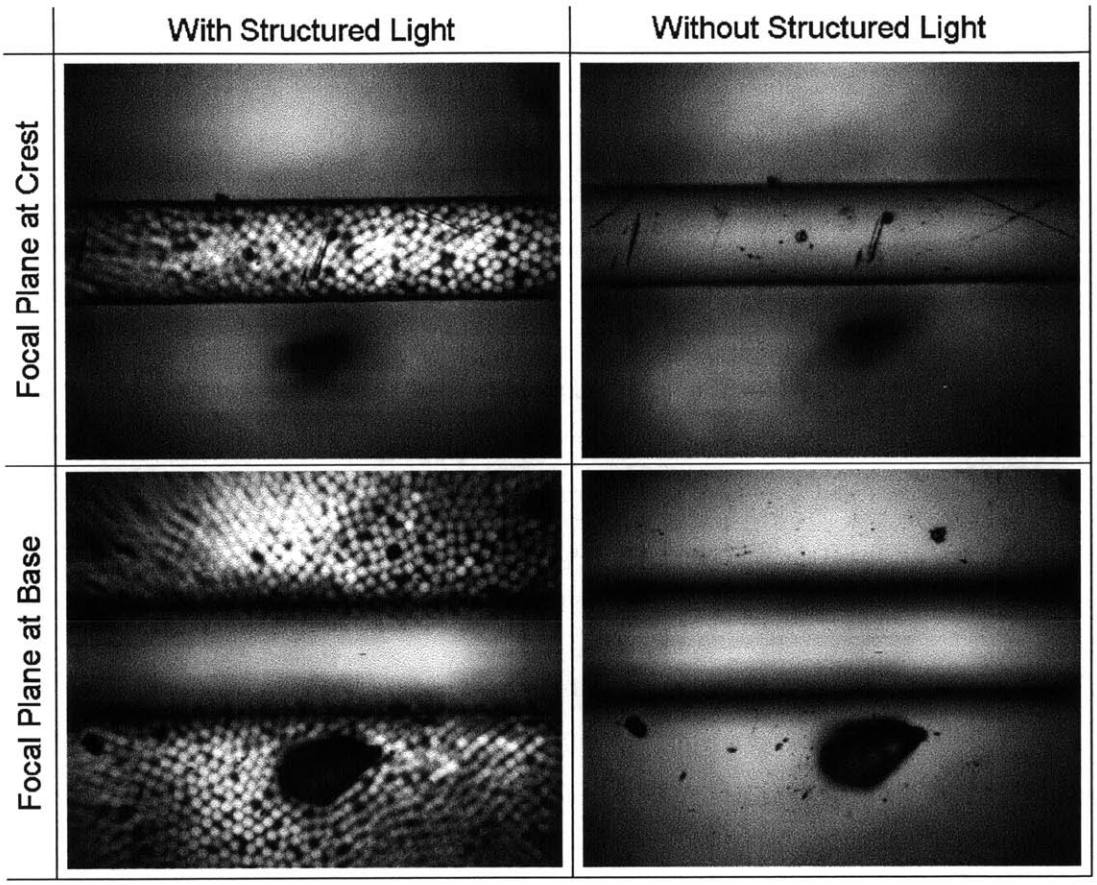

Figure 7-18: Use of Structured Light Via a Fiber Bundle. The four images in this figure illustrate the application of structured light onto a smooth part. The structured light provides contrast where the part otherwise had no features. The focal plane of the camera was set onto the top and bottom of the channel in the top and bottom images.

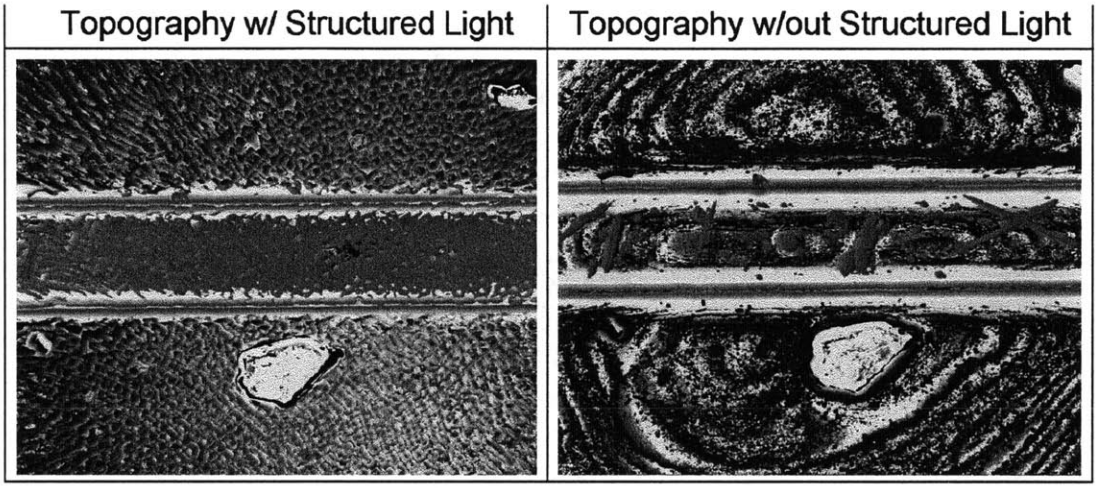

Figure 7-19: Improvement of Output Topography Measurement. This figure shows the computed topography of the micro channel with and without structured lighting. The improvement in accuracy is less dramatic for rough parts that intrinsically show contrast.

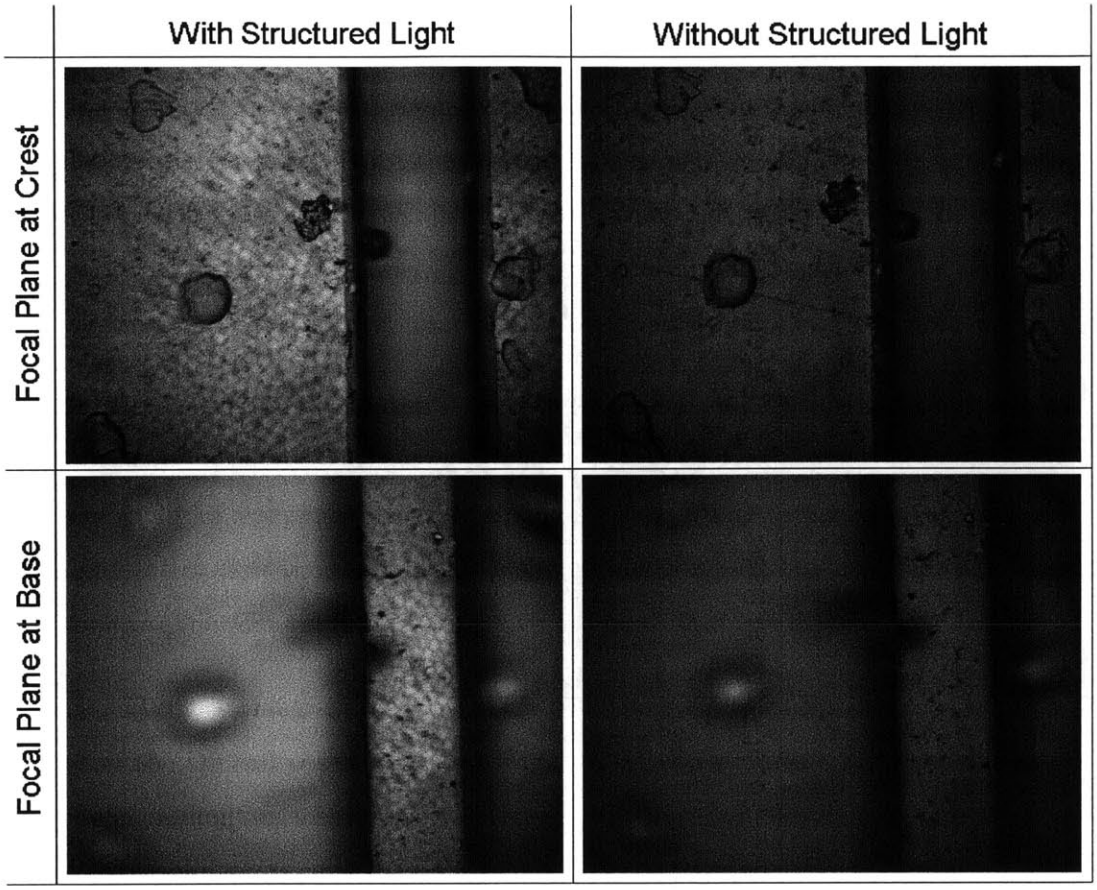

Figure 7-20: Use of Structured Light on Transparent Parts. These four images were taken on of a transparent μFac part. The top two images exposures were captured with the focal plane coinciding with the crest of a channel while the bottom two focused on the trough. The left two exposures were taken with the use of structured light while the right two were not.

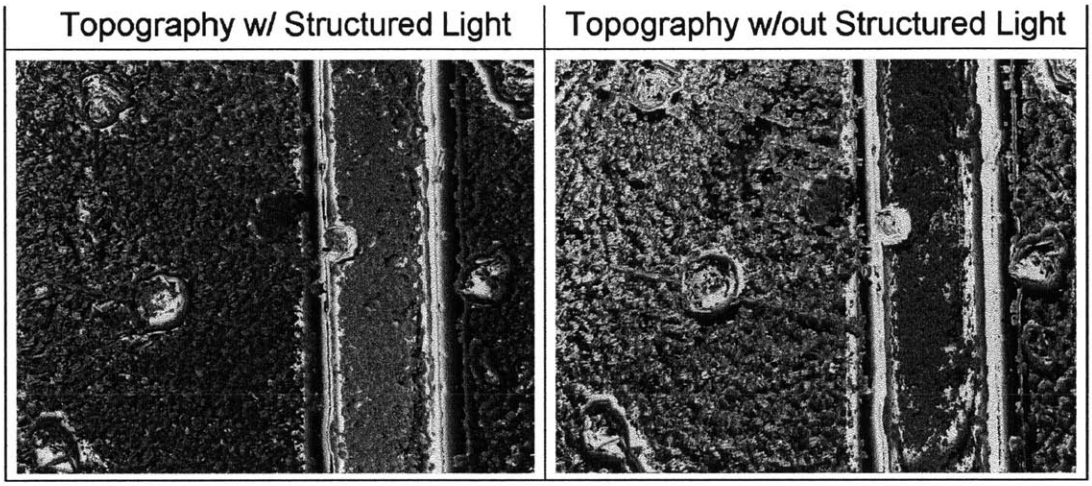

Figure 7-21: Improvement of Output Topography Measurement on Transparent Parts. This figure shows the computed topography of a channel from a transparent μFac part with and without structured lighting.

Chapter 8

Software Design

The purpose of this chapter is to explain and document all of the code and software programs that control the high speed 3D profilometer. The programs PolluxTerm, SysReg, CamEd, CCT+, CiView, BiFlow, and PEWin32Pro are software packages that came directly from a third party that enabled the automation of machinery and capture of data. Once collected, this data is processed using a series of scripts in MATLAB, each of which were uniquely constructed to perform specific functions to enable 3D topological reconstruction. The contents of this chapter can be used help improve the high speed profilometer.

8.1 PEWin32Pro

The PEWin32Pro program acts as the interface between the user and the X,Y air bearing stage. The stage itself is controlled by Delta Tau Data Systems hardware: a control unit developed with the flexibility to apply motion control to a host of industrial applications. The control unit is called the "Programmable Multi Axis Controller" or PMAC for short. The flexibility of the system leads to a large number of confusing options each of which are independently useful for some aspect of motion control. This thesis focuses on the pertinent functionalities explaining only the portions of the Delta Tau controller and PEWin32Pro program that need to be understood in order to grasp the concepts that pertain to the high speed 3D

profilometer. Further information on the PEWin32Pro functionalities can be found in the Turbo PMAC User and Accessory Manuals.

8.1.1 Hardware Initialization

A frontal view of the hardware and air bearing stage witnesses four very important switches and valves integral to initializing the stage. All four components are photographed and labeled in Figure 8-1. A red push valve located underneath the carriage of the granite table controls the flow of air to the air bearing stage. This valve should be the first item to turn on and the last to turn off to protect the air bearings. The Delta Tau hardware has a pressure sensor that will turn off power to the linear motors in the air bearing stage if it senses that the air has been shut off. The use of sensor to turn off the linear motors should only be used in emergencies. Also note that the X,Y stage may drift in position once the air has been turned on because of the position of the cables or pitch of the floor. The top red switch on the black control unit gives power to the PMAC system and Heidenhain optical sensors. The bottom red switch turns on the amplifiers that deliver power to the Trilogy 200 series linear motors. Lastly, the large circular red push button serves as the emergency stop to kill power to the entire system.

8.1.2 Homing Processes

Once the stage is fed the appropriate power and air connections an important sequence of commands must be input into the PEWin32Pro to begin the automated movement of the air bearing stage. The first commands jitter the X and Y axis such that the hall effect sensors can register the linear motors to the stage position. These commands can be typed into the Command Terminal on the PEWin32Pro Software as shown in Figure 8-2. The PEWin32Pro assigns the numbers 1, 2, and 3 to the X, Y, and θ_z axis respectively. The first command "#1$" tells the stage to jitter the X axis while second command "#2$" does the same for the Y axis. The θ_z

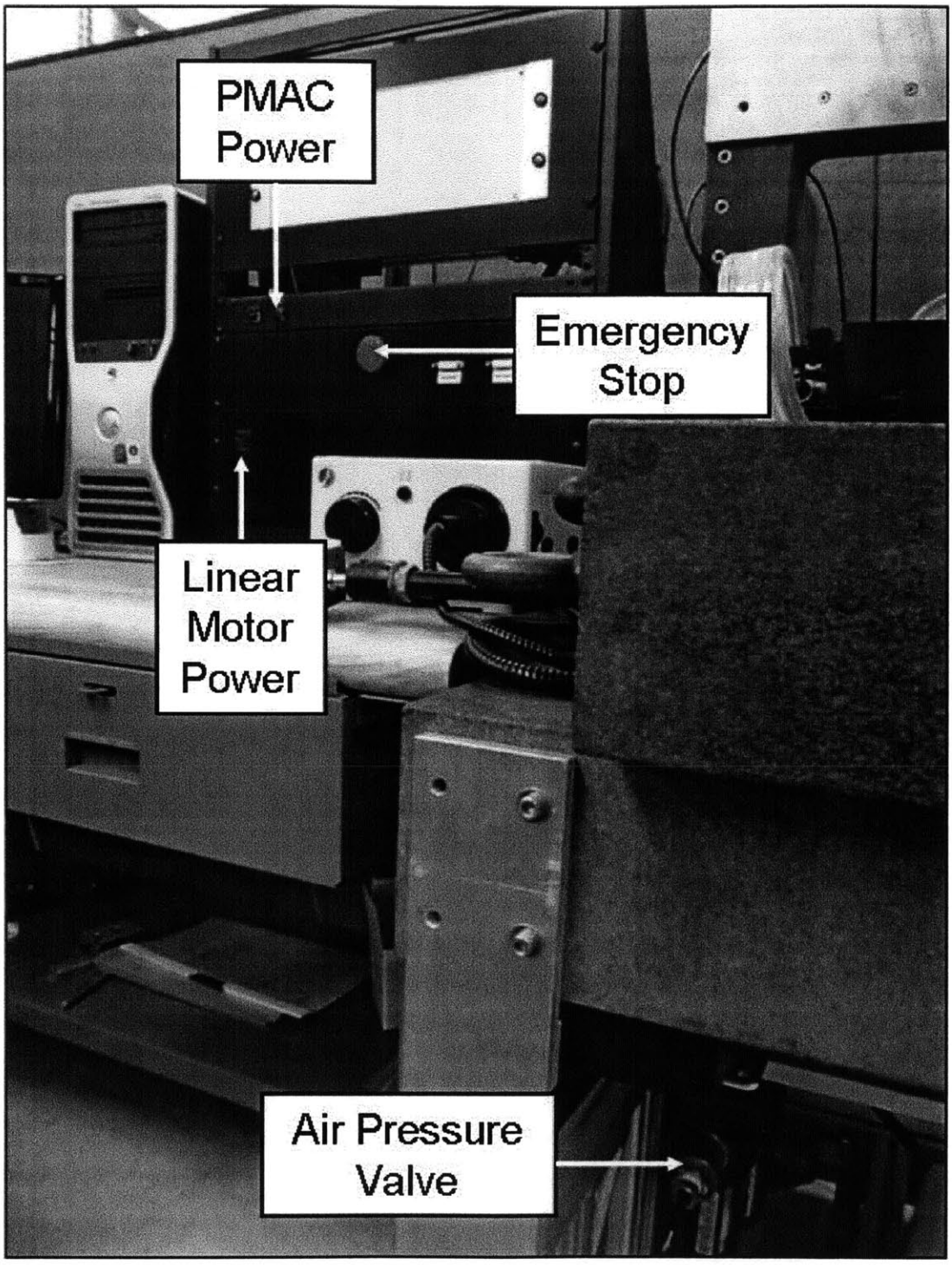

Figure 8-1: Locations of Important Components for Setup of the Air Bearing Stage. This picture shows the locations of the air and power supplies for the X, Y air bearing stage.

Stage	Number	Jitter	Home	Range	Resolution	Max Velocity
X	1	#1$	enaplc2	200mm	20 nm/count	40mm/sec
Y	2	#2$	enaplc3	200mm	20 nm/count	40mm/sec
θ_z	3	#3$	enaplc4	360°	0.0002°/count	40° / sec

Table 8.1: This table holds useful information on how to activate, home, and run each of the three axis on the air bearing stage.

axis does not need to be jittered for it is neither in closed loop control nor supported by air bearings.

The air bearing stage can also be homed in all three axis. The homing process ensures that the stage will not exceed its travel limits if commanded to do so by the user. The commands "enaplc2," "enaplc3," and "enaplc4" are typed into the command terminal to home the X, Y, and θ_z stages respectively. Once the stage has homed an axis, the position readout will display the position as "0 counts." Table 8.1 summarizes all the pertinent information regarding the commands and attributes of each axis.

8.1.3 X Position / Camera Synchronization

The PMAC controller is programmed trigger the camera exposures based upon the X position of the stage. This closed loop feedback control enables precise registration between the camera and stage required in later image processing to overlap subsequent images. The Heidenhain LIF481 optical encoders have a resolution of 20 nanometers with at a 25MHz bandwidth. The PMAC is programmed to output a square wave with a spatial period equivalent to programmable distance set as any integer N multiplied by 20 nanometers. This square wave is fed into the external synchronization (ExSync) input of the camera that triggers the image capture. The camera is programmed to start its exposure once the ExSync digital input switches from low to high. The code that programs the square wave signal is displayed in Figure 8-2 and also repeated below. A graphic describing the variables in the program is taken from Page 382 of the Turbo PMAC

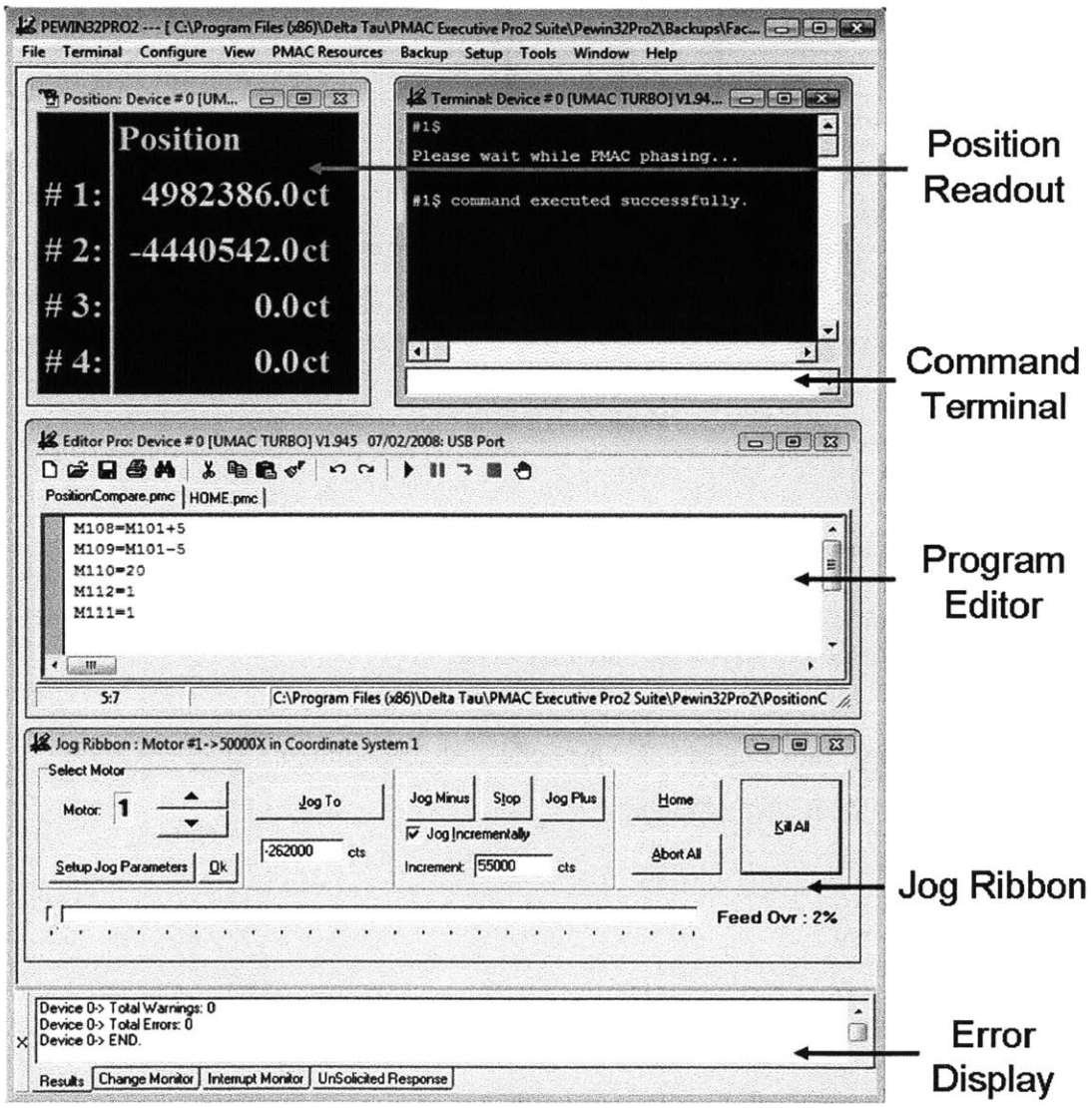

Figure 8-2: Screenshot of the PEWin32Pro Software. The program PEWin32Pro is used to monitor and control the X,Y air bearing stage. This screen shot of the PEWin32Pro labels each of the graphic interfaces the user requires to command the stage.

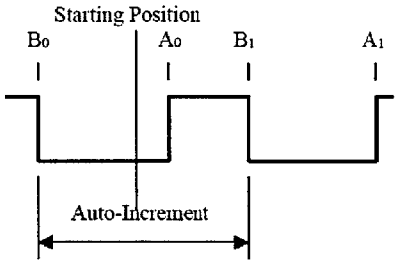

Example: Starting from the above example, desiring the compare output on between 1000 (A_0) and 1010 (B_1) counts, but adding an auto-increment value of 2000 counts, with a starting position of about 100 counts, program code to start the sequence could be:

```
M110=2000                    ; Auto-increment of 2000 encoder counts
M108=1000                    ; First front edge (A0) at 1000 counts
M109=1010-M110               ; First back edge (B1) at 1010 counts
M112=0                       ; Prepare initial value of 0
M111=1                       ; Enable direct write (resets immediately to 0)
{Command to start the move}
```

Figure 8-3: Synchronization Graph from PMAC User Manual. This graphic and code was taken directly from the Turbo PMAC User Manual to describe how the user programs the position-compare function. The Auto Increment sets the spatial pitch while variables M108 and M109 set the duty cycle.

User Manual copied into Figure 8-3. Our code is slightly different than the code presented in the PMAC User Manual.

M110 = 20

M108 = M101 + 5

M109 = M101 - 5

M112 = 1

M111 = 1

The PMAC system has different "I" and "M" variables. "I" variables tend to describe hardware oriented things that are static while "M" variables typically describe software or output variables that are dynamic. All variables between 100 and 199 refer to the 1st axis while variables between 200 to 299 refer to the 2nd axis. For example, the current position of the X stage is variable "M101" which constantly changes as the stage moves around. As demonstrated in the provided

code, the M110 variable programs into the PMAC the spatial frequency of the output sine wave used in the camera synchronization. The spatial frequency is equal to 20 nanometers multiplied by the M variable M110. For example, if the user wanted the camera to capture images every 400 nanometers M110 is set to a value of 20. The M Variables M108 and M109 are used to set the duty cycle of the square wave. These values tell the computer when to switch the output from high to low on a "front edge" and "back edge." Whereby M101 is the current position of the stage, the provided code tells the signal to remain high for $\pm$ 5 or a total of 10 counts. These values set a 50% duty cycle given a 20 count spatial period. Lastly, M112 tells the software whether or not to start with a high or low output signal and M111 acts as a write enable for the program. The program is downloaded to the system by pressing the yellow down-arrow at the right hand side of the Program Editor window.

The output signal generated by the PMAC software must be hardwired into the camera in order to communicate between the two instruments. The PMAC Accessory ACC-24E2A is a 4-Axis interface used by our instrument to send and receive the proper signals from the X, Y, and θ_z stages. Each axis has digital output channels EQU1 and EQU2 reserved for position-compare or synchronization signals. The output EQU1 is hardwired into the input pin 2 on the BitFlow Frame Grabber breakout board while the ground output is hardwired into pin 11.

8.2 PolluxTerm

The PolluxTerm program is a relatively straightforward piece of software that controls the height of the Z stage. The software communicates to the PolluxBox® power amplifier via the serial port on the CPU. The amplifier in turn sends the correct power and signals to the Micros MP-21 12mm actuator to engage the Z axis and monitors the limit switches. Figure 8-4 captures a screen shot of the PolluxTerm software. After establishing communication with the power amplifier via

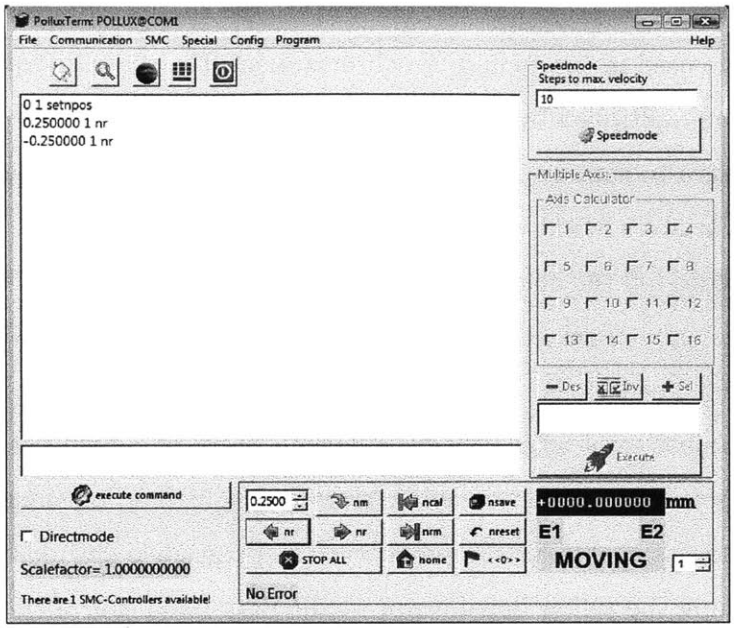

Figure 8-4: Screenshot of the PolluxTerm Software. The program PolluxTerm was used to send commands to the Z axis. This screen shot serves as a visual guide to help the reader locate the features cited in the text.

the leftmost "plug" button, the user can automate movements of the Z stage. The two "nr" buttons move the stage up or down the distance specified in the field box located directly above. Once a "nr" command is issued, a record of the movement is displayed in the large white box. The blue box at the right of the screen keeps a running tally on how far the stage has been moved. Pressing the "home" button will zero out this display. All distances used in the PolluxTerm software are in units of millimeters. The user must be cognizant of the 1/2 reduction in travel as a result of the wedge geometry of the Z stage meaning that a 1 mm commanded move on the PolluxTerm software will result in a 0.5mm Z displacement.

8.3 Camera Configuration Tool Plus (CCT+)

As indicated by its name, the program Camera Configuration Tool Plus (CCT+) is the software interface used to configure the inputs and output of the Basler A504k high speed camera. A screen shot of the Java based applet in Figure 8-5 is used as

an outline to explain the important features of the user interface. First, the "Exposure Time Control Mode" must be set to either "Free Run" or "External Sync." The Free Run option triggers image capture based upon a selected time intervals while the External Sync option triggers image capture via an external square wave signal. During troubleshooting and general use the camera is typically set to Free Run such that the user can see a continuous update of the images captured by the camera. The Exposure Time Control Mode must be switched to External Sync to capture synchronized imagery once the stage and sample are prepared for automated movement. Either mode can be set to a "programmable" setting which indicates that the user will set the exposure time specified below under "Exposure Time [μsec]." Alternatively, in the "edge-controlled" setting the camera collects information or extends its exposure time until the next frame is triggered. Lastly, the frame rate of the camera while in Free Run mode can be set by the "Frame Rate [fps]" field.

While the sensor outputs at maximum a 1280 x 1024 pixel image, the image can be downsized such that any rectangular subset of the overall image is saved. The resulting saved area is referred to as the "Area of Interest" or AOI. To specify the size and location of the downsized output image, the Basler CCT+ program prompts the user for the AOI Starting Column, AOI Width, AOI Starting Line, and AOI Height. For example, if rows 100 through 900 and columns 200 through 600 were to be selected the values for these four inputs would be 100, 800, 200, and 400 respectively. It is again noted that for the Basler A504k camera a reduction of rows allows a proportionally faster frame rate while a reduction of columns does not.

8.4 SysReg and CamEd

SysReg and CamEd are vital but seemingly redundant programs used to program the BitFlow frame grabber. The frame grabber is an electronic device that acts as the interface between the camera and CPU. It captures the data streaming off the

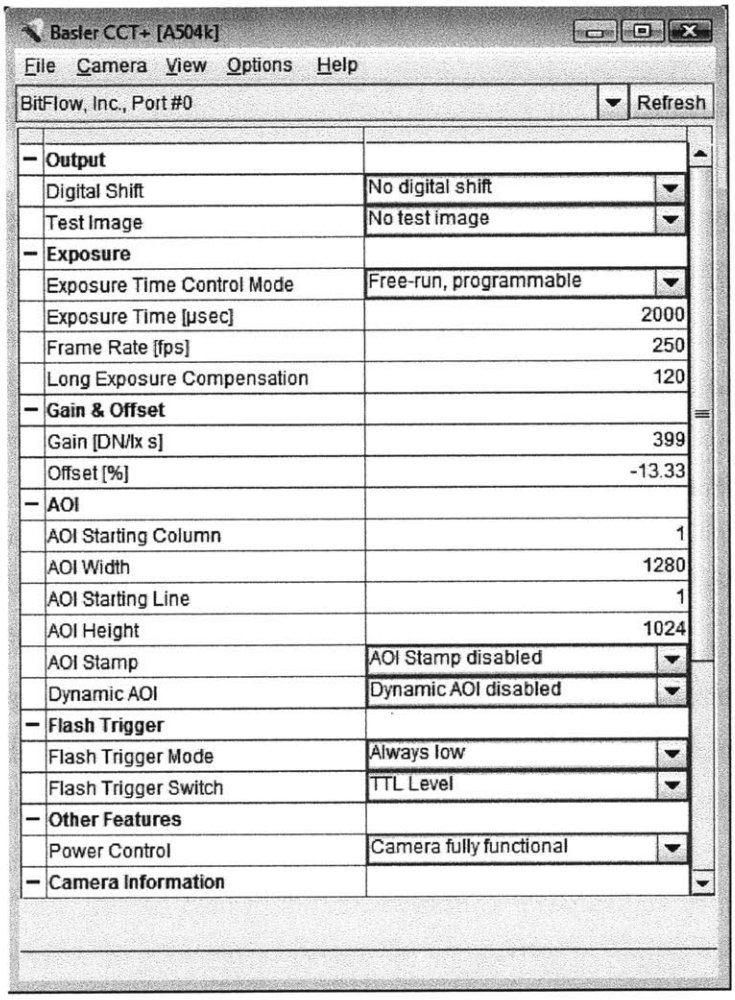

Figure 8-5: Screenshot of the Basler CCT+ Software. The Basler CCT+ Java applet is used to program the Basler A504k camera. This screenshot displays the most important functions accessible through this program notably the exposure time control mode, frame rate, and AOI settings.

camera and processes it into a form consumable by the CPU. Both programs SysReg and CamEd perform analogous duties for the frame grabber as the program CCT+ performs for the camera. The CamEd software creates and edits an ".r64" file which holds the same AOI and Exposure Time Control Mode information edited by the CCT+ program. SysReg in turn uses the ".r64" file to initialize the frame grabber that its inputs and outputs are compatible with the camera. When the user wants to change any parameter on the camera output such as switching from ExSync to Free Run mode, both the CCT+ and SysReg software must be updated.

8.5 CiView and BiFlow

The two programs CiView and BiFlow allow the user to see and capture the data saved by the frame grabber. CiView shows the data as it is being output by the camera. The video shown by CiView will update every time the camera collects a new frame. It is suggested that CiView is used in Free Run mode such that no movement of the stage is required to witness a streaming video of camera output. The most important function in CiView is the "capture" option which saves whichever frame is currently displayed to the user when the button is pressed. Conversely, BiFlow is best used while under ExSync mode. BiFlow saves a predetermined number of frames as they are captured by the camera. While each frame must be individually saved and titled using the "capture" option in CiView, BiFlow instead saves and labels an entire series of images as either individual image files or as one video. BiFlow is used to tell the camera when to start and stop saving the output images.

8.6 MATLAB Code

In Chapter 5 a series of images are used to describe how the camera is able to measure topography from depth from focus techniques. All the upcoming images shown in this chapter were generated by processing the sequence of images captured

by the camera. The purpose of this section is to explain in detail these processing techniques. The MATLAB code used to create the topological images is segmented into pieces then commented on and augmented with various figures and pictures.

8.6.1 Formation of the Height Slices

The first task of the image processing software is to transform the images into what have been dubbed "height slices." Each height slice represents a line scan image collected by each row of the area scan camera. This transformation would take 5,000 camera images of resolution 1,280 x 1,024 and transform them into 1024 height slices of resolution 5,000 x 1,280. Based upon the area of interest, the code selects only a subset of the available rows from the first row of interest to the last row of interest. This reduction cuts down on the vertical range simply for computational purposes. Similarly, it is found that using all 1024 lines are redundant or add marginal information. A reduction factor is used to only select every 5th line. The code imports each image and then parcels it apart into the various height slices. A repetition of code for every logarithmic interval is required to properly import the image based upon its assigned name.

8.6.2 Rectification of Data

After the height slices have been complied they must be properly rectified to take into account the tilt of the camera sensor. Ultimately the data is complied into vertical vectors to find the height of any given point. Whereas the camera is tilted, the (1,1) pixel of height slice 1 does not lie vertically above the (1,1) pixel of height slice 1024. This concept is demonstrated in Figure 8-6. The incomplete data on the front and back end of each scan must be discarded.

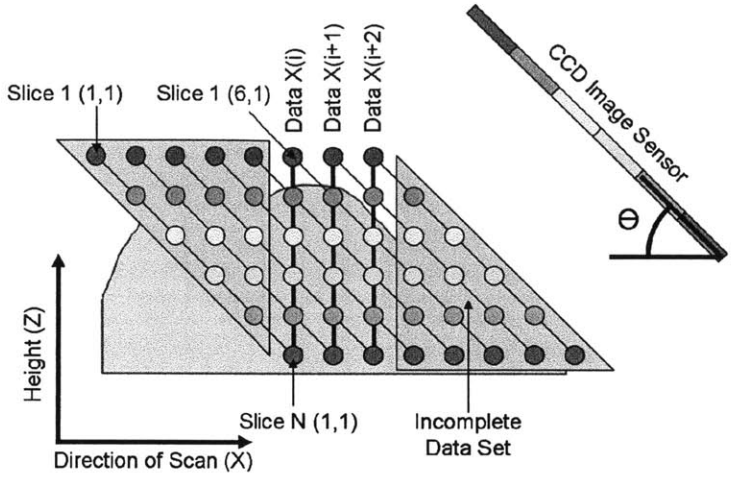

Figure 8-6: Accounting for Incomplete Data Sets. This diagram illustrates how the height slices must be shifted in order to select the data which forms a complete data set. The areas selected in red show incomplete data sets whose information is typically discarded from the topography measurement.

8.6.3 Image Processing

Next, the data is processed and filtered in different ways in order to "clean up" the images. The algorithm eventually used to detect height works by identifying locations with high levels of contrast. If there is a dead pixel or dust on the camera sensor that pixel will collect less light intensity than its neighbors. This behavior manifests itself as a dark streak on the line scanned height slices. The difference in light intensity will be interpreted by the height finding algorithm as evidence of the surface rather than a bias in pixel sensitivity. The standard deviation of each column of each height slice is calculated. If the pixel is dead the standard deviation will be relatively low for its maximum intensity value will be reduced by some factor. A pixel is considered to be "dead" if the standard deviation of its column is 15% less than the average of the neighboring fourteen columns. Any information from a pixel that is identified as dead is in turn be erased and replaced by the average of the columns to its left and right. Figure 8-7 was constructed to show the effect of a dead pixel. The left side of the image shows a portion of a height slice captured by our camera. The right side of the figure graphs the standard deviation

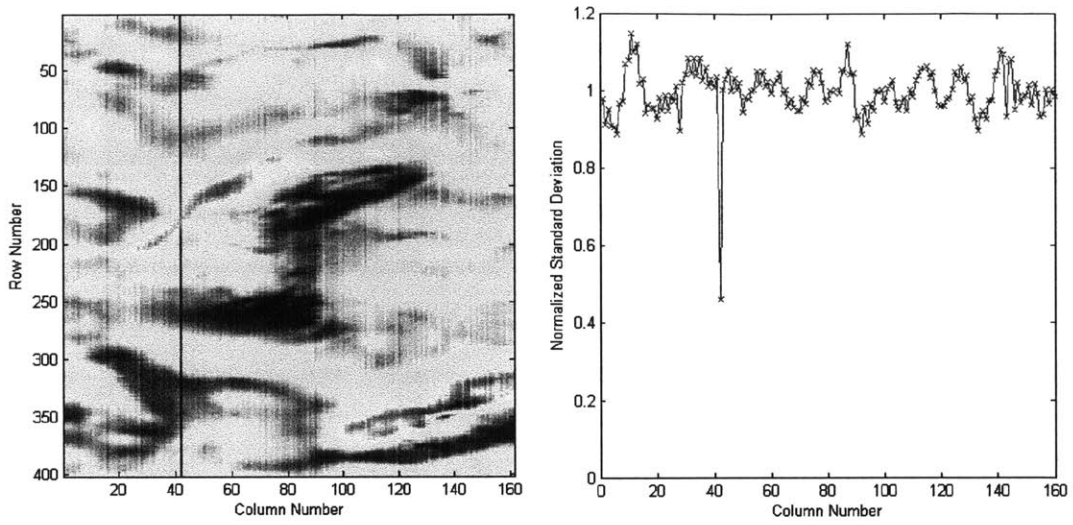

Figure 8-7: Dead Pixel Recognition. The side by side diagram shows on the left a portion of a height slice captured by our camera and on the right the results of an algorithm crafted to identify dead pixels. A significant dip in the normalized standard deviation measure singles out dead pixels.

of each column of a height slice against the column number. From this figure it is evident that column number 42 was imaged by a dead pixel.

Next, the image is altered to take account for pixel to pixel changes in light intensity caused by effects such as vignetting. Vignetting is an optical effect in which the pixels on the outside edge of the sensor receive less light than those in the center. The effect stems from the geometry of the lens whereby the center pixels accept light from a greater divergence of angles. Furthermore, each pixel itself will have a variation in sensitivity again giving rise to artificial intensity variations. These effects can fool our standard deviation algorithm for higher intensities will result in higher standard deviations while the relative intensities remain constant. Each column of pixels is then divided by the average standard deviation of its seven neighboring columns to standardize the light intensity across the sensor processed by the code. The effect of image processing can be seen in Figure 8-8 which shows side by side the a height slice before and after manipulation by this code.

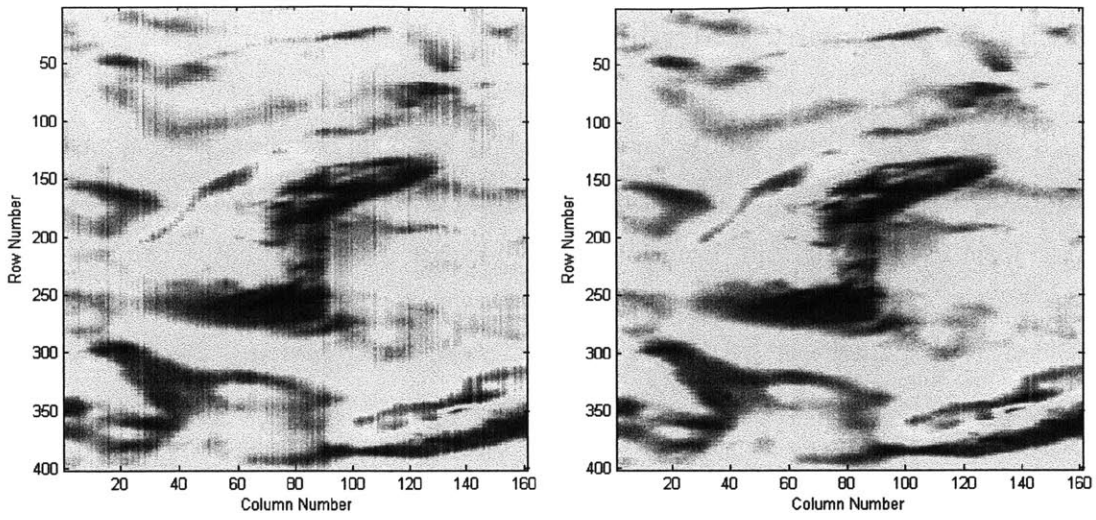

Figure 8-8: Adjusting for Differences in Pixel Sensitivity. The left side of this figure shows the results of removing the dead pixel from out image. The right side shows the smoothing effect of employing the image processing.

8.6.4 Calculation of Localized Standard Deviation

The next step our image processing is to compute the localized standard deviations of the filtered height slices. For each pixel of each height slice, the algorithm first selects the m x m matrix of values that circumscribe the pixel itself. The average of this m x m matrix is calculated using a filtering operation. This average value is now subtracted from each value in the m x m matrix. Next, the absolute value of the result is taken. Lastly, the summation of this group of numbers is calculated. Technically this operation calculates the variance of the m x m matrix which can be square rooted to solve for the standard deviation. The standard deviation are compiled into a large 3D matrix. The 1st and 2nd dimensions of the matrix describe the X, Y location of standard deviation measure inside the height slice while the third dimension describes its Z location.

8.6.5 Topography Calculation

Once the 3D matrix of standard deviation values has been computed, the algorithm can finally solve for the topographical information of the sample. A subset of data is taken from the 3D standard deviation matrix for each X,Y coordinate. The subset of data collects one standard deviation value from each height slice at the same X,Y location. This vector is first low pass filtered and then solved for its maximum. The maximum value is selected as the height of the sample at each X,Y location and input into a "Height" matrix. Simultaneously a measure called "Assurance" is also calculated. The "Assurance" matrix shows the maximum standard deviation of the vertical vector as a function of position. The Assurance is high where the camera has imaged high frequency content. An example of both the Height and Assurance matrixes are shown in Figure 8-9.

8.6.6 Extended Depth of Field Imagery

Lastly the MATLAB code is able to create an extended depth of field image of the sample. The standard deviation algorithm determines where is the plane of most focus based upon the height slices for each X,Y pixel. Using this information, the MATLAB program grabs the intensity value for each X,Y point at the plane of focus and compiles it into one image. First, the height slices themselves are compiled into a 3D matrix similar to that of the 3D standard deviation matrix. This 3D matrix of images is boiled down into a 2D image of the most in-focus intensity values. A comparison of the extended depth of field imagery against the original image shows the results of this process in Figure 8-10.

8.6.7 MATLAB Code Optimization

The choices made in the code were often times evaluated by observing their effect on the output topography. This section examines two such choices. First it was decided to use a 5 x 5 pixel array when calculating the localized standard deviation.

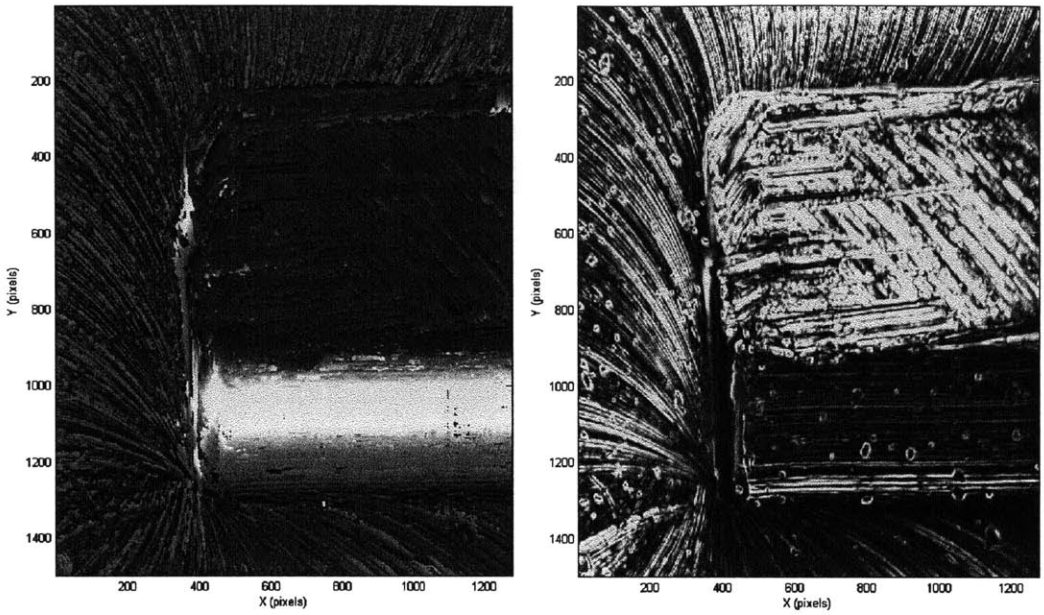

Figure 8-9: Output Plots from Micromachined Part. This figure shows the height and assurance plots generated by the image processing software. The part being imaged was a micromilled aluminum demolding piece generated by Matt Dirckx. The height map shows the part's elevation while the assurance map indicates the relative local accuracy of the measurement.

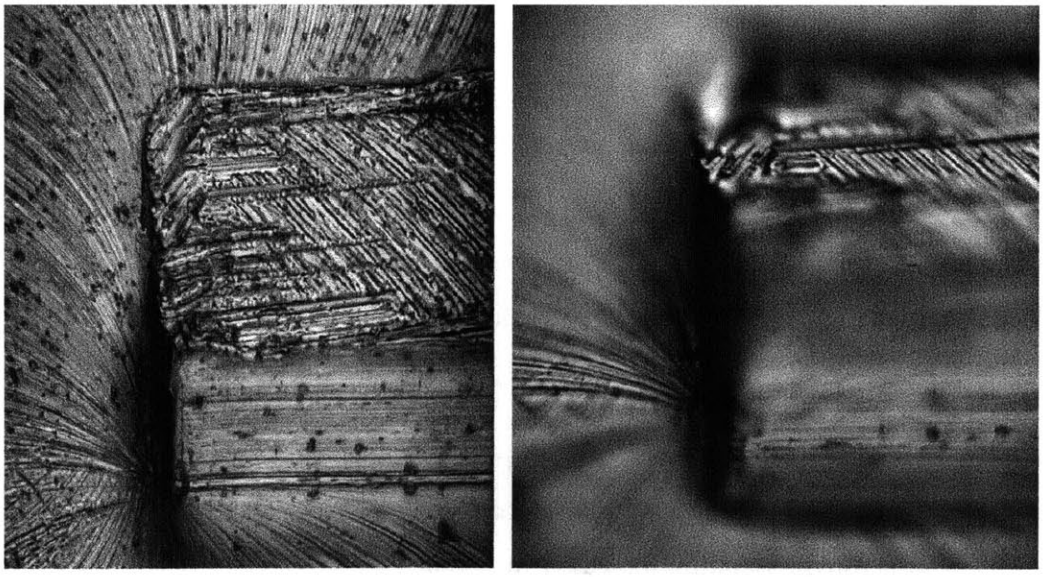

Figure 8-10: Extended Depth of Field Versus Original Imagery. This side by side image shows the extended depth of field image compiled by the above code against the original image captured by the camera.

An odd number was chosen such that there was an unambiguous center pixel. The results of using a 3 x 3, 5 x 5, and 7 x 7 array are displayed in Figure 8-11. It was found that using the 3 x 3 array output topographies that were too noisy while the 7 x 7 array made the topographies too blotchy. This part of the algorithm could be served better by producing a more rigorous or quantitative metric to evaluate its performance.

Secondly effect of the image processing was observed. In the image processing code, the algorithm attempts to compensate for differences in pixel sensitivity. The filtering algorithm creates images without jagged edges that often can fool the height detection algorithm. The image processing code became a staple algorithm after observing the topographical output with and without filtering seen in Figure 8-12. It is possible that the rainbow artifact seen in the filtered image may have been caused by the filtering process.

8.7 Parallel Processing Power

The inspection machine must both collect and process the topographical information in real time to meet the requirements of the manufacturing process. The instrument in research project collected the information and then processed off-line. Though it is not necessary to implement inline processing to demonstrate the capability of the instrument, it is necessary to show that inline processing is indeed feasible. This section of the thesis addresses this need.

The concept of "processing power" must be first understood and defined in order to assess the feasibility of the project. The rate at which a processor can execute commands can be quantified by a measure of computer performance called FLOPS. FLOPS is an acronym standing for **FL**oating-point **O**perations **P**er **S**econd whereby one flop represents a single mathematical operation such as an addition or subtraction. Thus, the processing power of a computer can be rated by the number of floating point operations it can calculate per second. The number of FLOPS

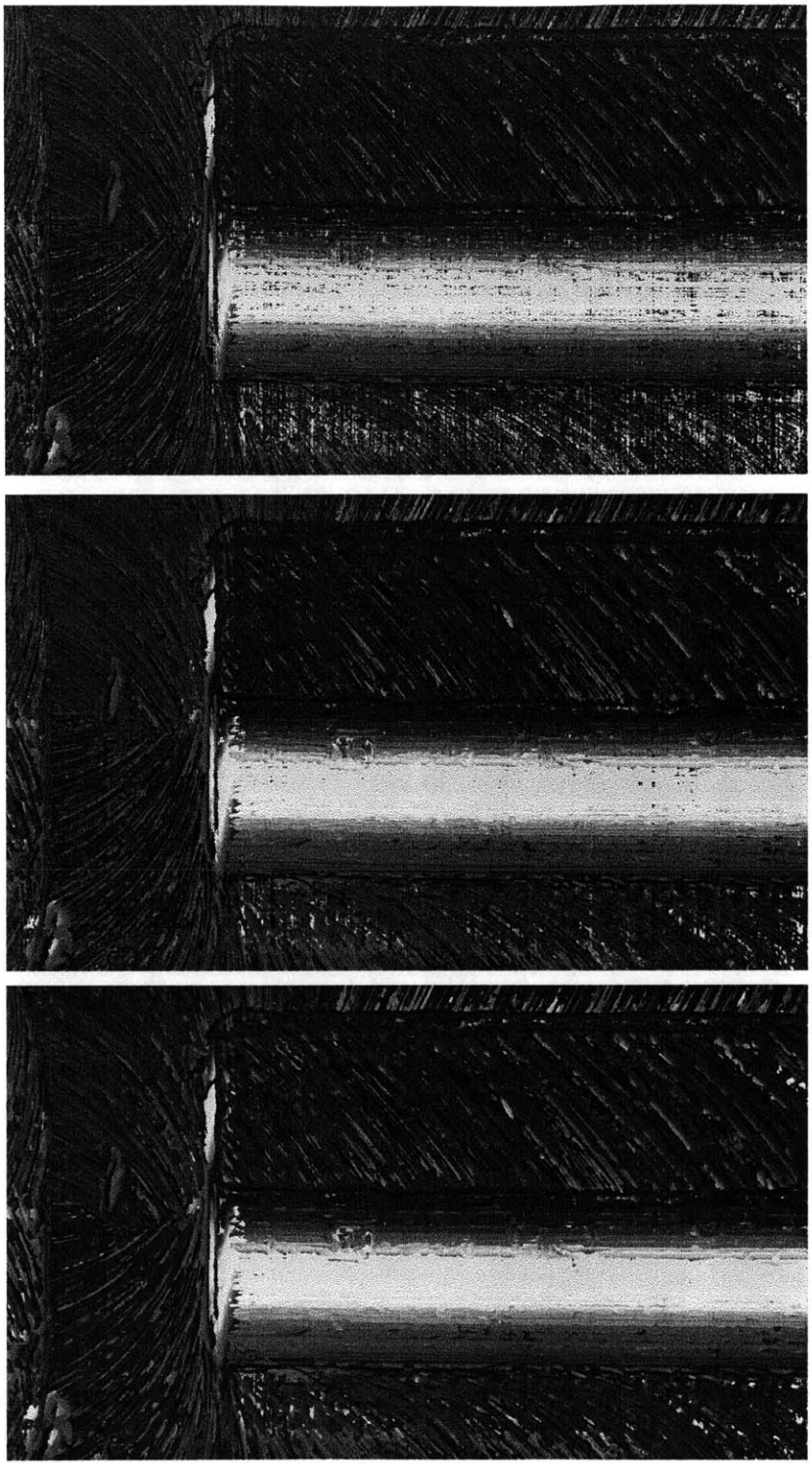

Figure 8-11: Effect of Window Size on Output Topography. This figure shows the effect of using different sized arrays when computing the localized standard deviation. The first, second, and third images were computed from the same data while using 3 x 3, 5 x 5, and 7 x 7 pixel arrays respectively.

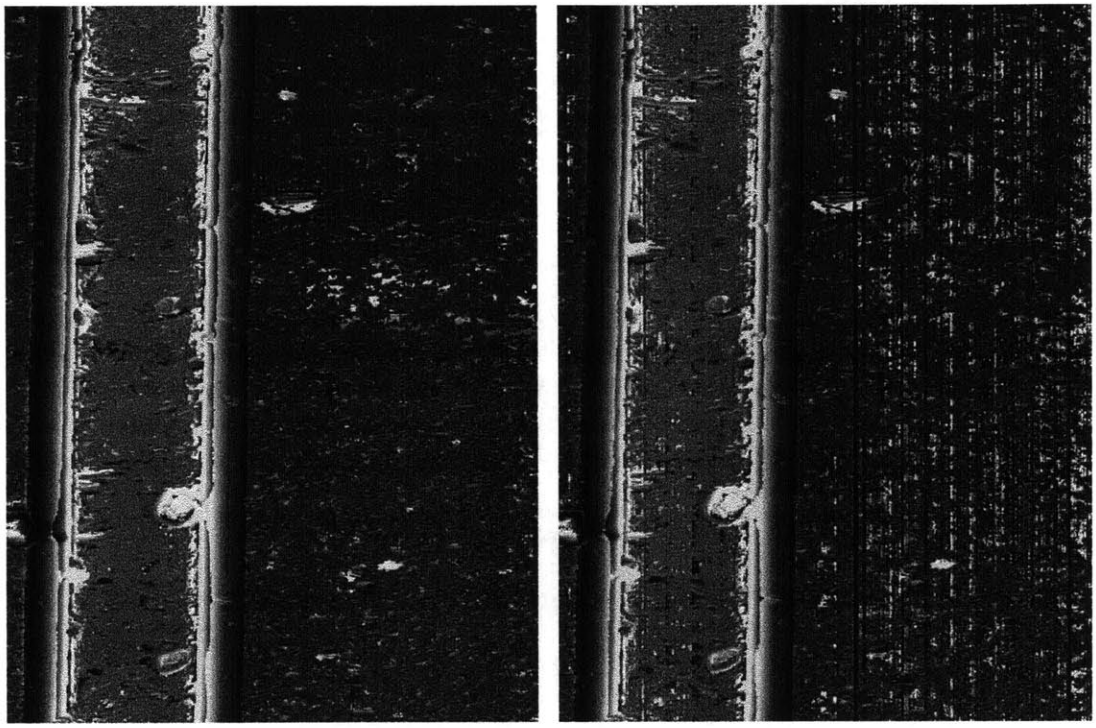

Figure 8-12: Effect of Dead Pixel and Pixel Sensitivity Corrections via Image Processing. This figure shows the effect on the output topography by using the image processing algorithms described in section 8.6.3. The topography on the left has been enhanced while the topography on the right operates on the original data taken by the camera.

Year	Cost/GFLOP	Technology
1961	$8.3 trillion	17 million IBM 1620 units
1984	$33 million	Cray X-MP
1997	$42,000	2 Beowulf Clusters
2000	$1,300	Bunyip Beowulf cluster
2000	$836	KLAT2
2003	$100	KASY0
2007	$52	Microwolf
2011	$1.80	HPU4Science
2012	$0.73	Quad AMD7970 GHz System

Table 8.2: This table shows the cost of processors per GFLOP adjusted for inflation in 2012 dollars as a function of time.

required to process the data inline can be calculated and then compared against commercial processors to get an idea of the expected cost and feasibility.

The processing power of computers has drastically improved over the past fifty years in accordance with Moore's law. This improvement is coupled with an impressive reduction in cost making high powered computer processors accessible to everyday applications. This progression is witnessed in Table 8.2 which tracks the cost per gigaFLOP (or GFLOP) through the past five decades in 2012 inflation adjusted dollars.

With a good estimate of computing power cost in place, the amount of computing power required to process the data in real time is now estimated to assess the feasibility of the project. The algorithm used to process the raw data into the final topography is broken down into discrete mathematical operations. For each captured pixel the processor must compute the variance of a P x P matrix. The mathematical operations required to compute this value are summarized below. The number of FLOPS tabulated represent an inefficient method of calculating variance making this estimate the upper boundary of FLOPS required.

Find the average value of a P x P matrix: P^2 Additions, 1 Division

Subtract average value from every entry: P^2 Subtractions
Take the absolute value of each entry: P^2 Comparisons
Add the remaining values together: P^2 Additions

It is found that computing the variance requires $4P^2 + 1$ FLOPS per pixel where P is the length of the square matrix used in the variance calculation. Given a camera with a M x N pixel array that takes f frames per second, the processor must compute $M \cdot N \cdot f \cdot (4P^2 + 1)$ FLOPS per second for the variance calculation.

Once this calculation is complete the algorithm then searches each column of data for the greatest variance value. The number of required computations is tabulated using the same parameterized values: The camera will collect M topographical data points points per frame. Each data point must find the largest value out of N calculated variances. To complete this operation the processor must compute $M \cdot N$ computations per frame. Adding this to the variance calculation it is found that a camera with an M x N pixel array taking f frames per second on a P x P variance matrix must compute $M \cdot N \cdot f \cdot (4P^2 + 2)$ FLOPS per second to process the raw data into an output topography.

Lastly the values based on the physical hardware are input into this estimation to find the processing power required to compute the data in real time. The v1210 Phantom camera is capable of taking 640 X 480 pixel images at 45,700 frames per second. Our tests have found a 5 x 5 matrix is optimal for image processing. Given these numbers it is calculated that a 1.4 terraFLOP processor is required to churn the raw data into the output topography. Based upon the analysis presented in this section, a 1.4tFLOP processor is not only available but relatively low cost of under $1,000. This processing power is sold commercially through a variety of vendors that sell high performance graphics cards. For example, AMDs Radeon HD 7970 can compute 4.3tFLOPS at single precision (8 bit) or 1.01 tFLOPS at double precision (16 bit) computing for at a cost of $560.

Once the topography of the sample has been calculated, further computations can

be made to detect defects and measure parameters of the physical channels. To detect for defects the computer will subtract the measured topography against the master copy. Afterward, a thresholding operation on each pixel can be used to isolate the defective region. To preform this operation the processor would have to compute $2 \cdot M \cdot f$ FLOPS for each output topography data point would require two operations. Substituting in the hardware based numbers referenced prior it is found that this postprocessing would require an additional 58megaFLOPS, or an additional 0.004% more calculations than had previously been computed. While other postprocessing computations would be more complex than this defect detection, it is safe to say that their computation could easily be handled by the processor already employed to crank the raw data into the object's topography.

Chapter 9

Results

This chapter presents and analyzes the results acquired from the high speed 3D profilometer. The results first focus on textured samples such as micromachined aluminum and later move on to transparent products created either by hot embossing or injection molding. A comprehensive study is conducted comparing the performance and output of the profilometer against white light interferometers, laser scanning microscopes, and structured light profilometers. Lastly, the results from the high speed 3D profilometer are used to characterize a manufacturing process demonstrating automatic defect detection, repeatability analysis, and run charts that can be used in process control.

9.1 Bird's Eye vs Axonometric Projections

The color coded topographical maps generated by our instrument can be confusing to the untrained eye. While most instruments project a bird's eye or top down view of the measured part, the high speed 3D profilometer uses instead an "axonometric" projection. An axonometric projection shows an image of an object as viewed from a skewed direction in order to reveal faces that were otherwise obscured when viewed in a bird's eye 2D projection. The three main types of axonometric projection are isometric, dimetric, and trimetric projections. Figure 9-1

demonstrates the difference between bird's eye and axonometric projections by using images of Boston's iconic state house downloaded from Google maps. The bottom axonometric image reveals the front face of the edifice which is otherwise hidden in the top bird's eye view perspective. This view can be used to gather additional information such as the number of stories in the state house. The user can intuitively understand the axonometric view from the visual cues such as windows and columns present in the image. Whereas the parts measured by our instrument do not contain such visual cues, it is not intuitively obvious from which projection they are being viewed. The first two objects reviewed in the results section are solid modeled and depicted from various angles such that the reader can understand the geometry of the part and the axonometric angle in which it is viewed by our instrument.

9.2 Aluminum Micromachined Parts

The first topological maps measured by the high speed 3D profilometer were conducted on micromachined aluminum parts. Many of the results from measuring the aluminum parts have already been presented in Chapter 5 while explaining the fundamental optomechanics that drive the measurement. This section presents again the topological maps and extended depth of field imagery but also supplements with cross sectional line scans, 3D renditions from multiple perspectives, and isometric viewing angles that show the strengths and weaknesses of the instrument. The section begins by showing a 3D modeled rendition of the part along with its dimensions in Figure 9-2 to visually explain the projection of the part in our results.

The next image presented in this section shows the topographic map and extended depth of focus image captured of the aluminum micromachined part in Figure 9-3. The topographic maps can instead be presented in an isometric view as to demonstrate more intuitively the shape of the measured object. In Figure 9-4 the data in Figure 9-3 has been reshaped into a three axis projection using the darkness

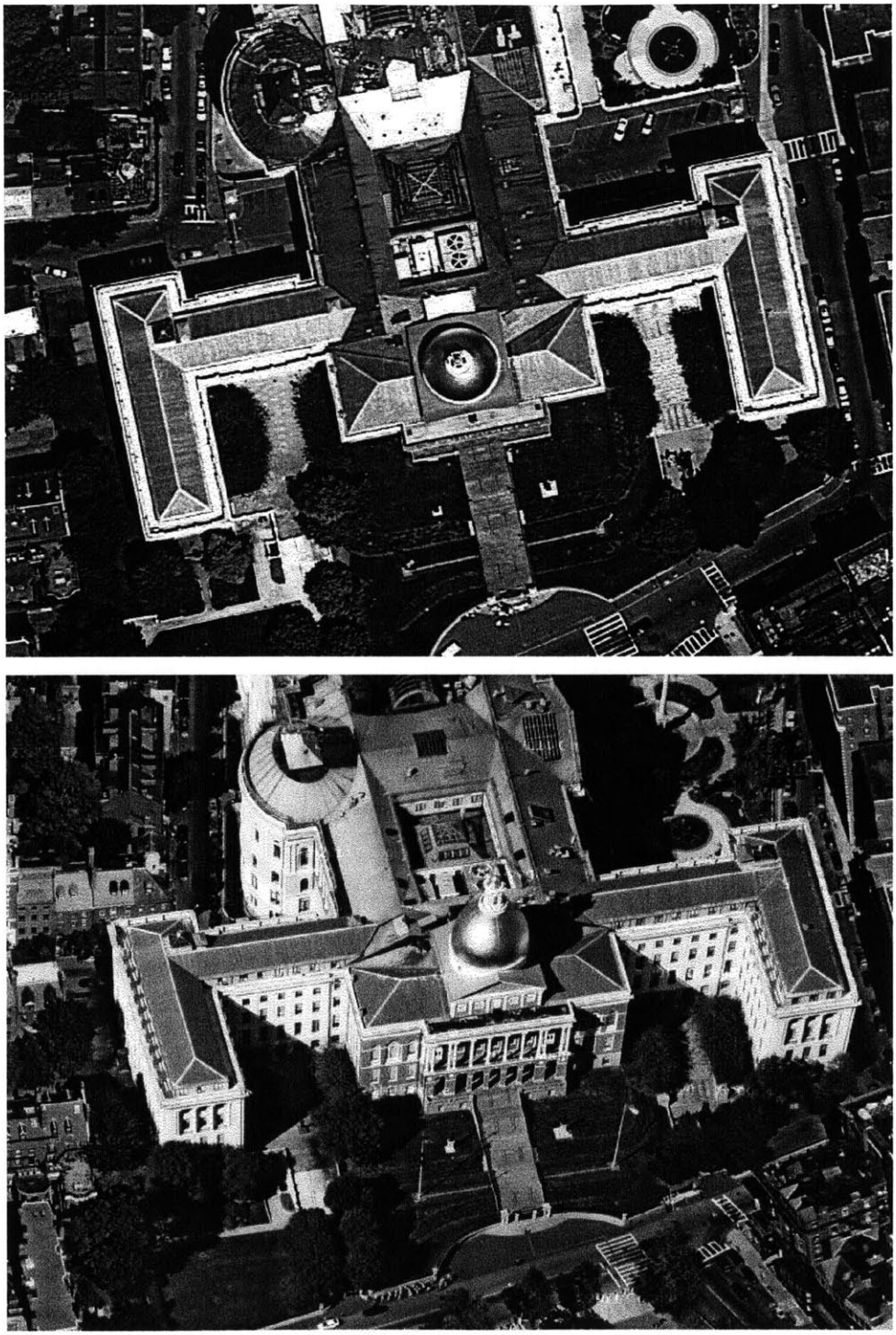

Figure 9-1: Demonstration of Axonometric Versus Bird's Eye View Projection. This figure's top and bottom images of the state house downloaded from Google Maps show the difference between bird's eye and axonometric projections respectively. This distinction is used later to describe how our instrument images the subject.

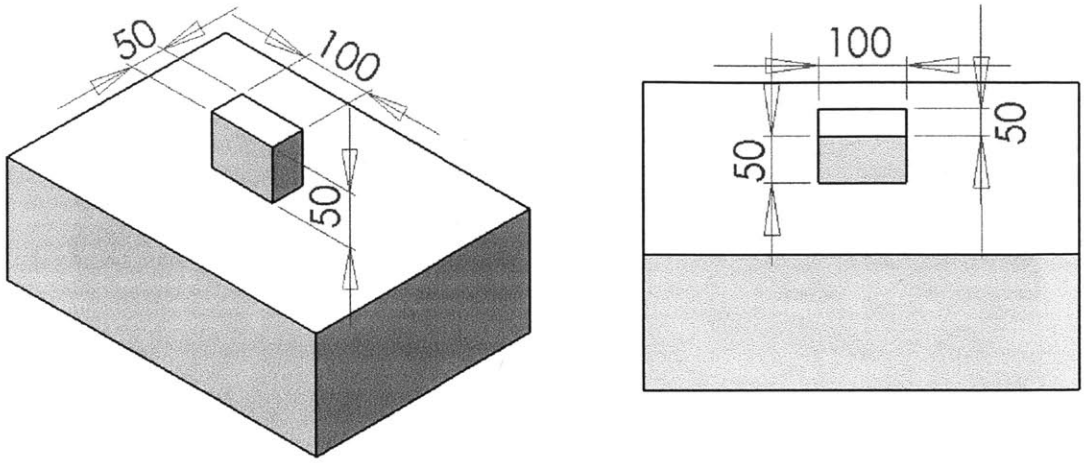

Figure 9-2: Solid Model of the Imaged Part. The figure on the left shows an isometric view of the sample part that was measured. The figure on the right shows the same part from the angle it was captured. Both projections also show the dimensions of the part in units of microns.

of the pixel to represent height. In this view it becomes more clear which regions of the measurement are on vertical surfaces, horizontal surfaces, or eclipsed whereby no information can be seen from the vantage point of the camera. Two additional scans from opposite directions were conducted to recover the geometry of these eclipsed regions. The data from these scans are colored green and blue to distinguish the angle in which they were taken and summed together in Figure 9-5. This figure demonstrates that it is possible for the high speed profilometer to measure all free surfaces of an object whether they be vertical or horizontal. This measurement strategy can be used to fully characterize the geometry of features with an aspect ratio less than 1:1. Figure 9-6 shows a 2D singular slice of information taken from Figure 9-5. As seen in the figure, no one scan can measure the complete contour of the extrusion for its view becomes eclipsed by the part: the red scan captures the left vertical sidewall, the green scan captures the right vertical side wall, and the blue scan is unable to capture either.

The aluminum micromachined part was also rotated 45° and measured by our instrument. In this configuration the light sources reflecting off the sample were not

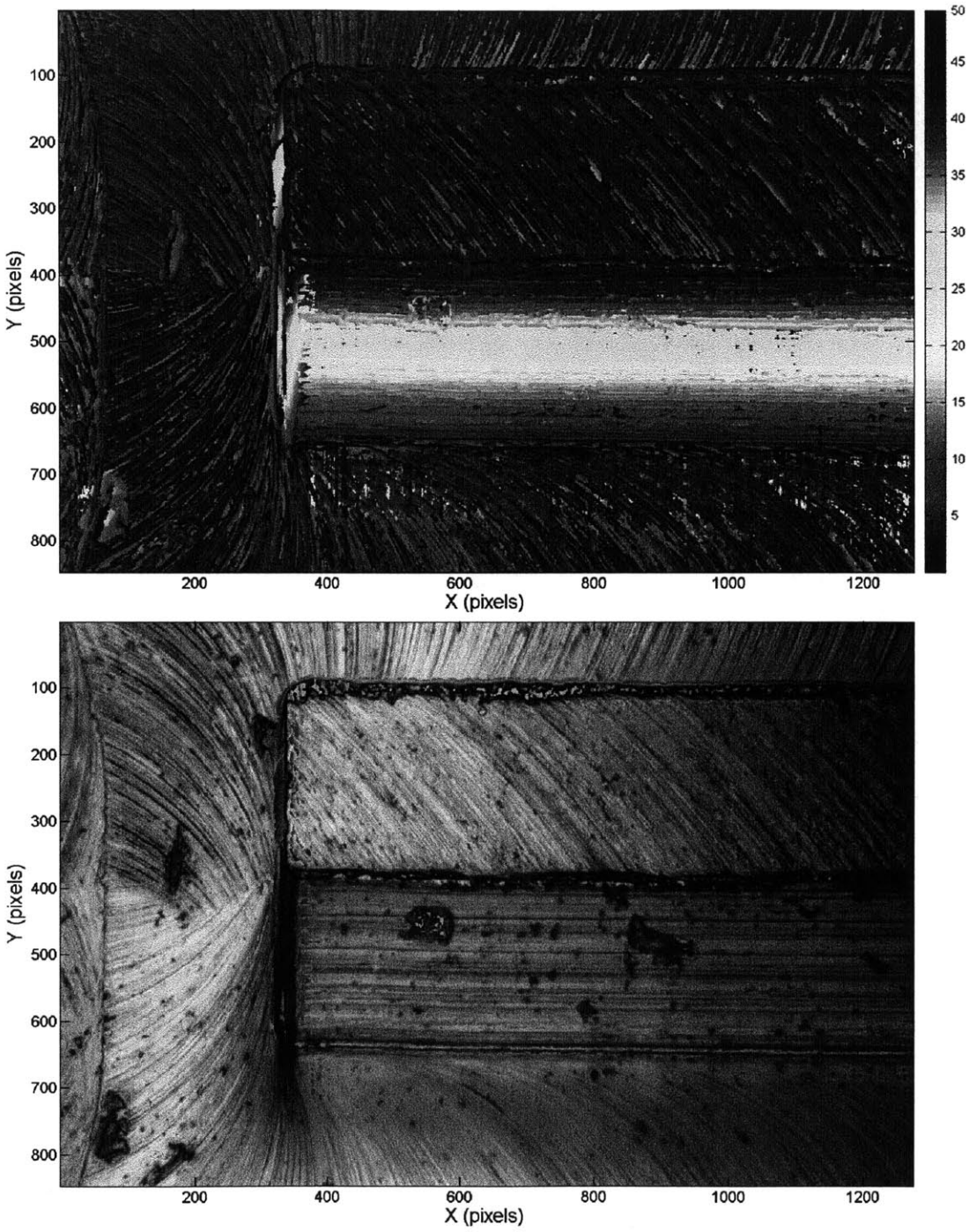

Figure 9-3: Demonstration of Both Topography and Extended Depth of Field Imagery. This figure shows both the topographic map of the aluminum micromachined part and its extended depth of field image. The colorbar to the right of the top image, shown in units of microns, relates the color to height.

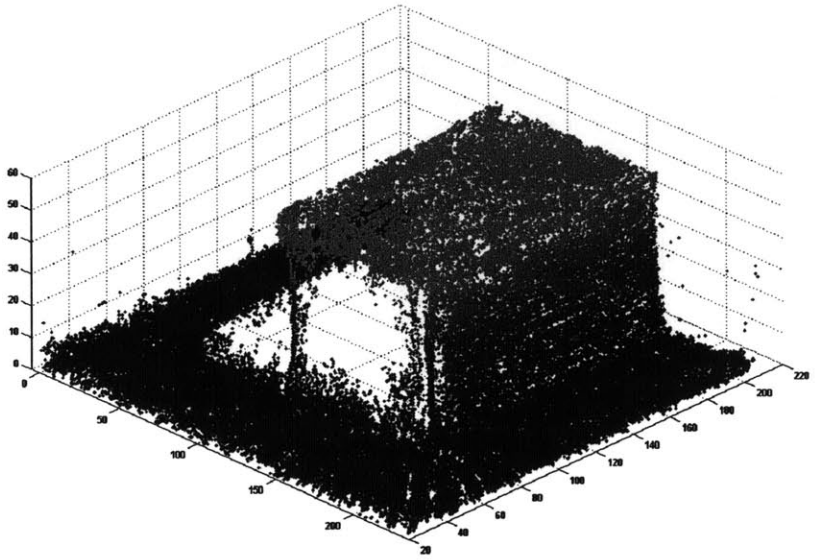

Figure 9-4: 3D Projection of Sampled Data. This 3D image presents the data in Figure 9-3 on 3D axis. The darkness of each data point on this image is proportional to its height.

fully directed back into the camera. The resulting low light conditions created blotchy and somewhat inaccurate measurement of these locations as seen in Figure 9-7. It is postulated that different lighting conditions could have addressed this problem through the use of omnidirectional lighting. Such a setup would have required either multiple point sources of light or a diffuser to shower the part with light from multiple angles. Any solution used to address this problem must ensure that the light flux from the additional angles has the same intensity as the on axis lighting employed in the previous sections. This constraint becomes more and more difficult to satisfy as the frame rate of the camera increases thereby shortening the maximum possible exposure time.

9.3 Plastic Demolded Parts

This section displays the results measured on a transparent plastic piece created by Matt Dirckx in his Ph.D. thesis at MIT. [39] Dr. Dirckx studied the effects of demolding plastic from its metal mold in a hot embossing process. The aluminum

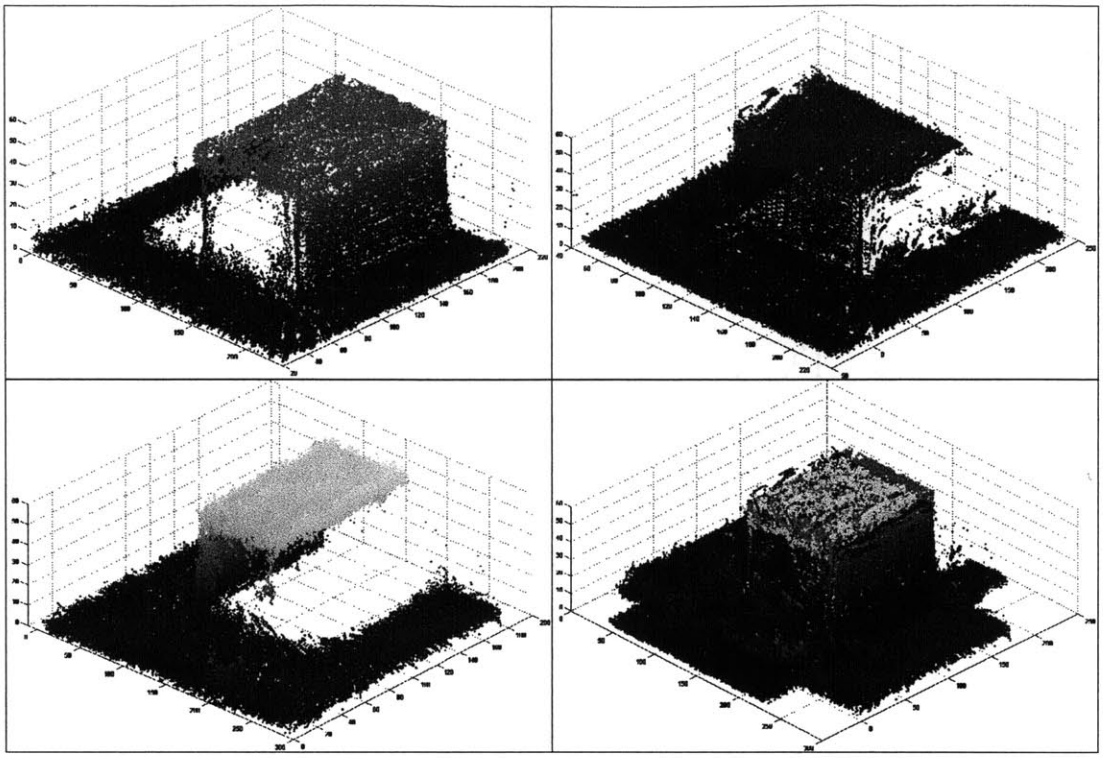

Figure 9-5: Using Different Angles to Capture Data on All Free Surfaces. The green, red, and blue data represent scans taken from three different angles. The three scans can be combined to measure all the free surfaces of the aluminum extrusion.

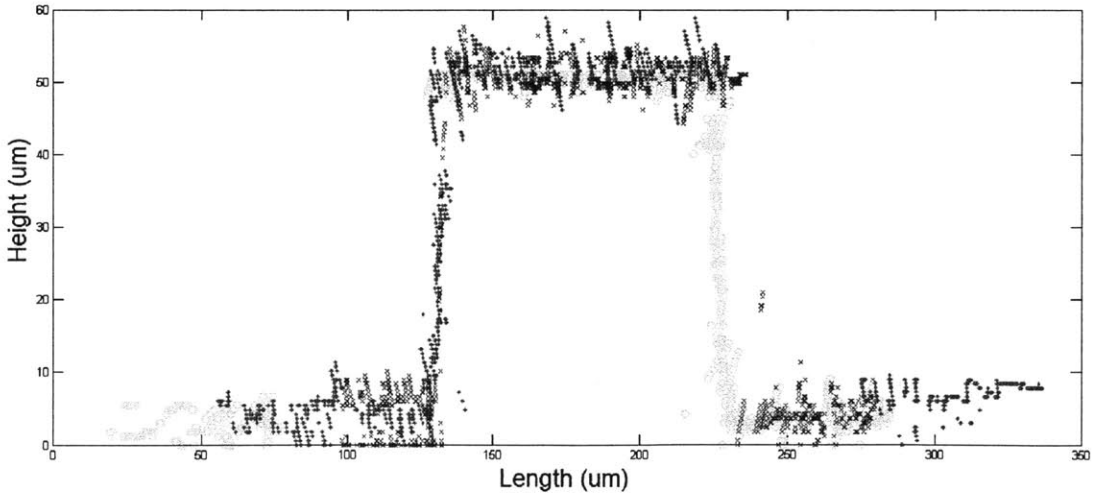

Figure 9-6: Cross Sectional Data Slice to Show Vertical Resolution. A 2D slice of the 3D data from Figure 9-5 is presented. Each vertical wall can only be viewed by one viewing angle as shown with the red and green data.

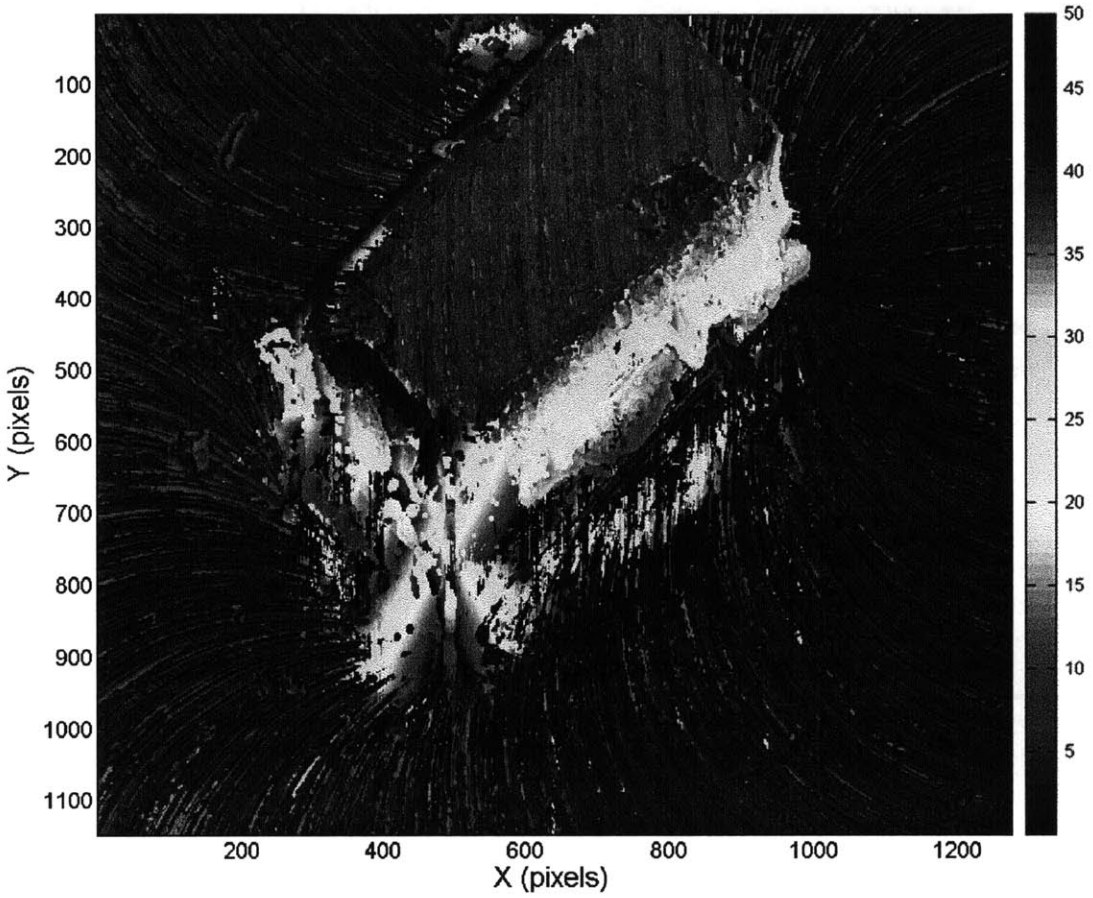

Figure 9-7: Negative Effect of Shadows on Topographical Accuracy Seen By an Askew Image. This figure shows the micromachined part imaged at an askew angle with respect to the camera. It is clear from the image that the shadows cast upon the vertical sidewalls can present trouble for the image processing algorithms.

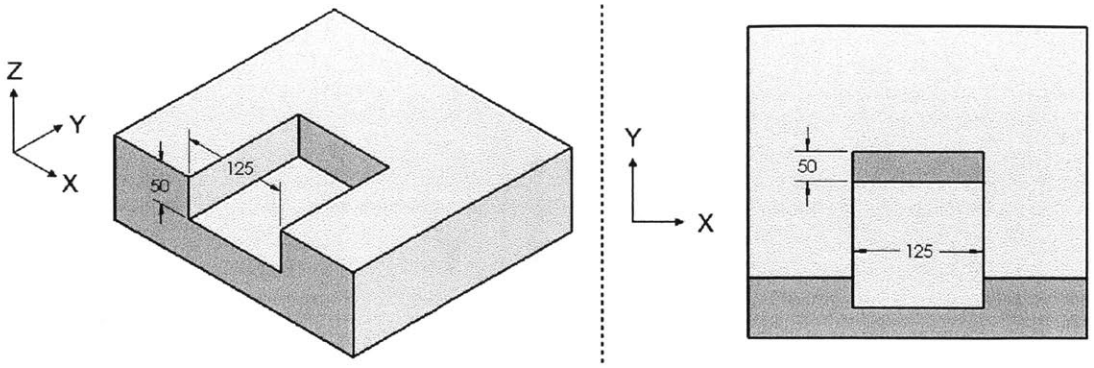

Figure 9-8: Solid Model of Depression in Transparent Part. This solid model shows the dimensions and geometry of the plastic demolded part measured in this section. The diagram is measured in units of microns.

micromachined parts measured in the last section were used as a mold to create a plastic negative. This plastic negative picked up many of the features in the aluminum part resulting in a surface rich in texture. Our instrument is able to use these textured surfaces to create an accurate topographical map via the depth from focus method. A 3D modeled rendition of the part along with its dimensions in units of microns is presented in Figure 9-8.

Figure 9-9 displays four height slices and the corresponding focus detection calculated from the standard deviation algorithm. An extended depth of field image is formulated by selecting the intensity values for each pixel at the measured height. This effectively allows the instrument to expand depth of field from one micron to 130 microns as shown in Figure 9-10. Figure 9-11 shows the topographical map formed by the height finding algorithm. It is important to note that the portion of the scan exhibiting a gradient of color is measuring a vertical sidewall. This normally eclipsed section of data looks elongated as a result of the orientation of the sensor with respect to the camera.

An important part of the research is to validate the performance of our instrument by comparing it against other commercial instruments. Chapter 4 compared the inspection speed and lateral resolution of structured light profilometers and white

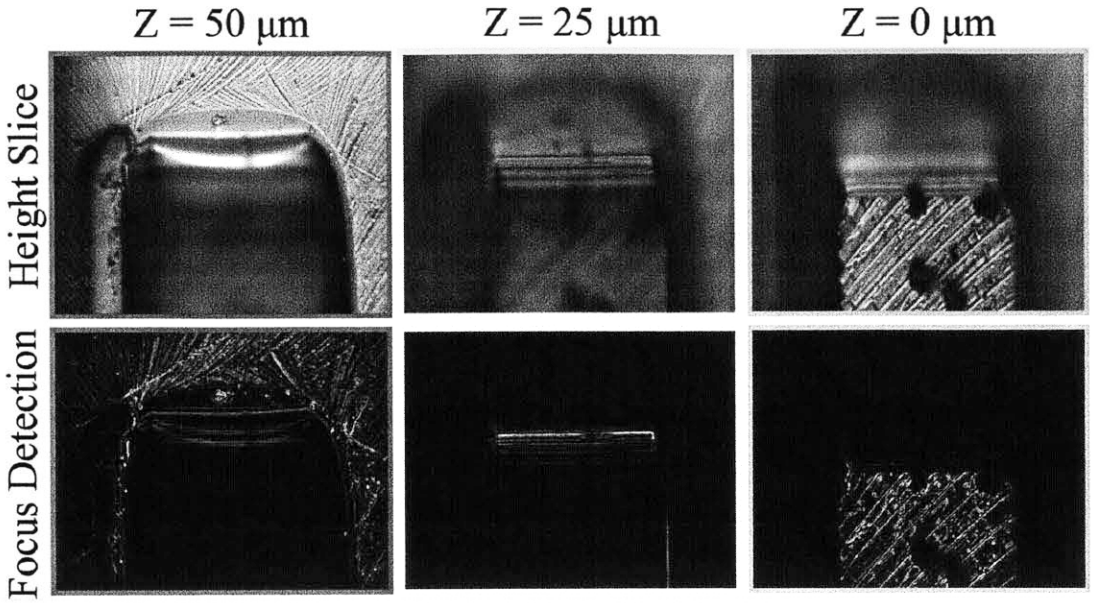

Figure 9-9: Combination of Height Slices and Focus Detection Algorithms. This figure displays three height slices taken from the top, middle, and bottom of the depression in the PMMA plastic. The result of the focus detection algorithm is also displayed for each slice on the bottom half of the image whereby dark portions represent blurry sections and light portions represent sections high in contrast.

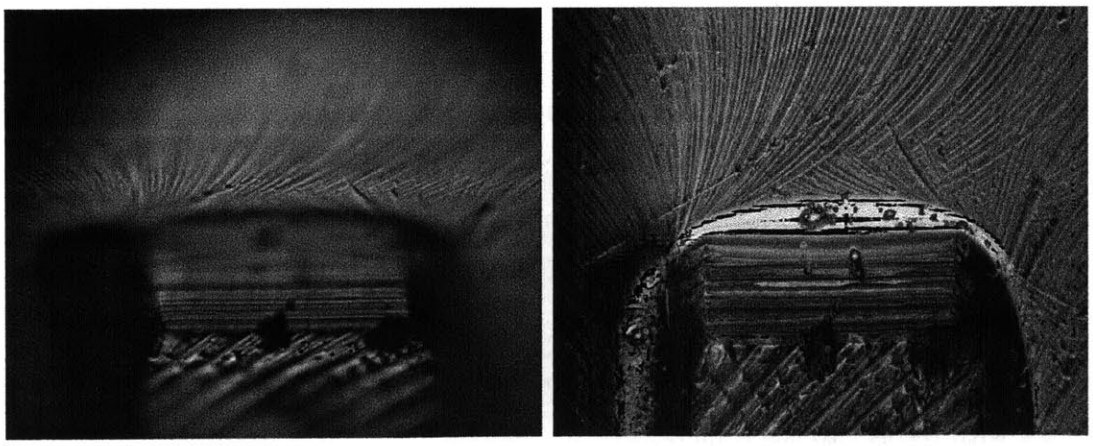

Figure 9-10: Extended Depth of Field Imagery Taken on the Transparent Part. A raw image frame taken from the high speed camera (left) and is compared against the extended depth of field image (right).

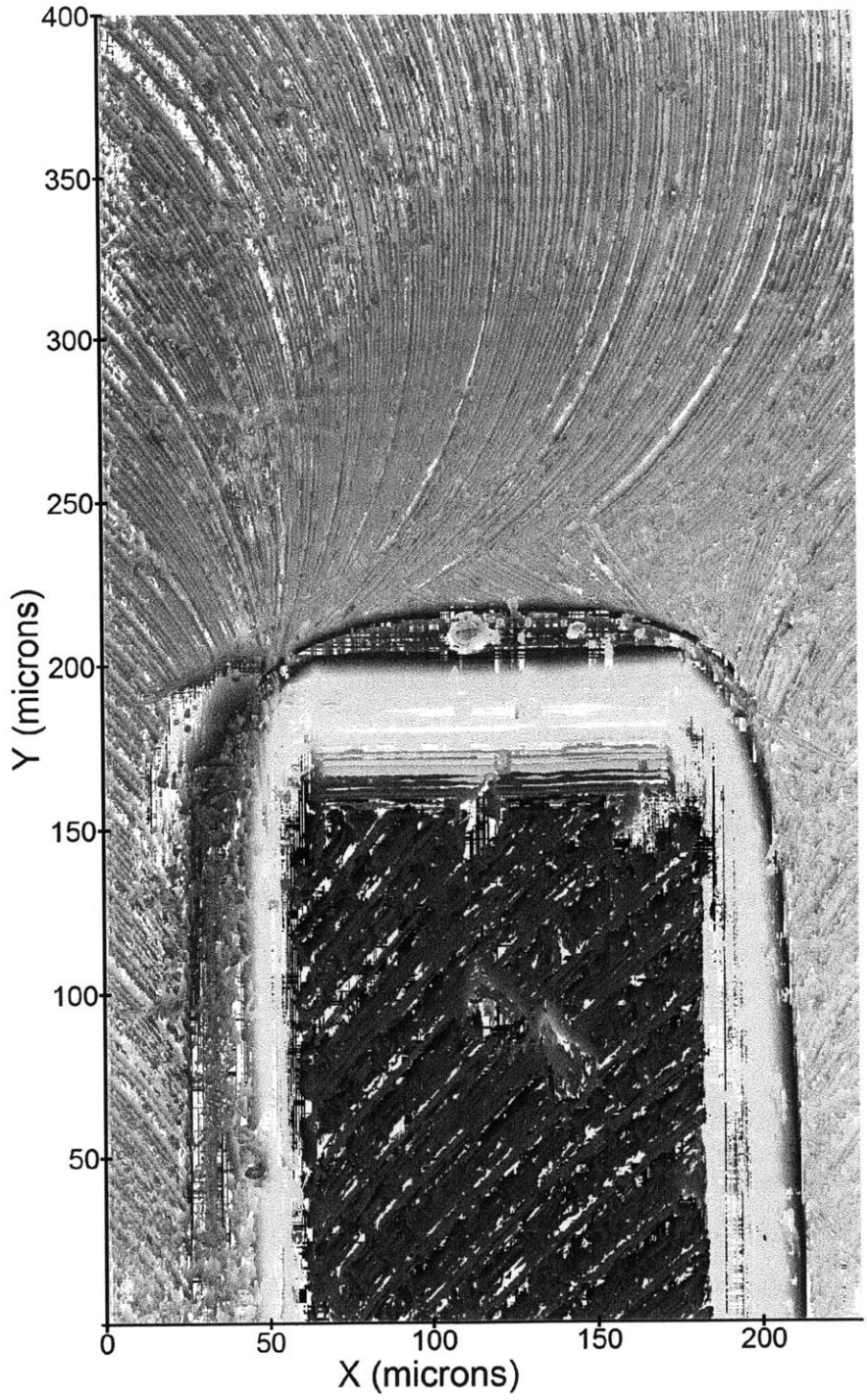

Figure 9-11: Large Topographical Measurement of the Transparent Part. This image shows the three dimensional profile of the rectangular depression. The white portions of the image represent areas where not enough information was collected to make an accurate measurement. In this image, the blue and red sections correspond to heights that are high and low respectively.

light interferometers against our high speed profilometer. Yet, there exist other parameters such as noise (vertical resolution) or completeness of a scan that are best addressed by looking at the actual scans themselves. One feature on the same plastic demolded part was measured by a Zygo white light interferometer, a Keyence color laser scanner, and our instrument to carry out this comparison. The top of the line Koh Young structured light profilometer proved unable to measure transparent objects and was thus left out of this study. The topographical scans produced by the remaining instruments are presented in Figure 9-12. It is important to note the colorbar has been changed from the previous section such that yellow is high, purple is low, and black means that not enough data was collected to output a meaningful result. It is shown from this apples to apples comparison that the white light interferometer looses much more data comparatively than the other two instruments but has significantly less noise in its measurement. A 2D line scan of this data is shown in Figure 9-13 to demonstrate the noise of each measurement. Again it is shown that the high speed profilometer is the only instrument capable of measuring vertical sidewalls. The apparent burr at the top of the line scan from the high speed profilometer data can be attributed to low contrast texture and therefore inaccurate results. The top and sides of the channel have a tendency to underfill and leave behind a very smooth surface that is difficult to measure with our instrument.

The main characteristics of each instrument are presented in Table 9.1. Note that these instruments are not being rated on lateral resolution but instead lateral pixel spacing. The lateral resolution depends solely on the numerical aperture of the objective and mean wavelength of incident light used during the measurement, both quantities of which were not recorded on the two commercial instruments for these specific scans. The vertical resolution was defined by taking the standard deviation of a localized value of heights otherwise assumed to be flat. The white light interferometer shows the least noisy data and is likely to be measuring true surface roughness. The inspection speed presented is not the maximum inspection speed achievable but simply the inspection speed that was achieved while conducting these

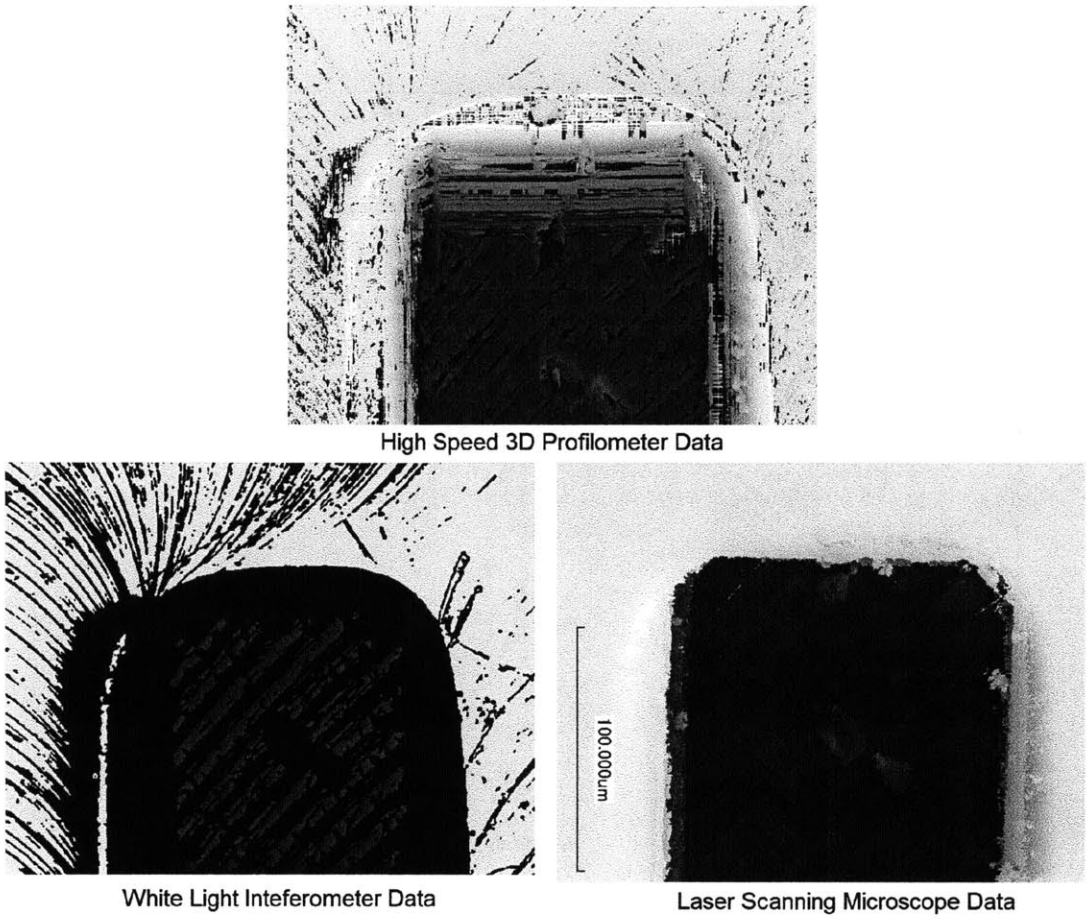

Figure 9-12: Apples to Apples Topography Comparison Against Commercial Profilometers. This figure presents three topographical scans taken of the same feature on the same part by a white light interferometer, color laser scanner, and our instrument.

scans.

9.4 Hot Embossed μFac Parts

The high speed 3D profilometer was originally built in order to provide inspectional services to a new manufacturing initiative called "Microfactory" or "μFac" for short. Each polymer hot embossed μFac part was to be measured by the instrument in order to employ defect detection and process control. This section presents the

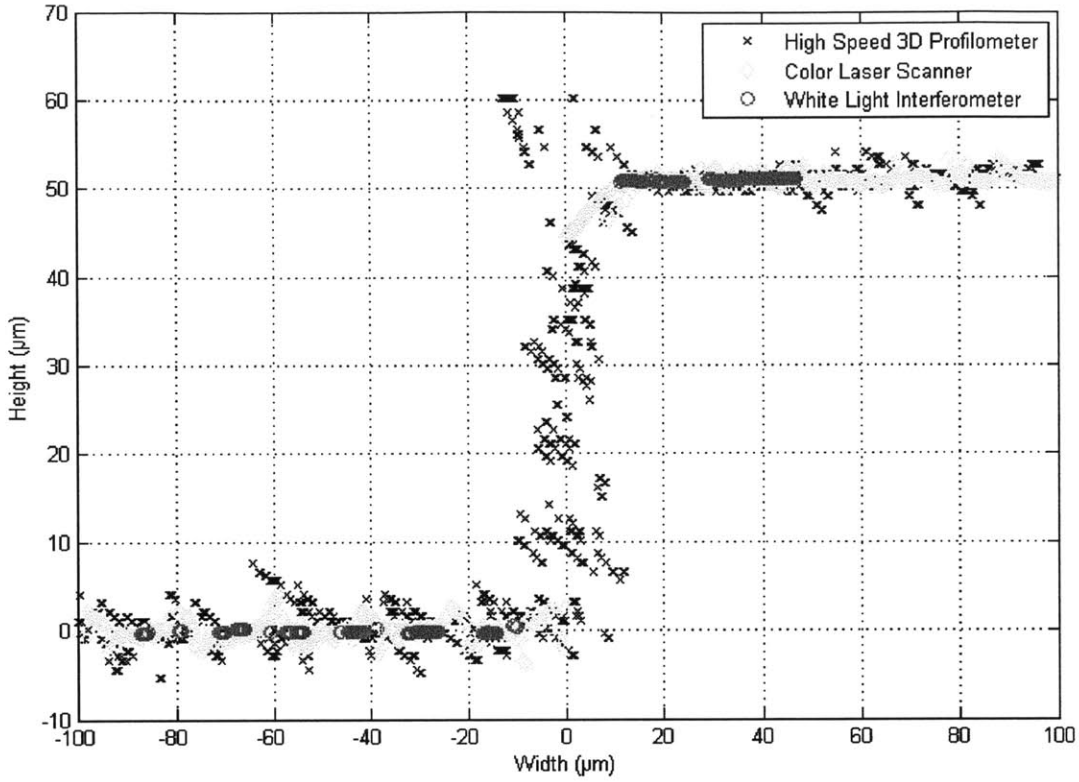

Figure 9-13: 2D Slice of All Instruments Demonstrating Vertical Resolution. A cross sectional view of the data was taken from each of the three instruments. The high speed profilometer is the sole instrument with the ability to measure the vertical sidewall of the channel.

Instrument	**Lateral Spacing (nm)**	**Vertical Resolution (nm)**	**Inspection Speed (voxels/sec)**
High Speed Profilometer	180	987	640,000
White Light Interferometer	285	41	11,478
Color Laser Scanner	274	420	4,195

Table 9.1: This table summarizes the performance for the three metrology instruments used to measure a single part.

results of measuring features on the μFac part with the high speed 3D profilometer.

The hot embossing process used a stamp or mold made from a bulk metallic glass or amorphous metal. The metal becomes rapidly cooled over an amount of time too short for the crystals to align themselves along grain boundaries. The resulting metal is tougher, less brittle, and more resistant to wear or corrosion than molten metals cooled at a slower pace. As a result of this process, the metal stamp used to hot emboss the polymer is very smooth and leaves very little surface texture on the polymer part. The only surface texture seen is thought to be the result of trapped pockets of air that form recesses on the hot embossed polymer parts. This surface geometry proved to be a difficult object to measure with our instrument for the process provided very little texture on the transparent body of the μFac part.

The topographical maps presented in this section demonstrate the main weakness of the high speed 3D profilometer. The scans presented represent the best scans taken of the μFac part which are clouded with artifacts leading to confusion. The extended depth of field imagery has been included with every scan for commonly it can give the user additional information to make sense of the topographical scan. First, Figure 9-14 shows a side by side topographical map and in focus image of a channel as well as a triangular depression used to signify the direction of the serpentine channel. Secondly, Figure 9-15 displays a field of lines on the polymer part spaced at 10 microns apart. It is clear from the extended depth of focus image that many of the lines are not fully formed. Lastly, shows a simple channel that is fifty microns wide and forty microns deep is shown in Figure 9-16. This scan prominently displays a rainbow artifact appears signifying an area of poor information that our algorithm has falsely determined to be the surface.

9.5 Injection Molded μFac Parts

A second set of μFac parts were made through an injection molding process that proved much easier to measure with our instrument. These plastic parts were made

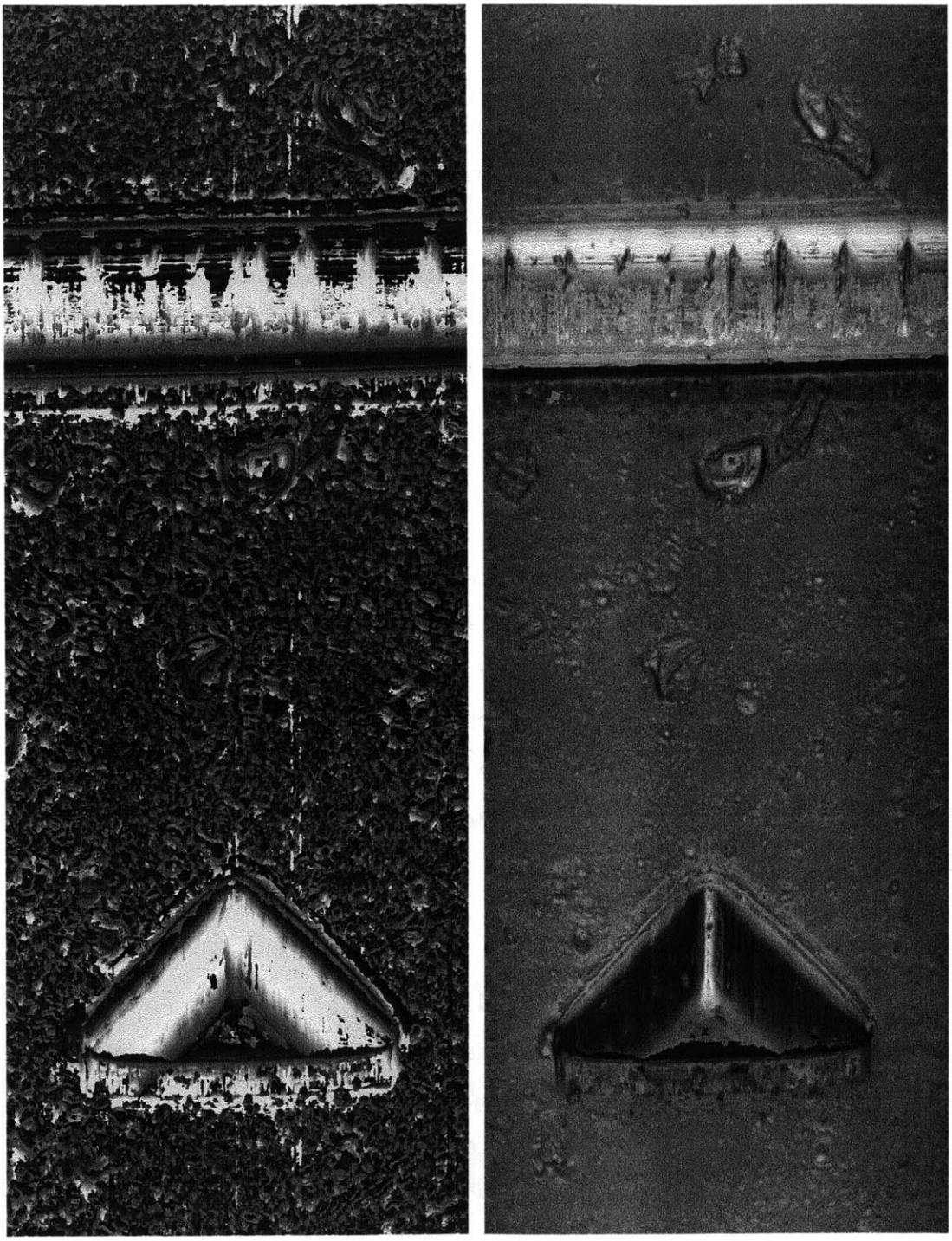

Figure 9-14: Measurements Taken on the μFac Part. This side by side image shows the topographical map and extended depth of focus imagery generated by our algorithm of two features on the μFac part. The errors in the vertical sidewall demonstrate our instrument's difficulty in measuring parts with low contrast.

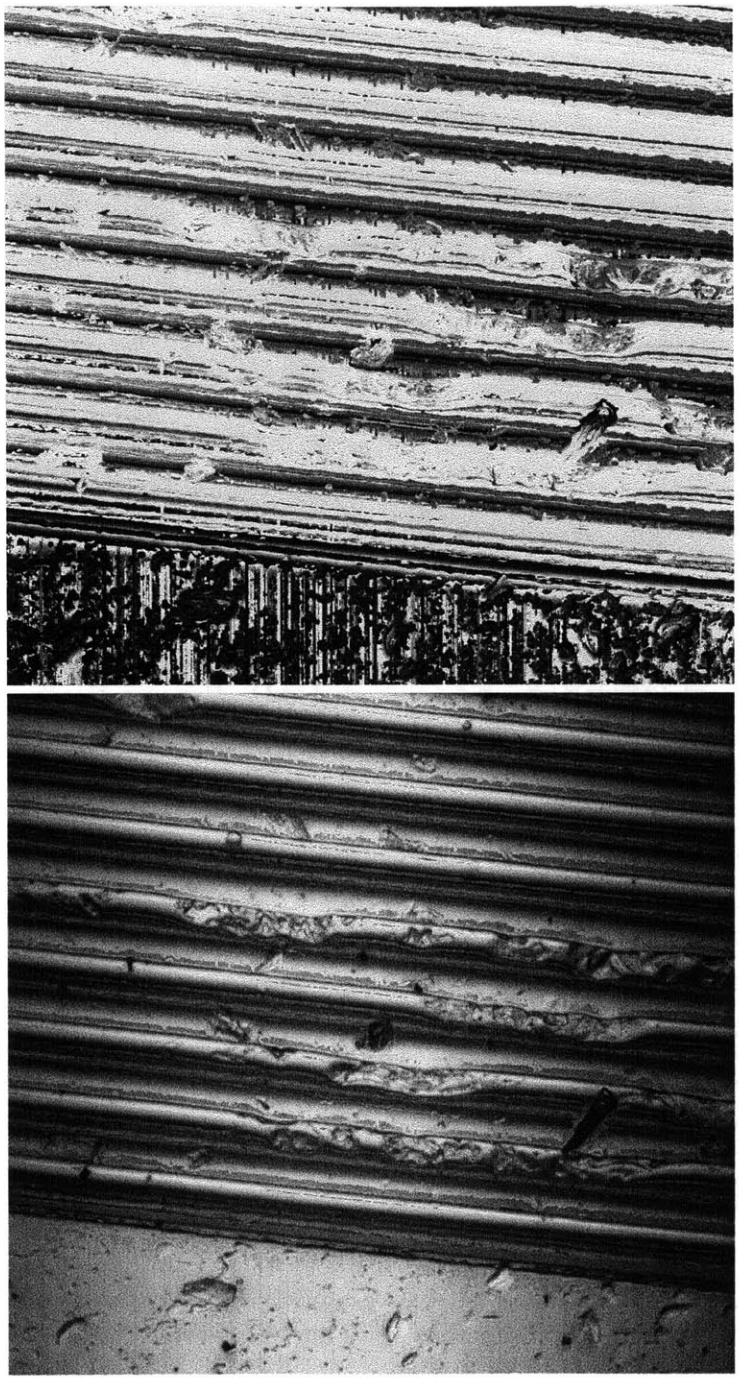

Figure 9-15: Line Fields on the μFac Part Imaged by the High Speed Profilometer. These two images show the height map and extended depth of field imagery on a 10 micron line field on the μFac part.

Figure 9-16: Zoomed in Image of a μFac Channel. This third scan shows a channel on the μFac part measuring 50 microns wide and 40 microns deep.

in the LMP laboratory by Post Doctoral student Fu Gang from the Singaporean university SIMTech. More details regarding the manufacture of these parts can be found in Fu Gang's paper. [40] [41] Unfortunately the mass of parts left behind by Fu Gang were not labeled in the order in which they were made eliminating the possibility for a run chart that can observe how the injection molding process changes with time. Yet, a random sampling of these parts can tell much about the process itself such as the repeatability of the parts and probability of defects. This section lays out the results collected by our instrument and the subsequent conclusions and measurements made of the process.

Before presenting the results from our instrument the basic geometry of the part is reviewed. The part was sized to emulate a microscope slide as its dimensions are 75mm wide, 25mm long, and 1.5mm deep. All the features of the μFac part were stationed in the center 25mm x 25mm portion of the part as shown in Figure 9-17. Figure 9-18 has been created to outline the important features on the injection molded μFac part measured by the profilometer for they appear faintly in Figure 9-17. The topographical maps in this section will chiefly be concentrated on the Swiss flag feature and channel highlighted Figure 9-18's red boxes. Both Swiss flag and channel features are designed to be 40 microns deep.

9.5.1 Comparison against White Light Interferometer

The topography of the Swiss flag and channel features were measured both by the high speed 3D profilometer and a white light interferometer. The white light interferometer measurement was made with both a 20X and 50X microscope objective creating two different plots with 1.5 and 0.6 micron lateral resolution respectively. These plots of the Swiss flag are compared against the topographic map captured by the high speed profilometer in Figures 9-19 and 9-20. The second figure shows a zoomed in view of the bottom leg of the Swiss flag. It is clear from these plots that the surface of the injection molded parts yields a much clearer

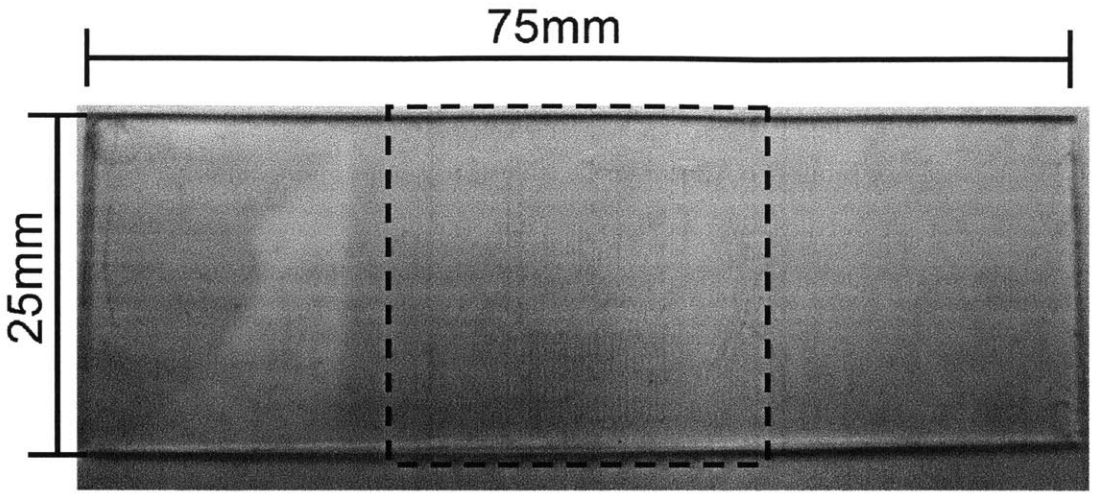

Figure 9-17: Size and Shape of the Injection Molded μFac Part. This photograph shows one injection molded μFac part made by Fu Gang with its dimensions overlaid. All the microfeatures exist within the black dotted box.

image than that of the hot embossed parts. As the colorbar shows, the blue regions are high, red regions are low, and the black regions represent areas with insufficient data to measure the surface. Again it is noted that the Zygo and high speed profilometer use bird's eye view and axonometric perspectives respectively.

The remainder of the measurements taken by our instrument focused on the channels located beneath the input and output ports. Figure 9-21 shows a measurement taken by our instrument compared to a measurement taken by the white light interferometer with the 50X objective. As there are no distinguishing marks on the channel measured by the Zygo, there is no certainty that both images were taken of the same area. The large blacked out area presented by the Zygo makes it very difficult to find these features inside the buried channel or to get a reasonable estimate of the channel width itself.

Overlaid on top of the high speed profilometer image are visual cues that help point out specific features in the scan. The two "areas of interest" point to two distinguishable, repeatable features that are found across all the manufactured parts and used later on in this section to track repeatability and warpage. The

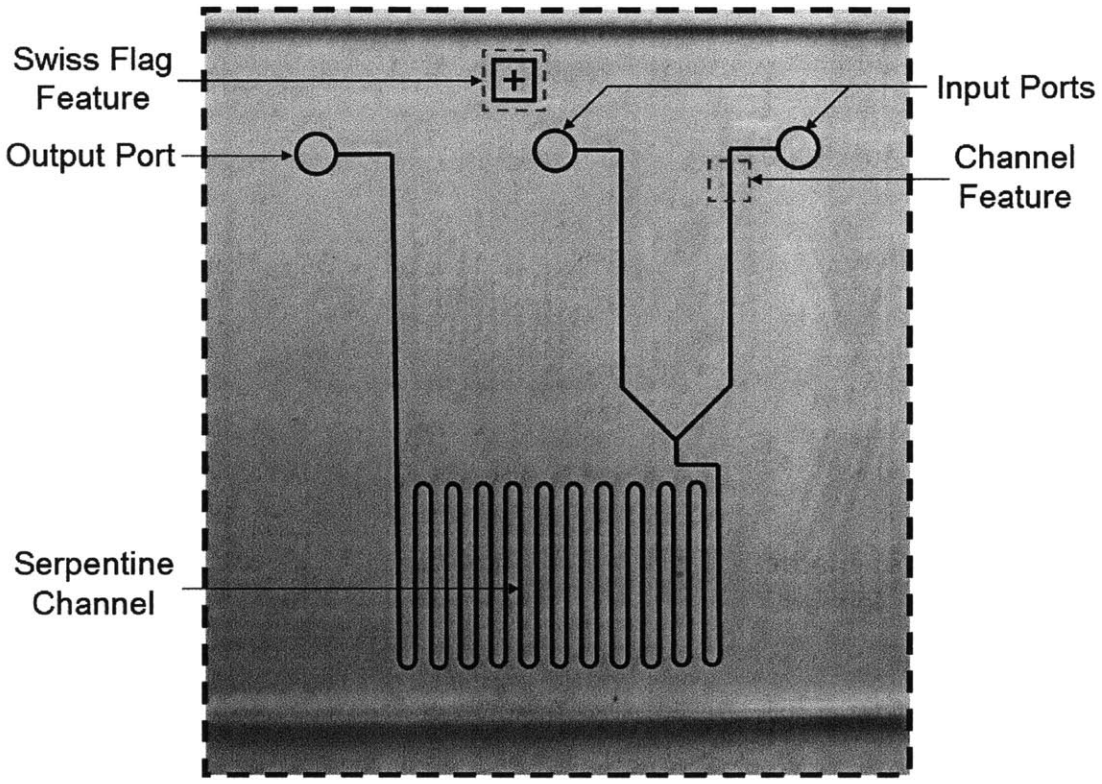

Figure 9-18: Zoomed in View of the Micro Features. The important features are outlined with black lines. The red boxes show the areas of interest that were measured by our instrument.

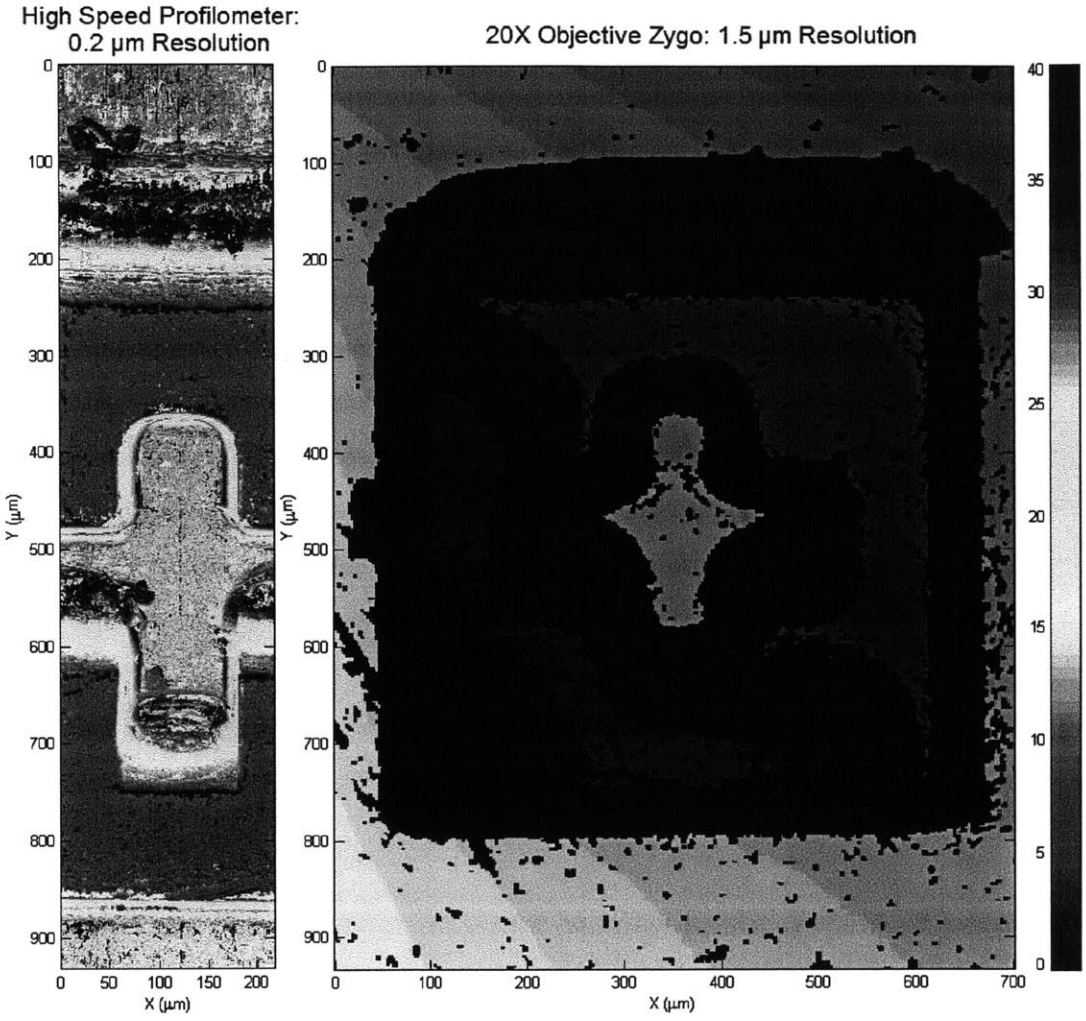

Figure 9-19: 1.5 micron Lateral Resolution Comparison. This figure compares scans taken of the Swiss Flag feature by the high speed profilometer and 20X magnification Zygo white light interferometer with lateral resolutions of 0.2 and 1.5 microns respectively.

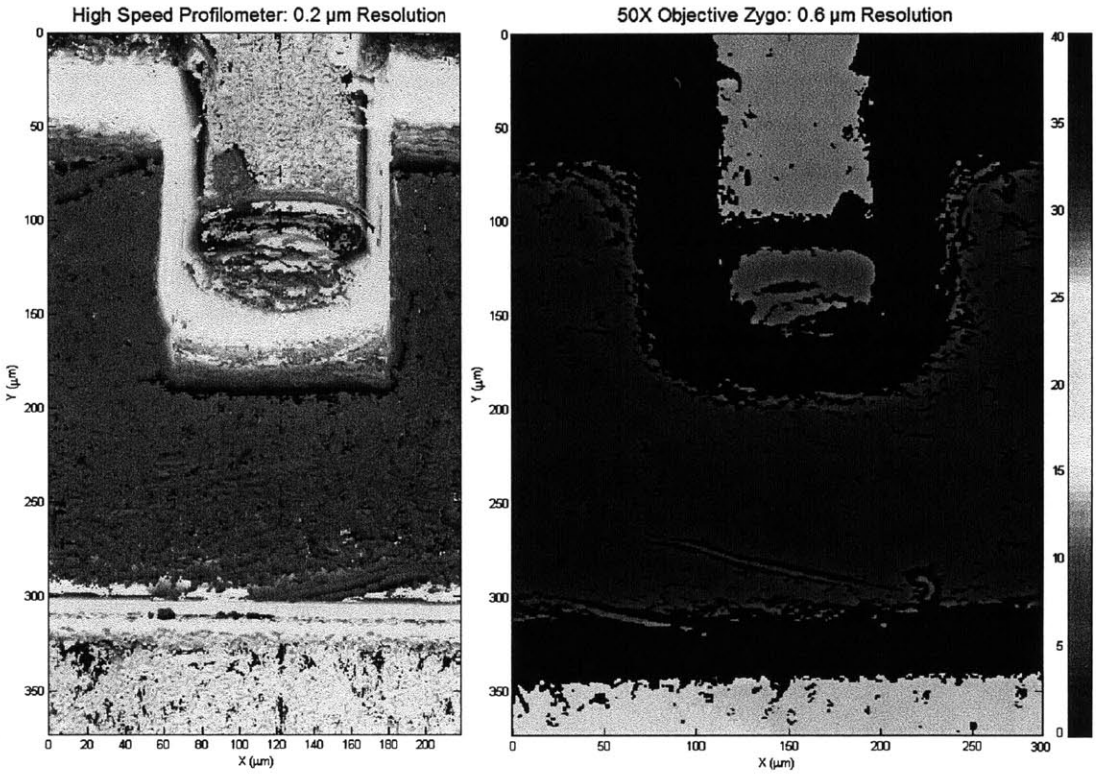

Figure 9-20: 600 nm Lateral Resolution Comparison. This zoomed in image of the lower leg of the Swiss flag also compares scans of the high speed profilometer against the 50X magnification white light interferometer with 0.2 and 0.6 micron resolution respectively.

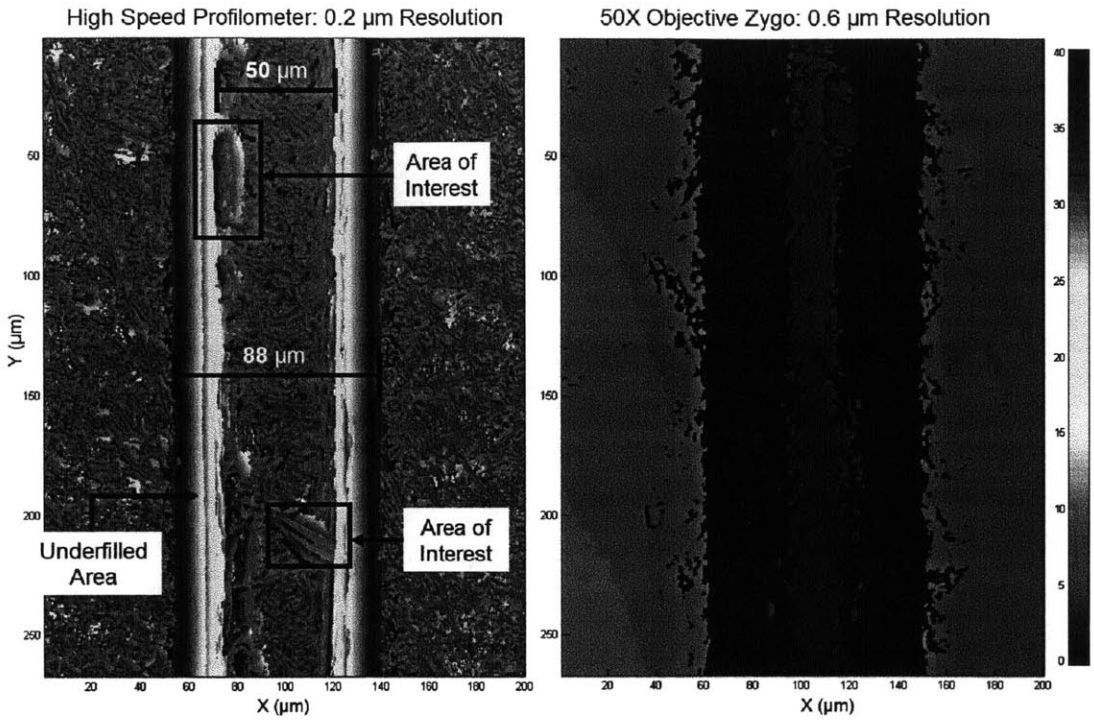

Figure 9-21: Measurement of a Channel on Both High Speed Profilometer and Zygo Instrumentation. This image of the microfluidic channel taken by both the high speed profilometer and Zygo white light interferometer showcases the difference between the two measurements' noise, lateral resolution, and completeness of scan. Overlaid on top of the left scan are visual cues to point out various measurements and areas of interest used later in this section.

"underfilled area" refers to the under formed portion of the channel where the liquid plastic did not have enough time or pressure to be pushed into the corner of the mold. This free surface solidifies with a very smooth texture making it difficult to be measured by our instrument. The measurements of the surface taken in this underfilled area are characteristically different than the rest of the scan and resemble the rainbow artifacts shown in previous scans. Despite the higher level of inaccuracy in the underfilled region, the topographic scan can still be used to measure its width as shown in Figure 9-21 by the 88 micron wide bar.

Figure 9-22 shows 2D slice of the 3D data presented in Figure 9-21 that offers more insight on the underfilled area. This area is highlighted in yellow. It is clear from

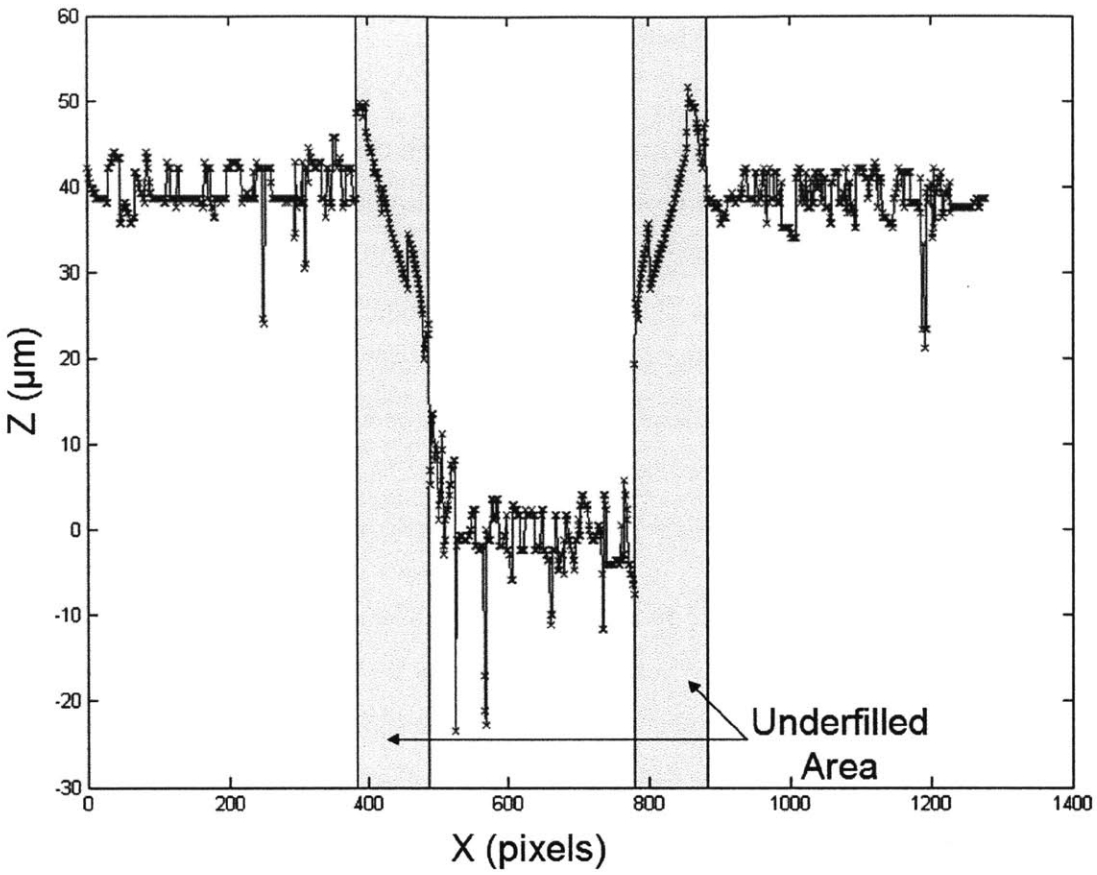

Figure 9-22: 2D cross section of Channel Data. This figure shows the difference in nature of the data inside and outside the underfilled region. The flat portions of the data look to be bimodal suggesting that an artifact in the code or images could be addressed to smooth out this profile.

this 2D slice that the character and nature of this data inside the yellow zone is different than the data outside: the data points are tightly packed together and sequentially follow one another instead of seemingly random three micron jumps. Although the slope and direction of the data points are commensurate with what is expected, the artifacts such as the burr on either side of the channel and the height measurement itself are very suspect. It is possible that future work can understand the shadows cast upon this underfilled region to shed some light on how these data points either reflect or misrepresent the ground truth.

9.5.2 Repeatability Analysis

The first test to characterize the injection molding process conducted by our instrument was to measure the positional repeatability of a single feature. The repeatability analysis measures the position of a single feature on each part with respect to a global origin set by the part's outer boundary. The outer boundary is held by a special fixture designed as a kinematic mount. Once inserted into the fixture, the X,Y location of a distinguishable feature present on all parts is measured. In this analysis tests how well the process can repeatedly produce parts to hold the same distance between its outer boundaries and a feature on the part.

A kinematic fixture was created in order to conduct the repeatability analysis. The fixtures used basic kinematic principles to apply exactly six constraints to the six degrees of freedom on any singular part. Figure 9-23 shows the fixture with overlaid visual cues to explain how it works. An injection molded part was to sit on the aluminum face thus constraining its Z, θ_x, and θ_y degrees of freedom. Two microscope slide springs are used to apply a preload force that ensures contact between the plastic part and aluminum plane. Three springs were used used to push the measured part into a corner defined by three dowel pins. The placement of these dowel pins is designed to constrain the remaining X, Y, and θ_z degrees of freedom.

There are three sources of repeatability error that have been identified: the repeatability of the measurement, fixture, and process. These three sources of error are added together when observing the change in position of a feature from part to part. Three experiments are conducted to individually quantify each source of error. First, repeatability of the measurement is assessed by repeatedly measuring a single part without removing it from the fixture. Second, the positional repeatability of the fixture is measured by inserting the same part in and out of the fixture between measurements. Lastly, the conglomerate repeatability of all three sources of error is assessed by measuring a series of parts from the same manufactured line. If the repeatability error significantly appreciates with each step in our process, the

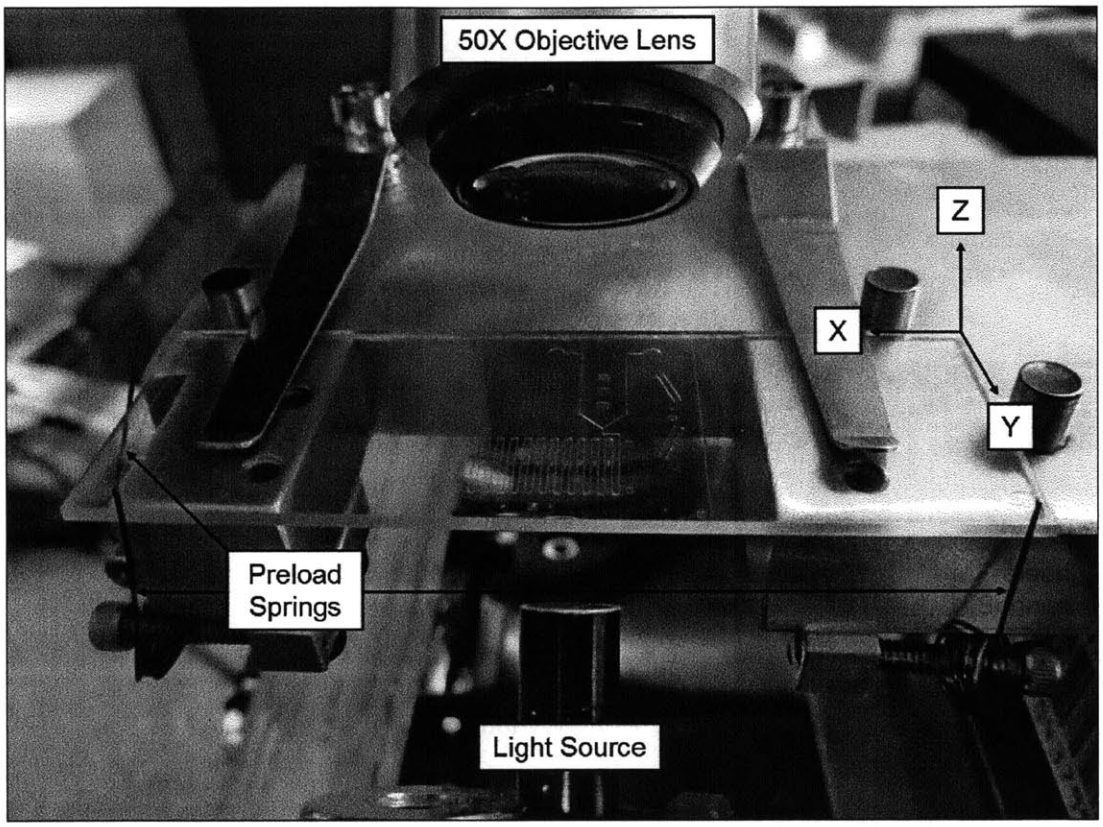

Figure 9-23: Fixture Used for Repeatability Analysis. This photograph shows the kinematic mount used to hold the injection molded parts during the repeatability analysis. The part was preloaded via springs into the three vertical posts. A set of microscope slide springs held the part down onto the aluminum bar. The slide was taken in and out of the fixture multiple times to test its repeatability.

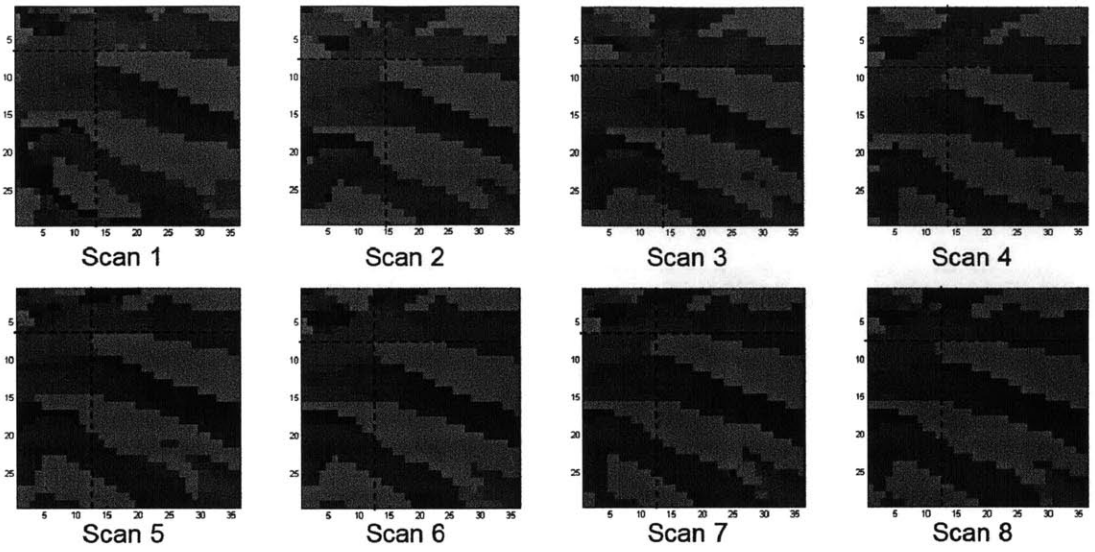

Figure 9-24: Finding the Location of Localized Features. These eight images are each taken from a topographic height map created by our instrument. This figure demonstrates how the repeatable features were located from scan to scan. The pixel row and column of the top, left corner in this feature was recorded for each scan.

sources of error can be identified.

The repeatability error is measured by observing the location of a distinguishable feature present on every part. The X,Y location of this feature within the scan is then recorded as the row and column it appears on the scan. This process is demonstrated in Figure 9-24. Here eight individual measurements of the claw-shaped "area of interest" shown at the bottom of Figure 9-21. The X,Y position recorded for each measurement is then plotted to show its repeatability in Figure 9-25. This plot shows that the results are heavily discretized where the average error in X and Y positioning is equal to one pixel spacing or 0.2 and 0.4 microns respectively. Concurrently the Z surface height is recorded and plotted as a function of measurement number.

The same process is used to determine the repeatability of the jig. Figure 9-26 shows the measured X,Y location after placing the same part into the fixture 20 times. The results of 9-25 are overlaid on top of this plot in order to show the

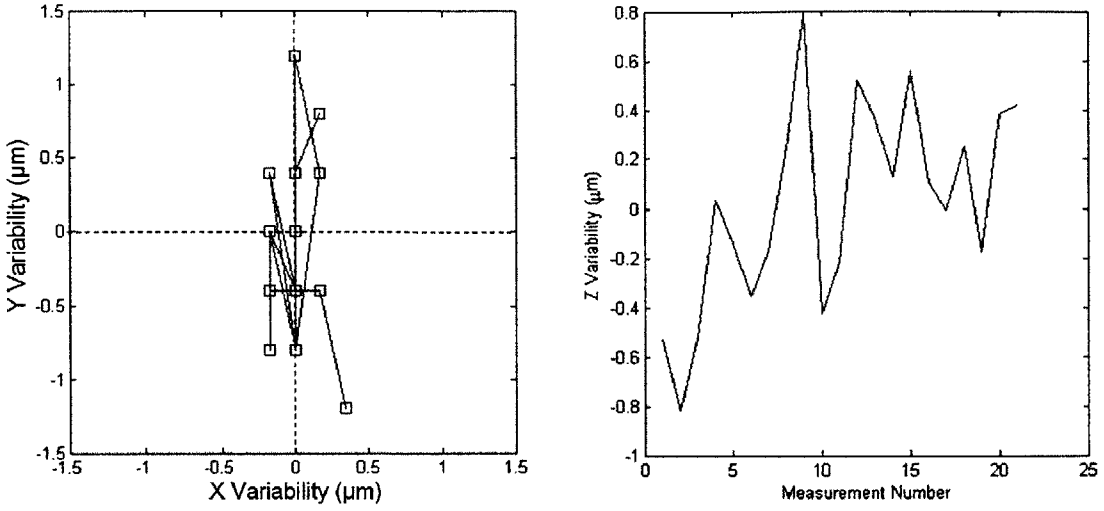

Figure 9-25: Repeatability Results for the Measurement. The same part was imaged twenty times without taking it out of the fixture. These two graphs show how our instrument measured the position of the part as a function of measurement number. The left graph shows the X,Y position while the right graph records Z.

relative difference in repeatability. It is found that the average repeatable positioning error of the fixture and the measurement is 1.0, 2.0, and 1.4 microns in the X, Y, and Z axis respectively.

Lastly the repeatability of the process is measured and presented in Figure 9-27. In this figure, the X,Y location of the distinguishable feature is presented as a red asterisk. Encompassing each point is a blue circle representing the combined repeatability of the fixture and the measurement. Due to the repeatability error from both these sources, the actual position of each feature can lie anywhere within its blue circle. As most of the circles do not overlap, it is concluded that the majority of the error in positioning is inherit to the process itself rather than any positioning error induced by the fixture or the measurement. Again, the run chart for both the fixture and measurement errors are overlaid upon this plot to show their relative magnitudes. Similarly, the error in Z height is displayed in 9-28. The repeatability of each test in X, Y, and Z axis are summarized in Table 9.2. It is found that the dominant source of repeatability error is in the X location of the

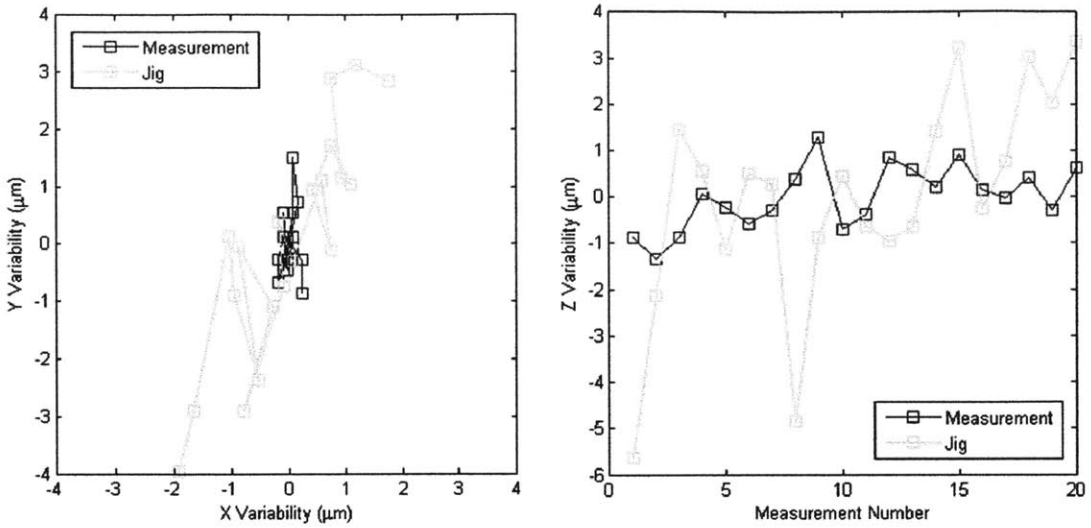

Figure 9-26: Repeatability Results for the Fixture. Similar to the previous figure, this graph shows the measurement of the part's position inside the figure as a function of measurement number. Between each measurement the same part was taken out and then placed back into the fixture.

Repeatability	**X (μm)**	**Y (μm)**	**Z (μm)**
Measurement	0.138	0.608	0.416
Fixture	1.00	1.98	1.42
Process	45.4	4.15	10.30

Table 9.2: This table holds the positional repeatability values for the measurement, fixture, and process in all X, Y, and Z axis.

distinguishable feature from part to part in the process.

9.5.3 Shrinkage Analysis

In the previous section the high speed profilometer measured the positional repeatability of a feature with respect to its outside boundary. It is unclear from this test if the features or the boundary itself had changed from part to part. The geometry of outer boundary is subject to change from various phenomenon such as "flash" when the injected polymer escapes the cavity formed by the mold upon opening. Conversely, the distance between two features in the center of the part will

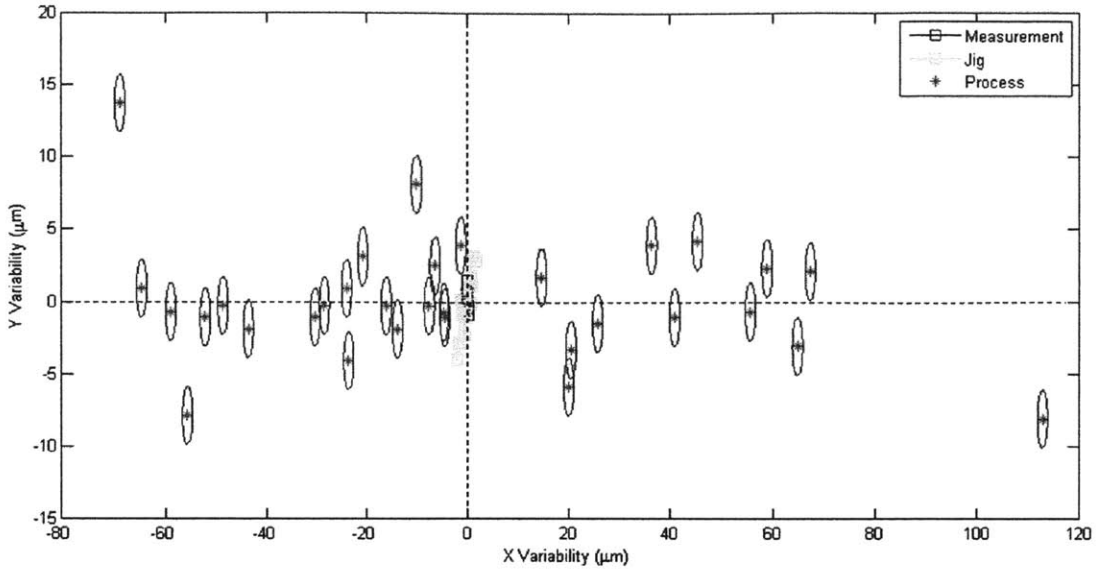

Figure 9-27: Repeatability Results for the Process. This graph shows the positional repeatability of twenty different parts placed into the fixture one after another. The red mark represents the measured position while the blue encompassing circle represents the measurement uncertainty.

change via "shrinkage" if the entire part has shrunk uniformly. To test the shrinkage of the part, the high speed profilometer measures the distance between the two channels signified in Figure 9-29.

The center of both channels in the X axis X_1 and X_2 was measured for each injection molded part in the study. The average distance between the channel centers X_1 and X_2 was measured to be 12,083.5 microns. As the metric of shrinkage is defined the change in distance between two points X_1 and X_2, the mean values of these quantifies can be subtracted out of the equation. Thus, the quantity L_1 is calculated by subtracting the away the mean value of X_1 away from itself as defined in Equation 9.1. The shrinkage is then defined in terms of L_1 and L_2 in Equation 9.2.

$$L_1(n) = X_1(n) - \frac{\sum_1^n X_1(n)}{n} \tag{9.1}$$

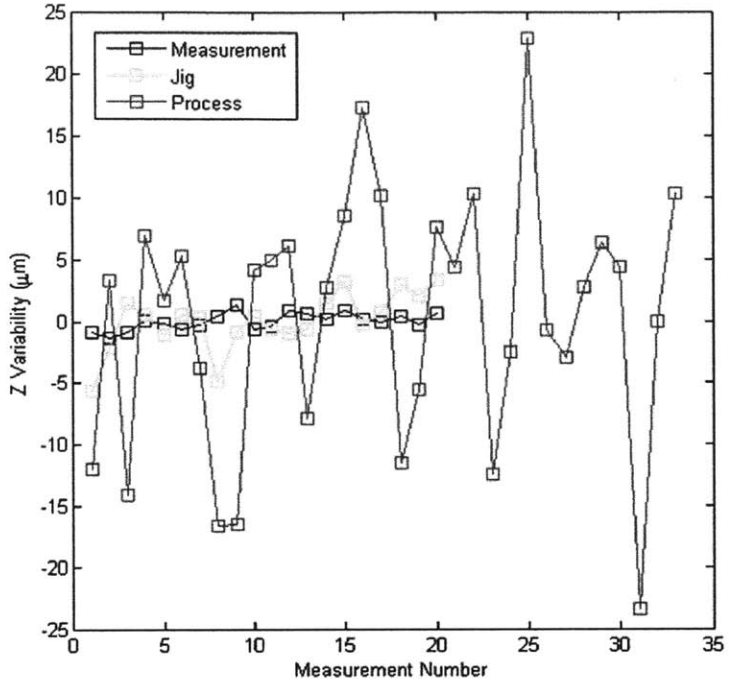

Figure 9-28: Repeatability in Position on the Z Axis for All Three Tests. This graph shows the recorded Z height for all three tests. The blue, green, and red data represent the Z height of the three tests.

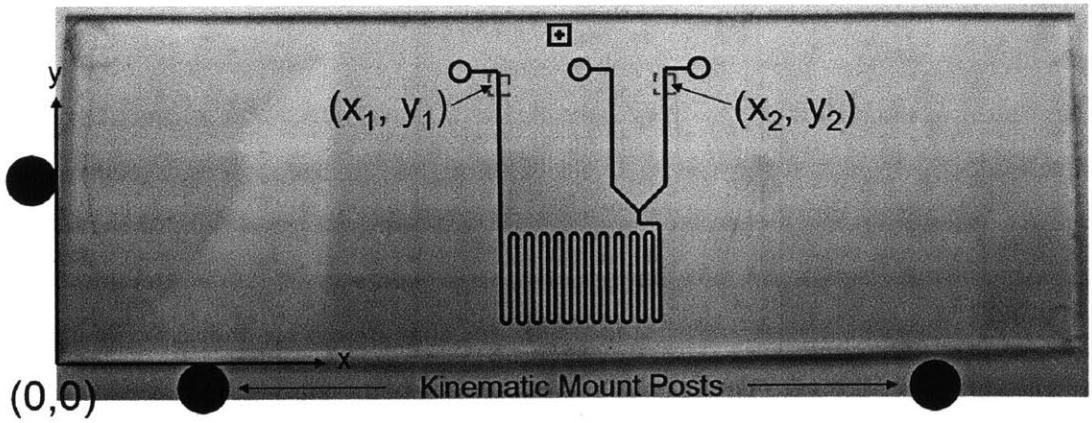

Figure 9-29: Diagram Demonstrating the Position of the Two Points Used to Evaluate Shrinkage. The high speed profilometer is used to measure possible shrinkage in the μFac part. This photograph highlights the two features on the part that were located in order to conduct the shrinkage analysis.

$$S(n) = L_1(n) - L_2(n) \tag{9.2}$$

where S = Shrinkage (m)

X_1 = X position of channel 1 (m)

The meaning behind quantities L_1 and L_2 becomes more intuitive after observing the run chart in Figure 9-30. In this figure the position of both channels are plotted as a function of run number. The run chart clearly shows that although values L_1 and L_2 change from part to part, their difference remains relatively small. This difference, defined as the shrinkage in Equation 9.2, is plotted in green. The average difference in shrinkage is measured to be 0.76 microns. Said differently, the distance between the centers of the channels X_1 and X_2 is measured to be 12,083.5 $\pm$ 0.76 microns. This difference of 0.76 microns is measured to be less than two percent of the 45.4 micron positional reputability error from part to part. Thus, it is concluded that the shrinkage of the part is negligible compared to the change in geometry of the outside boundary.

9.5.4 Automatic Defect Detection

The topographic maps can also be used for automatic defect detection in the injection molded process. The defect detection analysis presented presumes that the parts have negligible shrinkage and can be aligned to one another, both principles of which have been demonstrated in the previous two sections. Having measured a series of repeatable parts, an algorithm can now average all the topographies together to create a "master." When any particular scan is subtracted from the master, the portions of the part that are different or defective become highlighted. Figures 9-31 and 9-32 have been constructed to demonstrate this capability. The first figure shows three line scans taken from our run of parts. The distinguishable features common to every line scan are highlighted in black while the defects are highlighted in white. When subtracting any scan against the master, the features highlighted in black will not trigger a defect detection response for these features

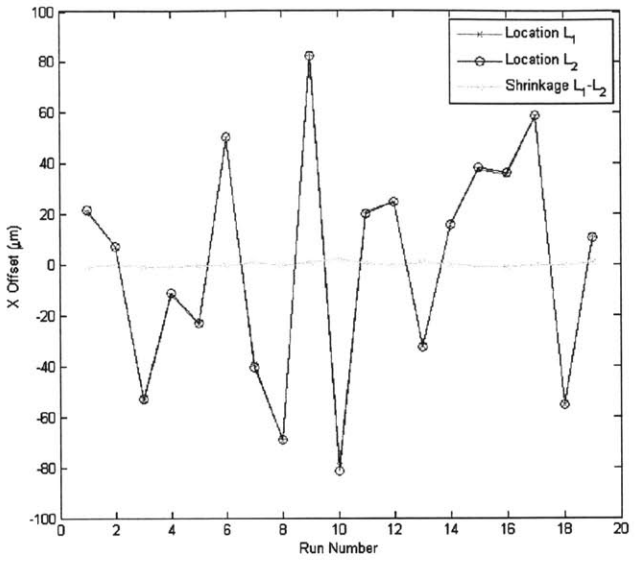

Figure 9-30: Comparing Shrinkage Versus Measured Location. This run chart shows the locations L_1 and L_2 as a function of run number. The chart shows the difference between L_1 and L_2 or the shrinkage is far less variable than the measurement of L_1 or L_2 themselves.

are present on every part. Conversely, the features highlighted in white show up prominently as indicated by their red color in Figure 9-32. The cooler blue and green colors signify that the part is normal while the hotter red colors show where the high speed profilometer has measured defects.

9.5.5 Channel Height and Width Measurements

Beyond defect detection, the high speed profilometer can also be used for process control. In such an application topography information would be used as feedback in the manufacturing process. The geometry of the channels in the μFac part have particular importance in our process and would likely be the observed quantity in the process control. This section shows how the height and width of the channel can be measured at every point along the channel. First, a simple algorithm was written to detect both edges of the channels seen in Figure 9-33. The locations of the left and right edges are signified by the dark red points. The points bend around the

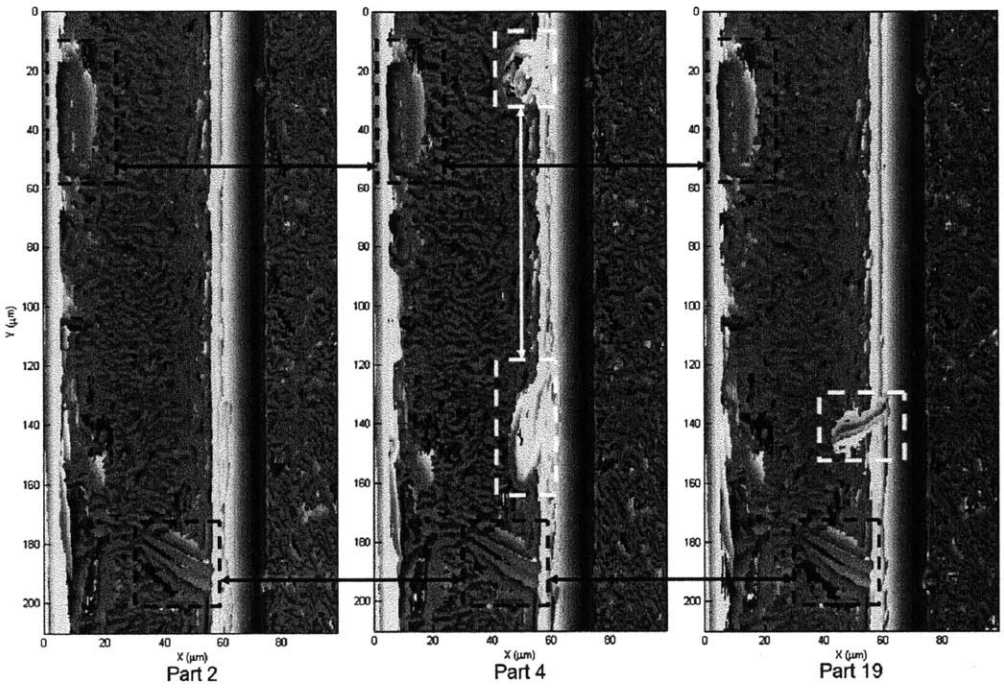

Figure 9-31: Using the Master Image for Defect Detection. The three topographical scans shown of parts 2, 4, and 19 demonstrate how the master can discriminate between defects and process features. The portions of parts 4 and 19 that are different than part 2 are identified as defects.

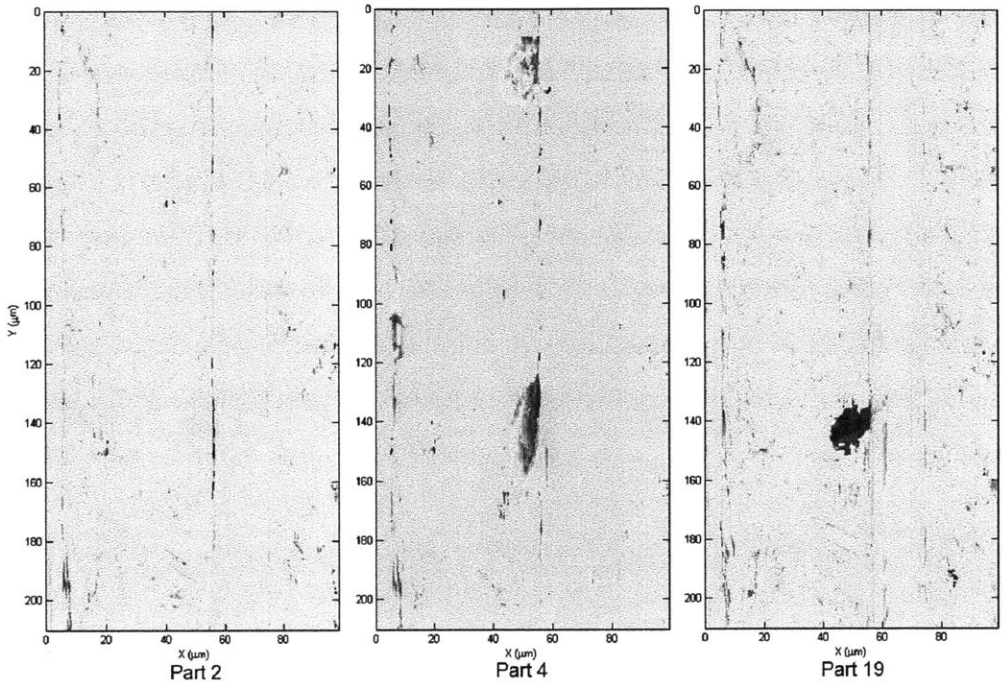

Figure 9-32: Highlighting the Defects. This figure shows the results of using the defect detection analysis to automatically highlight defects in the part. The image shown is the subtraction of each part away from the master. Any part of the image showing up in red or blue represents a departure from the master image

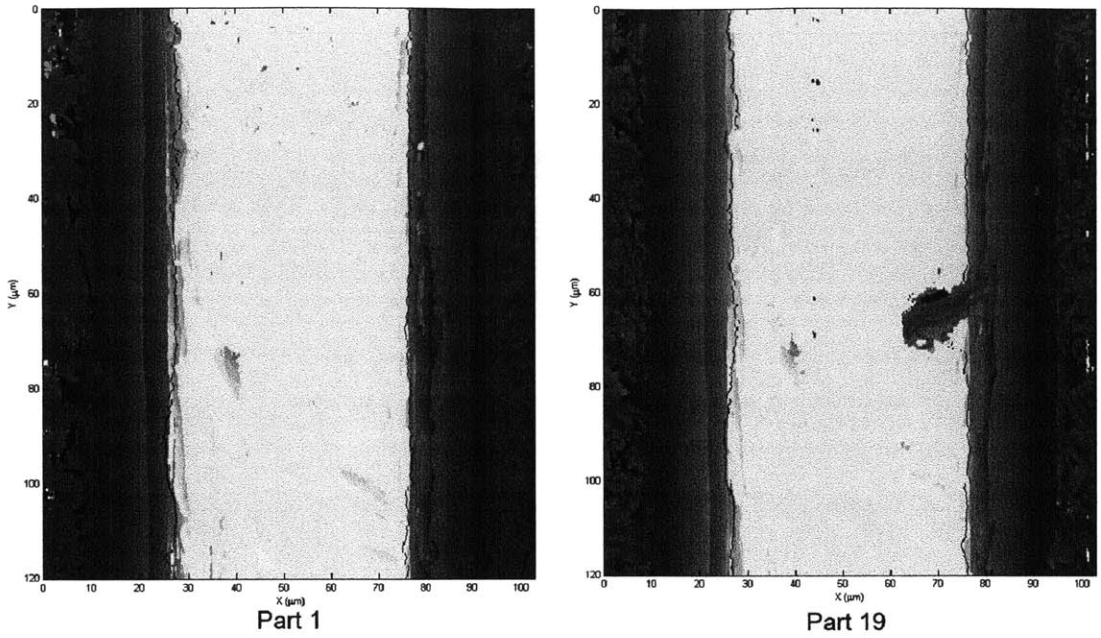

Figure 9-33: Automated Width Detection. The width detection algorithm identifies both edges of the channels in part 1 and part 19. The measured location of the right and left edges are signified by dark red points clearly identifying the defect in Part 19.

defect in Part 19 to signify the width of the channel at that point has been reduced. For every row of information, the width of the channel is measured by calculating the distance between the left and right edges. The widths of both part 2 and part 19 are plotted in Figure 9-34 as a function of Y position. Defects in channel width can easily be detected when the width of the channel surpasses a specified threshold, as signified by the dotted line at 45 microns. It is also clear from this plot that the two channel width measurements display repeatable deviations from their nominal width of 50 microns.

Similarly, the depth of each channel as a function of position can be measured by our high speed profilometer. Two columns of data are taken from part 2 and plotted against each other in Figure 9-35. As seen in this figure, the average depth of the channel is measured to be 40 $\pm$ 2 microns. The two microns of noise in the height measurement is peculiar for such surface roughness had not been measured with the

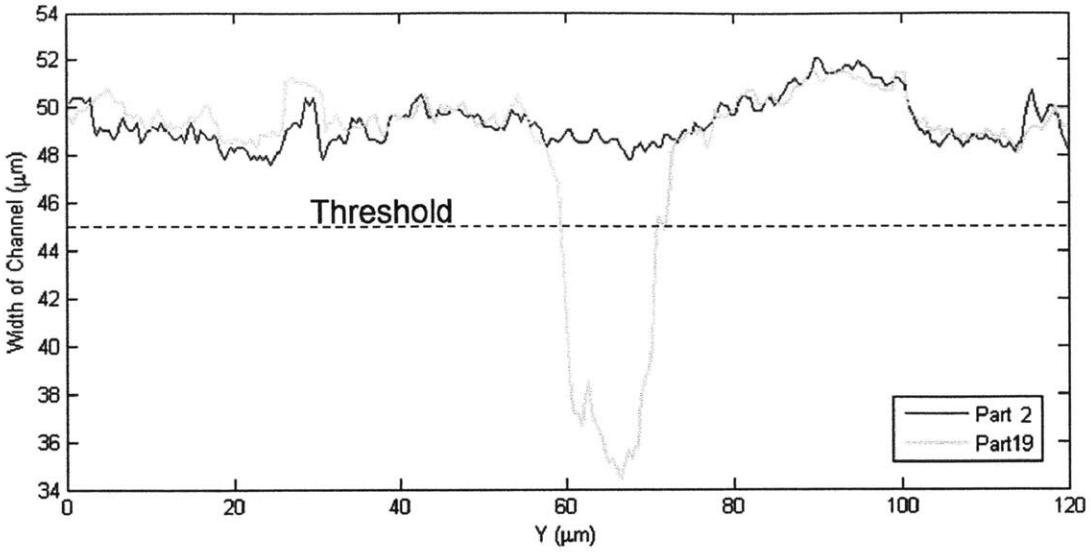

Figure 9-34: Automated Threshold Detection. This graph shows how an algorithm can set a threshold to automatically detect defects based upon the thickness of the channel. The width of the channel as a function of location is plotted in this figure for both part 2 and part 19.

white light interferometer. A subsection of the depth plot is analyzed to gain additional insight on the origin of this noise as noted by the black dotted box in Figure 9-35. The same subsection is grabbed for each of the 32 parts measured in this study and plotted on top of one another in Figure 9-36. It is clear from this plot that the measured noise in the depth measurement is highly repeatable from part to part.

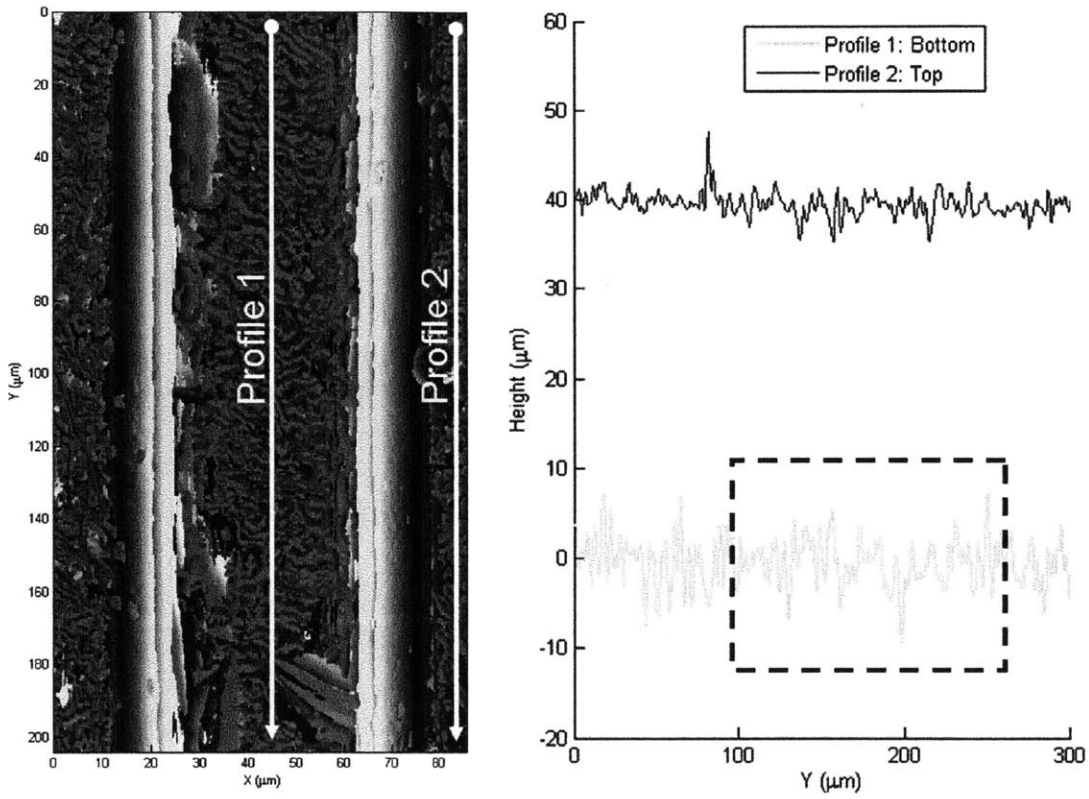

Figure 9-35: Automated Depth Measurement. Two columns of data at the top and bottom of the channel are selected and subtracted against each other to measure the depth of the channel as a function of Y position.

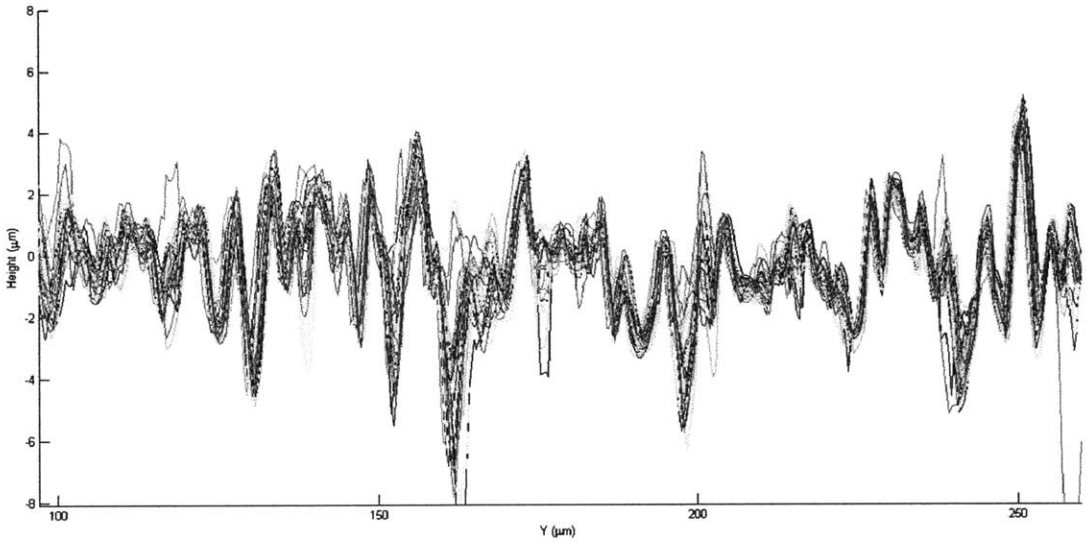

Figure 9-36: Similarities Across Measurements. The depth measurement across 32 parts are plotted against each other in this figure. It is clear from this figure that the noise in the depth measurement is not random. While each speck and crevasse on the μFac part may look random, these features are in fact cast by the ground truth.

Chapter 10

Edge and Thickness Detection Sensor

Roll to roll manufacturing processes provide high throughput production at economical rates. These processes require accurate positioning and handling of large sheets or "webs" that must be properly unwound, processed, and rewound in a continuous fashion. The accuracy in which the web can be positioned limits the intricacy and complexity of the features able to be manufactured via roll to roll processing. The sensors that measure the properties of the web face additional complications when the webs are made from transparent materials. By improving the sensing capabilities of tools that measure transparent webs, the economic benefit of roll to roll manufacturing processes can be used in a wider variety of applications.

Roll to roll manufacturing hardware must measure and control the position of the web perpendicular to the direction of travel. The precision in which the lateral position of the web can be measured and controlled affects the performance of the roll to roll process. For example, the density of data stored on magnetic tapes is chiefly limited by the fidelity of the spatial registration between the ribbon and the read head [42]. The most common measurement strategy used in industry will sandwich the web between a transmitter and a receiver. As the web moves further into the range of the sensor the received signal becomes attenuated as the

transmitted signal becomes blocked. Sensors measuring opaque webs typically use light as the transmitted signal [43],[44] while those measuring transparent webs will use sound [45],[46]. Ultrasonic sensors exhibit resolution that is poorer than the light based sensors given the greater diffraction of sound waves. Seshardi and Pagilla have demonstrated a sensor to measure both mediums with comparable performance [47].

In a variety of industrial roll to roll applications it is important to inspect and control the thickness of the web such as coating or extrusion processes. One prevalent method to measure thickness and index of refraction of transparent plates uses lateral shear interferometery to pass a spatially coherent laser multiple times through a transparent object in order to observe the subsequent interference pattern [48],[49],[50]. Other methods observe light reflected from the front and back surface of the transparent object to determine its thickness [51],[52],[53]. Although many of these methods are able to simultaneously measure both thickness and index of refraction, it is also common and easier to instead measure their product: the optical path length. With more accurate measurement of thickness the products made by roll to roll processes can be both more intricate and cost effective.

This chapter introduces a sensor that can simultaneously measure a transparent web's optical path length and lateral position with submicron resolution. Similar to the metrology approach proposed by Ri and Muramatsu on transparent objects [54], our sensor observes changes in intensity on a Ronchi grating illuminated by an LED light source. The chosen illumination is neither spatially or temporally coherent thereby simplifying the hardware and cutting down on cost. The method used by our sensor can also shares similarities to that of a thickness measuring system that utilizes DVD pickups [55]. The differences and similarities in hardware, software, experiments, and analysis of the novel edge and thickness detection sensor are all presented in detail in this chapter.

10.1 Experimental Hardware

The new edge and thickness detection sensor is made from conventional cameras and optical elements. The Basler A504K CMOS camera from the high speed profilometer is used again in this project. Similarly, the extra long working distance 50X Mitutoyo microscope objective is used to focus light onto a camera. The experimental apparatus is set up as depicted by the schematic in Figure 10-1. In the absence of a transparent sample, the high numerical aperture microscope objective lens focuses the light emitted from the plane at "Height Z_1" onto the CCD sensor as shown by the green path. When a transparent glass plate is introduced into the field of view of the camera, the light path becomes bent as seen in red and now focuses at a deeper plane located at "Height Z_2." A flat object is tilted at angle α with respect to the camera such that the object intersects both planes at Heights Z_1 and Z_2. By observing this known object through our unknown transparent sample, the sensor can measure both the sample's thickness and lateral position.

The properties of the known object were carefully chosen to optimize the performance of our new sensor. The base material object is made of quartz or "fused silica." A less expensive base material dubbed "soda lime" is commonly substituted for fused silica in cost prohibitive applications. The soda lime glass' coefficient of expansion is nearly 20 times greater than that of fused silica. In our high precision application, small changes in temperature can cause thermal expansion that impacts the reading of our sensor. This thermal expansion is often difficult or impossible to measure thus injecting randomly generated noise into our system which is unable to be compensated. Quartz (QZ) transmits a far greater portion of low wavelength light as shown in Figure 10-2. This property again has thermal implications for any light that is not transmitted is thus absorbed and turned into heat within the known object. The compositions of soda lime glass, fused silica and their derivatives as well as other important thermal and mechanical properties are listed in Table 10.1.

The reflective pattern was printed onto the quartz base using a photolithography

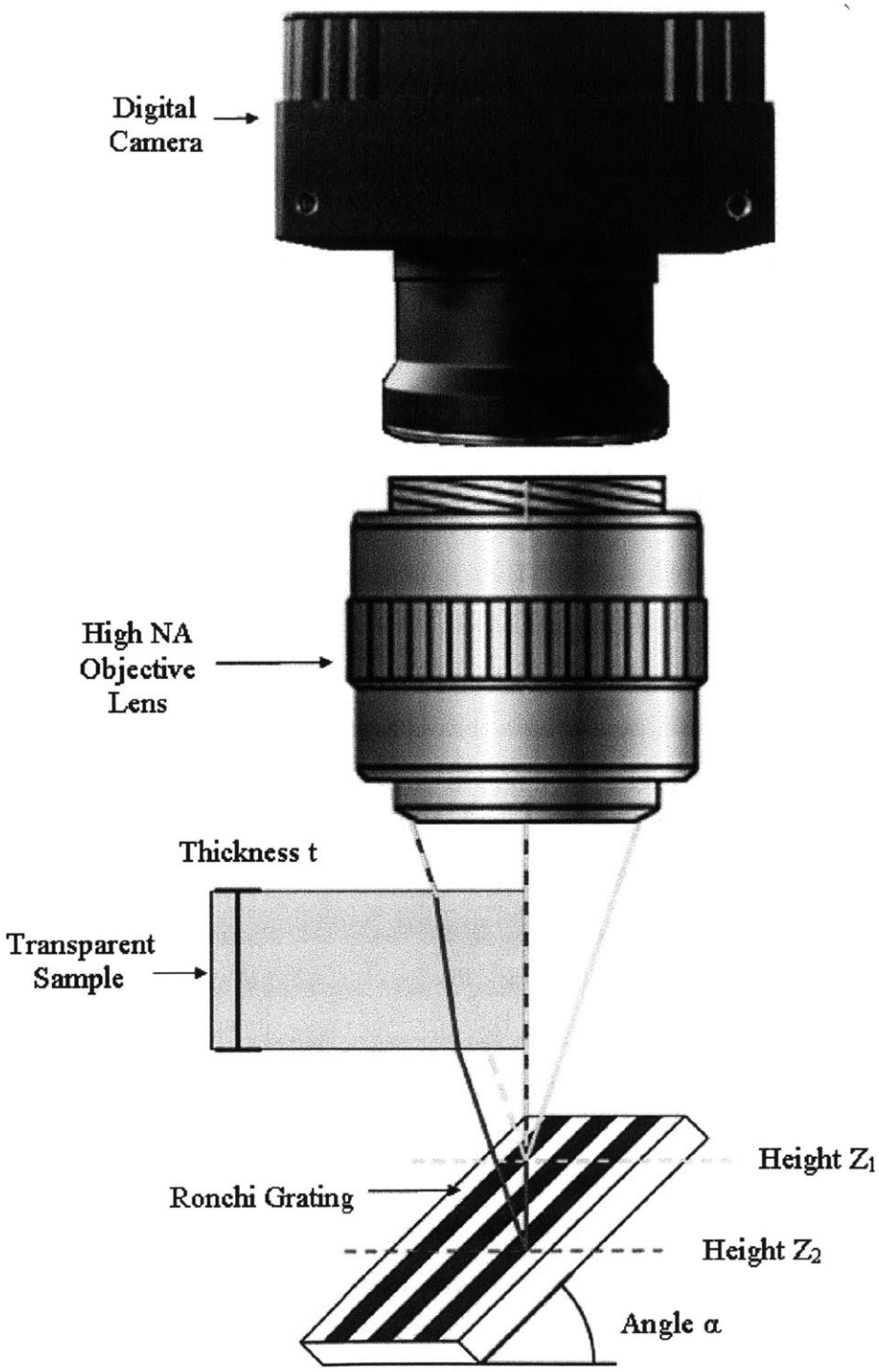

Figure 10-1: Schematic Showing the Basic Elements and Setup of the Sensor. The height of the focal plane will be dependent upon the thickness of the sample because of the bending of light through a higher index of refraction medium. By observing the Ronchi grating through the unknown part, the sensor can measure the thickness and lateral position of the transparent material.

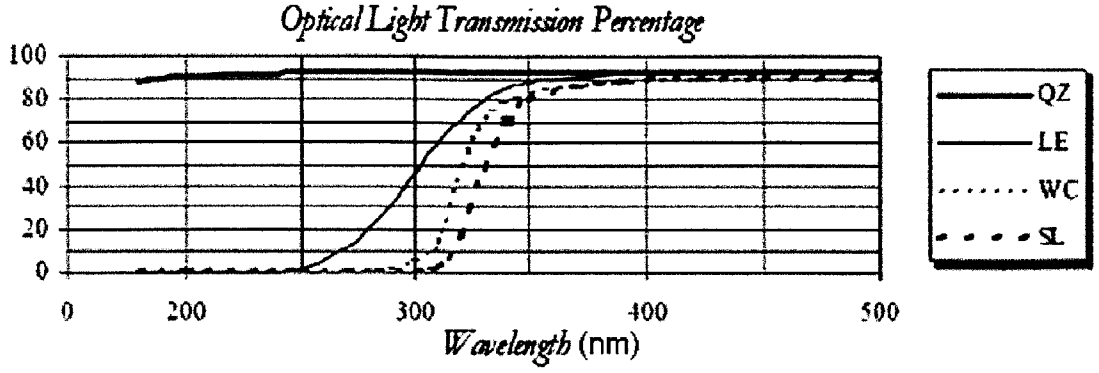

Figure 10-2: Differences in Transmission Due to Glass Composition. This chart shows the transmission percentage of four base materials as a function of incident wavelength.

Composition %	Soda Lime	White Crown	Borofloat	Quartz
SiO_2	73	70	60	100
B_2O_3	-	-	5	-
Al_2O_3	1	-	15	-
Na_2O	18	8	1	-
K_2O	1	9	1	-
RO	10	14	18	-
Thermal Exp. (μm/C)	9.4	9.3	3.7	0.5
Index of Refraction	1.52	1.52	1.53	1.46
Young's Mod (kg/mm^2)	7,000	7,340	7,540	7,413

Table 10.1: This table holds the important properties of the four types of glass used to create the known optical element in the sensor.

process with submicron resolution. To begin a thin layer of chrome is sputter coated onto one side of the glass providing a uniform coating of the order of several nanometers thick. The coating is then selectively blasted away with UV light resulting in the prescribed pattern. This process was used by Edmund Optics to provide commercially available patterns called Ronchi Rulings: a simple, repeating pattern of contrasting lines spaced apart at a given pitch. A light source is positioned to shine through the known target into the camera thus creating a series of contrasting lines based upon the transmission and reflection of light through the fused silica and chrome respectively. This pattern is imaged by the CMOS camera and analyzed by our image processing software to measure the thickness and position of a transparent glass plate.

10.2 Image Processing Algorithms

The image processing algorithm uses variation in light intensity values captured by the CMOS camera to make measurements of the transparent glass. As shown in Figure 10-1, the known object is tilted at an angle α with respect to the camera. The objective lens will focus the light emitted from any objects in the image plane onto the CMOS sensor. The image plane is defined to be one working distance below the microscope objective. The camera observes high contrast only in the area in which the surface of the known object intersects the focal plane. Upon this intersection the camera images a pattern of white and black striped lines while the rest of the CMOS sensor captures a uniform gray. This behavior can be seen on the top half of Figure 10-3 which shows one frame captured by the camera sensor. The orientation of the Ronchi ruling with respect to the camera was carefully chosen to simplify the code used to process the images. A different, randomized pattern of light and dark pits that shows variance in both planar dimensions could be used to produce more uniform results.

The microscope objective lens is subject to various nonlinearities such that distort

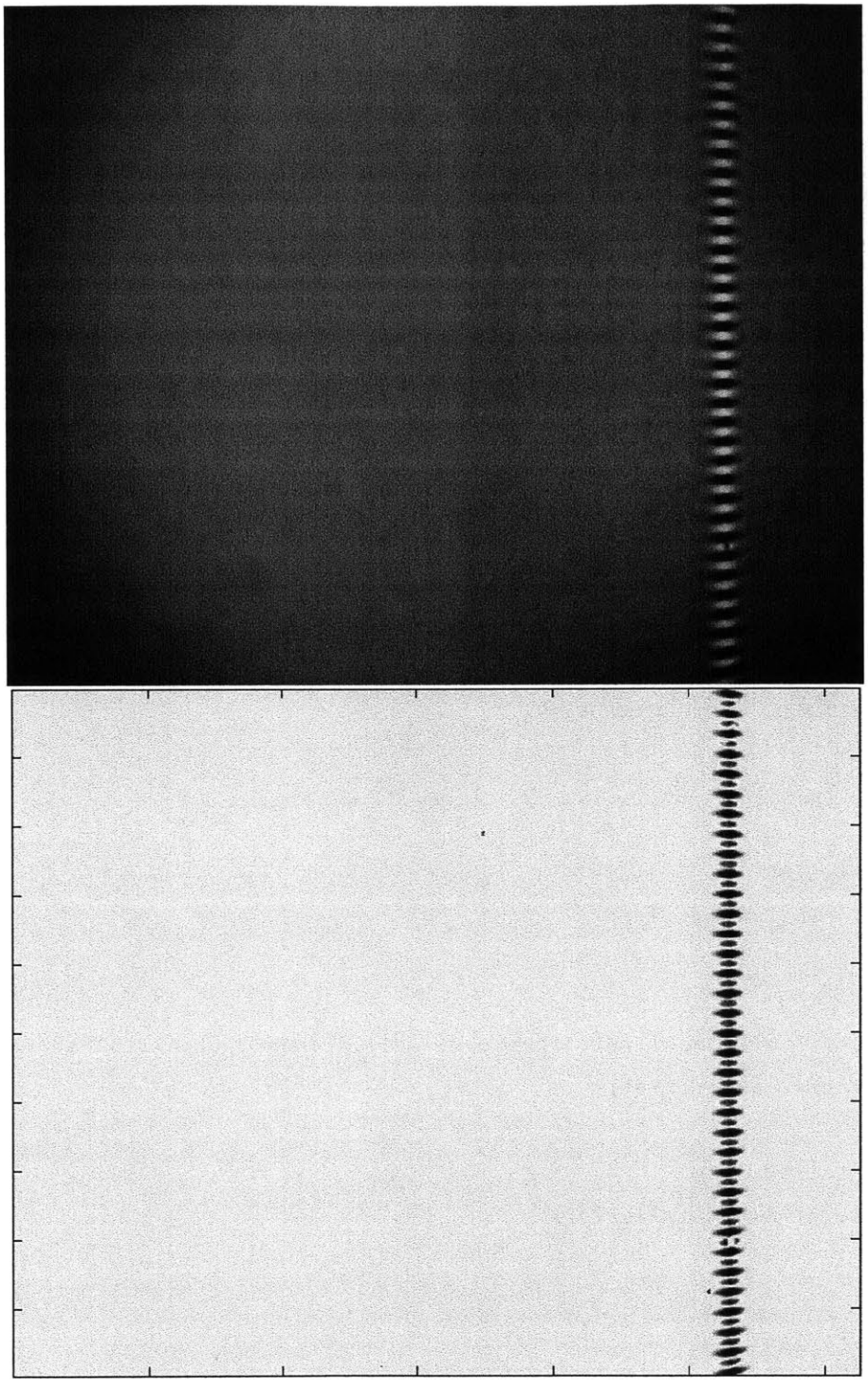

Figure 10-3: High Pass Filter to Account for Vignetting Effect. These two images show the raw data captured by the camera on top and the processed image to compensate for vignetting on the bottom. The series of light and dark lines appear only where the Ronchi grating intersects the image plane.

the image. First, each column of data can have a different sensitivity to light. This discrepancy is averaged out using image processing. The most pronounced effect seen by the camera is called "vignetting" whereby the periphery of the image has a reduction in brightness as compared to the image center. Image processing algorithm is used in order to compensate for vignetting. The image is essentially low pass filtered whereby the value of each pixel is divided by the average value of the pixel's neighbors. Thus a pixel on the periphery with a low intensity value will be normalized by the dark pixels that surround it. The effect of normalizing the image in order to account for vignetting is shown the bottom half of Figure 10-3. The processed image is displayed in false colors in order to more clearly visualize the information and to remind the reader that the image has been altered. In this false color representation a spectrum of colors sweeping through from blue to green to red is used to represent intensity values from dark to light. The code to carry out these operations is displayed below.

```
1
2  for j = 1:1280
3      A(j)=sum(Image(:,j));
4  end
5
6      LowP=filter2(ones(1,6),[ones(1,6)*A(1),A,ones(1,6)*A(1280)])/6;
7      LowPass=LowP(7:1286);
8
9  for j = 1:1280
10     Ratio(j)=A(j)/LowPass(j);
11 end
12
13 for j = 1:1280
14     Image(:,j)=Image(:,j)/Ratio(j);
15 end
16
17 [M,N]=size(Image);
```

```
18 LowPassMatrix=filter2(ones(35,35),Image);
19 Normalized=Image./LowPassMatrix;
20 Subset=Normalized(15:M-15,15:N-15);
21 StdColumns(i,:) = std(Subset);
```

The test target and image processing algorithm were chosen in concert to most accurately identify the location of the focal plane. The camera image shows the lines of the Ronchi ruling traverse left to right across the sensor. The portion of the image that is in focus stretches from top to bottom. The Ronchi grating is oriented such that the all pixels in each column are focused at the same height in physical space. Our algorithm calculates the standard deviation of each column of each image and uses it as the primary source of information. The columns with large standard deviations in intensity correspond to the portions of the image that are in focus and switch from light to dark as the lines of the Ronchi ruling are imaged. The value of the standard deviation measure corresponds to how much light has been focused at its particular plane. The chart in Figure 10-4(a) graphs the standard deviation of each column versus the column number. To the right side we see the graph in Figure 10-4(b) zoomed in to the peak value selectively displaying the columns around the peak focus. This type of graph will be called a "standard deviation plot" and will be used regularly in our analysis. In this particular plot a peak in the standard deviation measure is recorded around pixel column 1050. These peaks will be the subject of our analysis to determine the thickness and position of a flat, transparent object.

The definition of what is in-focus is a subjective measure whose answer depends upon the application. For this application, the measure of the focal plane location is a continuous function with a central peak. Curve fitting techniques can determine the location of maximum focus down to a fraction of a pixel. The optical system faces the same limitations imposed by the Raleigh criterion when calculating the finest pitched line pairs able to be resolved based upon its lateral resolution. Yet, because the standard deviation focus measure fades in and out of focus in a

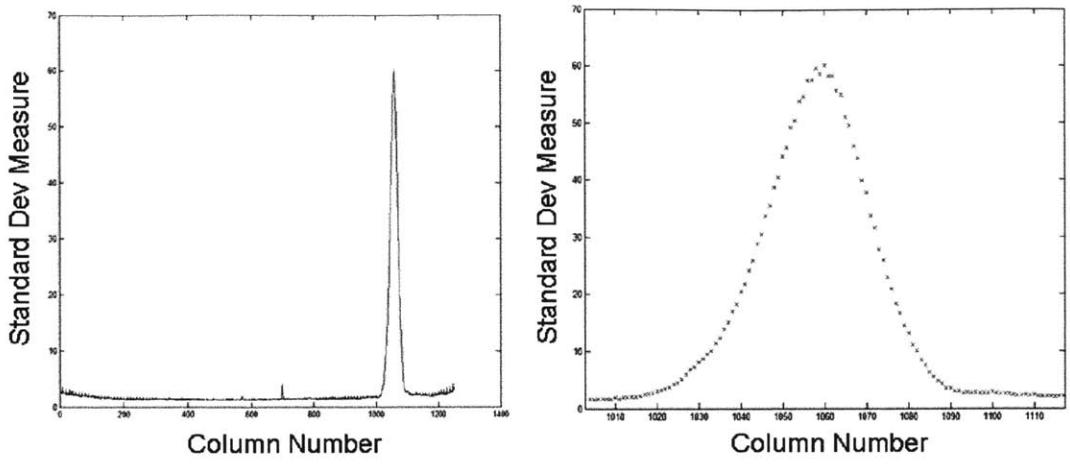

Figure 10-4: Identifying Position of Focal Plane Through Standard Deviation. The graphs shown here are the result of taking the standard deviation of each column. Calculating the peak of the graph allows the sensor to track the position of the focal plane in the Z direction.

continuum, the resolution in which the sensor can measure the depth of the focal plane is not limited by the Raliegh criterion. The sensor concerns itself not with counting the number of lines in the Ronchi grating, but instead looking to measure the relative focus among the different columns. The code used to find and calculate the center of the focal plane is shown below.

```
1       [StdMax CenterValue]=max(StdColumns);
2       Cutoff=StdMax*3/20;
3       Section = StdColumns((CenterValue-40):1:(CenterValue+40))-Cutoff;
4
5       Range=[];
6
7   for j=1:length(Section)
8       if Section(j) > 0
9           Range = [Range,j];
10      end
11  end
12
```

```
13 X = Range - 41 + CenterValue;
14 Y = StdColumns(X);
15 p = polyfit(X,Y,3);
16
17 XX = [X(1):0.01:X(length(X))];
18 YY = XX.*XX.*XX*p(1)+XX.*XX*p(2)+XX*p(3)+p(4);
19
20 [Value Position] = max(YY);
21
22 Center(i)=Position/100+CenterValue;
```

By introducing unknown transparent elements into the light path, the peaks of this standard deviation measure can shift, slide, split, or change in amplitude. Any change in output is broken down into a series of three fundamental movements. The geometry of the sensor and physics of light are used to describe and predict these fundamental movements and then empirically verify our predictions with experiments.

10.3 Peak Sliding

The first phenomenon observed and explored is peak sliding. Peak sliding occurs when the observed location of the focal plane changes while the geometry and position of the transparent medium remains constant. Understanding the basis of peak sliding will give a comprehensive review of how the camera sensor measures the location of moving focal plane.

A second look at the hardware is taken in order to explain how the camera reads the changing focal plane. As depicted in Figure 10-5, the Ronchi grating is tilted an angle α from the horizontal. If the focal plane were to be shifted vertically a distance "Δz," it would change the point of intersection with the Ronchi ruling horizontally by a distance "Δx." These variables "Δx." and "Δz," are related by the tangent of the angle α. The distance "Δx." is measured by the camera by a shift in pixels. By calculating the size of the magnified pixel we can convert the

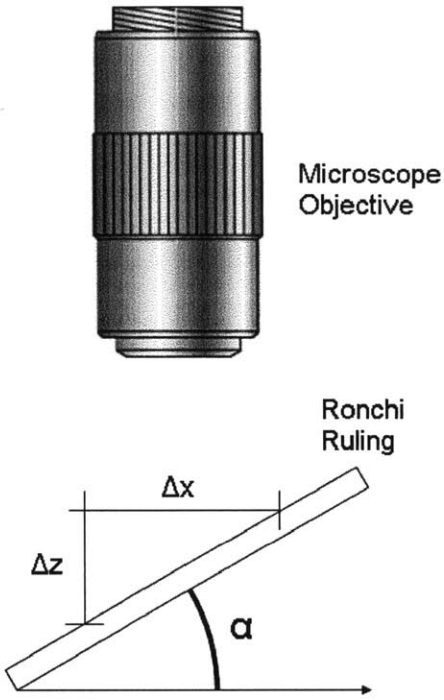

Figure 10-5: Conceptual Peak Sliding Schematic. A cross section of the sensor shown in this image shows how the measured change in pixels measured in ΔX is related determine the change in focal plane ΔZ.

measured pixel shift into a distance to solve for "Δz," The pixel size "p" is divided by the magnification of the lens M to calculate the size of the magnified pixel. Though these relations we relate the change in focal distance "Δz," to the observed pixel shift "Δp," in Equation 10.1.

$$\Delta Z = \frac{p \cdot tan\,(\alpha)}{M} \Delta P \tag{10.1}$$

An experiment was designed in order to validate this theoretical relationship between ΔZ and ΔP. The Ronchi ruling was placed on an automated Z stage capable of lifting an object with submicron precision. The ruling was incrementally lifted 2.5μm per step closer to the camera as the sensor registered the peak position of the standard deviation measure. Although the focal plane of the camera remains at the same height, the camera observes a relative focal plane shift between the

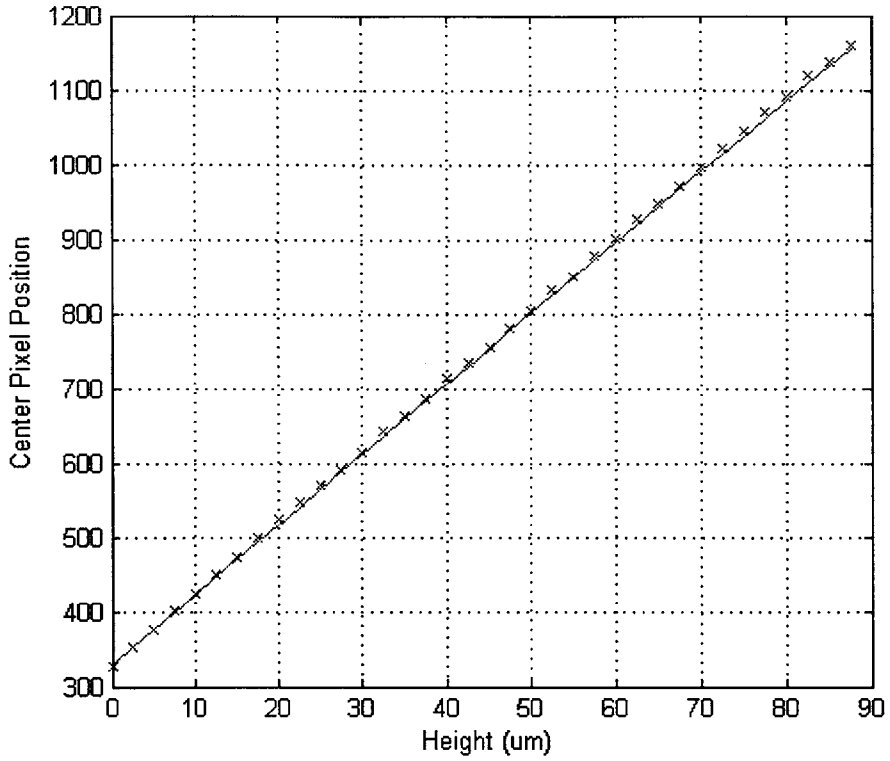

Figure 10-6: Results from Peak Sliding Calibration. This graph shows the results of the experiment designed to test the peak sliding phenomenon. For each point, the Ronchi grating was elevated to a height represented on the X Axis. While at rest, the center pixel position on the standard deviation graph was calculated. Here the center pixel position is shown to have a linear relationship to the height of the Ronchi grating.

ruling and the sensor induced by the lifting in the Z stage. In our experiment,the rise angle α was measured to be 30.0 degrees with a pixel size "p" of 12.0 m and a magnification "M" of 65.6X. Given these numerical values, the theoretical relationship $\frac{\Delta P}{\Delta Z}$ was calculated to be 9.464 pixels per micron of focal plane shift. Our experimental values corroborated this value by measuring 9.44 pixels per micron of focal planes shift. The results of this experiment are displayed in and Figure 10-6.

Data is collected from the camera over a long period of time in the absence of a transparent medium to observe the real time effects of peak sliding. Figure 10-7 plots the maximum location of the peak as a function of time. Although each

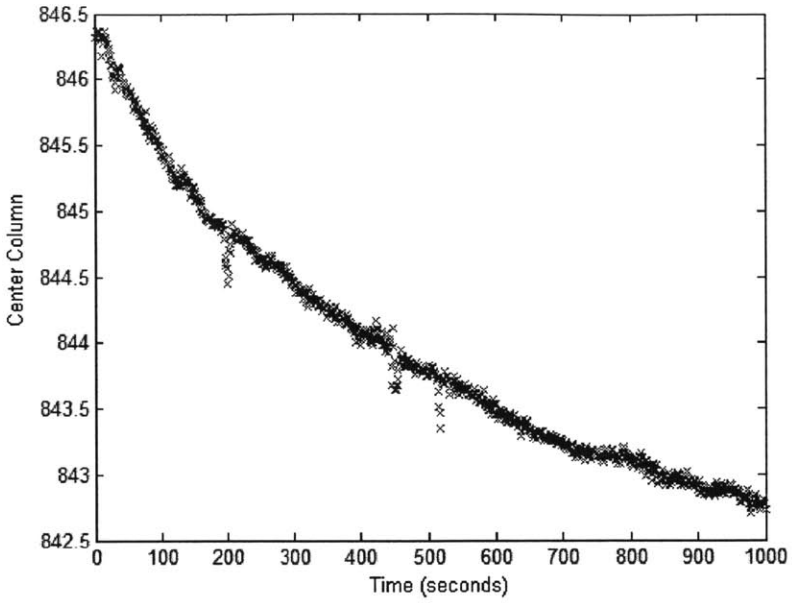

Figure 10-7: Effect of Thermal Drift on the Measured Focal Plane Location. This graph shows the center column measured by of the sensor over a relatively long period of time in absence of any change to the hardware. The drift is attributed to thermodynamic effects.

measurement will be slightly different because of sensor noise and light intensity fluctuations, it is clear from the data the center of the peak drifts with respect to time. This drift is attributed to thermodynamic effects that cause elements in the measurement loop to heat up and expand.

Any object whose change in geometry will affect the sensor output is by definition inside the metrology loop. The purpose of examining and quantifying the peak sliding phenomenon is to predict how these unintended changes in geometry will affect the sensor reading. The effect of geometrical changes in the hardware on the sensor output will be indistinguishable from changes in the measured object. The upcoming sections explain how to isolate these thermal effects of the expanding metrology loop from the measurement itself with a dual peak technique. This strategy makes the sensor more robust to changes in the environment such as shifts in temperature or humidity.

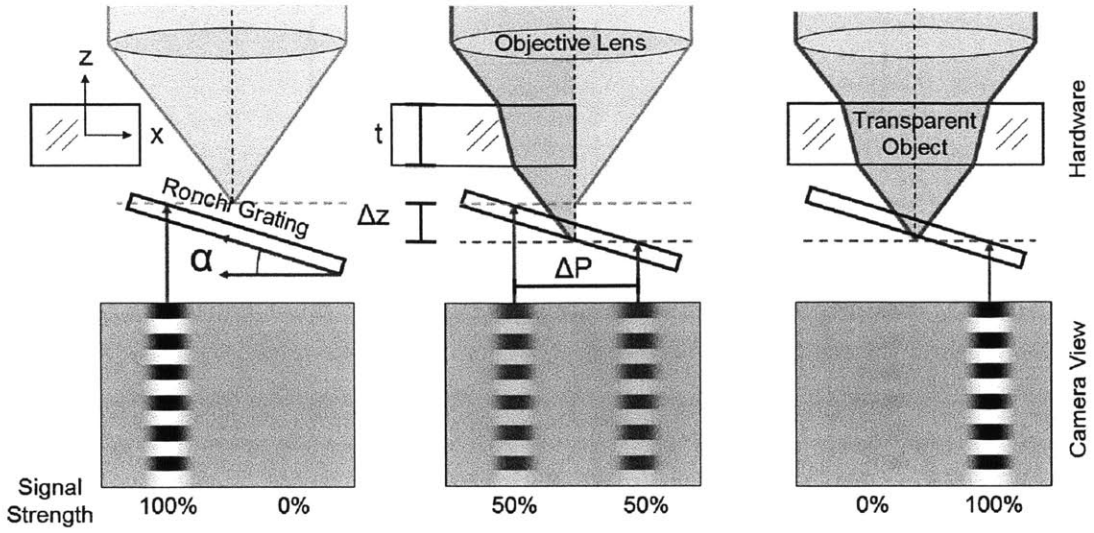

Figure 10-8: Comprehensive Cross Sectional Diagram of the Sensor. The three parts of the figure depict how the light bends about a transparent object that is absent, partially inserted, and fully inserted into the light path. The thickness of the object is measured by calculating the shift in pixels from the left and right signature while the lateral position is measured by observing their relative signal strength.

10.4 Peak Shifting

The second phenomenon observed and explored is peak shifting. Peak shifting occurs when a flat transparent object of uniform thickness and index of refraction is fully inserted into the field of view of the camera. Figure 10-8 gives a comprehensive visual explanation of the sensor's basic underpinnings. As shown on the right most image, the transparent object will bend the light rays and shift the location of the dark and light signature as viewed by the sensor. Though physical derivation it is found that the shift the focal plane is proportional to the thickness of the transparent object.

The analysis of the peak shifting phenomenon is derived from Snell's law of refraction and will be explored through ray tracing via a series of figures. Figure 10-9 follows two light paths that are outlined in red and green. Both paths share an incident angle θ measured from the vertical. The green path shows how the light behaves when focused by the microscope objective in absence of any transparent

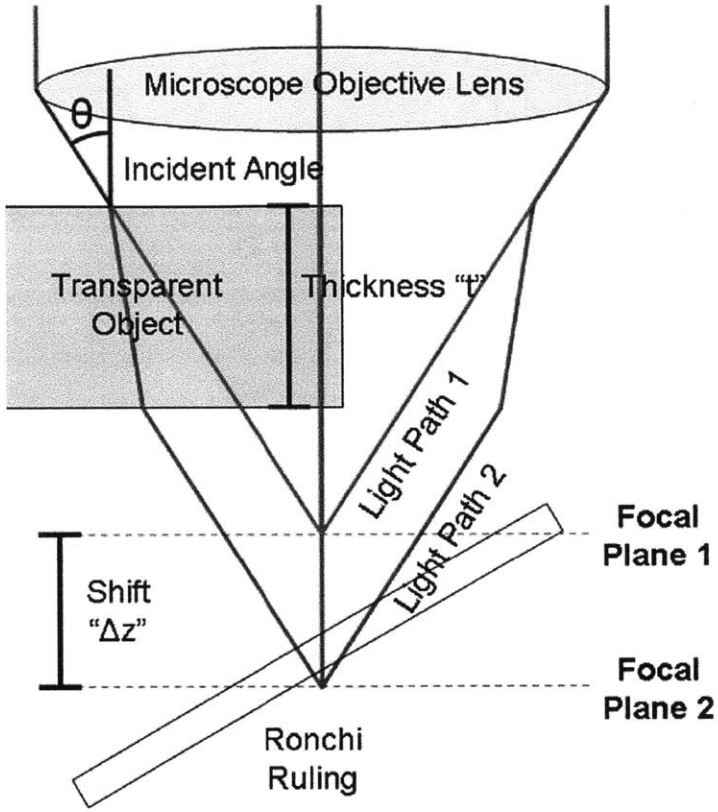

Figure 10-9: Schematic to Detail the Bending of Light. This figure shows in detail how the flat transparent medium will shift the focal plane of the camera a distance ΔZ. The change in focal plane is measured by the sensor and related back to the thickness of the medium.

medium. The red path shows the bending of light caused by a flat, transparent object. The introduction of a transparent object of thickness "t" causes the focal plane to sink a distance "ΔZ." The purpose of this analysis is to relate the two variables t and ΔZ as a function of the intrinsic properties of the physical hardware. Later it is described physically how this shift of the focal plane location manifests itself into a peak shift in the standard deviation plot.

The diamond shape with the blue outline in Figure 10-10 is highlighted in order to simplify the diagram. The light path highlighted in red continues upon a parallel path to its original incident angle after exiting the transparent object. Using this parallel nature the length of the vertical leg in the diamond is equated to the

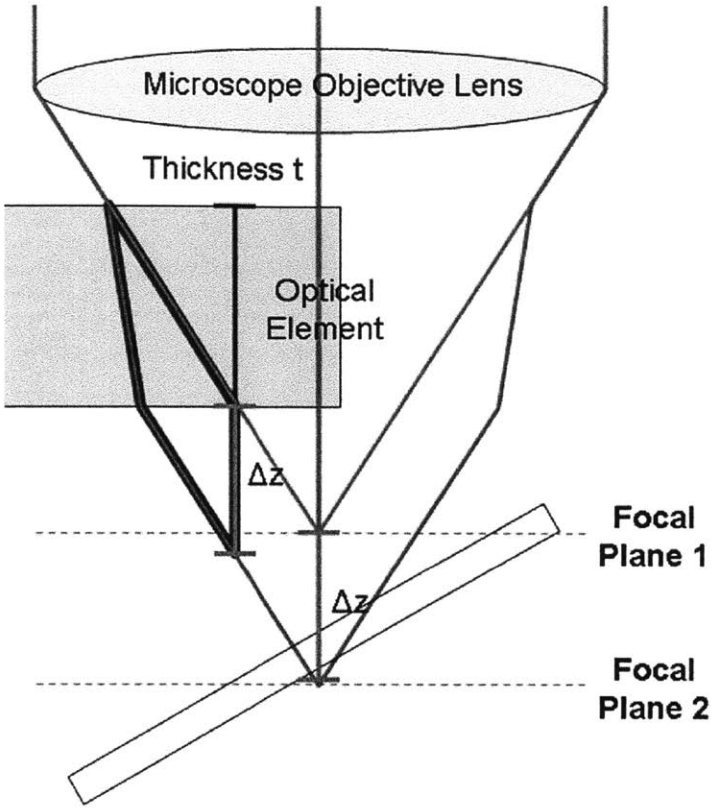

Figure 10-10: Identification of Blue Diamond in the Figure. The blue, highlighted portion of the light path shows the geometrical difference between the red and green trajectories of light. The orange section labeled ΔZ is subtracted from both paths to highlight their difference.

distance ΔZ, the unknown variable being solved for in this analysis.

Ray tracing is used to analyze the geometry of the light propagation. Figure 10-11 shows an enlarged perspective of the diamond defined in Figure 10-10. At the top of the figure, both red and green rays overlap each other as they both share the same incident angle θ_1. At the air glass interface, the red path bends to an angle θ_2 as measured from the vertical. The green path continues at its original trajectory demonstrating the path of light in absence of a transparent medium. The angle θ_2 is solved for in Equation 10.2 using Snell's law to relate the angles of incidence to the indices of refraction between the air and glass.

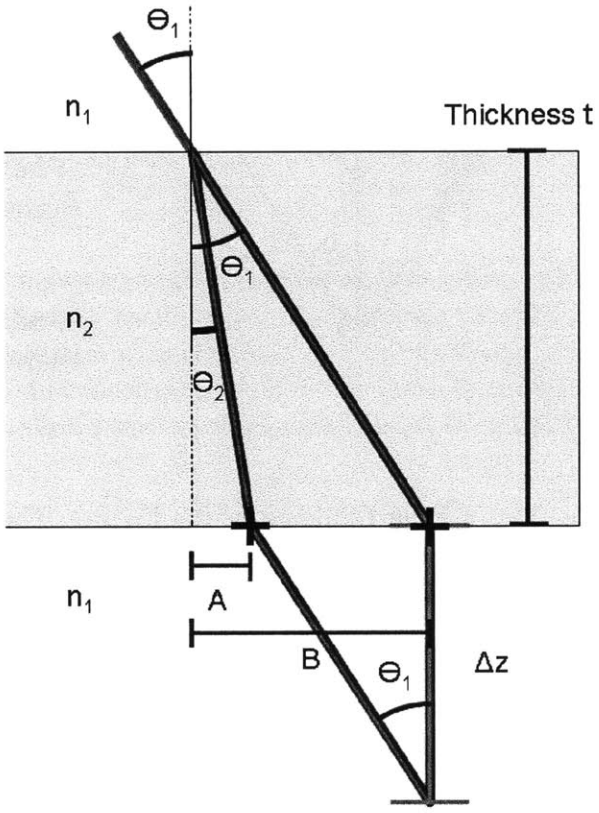

Figure 10-11: Analysis of Blue Diamond. The blue diamond defined in Figure 10-10 is now enlarged and marked to show dimensions and angles important to understanding the bending of light.

$$n_1 \cdot \sin\theta_1 = n_2 \cdot \sin\theta_2 \tag{10.2}$$

$$\theta_2 = \sin^{-1}\left(\frac{n_1 \cdot \sin\theta_1}{n_2}\right) \tag{10.3}$$

The two distances A and B are defined in Figure 10-11 resulting from these light paths. These distances represent the horizontal distance traveled by the red and green light rays respectively before propagating a vertical distance "t" equal to the thickness of the glass. Using simple geometry these intermediate variables are defined in terms of the physical properties of the hardware.

$$A = t \cdot \tan\theta_2 \tag{10.4}$$

$$B = t \cdot \tan\theta_1 \tag{10.5}$$

Once the light following the red path has exited the transparent material it continues on a path parallel to its original trajectory. This path creates the hypotenuse of a second triangle inscribed into the original blue diamond. As seen in Figure 10-11, the other two legs of this right triangle are mathematically defined as the distance (B-A) and ΔZ: the quantity being solved for for in this analysis. By the corresponding angle theorem it is recognized that the angle formed between the hypotenuse and vertical leg is the same angle θ_1 defined by the original rays entering the system. Using simple geometry these variables are related in Equation 10.6.

$$\Delta Z = \frac{B - A}{\tan\theta_1} \tag{10.6}$$

Using Equations 10.4 and 10.5 the intermediate variables A and B are substituted out to express the distance ΔZ in physical terms.

$$\Delta Z = t \cdot \frac{\tan\theta_1 - \tan\theta_2}{\tan\theta_1} = t \cdot \left(1 - \frac{\tan\theta_2}{\tan\theta_1}\right) \tag{10.7}$$

The equation is further simplified by expressing angle θ_2 in terms of angle θ_1 as defined by Equation 10.2 to define ΔZ by the physical quantities t, n1, n2, and θ_1.

$$\Delta Z = t \cdot \left(1 - \frac{\tan\left(\sin^{-1}\left(\frac{n_1 \cdot \sin\theta_1}{n_2}\right)\right)}{\tan\theta_1}\right) \tag{10.8}$$

10.4.1 Interpreting the Results

The relationship between ΔZ by the physical quantities t, n1, n2, and θ_1 derived in Equation 10.8 has some interesting consequences. First it is noted that the thickness of the glass "t" and the shift in the focal plane ΔZ are proportionally related. This theoretical relationship is verified in the observations and agrees with our intuition. Secondly it is found that this relationship is not purely proportional, but a function of the incident angle θ_1. The other two variables in the equation n_1 and n_2 are finite properties of the air and glass and are not subject to change based upon time or how the sensor and hardware are physically assembled. A different constant of proportionality is computed between the thickness "t" and focal plane shift ΔZ based upon the value of θ_1. Using the indices of refraction of air and glass of 1.0 and 1.52 respectively, this constant of proportionality as a function of θ_1 is charted in Figure 10-12.

The sensor will collect data from a range of incidence angles when focusing light through the microscope objective. The focal plane shift ΔZ perceived by the camera thus becomes an amalgamation of effects from the entire range of accepted incidence angles. The effect of incidence angle on ΔZ can be quantified by exploring its boundaries. At a minimum, angle θ_1 is set equal to zero. Under these conditions the small angle approximation becomes valid and simplifies the equations. The derivation is most clearly expressed by first solving for angle θ_2 by applying the small angle approximation to Snell's Law of Refraction.

$$\theta_2 = \frac{n_1 \cdot \theta_1}{n_2} \tag{10.9}$$

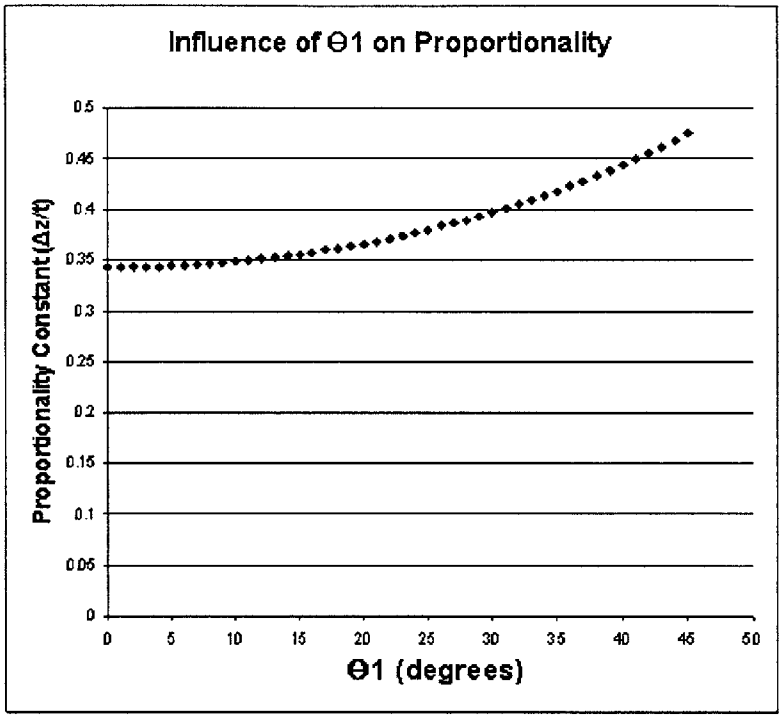

Figure 10-12: Graphic the Change in the Proportionality Constant. The theory predicts that the observed peak shift can be calculated by multiplying the thickness of the medium by a proportionality constat. This proportionality constant is a function of the incidence angle of light. This graph shows how the proportionality constant changes as the angle of incident light is increased from 0 to 45 degrees.

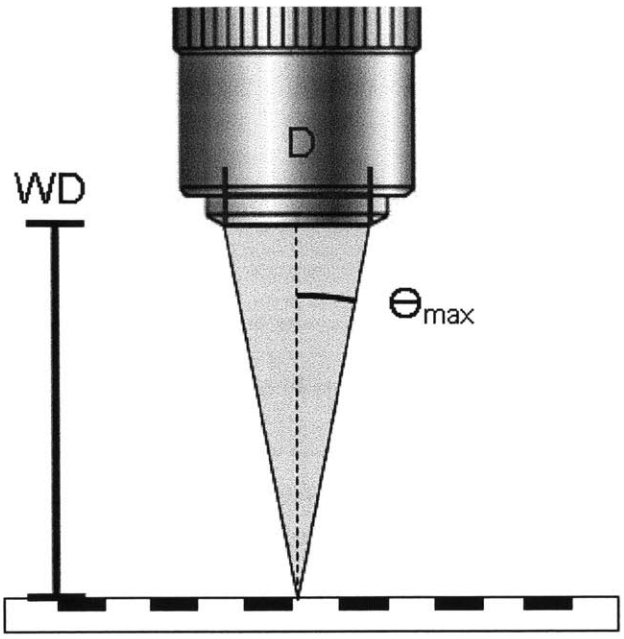

Figure 10-13: Relating the Maximum Angle of Acceptance to the Numerical Aperture. This figure demonstrates how the maximum accepted angle of incident light is directly proportional to the numerical aperture.

This relationship is then substituted into Equation 10.8 to solve for the minimum value of the proportionality constant between "t" and ΔZ.

$$\Delta Z_{minimum} = t \cdot \left(1 - \frac{\tan\theta_2}{\tan\theta_1}\right) = t \cdot \left(\frac{n_2 - n_1}{n_2}\right) \tag{10.10}$$

Conversely the maximum bound of the proportionality constant can be solved for. Conveniently, the maximum accepted value of incidence angle is a well known property of all microscope objectives as it is directly related to the numerical aperture. The numerical aperture of a lens relates the diameter of the objective to its working distance. As illustrated in Figure 10-13, these two physical parameters are related by the tangent of the maximum accepted incidence angle.

The two variables working distance and diameter of a microscope objective are related to the maximum accepted angle only in principle. In practice, the maximum accepted angle is found empirically and can be related to the numerical aperture

using Equation 10.11.

$$NA = \sin\left(\theta_{max}\right) \tag{10.11}$$

Akin to the index of refraction, the numerical aperture of a lens is an intrinsic property of the hardware. This relationship in Equation 10.11 is first substituted into Snell's law of refraction. Next, this entity is plugged into Equation 10.8 to calculate the maximum theoretical focal plane shift we can expect from the system based upon the physical hardware.

$$n_1 \cdot NA = n_2 \cdot \sin\theta_2 \tag{10.12}$$

$$\Delta Z_{maximum} = t \cdot \left(1 - \frac{\tan\left(\sin^{-1}\left(\frac{n_1 \cdot NA}{n_2}\right)\right)}{\tan\left(\sin^{-1} NA\right)}\right) \tag{10.13}$$

The minimum and maximum values of ΔZ calculated in Equations 10.10 and 10.13 represent the upper and lower boundaries expected from the physical analysis. The theoretical calculations are validated by the empirical results in the next section.

10.4.2 Exploring the Empirical Results

The measured output of our novel sensor is compared against its theoretical model to explore the phenomenon of peak shifting in this section. To demonstrate this concept, the novel sensor measures the thickness of six microscope slides. All six 3" x 1" pieces of glass were generously donated by a representative from Howard Glass in Worchester, MA. Each slide had a different thickness ranging from 22 to 63 thousandths of an inch (559 to 1,600 microns). Each piece of glass was also measured by a micrometer to get a second reading on its thickness. Figure 10-14 shows the output of the camera for all six thickness of glass side by side. This figure is most useful for the reader to get an intuitive understanding of how the raw images of the camera are translated into the thickness measurement via image

Slide	Micrometer Measurement (μm)	Sensor Measurement (μm)	Percentage Difference
1	22.3	22.69	1.72
2	26.8	27.06	0.97
3	37.0	37.22	0.60
4	42.8	43.06	0.60
5	48.3	48.23	0.14
6	63.1	63.23	0.21

Table 10.2: This table holds the values of thickness measurement on the six slides as measured by the novel sensor and a micrometer.

processing. The MATLAB code calculates the pixel shift from the zero position from each image. This pixel shift is transformed into a thickness measurement by the analysis outlined in the previous sections. Table 10.2 compares the thickness of the glass as measured by both the micrometer and the sensor. These results are also shown graphically in Figure 10-15.

It is found the average difference between the micrometer reading versus our sensor is 0.22 microns. This discrepancy is well within the 2.54 micron accuracy tolerance stated by the micrometer manufacturer Mitutoyo. Additionally, there may have been other sources of error such as discrepancy in positioning or thermal effects that may influence the reading. In light of these small errors it is concluded that our sensor is at least the same if not better accuracy as a micrometer when measuring the thickness of transparent glass.

Lastly, it is important to compare the measurements taken by the new sensor against the values predicted by the theory. The theoretical prediction was bound by two maximum and minimum values based upon the range of incidence angles present during the collection of information. In Figure 10-16, the maximum and minimum values are overlaid upon the measured values taken by the sensor. It is clear from this graph that the measured values fit well within the minimum and maximum bounds.

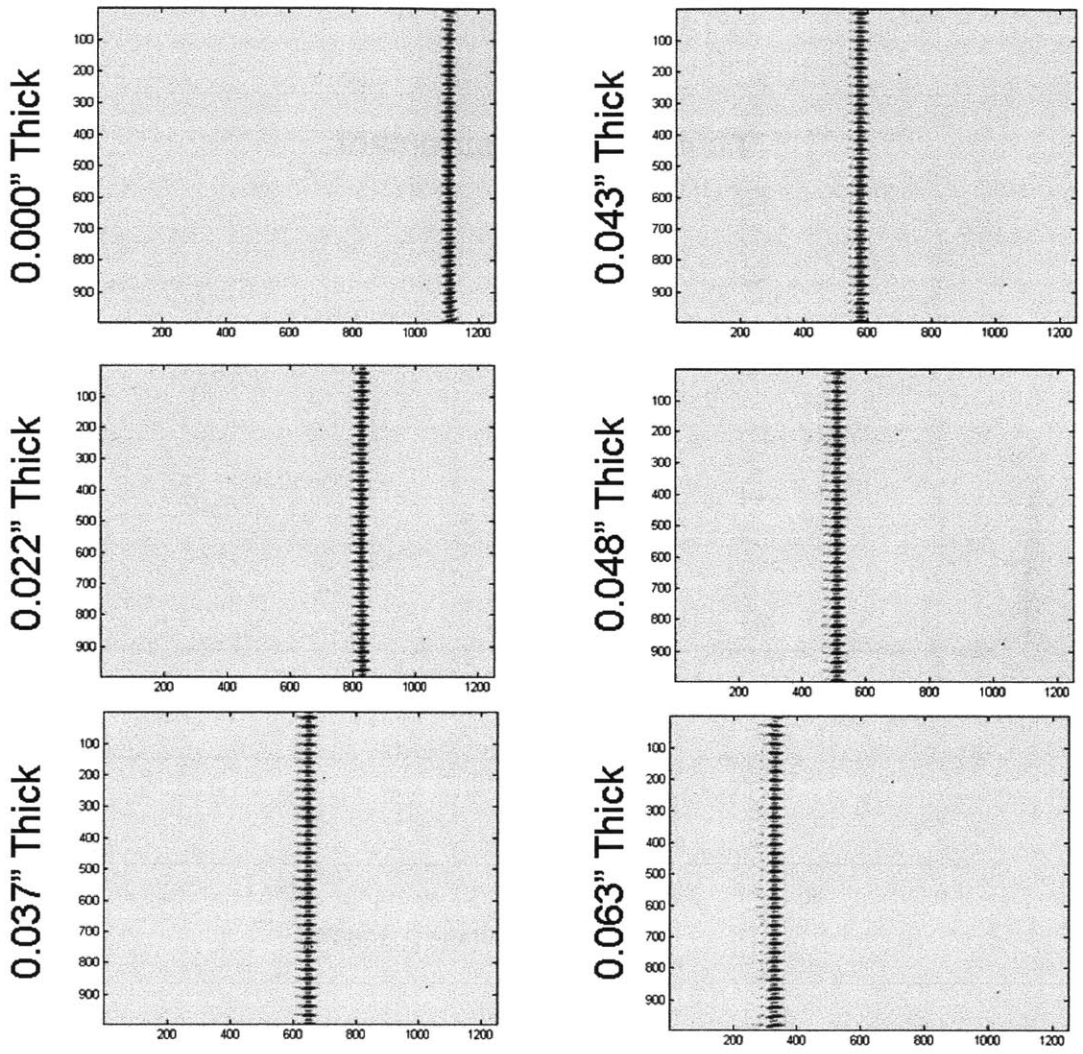

Figure 10-14: Changes in the Output Image as a Function of Thickness. The location of the observed signature will shift based upon the thickness of the medium being observed. Each one of these six photographs shows the output of the camera as the thickness of the observed medium is increased. This group of graphs gives the reader an institutive understanding of how the camera can detect changes in thickness.

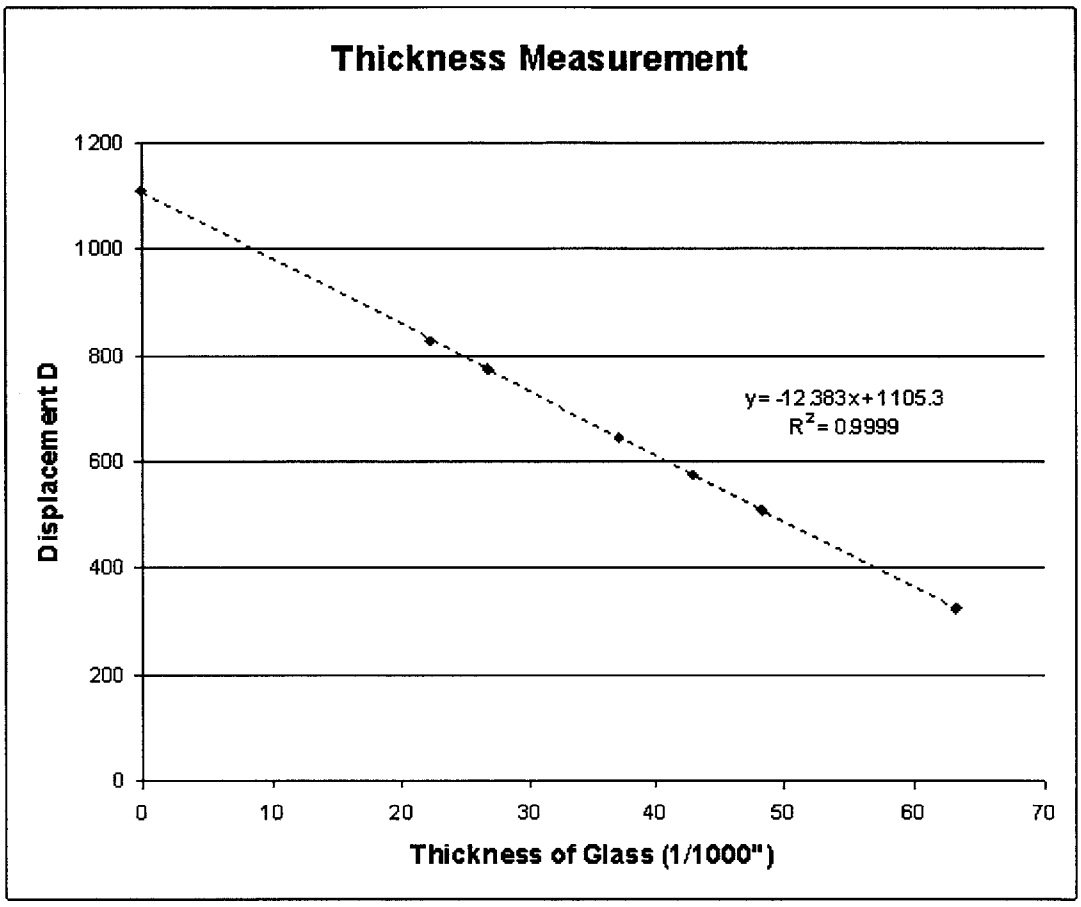

Figure 10-15: Sensor Thickness Measurement Compared to Micrometer Reading. The thickness of six slides were measured with both a micrometer and the novel sensor. This graph plots both measurements against each other. Also shown on the graph are the maximum and minimum values of the sensor measurement as predicted by our theory.

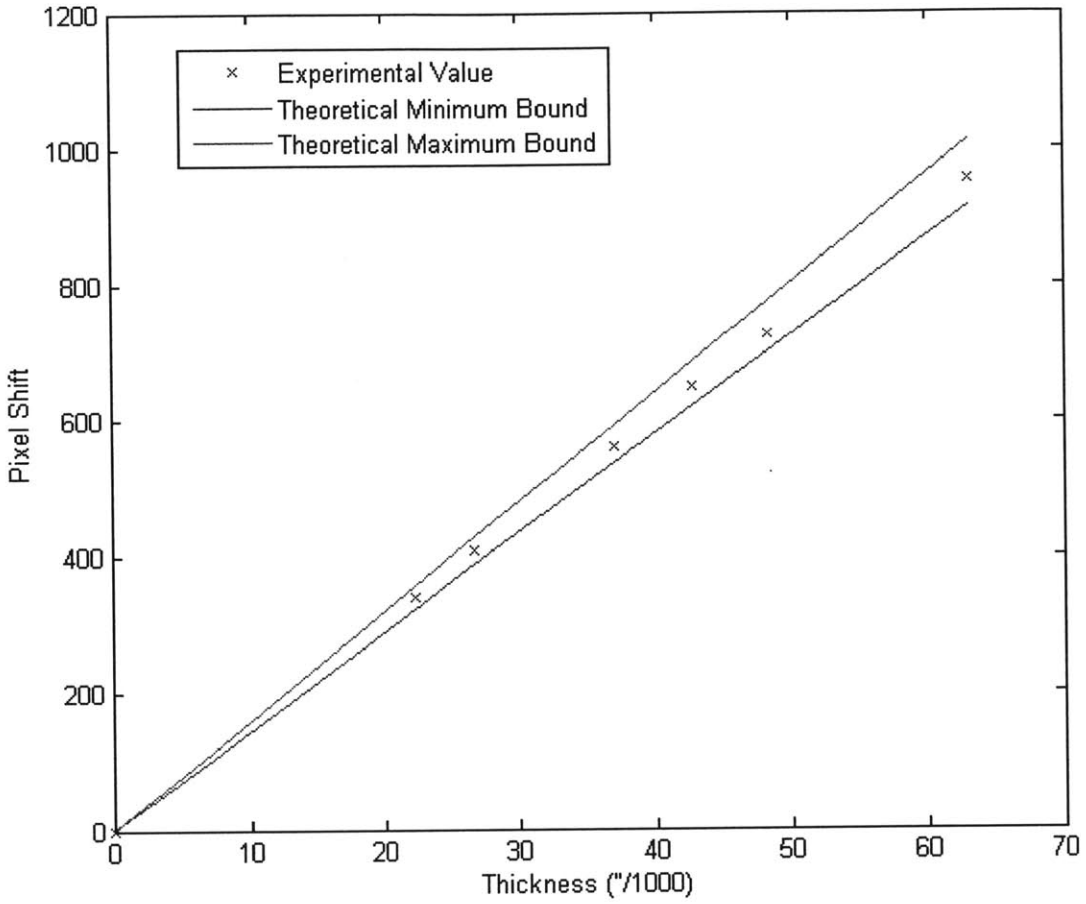

Figure 10-16: Pixel Shift Versus Micrometer Reading. Our theory predicted a maximum and minimum value for the pixel shift given the range of acceptance angles. As predicted, the empirical measurements fell in between these theoretical limits. The maximum limit is shown in red while the minimum limit predicted by the theory is shown in green.

10.5 Peak Splitting

Lastly the phenomenon of peak splitting is examined. Peak splitting occurs when a transparent object is partially inserted into the field of view. As a result, the light entering microscope objective becomes focused on two different planes. The standard deviation plot is altered to show two different peaks with reduced amplitudes. Analysis of this information enables the sensor to determine the lateral position of the transparent object with respect to the camera. Furthermore, the dual peak graph gives enough information to separate the thermal effects in the metrology loop from the desired measurement. Through these measurements the sensor demonstrates the capability to simultaneously measure the thickness and lateral position of a transparent object.

First we examine how the light is distributed between the two focal planes. As described in the previous section, the microscope objective focuses the light emanating from the focal plane onto the camera sensor. When a flat transparent glass is partially fully into the camera's field of view a portion of the light becomes focused on a second plane a distance ΔZ lower than the original plane. It is hypothesized that the percentage of light focused on the lower plane is proportional to the percentage of the field of view occupied by the transparent object. The theoretical analysis to substantiate this claim is derived in the following sections and experiments are crafted to test its validity.

10.5.1 Explanation of the Theory

A definition of the camera's field of view must first be established to properly evaluate the theory. The field of view is defined as the area visible by the camera sensor or eye observing an object through an optical system. All optical elements have physical limitations that constrict the area of light accepted by the lens. In the sensor's particular apparatus a C-Mount camera system was chosen for its standard size provided the largest field of view accompanied by sufficient commercial

products tailored for its geometry. Although digital cameras will always use square or rectangular sensors, the maximum field of view is circular for its boundaries are defined by the physical tube and lens elements.

The field of view definition is built upon by introducing a second quantity dubbed "active area." The active area refers to a horizontal slice from the conical volume highlighted in blue in Figure 10-17. The base of the cone is defined by the diameter of the last optical element in the microscope objective whereas the point of the cone is defined by the field of view at the focal plane. The volume of this cone represents the physical space included in the light path. Any object inserted into this volume will have an effect on the light focused unto the camera sensor. Conversely, any object outside of this cone will have no effect on the light focused on the camera sensor. Using this definition for the active area, the hypothesis is stated more precisely whereby the percentage of light focused on the lower plane is proportional to the percentage of active area occupied by the transparent object.

To test this theory we first solve the for amount of active area covered as a function of height and lateral position of the transparent medium. The coordinate frame is set up such that the Z axis is oriented concentrically with the microscope objective. The X and Y axis lie in the plane defined by the active area. The equation is first evaluated at a height Z_o. The active area is visualized as a circle with radius r_o when looking down the barrel of the microscope. Using the coordinate system displayed in Figure 10-18 the percentage of active area covered by a slide is described as a function of its height on the y axis in Equation 10.14.

$$\% \text{ Area Covered} = \frac{100}{\pi} \cdot \left(\frac{y}{r_o} \cdot \sqrt{1 - \frac{y^2}{r_o}} + \sin^{-1} \frac{y}{r_o} + \frac{\pi}{2} \right) \tag{10.14}$$

The percentage of active area covered as a function of the lateral position of the glass is displayed in Figure 10-19 to gain an intuitive perspective of Equation 10.14's nature. Here r_o is defined to be equal to 1 for simplicity. As expected, the slope of the graph equals zero at both ends representing where the glass enters and exits the

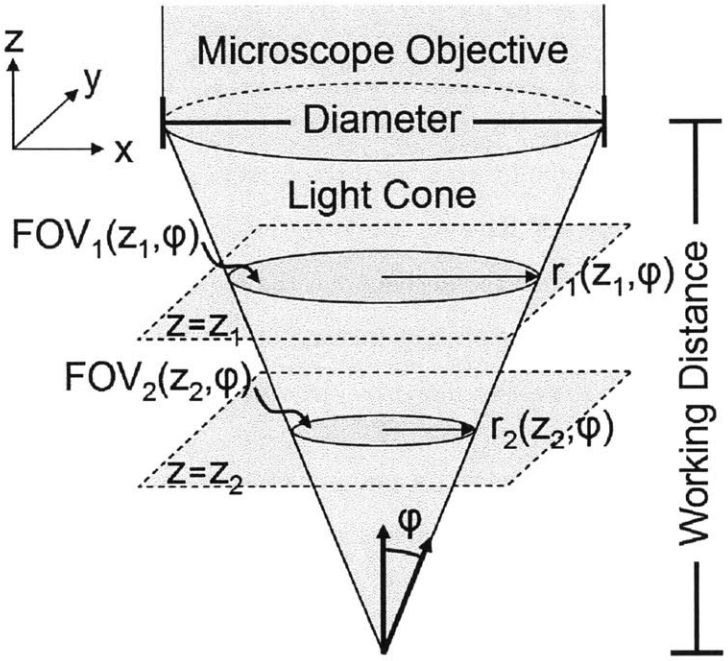

Figure 10-17: Active Area as a Function of Height. The light emitted from the part and accepted into the microscope objective has a cone shaped geometry. While the Ronchi grating is positioned at the focal plane of the camera, the transparent medium is able to enter this cone at any elevation. The radius of the field of view or 2D projection of this cone is dependent upon the elevation of the transparent medium. This figure is used to depict this concept.

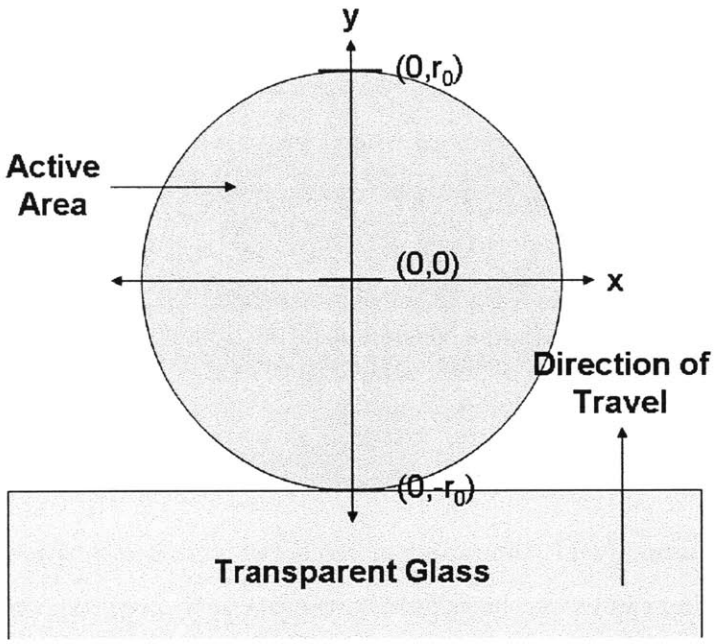

Figure 10-18: Measuring Active Area by Slide Position. Equation 1.14 references a coordinate frame defined by the field of view of the camera. The purpose of this figure is to show the reader graphically how said coordinate frame is laid out. The origin (0,0) is defined as the center of the field of view as visualized by looking down the barrel of the microscope. The transparent medium which partially covers the active area moves along the Y axis. The radius of the active area is denoted by variable r to signify that it changes with elevation.

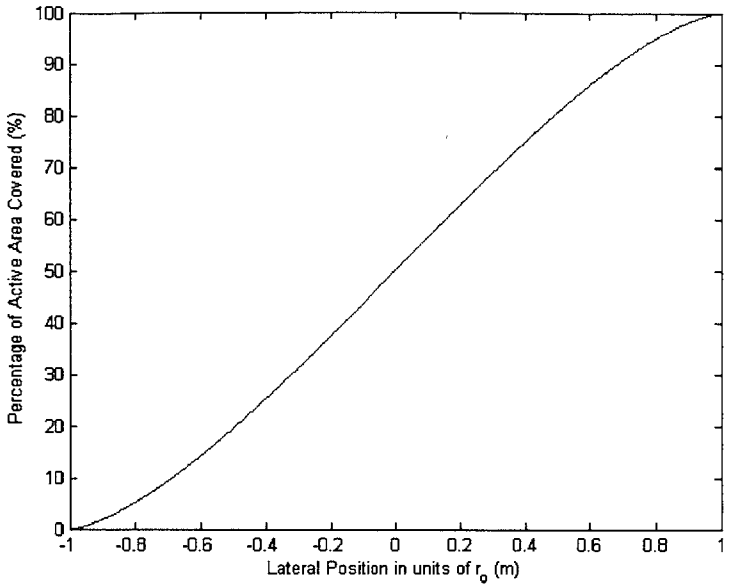

Figure 10-19: Active Area as a Function of Normalized Lateral Position. This graph shows the percentage of active area covered as a function of y position. The y position is parameterized as a fraction of the radius of active area at height Z_o.

active area.

As depicted in Figure 10-17, the radius of the active area is a function of its height on the Z axis. This radius can be related to the physical properties of the system by using the properties of the active area cone. In theory, the maximum radius of the base of the cone is equal to the diameter of the last lens while its height is equal to the working distance of the lens. This relationship is summarized in Equation 10.15.

$$r_{\text{Active Area}} = \frac{D \cdot z}{2WD} = \tan\phi \cdot z \tag{10.15}$$

where WD = Working Distance(m)

D = Diameter of objective lens (m)

ϕ = Spread angle of Light Cone

z = Elevation (m)

This equation is be substituted into equation 10.14 to define the percentage of active area covered as a function of the vertical and lateral position of the

transparent object. Using Equation 10.16 the lateral position of the transparent glass can be solved for by keeping its vertical position constant and measuring the amount of light focused on the second plane.

$$\% \text{ Area Covered} = \frac{100}{\pi} \cdot \left(\frac{y}{z \cdot \tan\phi} \cdot \sqrt{1 - \frac{y}{z \cdot \tan\phi}^2} + \sin^{-1} \frac{y}{z \cdot \tan\phi} + \frac{\pi}{2} \right) \quad (10.16)$$

As per the hypothesis, the percentage of light focused on the lower plane is proportional to the percentage of active area occupied by the transparent object. This hypothesis is tested by comparing the values of both quantities. The first quantity is measured by our sensor via the standard deviation plot. The second quantity, percentage of active ares occupied by the transparent object, is estimated by the theory presented in this section. As the transparent glass slides further into the field of view, the second peak on the standard deviation graph grows taller. The strength of the second peak is calculated by numerically integrating the area underneath the curve for each frame taken by the camera. This numerically calculated value is used as a representation of the amount of light focused on the lower plane. This quantity is expressed mathematically in Equation 10.17 and graphically in Figure 10-20.

$$\text{Area}_k = \sum_{j=c-50}^{c+50} \sqrt{\sum_{i=1}^{M} \left(x_{(i,j)} - \sum_{i=1}^{M} \frac{x_{(i,j)}}{M} \right)^2} \quad (10.17)$$

where M = Number of Rows

$x_{(i,j)}$ = Intensity Value of Pixel in Row I, Column J

c = Center Column of the Peak Distribution

i = Row Number

j = Column Number

k = Frame Number

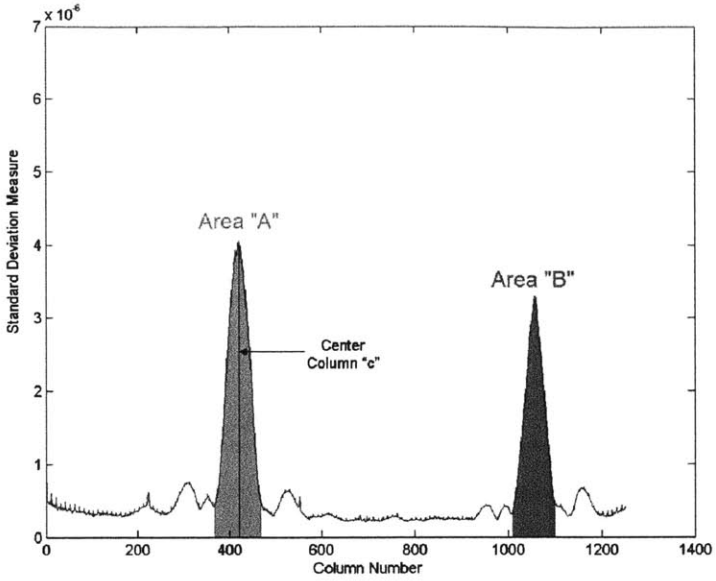

Figure 10-20: Measuring the Strength of Both Signals. This figure shows a standard deviation plot with two peaks generated when the active area is partially covered with a transparent glass. The lateral position of the glass can be determined by integrating the area under both peaks and then comparing their values.

10.5.2 Experimental Results

This section first describes the experiments chosen to confirm the theoretical analysis and then displays their results. The purpose of these experiments is to validate the hypothesis which states the percentage of active area covered by the transparent object is proportional to the percentage of light focused upon the lower plane. We find that the experimental results support the theory proposed in the previous section.

The first experiment was conducted to examine if the theory accurately predicted the behavior of the light measure as the active area became occupied by a transparent glass. A 0.042" thick microscope slide was placed on to an automated stage. The slide was positioned to be in the middle of the working distance although its exact height with respect to the focal plane or microscope objective was unknown. The slide was incrementally moved along the Y axis at a displacement of 25 microns per step. The camera was programmed to take an image of the Ronchi

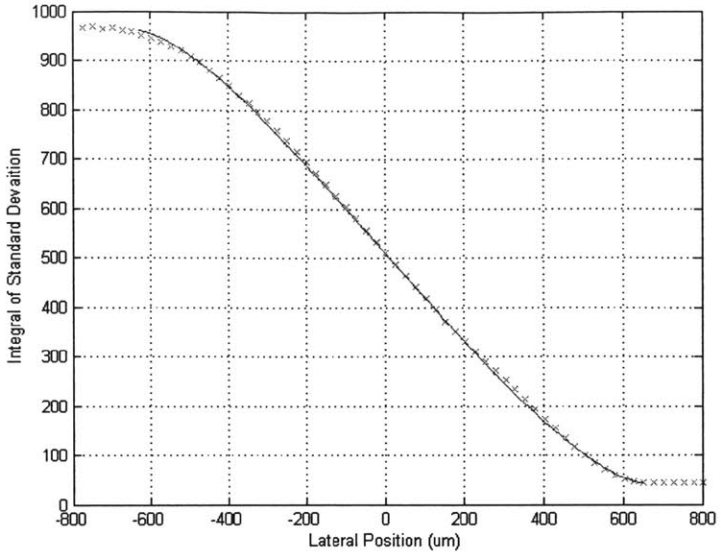

Figure 10-21: Lateral Position Sensor Output: Theoretical Versus Empirical Values. These results compare the measured standard deviation values in red against a fitted model shown in blue. The model is based from the active area theory presented in this chapter.

Ruling at the end of each step. After the data was collected, a standard deviation plot was created for each frame. The integral of the standard deviation centered about the first peak was calculated numerically. The standard deviation integral values are presented in red crosses as a function of lateral position shown in Figure 10-21. Overlaid on top of the data are the values predicted by our theoretical model in blue. The graph shows good correspondence between both sets of data.

The most important result found in this experiment is that the measured data and model share the same shape. This is testament that the standard deviation integral measurement was indeed representative of the amount of light focused on the lower plane. Furthermore the results suggest that the active area can be modeled as circular and its percentage of covered area affects the positioning of light in a linear fashion. Many of the variables in the model were not able to be measured such as Z height of the glass slide, working diameter of the microscope objective, and baseline noise in the standard deviation model and had to be fit to the data. Some of these variables such as the baseline noise need to be fit to the data for they are relative

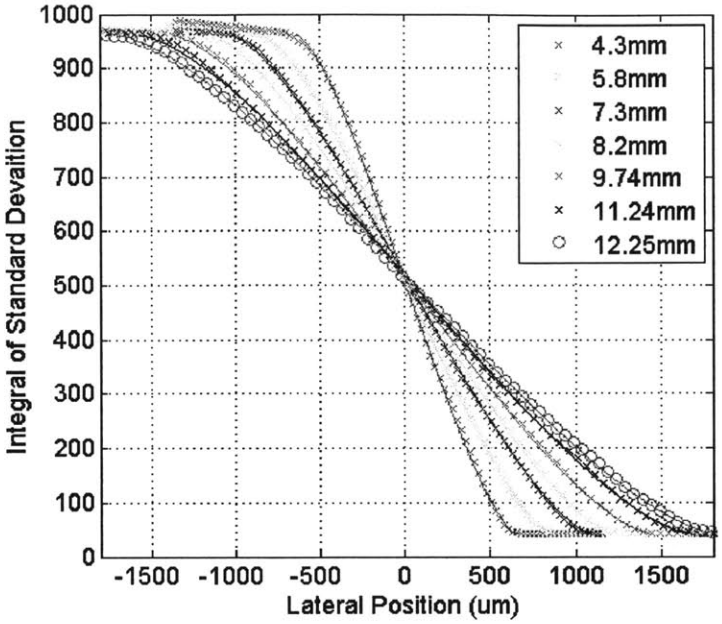

Figure 10-22: Repeat of Lateral Position Measurements at Seven Heights. The previous experiment compared the measured standard deviation against the model at a fixed elevation. The experiment was then repeated at different elevations. The results of each experiment as well as their theoretical values are presented in this figure.

measurements and require calibration in the field. Future experiments will be used to more rigorously test the model for the remaining fitted variables.

The second experiment was conducted to test if the measure of light cast upon the second level could be accurately predicted as a function of both height and lateral position. Again a microscope slide of 0.042" thickness was drawn across the field of view in discrete steps of either 25 or 50 microns. The Z stage was used to lift the microscope slide to repeat the test at seven different elevations spanning over eight millimeters in height. Figure 10-22 plots the integral of standard deviation against lateral position for each of the seven different tests. The data collected by the camera is displayed as cross marks while the model for each set of data is overlain with its corresponding color. Again there exists good correspondence between the model and the measured data.

The values of working diameter and baseline noise needed to be fit to the data.

Once these two parameters were fixed, their values were used unilaterally to predict the behavior of the sensor for all seven elevations. These results suggest that our model correctly predicts how the elevation of a transparent slide affects the amount of light focused on the second plane. Secondly, they reaffirm the suggested conical shape of the light path which first illuminates the sample and then gets collected by the microscope objective. This data gives confidence that our model can correctly predict the output of our sensor based upon the lateral and vertical position of the transparent glass.

The sensitivity of the sensor can be measured from the data collected in the previous experiments. From Figure 10-22 it is shown that at a height of 4.3mm the data shows that the output of the sensor goes from its maximum to minimum value over a lateral range of approximately 1.2 millimeters. Conversely at height of 12.3mm the same range of output is spread over 3.5 millimeters. Based upon the application the user can position the elevation of the transparent object to achieve their desired sensitivity or range.

The results of the experiment are presented in a more intuitive manner in Figure 10-23. The purpose of this figure is to visualize the data in a geometric nature. Seven horizontal lines of data are presented. The vertical and lateral position of each data point on the graph represents the position of the transparent glass when the data point was taken. The vertical position is measured from the height of the image plane. The darkness of the data point represents the change in output per lateral position. Thus, once the data turns white the transparent object has left the light cone and no longer has an effect on the output of the sensor. The geometry of the light cone can be empirically assessed from this data.

10.6 Dual Peak Measurements

The sensor registers two different peaks when a transparent medium is partially inserted into the field of view. The magnitudes of these peaks represent the relative

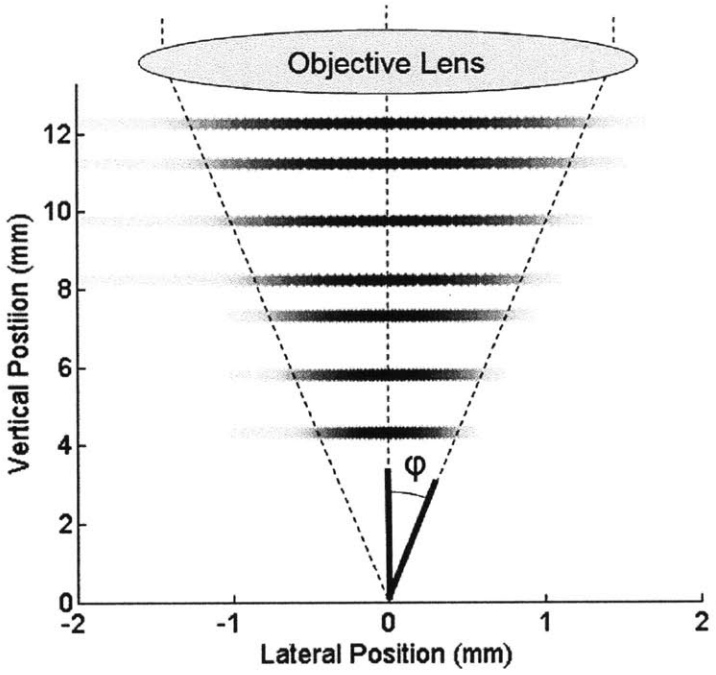

Figure 10-23: Visual Interpretation of Light Cone Geometry. The data from Figure 10-22 is recombined in this graph to visualize the shape of the light cone. The darkness of each pixel represents the change in standard deviation from one data point to the next. The point of this graph is to reinforce visually that the concept "light cone" predicted by our theory is indeed upheld by the experimental data. It is shown that once the object is outside of the light cone it no longer has any effect on the sensor reading.

amount of light focused on either of the two focal planes. This section explains how to use this second set of information to make our measurements of thickness of the transparent object more accurate.

Our sensor tracks the thickness and lateral position of a transparent object by first constructing the standard deviation plot. The algorithm searches for the column with the maximum value in the standard deviation plot in order to measure thickness. As the metrology loop expands and contracts through thermal variation it has been observed that the peak value can drift to different columns while the measured object remains the same. By measuring both peaks the sensor can separate thermal drift in the metrology loop from our desired thickness measurement.

The light path becomes split when the transparent object partially inserted into the field of view. One portion travels through the object while the other bypasses it. The portion of light that bypasses the object becomes the reference arm of the measurement. By calculating the relative measurement between these two light paths the sensor isolate the effect that the transparent object has on the light. Any thermal effects on the metrology loop will affect both peaks equally thereby canceling out when subtracting one peak position from the next. Such thermal variation can be characterized as a "peak shift" detailed in Section 10.4. A series of figures have been complied to illustrate this effect. First, a standard deviation plot with two peaks is shown in Figure 10-24. The algorithm automatically detecting the peaks and then implementing a second order least squares fit to the data to calculate both center columns.

The camera was set up to take one measurement per second for 1,000 seconds. Over this time we see that both peaks drift over 3 pixels in the same direction shown in Figure 10-25(a) and 10-25(b). In 10-25(c) the location of the first peak is subtracted from the second whereby the difference is approximately 560.4 $\pm$ 0.1 pixels. In the last frame the drift of the relative measurement is compared against the absolute

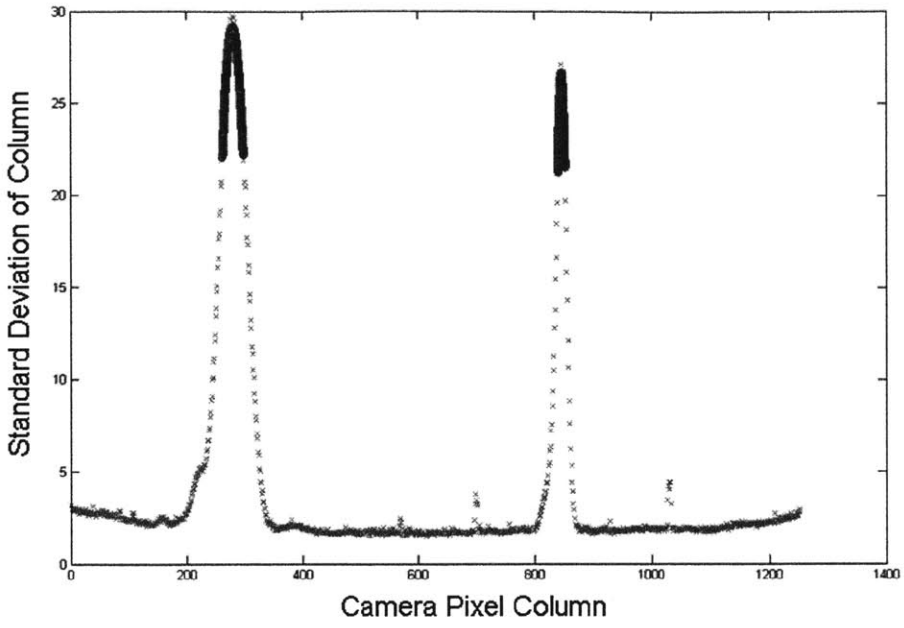

Figure 10-24: Dual Peak Measurement. When the transparent object is placed halfway into the field of view the sensor will measure two peaks. The center of each peak is first located and then calculated by MATLAB code. The difference between the two peaks is used as the thickness measurement.

measurement. This figure clearly illustrates the much improved stability of the reference measurement. The mean value of both the relative and absolute measurements has been subtracted away from itself to show the pixel drift as a function of time.

10.7 Sensitivity to Changes in Height

The sensitivity of the output to changes in height is examined. The sensor has but one measured output that is a function of both height and lateral position. Given the sensor has one measurement and two unknowns, it is impossible to tell if a change in the measured output was caused by either a change in height or lateral position. The data from the experiments is used to illustrate this point. Seven readings from the sensor, one at each elevation, are selected and displayed at the point where the transparent object was positioned 0.5 millimeters off center. The

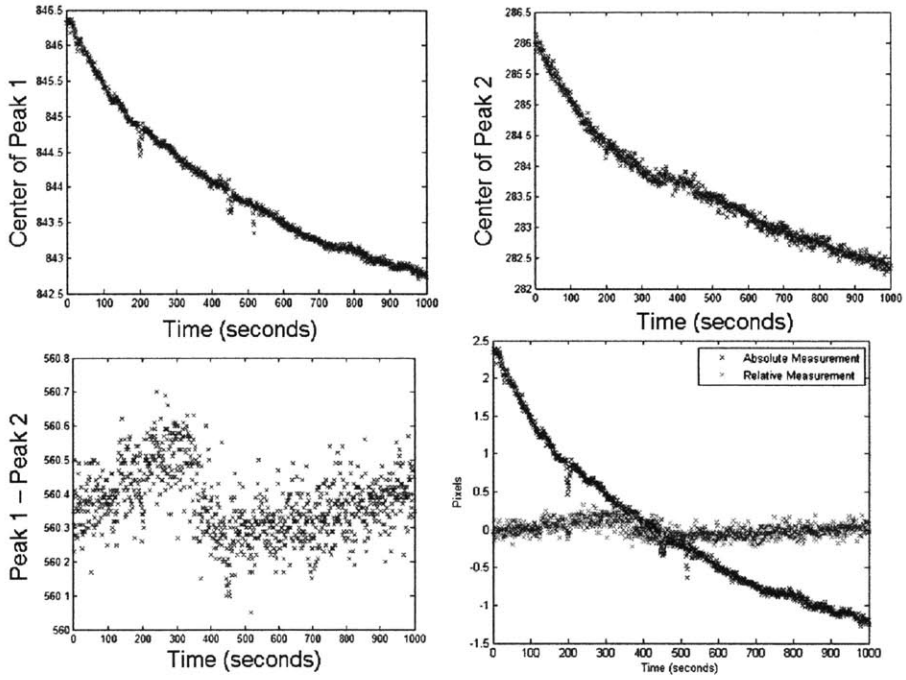

Figure 10-25: Tracking Thermal Drift Over Time. (a)Location of 1st peak over 1,000 seconds. (b) Location of 2nd peak over 1,000 seconds. (c) Relative measurement Location 1 minus Location 2 at each frame. (d) Relative thickness measurement versus absolute position of Location 1.

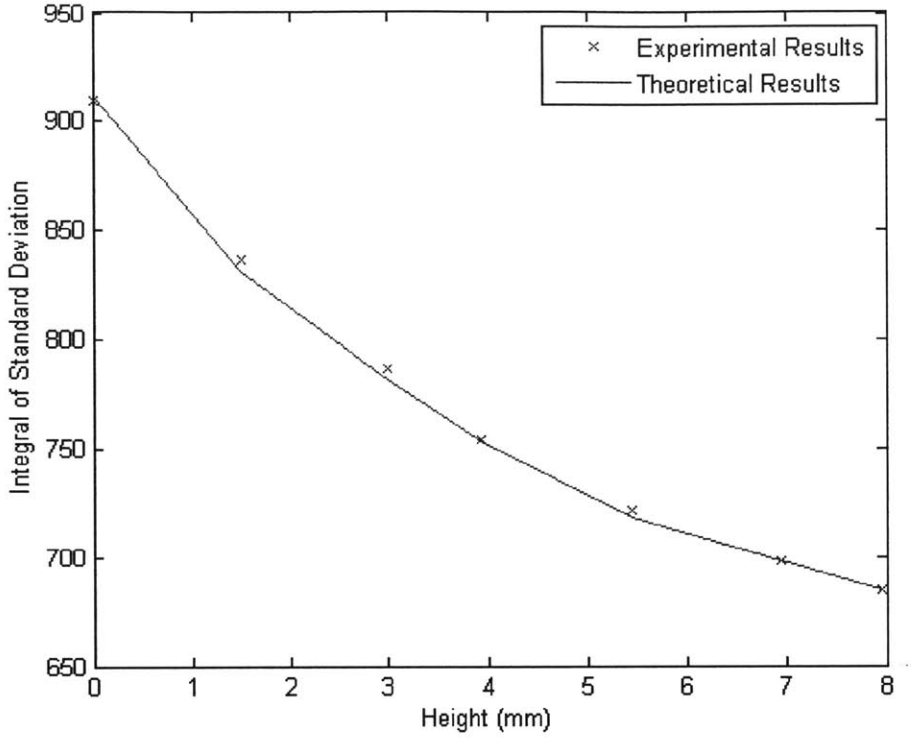

Figure 10-26: Predicting Change in Output as a Function of Height. This graph presents the output of our sensor for an object that has been moved vertically but remained in the same position horizontally. The values according to our theory are superimposed on the graph. The point of this figure is to show that our theory can accurately predict the output of the sensor as a function of the object's vertical position.

output of the sensor drops by 30% as the lateral position remains constant but the elevation is changed. The blue crosses display the measured data with the expected value from our model shown in green.

The intended application of this sensor assumes that the height of transparent medium will be fixed but will be able to move laterally. Under these conditions it is assumed that any change in the output will be a result of a lateral movement. Also it is assumed that the sensor can not be able to measure the height of the film. Given these assumptions, any unintended change in height will directly inject noise into the lateral position measurement. To mathematically evaluate the sensitivity to this error, the partial differential of the output with respect to change in height is

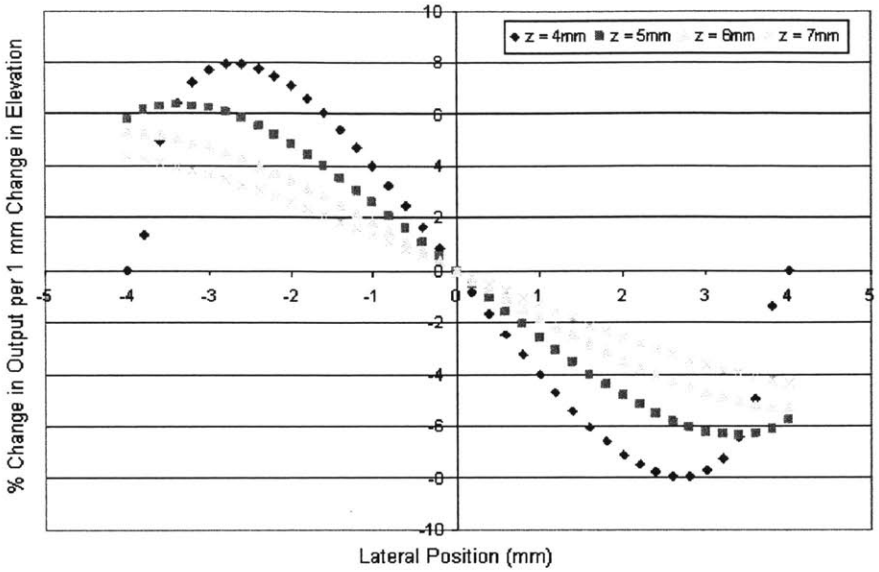

Figure 10-27: Estimating Output Error Caused by Changes in Elevation. This simulated data shows how the theory expects the output of the sensor to react to a 1 mm shift in elevation of the measured object as a function of that objects lateral and horizontal position. The X axis shows the lateral position of the object. The various curves each show the change in the sensor output (in percentage change) at the listed elevations.

calculated in Equation 10.18.

$$\frac{\partial \text{Output}}{\partial z} \propto \frac{y}{\pi \cdot \tan\phi \cdot z^2} \sqrt{1 - \left(\frac{y}{\tan\phi \cdot z}\right)^2} \tag{10.18}$$

The partial differential is evaluated at four different heights as a function of lateral position. In Figure 10-27, the X axis is in units of millimeters while the Y axis shows the percentage difference in output per 1 millimeter change in elevation. The data on the graph assumed the physical parameters a system with a numerical aperture of 0.43 and 20X magnification.

This sensitivity analysis can calculate and bound the amount of expected error from unintended changes in height. The data from the blue curve is used. The transparent object placed four millimeters above the focal plane during the capture of this data. The maximum sensitivity to error is found at the inflection point when

the transparent object is positioned laterally 2.6 millimeters off center. It is found that if a transparent object in this location were to be elevated by one millimeter it would change the output of the sensor by 8%. This effect is scalable for if the maximum uncertainty in height is estimated to be 1/10th of a millimeter, we can expect 1/10th the change in sensor output at 0.8%. In this manner the model can predict the maximum error in the sensor given the transparent object's vertical position, lateral position, and height uncertainty.

This sensitivity analysis can also be used to mitigate the errors that can arise from unintended changes in height. The model suggests an operating point where the transparent object is placed in the center of the field of view. It is found for all elevations in Figure 10-27 the change in height of the object in this position has in zero effect in theory on the output of the sensor. In this position the sensor output has the highest certainty that any change in the output is directly related to a lateral movement. The blue curve on the graph has a second point where the effect of height does not change the output stationed at ± 4 millimeters lateral displacement. The low sensitivity here is a result of the sensor becoming saturated where it is either outputting its maximum or minimum value. This is a poor choice to operate the sensor for the sensitivity to lateral positioning is also zero meaning that a change in lateral position will also have no effect the sensor.

10.8 Sensitivity to Changes in Tip and Tilt

This section reviews how the sensor reacts to movement of the web as it tips or tilts. The geometric optics and coordinate frame of such a motion are shown visually in Figure 10-28. Here, a transparent object of thickness "t" with index of refraction n_2 tipped off-axis at an angle α will cause the lateral displacement of a vertical light ray by a distance "S." This lateral shift of light causes the edge detector to observe the Ronchi grating pattern at a different column on the camera sensor. The effect of tip or tilt is indistinguishable from and increase or decrease in the thickness of the

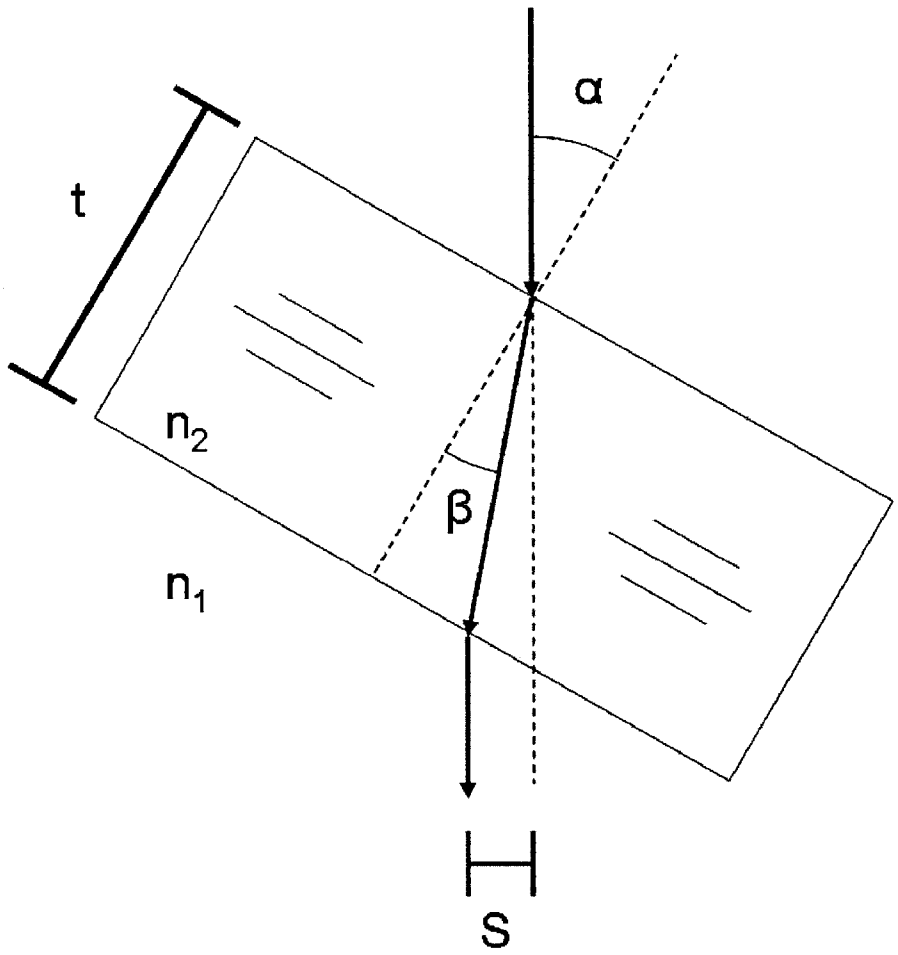

Figure 10-28: Accounting for Changes in Tip or Tilt. This cross sectional figure shows how a tip or tilt error can displace laterally a distance "S" the light collected by the camera sensor.

transparent medium. Thus, it is important to conduct a sensitivity analysis such that the effect of the tip tilt error can be quantified. Using geometric optics and Snell's law of diffraction, the distance "S" can be defined by the following equations.

$$\beta = \sin^{-1}\left(\frac{n_1}{n_2} \cdot \sin\alpha\right) \tag{10.19}$$

$$S = t\left(\sin\alpha - \tan\beta \cdot \cos\alpha\right) \tag{10.20}$$

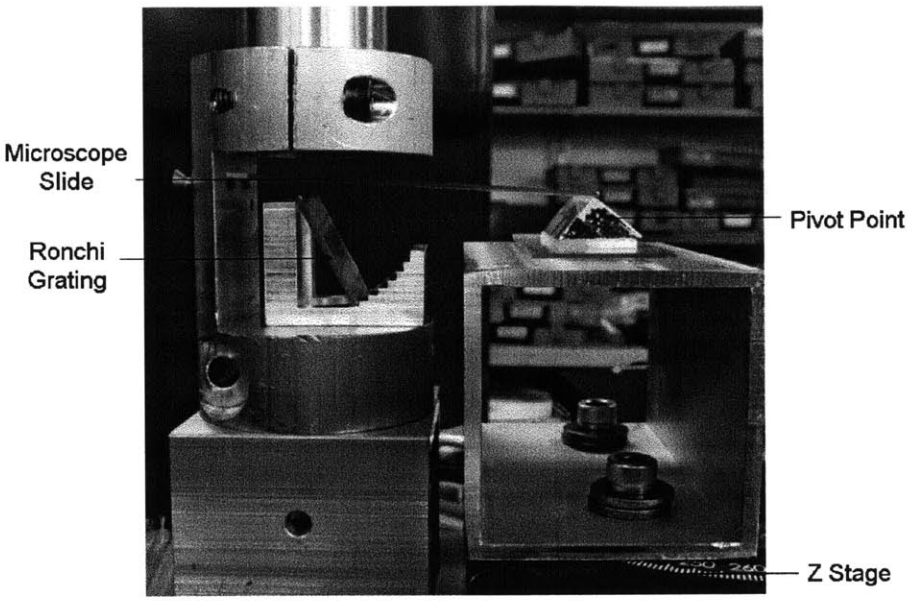

Figure 10-29: Experimental Setup for the Tip Tilt Experiment. This setup was used to evaluate the errors caused by tip or tilt. The observed microscope slide sits on a stationary post on the left and is elevated by the Z axis actuator on the right. The change in the standard deviation plot taken by the camera is recorded at each elevation.

An experiment was conducted to observe and measure this effect. The setup of the experiment is shown in Figure 10-29. A microscope slide was placed such that it covered the entire field of view of the camera. One end of the slide was allowed to rest on a stationary ground while the other was lifted by discrete increments by the Z stage. A picture was taken after every change in elevation. The standard deviation plot was calculated for every picture. Lastly, the curve fit was used to find the column that represented the center of the peak. The standard deviation plots with curve fits are shown in Figure 10-30 for glass thicknesses of 1,600 μm and 940 μm. These plots show how the lateral shift in light is proportional to thickness as proposed in the theory.

The center column of the standard deviation peak can be recorded for each change in elevation on each thickness of glass. Figure 10-31 shows all of these points plotted against each other. Again it is clear that the thicker glass causes a greater pixel shift for the same change in elevation. The slopes of each data set is then calculated

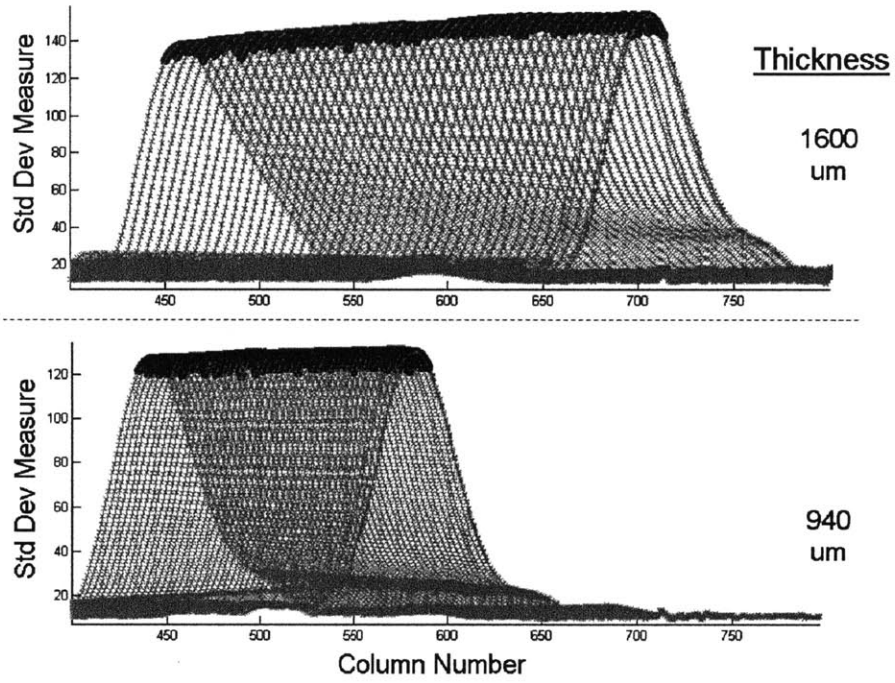

Figure 10-30: Output from the Tip Tilt Experiment. The standard deviation plot was recorded at each elevation or change in tilt prescribed by the experiment. This experiment was repeated about 30 times. Each of the 30 standard deviation plots are presented simultaneously on the top portion of this figure to show how the center of the peak shifts. The bottom portion shows a similar experiment using a 940 micron thick glass. Showing both of these figures in one graph illustrates clearly that the shift in the standard deviation plot is less pronounced for the thinner medium.

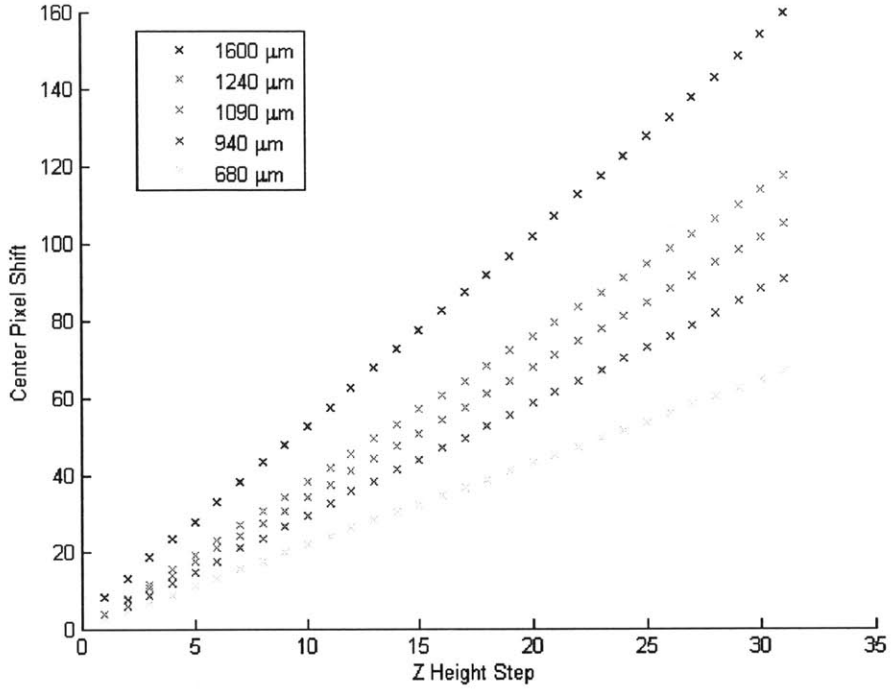

Figure 10-31: Plotting the Tip Tilt Information. This plot graphs the center of the standard deviation plot shift on the Y axis and height of the sample's side on the X axis. There are five different thickness shown on the graph again illustrating that the shift in the standard deviation plot is linearly proportional to the thickness of the medium.

and graphed against the thickness itself in Figure 10-32. The high correlation between the two sets of data with and R^2 value of 0.9997 again shows that the lateral shift seen by the camera is proportional to the thickness of glass.

This experiment validates that the change in tip tilt angle of the transparent medium is proportional to the pixel shift observed by the sensor. This information can be used as a second way to measure the thickness of a part by controlling the tilt angle and measuring the resulting pixel shift. Unfortunately by changing the tilt of the part, the light may propagate through a portion of the transparent medium with a different thickness thereby compromising the fidelity of the measurement. Alternatively, the analysis can be used to understand and estimate the errors due to tip and tilt. As stated prior, the effect of tip and tilt on the location of the pixels is indistinguishable from a change in thickness. By estimating the maximum expected

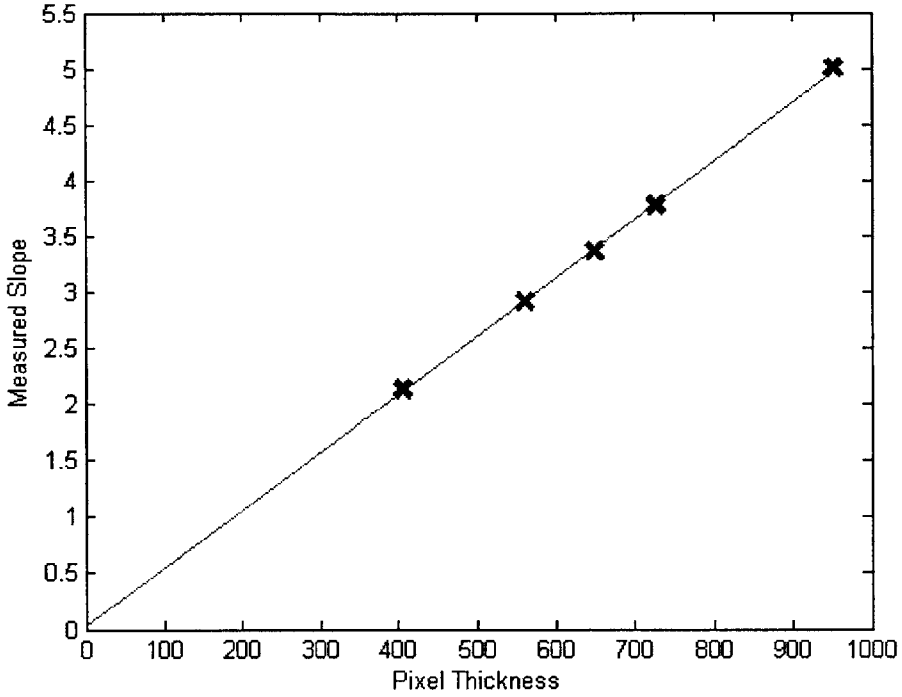

Figure 10-32: Relating the Slope of the Measurement Against Thickness. The slope of the data measured as change in pixel shift per change in elevation for each of the five thicknesses is plotted against the thickness itself to show the large correlation between the two measures.

tip or tilt, the error injected into the thickness measurement from this source can be quantified.

10.9 Comparison Against Commercial Technologies

The sensor described in this chapter has demonstrated the ability to measure the thickness and lateral resolution of a transparent web in a roll to roll process with a repeatability of 0.5 and 0.2 μm respectively. While various sensors have demonstrated measurement of thickness to a compatible degree, the state of the art sensors to measure lateral position of a transparent web can achieve 6 μm lateral resolution at best [56]. These sensors rely on acoustic signals that are easily refracted and dispersed though air. The state of the art sensor was purchased and installed next to our hardware in order to make an apples to apples comparison between itself and the novel sensor. A photograph sensor used in the experiment is shown in Figure 10-33 while its pertinent information is listed below:

Manufacturer: Re
Model: SU m-25
Serial #: ES 12124.0312

Both sensors recorded the position of a 20 micron step in lateral position. The results of this experiment are shown in Figure 10-34. This figure clearly shows the 30X improvement in resolution of our sensor over the state of the art alternative.

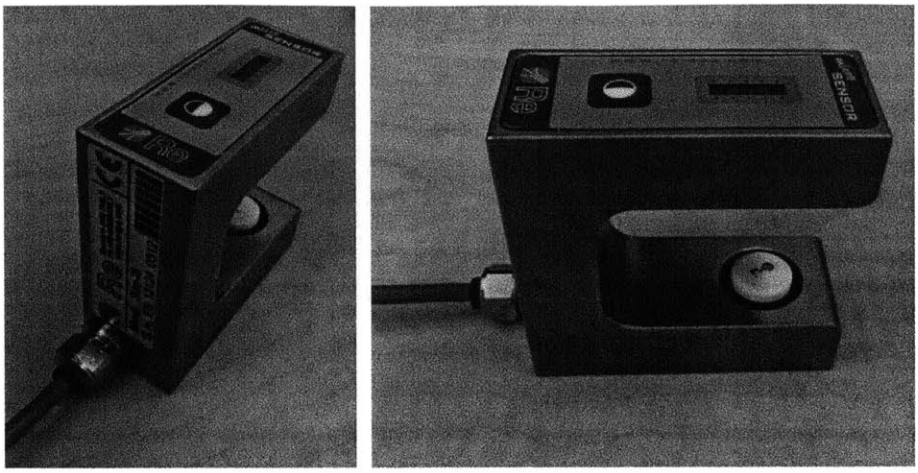

Figure 10-33: Photograph of the State of the Art Equipment. This photograph shows the state of the art acoustic sensor that was used to compare performance against our novel sensor.

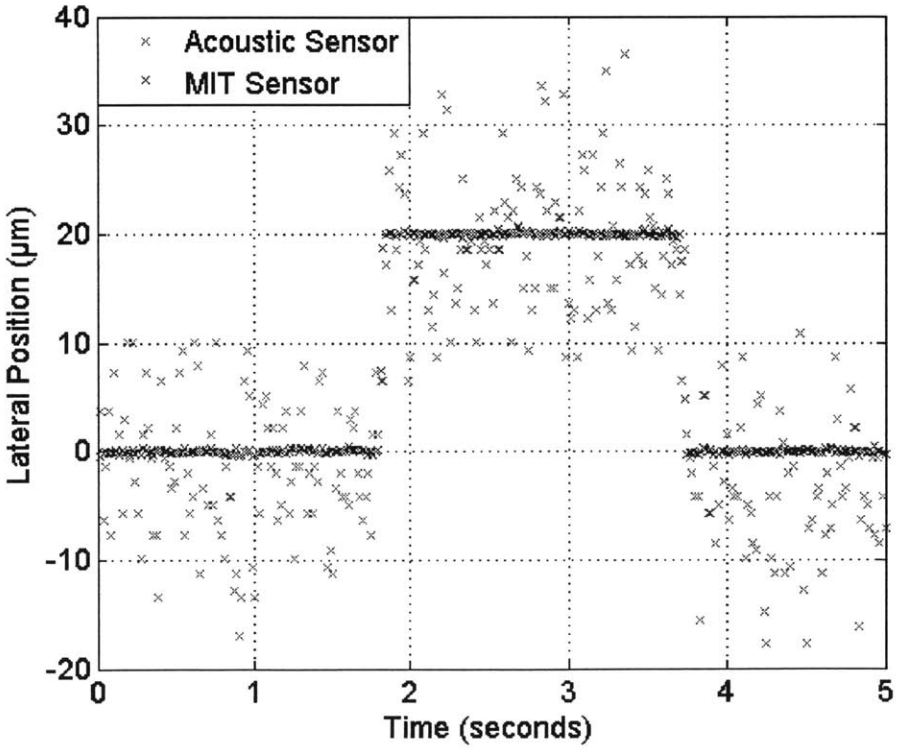

Figure 10-34: Apples to Apples Comparison Against the State of the Art Equipment. This graph shows the data taken from a state of the art acoustic sensor and our light based sensor while they simultaneously measured a 20 micron step change in lateral position.

Chapter 11

Future Work

This chapter serves to first recap the advances made in both arms of the PhD research and secondly to plot out the future work and challenges that need to be tackled in order to bring them to market. As is, both the high speed profilometer and edge and thickness detection sensor are in a research stage. The state and functionality of both instruments serves only to demonstrate their potential. Much of the hardware's flexibility and capability would need to be reorganized in a second iteration to optimize the performance with respect to cost. This chapter presents the suggested changes to the instruments for their second generation design.

11.1 High Speed 3D Profilometer

The high speed profilometer met or addressed all of the functional requirements laid out in the first chapter. The instrument distinguishes itself from current profilometers with the ability to measure topography at submicron lateral resolution while collecting the data for over half a million data points per second. It is important to note that the instrument does not yet have the capability to process the data in real time. The increase in inspection speed comes at the cost of poorer vertical resolution and a requirement of surface roughness on the measured part. The transparent nature of the measured part, typically seen as a obstacle given because of its poor reflection properties, was taken advantage of in order to transmit

a flood of light from the source into the camera. This lighting configuration provides enough light flux into the camera to support a high speed frame rate. In all, the final instrument designed in this research project demonstrated unique performance as compared against the other profilometers in the field whose weaknesses can be improved upon in the following ways.

11.1.1 Higher Speed Cameras

The first and most important improvement to the camera is to increase the rate at which the camera collects information. Currently, the Basler A504k camera captures 500 frames per second at a resolution of 1,280 x 1,024 pixels each. This equates to a 655 MB per second output. The Basler A504k camera used in the research provided adequate performance at a reasonable price. This camera allowed for demonstration of the basic principles and paved the way for a second iteration. It is suggested instead to use the Phantom v1610 which outputs 640 x 480 pixels at 45,700 frames per second. The reduced area of interest is limited by the diameter of the tube lens as explained in the next subsection. Although it can collect 14 gigapixels per second, the Phantom v1610 camera can only export 2 gigapixels per second. These cameras are built primarily to capture a short burst of information into RAM and then export and process the data offline. This limitation would need to be addressed or overcome to unlock the full potential of the high speed profilometer. Access to this data would push the performance of the instrument into the regime detailed in Figure 11-1

11.1.2 Larger C Mount Optics

The light collected by the microscope objective must be throttled through the lens tube before becoming focused on the camera sensor by the eyepiece lens. The diameter of the lens tube limits the diameter of light able to be focus onto the sensor. This relationship is summarized in Table 7.1. Currently the instrument uses a 1" format C-Mount lens resulting in a 16mm diameter output. Changing to a

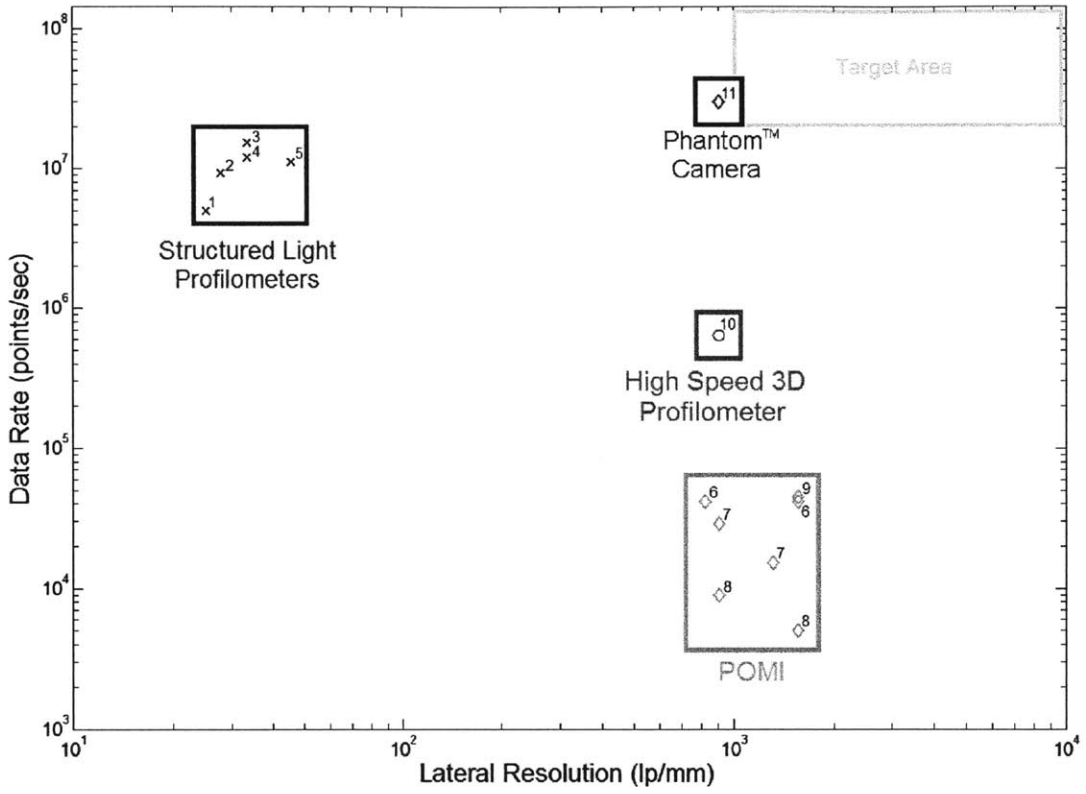

Figure 11-1: Performance Comparison Against Commercial Profilometers. Lateral resolution and inspection speed have been identified as the two most important performance parameters when evaluating commercial profilometers. Our instrument has demonstrated the ability to collect 640,000 data points per second at 0.5 micron lateral resolution and process the data off line. With faster cameras it may be possible to increase this speed by an additional factor of 50 as shown by the brown data point.

4/3" format would increase the diameter to 21.6mm. This increase in diameter serves to increase the light flux captured by the system and thereby increases the light limited frame rate. A larger diameter light circle also allows for bigger pixels which correlate to higher fill factors. Moreover, the larger pixels are better suited to be used with commercially available 50X extra long working distance objective lens ensuring that the magnified pixels are sized appropriately based upon the Raleigh Criterion. The Phantom v1610 suggested camera has a 1280 x 800 pixel array with each pixel sized at 28 microns. Using the 1" C-Mount sensor format allows for only 25% of this sensor to be utilized while the 4/3" sensor format increases this percentage to 46%. Although a reduction in rows in columns used by the sensor will in turn increase the frame rate, the reduced use configuration will output less data per second. Thus, a larger tube lens and C-Mount sensor format allows for more of the camera sensor to be utilized at a higher fill factor ultimately increasing the light flux collected by the camera.

11.1.3 Real Time Processing

The commercial version of the high speed profilometer must be able to process the camera's data at the rate in which the data is acquired. Currently our hardware collects the data and stores it into the computer's RAM. Once the acquisition is complete, the information is then loaded into MATLAB and processed offline over a series of hours. The calculations on processing power in Chapter 8 concretely show that a well powered processor could process 14 gigapixels per second of information in real time. This 14 gigapixel per second rate represents the maximum amount of data that the fastest camera can collect. While the theoretical calculations are sufficient to prove the viability of the processing, there are many logistical and practical issues that would need to be solved to implement such a device. The implementation of the real time processing is a integral part of making the high speed profilometer a useful tool.

11.1.4 Structured Lighting

The major drawback to the high speed profilometer as compared other instruments in the field is its compromised vertical resolution. At best, the high speed profilometer was able to output a resolution of 500 nanometers which is orders of magnitude more noisy than the 0.1 nanometer resolution quoted by white light interferometers. Furthermore, this resolution could only be achieved on parts that had adequate surface roughness. Although the structured light configurations attempted during the research project were not fruitful, it is possible that some type of structured lighting can be implemented to address both of these problems. Such as system would need to be implemented while transmitting light through the part to retain the high levels of light flux. This approach would represent a shift in implementation from the current tools given that white light interferometers, color laser scanners, and structured light profilometers rely on reflection to conduct their measurements.

11.2 Thickness and Edge Detection Sensor

The thickness and edge detection sensor developed in this research demonstrates superior performance to the state of the art technology when measuring the lateral position of a transparent web. The device can simultaneously measure the thickness of the web in a fashion that is insensitive to temperature and force loop variations. Moving forward, the hardware used to show the capability of the device needs to be paired down and simplified. The Basler A504k camera and Mitutoyo microscope objective used in this application need to be replaced with a different components that are less powerful and bareboned to save on cost. This evolution of the instrument is antithetical to the changes that need to be made on the high speed profilometer. The budget of the next generation sensor must to be commensurate with the current $1,000 price tag on the state of the art sensors. The following measures are suggested in order to meet this constraint.

11.2.1 Cost Effective Components

The second generation sensor needs to use less expensive components in order to meet the market needs. The full flexibility and power behind the Basler A504k camera is not necessary to operate the sensor. The cost of the camera is found to be largely driven by the amount of data that the it can output per second. Given the sensor configuration, the information collected by the columns is largely redundant and serves only to make a better measurement. One cost cutting measure is to use a fairly slow camera and speed up the frame rate by reducing the number of columns per image. The user may find it more advantageous to run at 500 frames per second while using 100 columns rather than 50 frames per second at 1,000 columns. Such a setup could be serviced by a camera that outputs 10 times less data than the Basler A504k which should drive the cost down significantly. Furthermore, it is suggested to use a lower powered microscope objective that has an adequately narrow depth of focus to single out the lines of the Ronchi grating. Lastly, it is advised to equip the camera with an onboard processor capable conducting the image processing without a secondary CPU. This addition would save both on cost and physical space required to run each sensor.

11.2.2 Simplified Geometry

The redesign of the sensor needs to incorporate a significant reduction in size to be easy incorporated into the current roll to roll manufacturing hardware. The current hardware is over 500 cm long from the front of the objective lens to the back of the camera. Most of this distance is eaten up by the infinity corrected microscope objective that needs to be placed one focal distance away from the eyepiece lens. Reducing the power of this lens is projected to save both on cost and space. Secondly, there should be a concrete connection between the lens apparatus and the Ronchi grating whereby the grating can be properly positioned and tilted. The flexibility of this link is important to properly interest the focal plane of the camera with the Ronchi grating. Lastly, there should be a well designed interface between

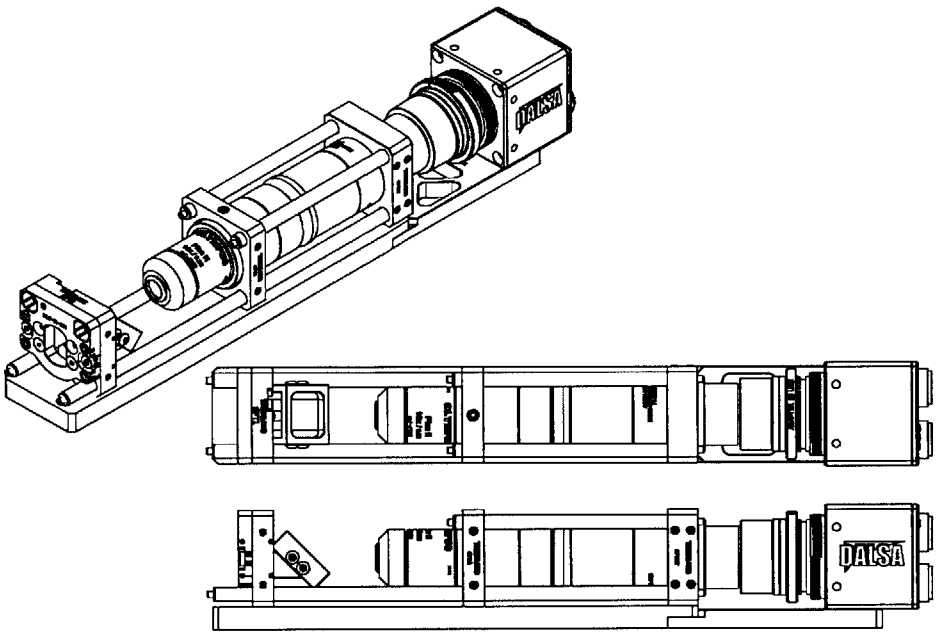

Figure 11-2: CAD Drawing of the Next Generation Sensor. This solid model capture outlines the geometry for the second generation lateral position sensor. The design emphasizes a significant reduction in size and simplification of components.

the light source and the sensor. The light source needs to be positioned properly such that the transmission shines through the grating and onto the camera pixels. Optimally the light source would be concentrated on the plane of focus such that superfluous light does not heat up the part nor the sensor. The basic effect of these changes can be seen in Figure 11-2 which outlines the basis for the second generation instrument.

Bibliography

[1] C. Hidrovo and D. Hart. Emission reabsorption laser induced fluorescence (erlif) film thickness measurement. *Measurement Science and Technology*, 12:467–477, April 2001.

[2] S. Li, Z. Xu, I. Reading, S. Yoon, Z. Fang, and J. Zhao. Three dimensional sidewall measurements by laser fluorescent confocal microscopy. *Optics Express*, 16:4001–4014, March 2008.

[3] A. Ishii, J. Mitsudo, and Y. Fujinaka. Three-dimensional shape sensor based on lateral focused-plane sectioning. volume 5602, pages 99–106. SPIE-INT SOC Optical Engineering, October 2004.

[4] Artur Olszak. Lateral scanning white-light interferometer. *Applied Optics*, 39:3906–3913, 2000.

[5] Artur Olszak. *Lateral Scanning Interferometer with Tilted Optical Axis*, September 2002. US Patent 6,449,048.

[6] U. Paul Kumar, Basanta Bhaduri, M. P. Kothiyal, and N. Krishna Mohan. Two-wavelength micro-interferometry for 3-d surface profiling. *Optics and Lasers in Engineering*, February 2009.

[7] P. Montgomery, F. Anstotz, and J. Montagna. High-speed, on-line 3d microscopy using continuously scanning white light interferometry with a high-speed camera and real-time fpga image processing. volume 8082. SPIE, May 2011.

[8] T. Marschner and C. Stief. Characterization of 193-nm resist layers by critical dimension-scanning electron microscopy sidewall imaging. *Journal of Microlithograpy Mircofabiraction and Microsystems*, 4, March 2005.

[9] Shiguang Li and Zhiguang Xu. Review of production of microfluidic devices: material, manufacturing and metrology. *Proceedings of SPIE*, 6993, April.

[10] T. Kurfess and T. Hodgson. *Micromanufacturing: International Assessment of Research and Deveolpment.* Springer-Verlag, Dordrecht, The Netherlands, 2005.

[11] I. Young, R. Zagers, and L. van Vliet. Depth-of-focus microscopy. In *Proc. of the 8th Scandinavian Conference on Image Analysis*, pages 493–498, Tromso, Norway, 1993. SCIA.

[12] Edmund Optics. *Edmund Optic Digital Catalog: B121*, Accessed March 2012.

[13] Curtis Chin. Microfluidics-based diagnostics of infectious diseases in the developing world. *Nature Medicine*, 17(8), 2011.

[14] Quan Guo, Sarah Reiling, Petra Rohrbach, and Hongshen Ma. Microfluidic biomechanical assay for red blood cells parasitized by plasmodium falciparum. *Lab on a Chip*, 12(6), 2012.

[15] Chih-Hao Wang and Gwo-Bin Lee. Automatic bio-sampling chips integrated with micro-pumps and micro-valves for disease detection. *Biosensors and Bioelectronics*, 21(3):419–425, 2005.

[16] Lisong Wang, Chuan Leng, Sheng Tang, Jianping Lei, and Huangxian Ju. Enzyme-free signal amplification for electrochemical detection of mycobacterium lipoarabinomannan antibody on a disposable chip. *Biosensors and Bioelectronics*, 38(1):421–424, 2012.

[17] Nicolaos Christodoulides, Sanghamitra Mohanty, and Craig Miller. Application of microchip assay system for the measurement of c-reactive protein in human saliva. *Lab on a Chip*, 5:261–269, 2005.

[18] Ronalee Lo, Po-Ying Li, and Saloomeh Saati. A refillable microfabricated drug delivery device for treatment of ocular diseases. *Lab on a Chip*, 8:1027–1030, 2008.

[19] Michael Mauk, Barry Ziober, and Zongyuan Chen. Lab-on-a-chip technologies for oral-based cancer screening and diagnostics. *Annals of teh New York Academy of Sciences*, 1098(1):467–475, April 2007.

[20] Curtis Chin, Vincent, Linder, and Samuel Sia. Lab-on-a-chip devices for global health: Past studies and future opportunities. *Lab on a Chip*, 7:41–57, October 2006.

[21] Matteo Calaon, Aminul Islam, Hans Hansen, and Christian Ravn. Experimental investigation of new manufacturing process chains to create micro-metal structures on polymer substrates for lab-on-chip sensors. *International Journal of Advanced Manufacturing Technology*, 59(1-4):101–109, 2012.

[22] Asger Vig, Tapio Makela, and Paivi Majander. Roll-to-roll fabricated lab-on-a-chip devices. *Journal of Micromechanics and Microengineering*, 21:1–6, 2011.

[23] Curtis Chin, Vincent Linder, and Samuel Sia. Commercialization of microfluidic point-of-care diagnostic devices. *Lab on a Chip*, 12:2118–2134, 2012.

[24] Brian Anthony, David Hardt, Melinda Hale, and Nadege Zarrouati. A research factory for polymer microdevices: mufac. volume 7593 of *Proceedings of SPIE*. Society of Photo-optical Instrumentation Engineers, August 2010.

[25] N. G. Shankar and Z.W. Zhong. Defect detection on semiconductor wafer surfaces. *Microelectronic Engineering*, 77:337–346, April 2005.

[26] H.N. Hansen, K. Carneiro, H. Haitjema, and L De Chiffre. Dimensionalmicro and nanometrology. *CIRP Annals - Manufacturing Technology*, 55(2):721–743, 2006.

[27] H. Ikeoka and T. Hamamoto. Depth estimation using variant of depth of field by horizontal planes of sharp focus. volume 5744 of *12th International FIRA RoboWorld Congress*, pages 282–291. Springer-Verlag Berlin, August 2009.

[28] T. Marschner, G. Eytan, and O. Dror. Determination of best focus and exposure dose using cd-sem side-wall imaging. volume 4344 of *Metrology, Inspection, and Process Controll for Microlithography XV*, pages 355–365. SPIE-INT Society Optical Engineering, March 2005.

[29] P. de Groot and L. Deck. Three-dimensional imaging by sub-nyquist sampling of white-light interferograms. *Optics Letters*, 18(17):1462–1464, 1 Sept 1993.

[30] S. Caspar and M. Honegger. High speed fringe projection for fast 3d inspection. volume 8082 of *Proceedings of SPIE*. Optical Measurment Systems for Industrial Inspection VII, August.

[31] Koh Young Technology. Prime. the world's first profilometeric measurement-based 3d in-line bump inspection system. `www.kohyoung.com`, 2009.

[32] Parmi Co. Spi hs60 3d solder paste inspection system. `www.easybraidco.com/pdfs/SPIHS60_Eng.pdf`.

[33] VI Technology. 3d spi solder paste inspection. `www.vitechnology.com/rep-smt/ido-1/3d_spi.html`, April 2010.

[34] CyberOptics. Se500cp solder paste inspection system. `www.cyberoptics.com/client_files/documents/SE500cp_lit.pdf`, 2010.

[35] CKD Corporation. Solder printing inspection machine vp6000 series. `www.ckd.co.jp`, 2008.

[36] Olympus. Microscope components guide. `www.olympusamerica.com/seg_section/files/scientific_component_guide.pdf`, 2008.

[37] Edmund Optics. Mitutoyo infinity-corrected long working distance objectives.

[38] Basler. Basler cameras: Product line overview. www.baslerweb.com/media/documents/BAS1301_PLO_e_web.pdf.

[39] Matt Dirckx. *Demolding of Hot Embossed Polymer Microstructures.* PhD thesis, Massachusetts Institute of Technology, Cambridge, MA, 2010.

[40] Meng, Junhu, and Gang. Replication and characterization of 316l stainless steel micro-mixer by micro powder injection molding. *Journal of Alloys and Compounds*, 496:293–9, 2010.

[41] Meng, Loh, and Gang. Micro powder injection moulding of alumina micro-channel part. *Journal of the European Ceramic Society*, 31, 2011.

[42] Bart Raeymaekers and Frank E. Talke. Measurement and sources of lateral tape motion: A review. *Journal of Tribology-Transactions of the ASME*, 131(1), 2009.

[43] M. Haque and D. Winter. *Synthetic Light Sensor for Web-Guiding Apparatus*, November 2001. US Patent 6,323,948.

[44] A. Goldade and B. Bhushan. Measaurement and origin of tape edge damage in a linear tape drive. *Tribology Letters*, 14(3):167–180, April 2003.

[45] Wen H Ko. *Ultrasonic Edge Detector*, June 1992. US Patent 5,126,946.

[46] M. Haque and D. Winter and D. Hueppelshueser. *Ultrasonic Sensor for Web-Guiding Apparatus*, September 2001. US Patent 6,289,729.

[47] Aravind Seshadri and Prabhakar Pagilla. "design and development of a new edge sensor for web guiding. *IEEE Sensors Journal*, 7(5):698–706, May 2007.

[48] G. Coppola. Method for measuring the refractive index and the thickness of transparent plates with a lateral-shear, wavelength-scanning interferometer. *Applied Optics*, 42(19):3882–3887, 2003.

[49] Mohammad Fathi and Silvano Donati. Thickness measurement of transparent plates by a self-mixing interferometer. *Optics Letters*, 35(11):1844–1846, 2010.

[50] Y. Kumar and Sanjib Chatterjee. Thickness measurement of transparent glass plates using a lateral shearing cyclic path optical configuration setup and polarization phase shifting interferometry. *Applied Optics*, 49(33):6552–6557, 2010.

[51] Peter de Groot. Measurement of transparent plates with wavelength-tuned phase-shifting interferometry. *Applied Optics*, 39(16):2658–2663, 2000.

[52] H. Mansoor, H. Zeng, and M. Chiao. A micro-fabricated optical scanner for rapid non-contact thickness measurement of transparent films. *Sensors and Actuators A-Physical*, 167(1):91–96, 2011.

[53] T. Fukano and I. Yamaguchi. Simultaneous measurement of thicknesses and refractive indices of multiple layers by a low-coherence confocal interference microscope. *Optics Letters*, 21(23):1942–1944, 1996.

[54] Shein Ri and Takashi Muramatsu. A simple technique for measuring thickness distribution of transparent plates from a single image by using the sampling moire method. *Measurement Science and Technology*, 21(2), 2010.

[55] Chien-Hung Liu, Shien-Chang Yeh, and Hsueh-Liang Huang. Thickness measurement system for transparent plates using dual digital versatile disc (dvd) pickups. *Applied Optics*, 49(4):637–643, 2010.

[56] Re. Guiding systems catalogue. `www.re-spa.com/Re_EN/relink_sf.html`.